Search for Standard Model Higgs Boson in $ZH \to \nu\bar{\nu}b\bar{b}$ channel in $p\bar{p}$ collisions at $\sqrt{s} = 1.96$ TeV

THESIS SUBMITTED TO THE UNIVERSITY OF DELHI
FOR THE DEGREE OF

DOCTOR OF PHILOSOPHY

ABHINAV DUBEY

SUPERVISORS: PROF. BRAJESH C. CHOUDHARY
PROF. SATYAKI BHATTACHARYA

DEPARTMENT OF PHYSICS & ASTROPHYSICS
UNIVERSITY OF DELHI
DELHI 110 007
INDIA

2011

Declaration

This thesis presents a search for the standard model higgs boson in $p\bar{p}$ collisions at the centre-of-mass energy ($\sqrt{s}$) of 1.96 TeV in $ZH \rightarrow \nu\bar{\nu}b\bar{b}$ channel using 5.2 fb^{-1} of data collected with the DØ detector at Fermilab. Most of the work presented in this thesis has been published.

This work has been done under the supervision of Prof. Brajesh C. Choudhary and Prof. Satyaki Bhattacharya. This work has been done by the candidate himself and to the best of his knowledge, no part of this work has earlier been submitted for any degree or diploma of this or any other university.

(ABHINAV DUBEY)

Candidate

(Prof. Brajech C Choudhary)

Supervisor

(Prof. Satyaki Bhattacharya)

Co-Supervisor

Prof. R. P. Tandon

Head

Department of Physics & Astrophysics

University of Delhi

Delhi 110 007

Search for the Standard Model Higgs boson in the ZH $\rightarrow \nu\bar{\nu}b\bar{b}$ Channel in $p\bar{p}$ Collisions at $\sqrt{s} = 1.96$ TeV

Abhinav Dubey
University of Delhi

ABSTRACT

A search for the standard model Higgs boson is performed in 5.2 fb^{-1} of $p\bar{p}$ collisions at $\sqrt{s} = 1.96$ TeV, collected with the DØ detector at the Fermilab Tevatron. The final state considered is a pair of b jets with large missing transverse energy, as expected from $p\bar{p} \rightarrow ZH \rightarrow \nu\bar{\nu}b\bar{b}$ production. The search is also sensitive to the $WH \rightarrow \ell\nu b\bar{b}$ channel, where the charged lepton is not identified. Boosted decision trees are used to discriminate signal from background. Good agreement is observed between data and expected backgrounds, and, for a Higgs-boson mass of 115 GeV, a limit is set at 95% C.L. on the cross section multiplied by branching fraction of $(p\bar{p} \rightarrow (Z/W)H) \times (H \rightarrow b\bar{b})$ that is a factor 4.57 expected and 3.73 observed larger than the value expected from the standard model.

Dedicated To My Parents

ACKNOWLEDGEMENTS

First I will like to say thanks to my supervisor Prof Brajesh C. Choudhary for providing me all his support and expertise. I am also sincerely thankful to all the members of zhnunubb analysis team who directly contributed into aspects of the work in my thesis. I am very much thankful to Walter Geist, I learned a lot from him and really enjoyed working with him. I will like to thank George Ginther and Dean R. Schamberger for their guidance in detector and related physics. I will like to thank Vishnu Zutshi and Sergey Uzynman for their support. I will like to thank Lidija and Ken Herner for guiding me through all my $\not\!\!E_T$ studies. I will also like to thank Brendan for his help. I will like to say thanks to all members of Calorimeter operation team for their assistance and support. I will like to thank Ashish Kumar for all his guidance.

I will like to thank everyone in High Energy Physics group at University of Delhi including my Co-Supervisor Satyaki Bhattacharya for their valuable guidance and help.

I will like to thanks all the DØ collaborators and Fermilab staff for their assistance. I will like to say thanks to all the group convenors, physics convenors and spokes for their guidance and assistance.

I will like to thanks Pooja, Sushil and Seema for all her guidance. I will also like to thank Vipin Bhatnagar for all his guidance. I will like to thanks Avdhesh, Ekta, Anju, Shilpee, Manoj, Ruchika, Arun Soma, Sonam, Ruchi, Sudha, Pooja for their support.

I am thankful to my family for providing their full support and encouragement.

I am grateful to Fermilab, CSIR-UGC and DST India for the finacial support I received.

ABHINAV DUBEY

Contents

List of Figures

List of Tables

Chapter 1

Standard Model

Human curiosity has no limits and it is very natural for a curious mind to think about the universe we live in. Some people think "what the world is all about" at a very philosophical level. Others think "what the world is made up of and how it functions". Particle physics tries to answer the very question about the existence of this world and its constituents, at a very fundamental level, by identifying the elementary building blocks of nature and the forces operating between them (interactions). Historically elementary particles have always played a significant role in the understanding of the universe and thats why this unique field of particles and their interactions has always been the center of attraction among physicists, enjoying special status among other physics disciplines. Particle physics is also known as high energy physics because most of the elementary particles do not occur in normal circumstances in nature due to very short lifetime so we need high energy collisions of particles to create and detect them. In the last century a lot of effort has been put in studying the particles and their interactions and the gathered knowledge has been incorporated into a theory which is known as the "Standard Model" of particle physics.

1.1 Historical Development

The history of particle physics can be rooted back to ancient Indian philosophy which says that the universe is made of five basic elements: water, earth, air, fire and space. Evidence of this belief was found in other civilizations also. Around 600 B.C. an India philosopher named Kanada, came with the idea of indivisible particles. Greek philosophers Leucippus and his disciple Democritus in 5th century B.C. developed this idea further by proposing that everything in the universe is made of small indivisible entities, - "the atomos". In Greek "atomos" stands for "indivisible". This concept was the first step towards quantifying macroscopic phenomena into fundamental particles and their interactions. This

philosophical idea evolved into an arena of natural science where one can experimentally verify the metaphysical theories of the universe involving fundamental particles and their interactions. The next step in the advancement of this theory came in 1802 in form of "atomic theory" proposed by Dalton which indicated atoms as constituents of chemical element. Dalton's idea was further supported by Mendeleev who came up with an idea of periodic table in 1869, which predicted existence of further new elements. Dalton's theory of atoms was a major step in understanding the nature of universe.

In 1897, world of particle physics was revolutionized by the discovery of electrons by J. J. Thompson [1], confirming the idea of atomic sub-structure. The rules of classical physics were not applicable inside the sub-atomic world. To explain the characteristics of sub-atomic particles at microscopic scale, concept of quantum mechanics were put on paper by Planck, Bohr, Heisenberg, Schrodinger and others [2]. Around same time Einstein came with the "theory of relativity" [3] which added additional depth in the knowledge of sub-atomic particle dynamics. In 1911 Rutherford came with the idea of positive charged nucleus surrounded by negatively charged cloud of electrons [4]. Later the discovery of proton by Rutherford in 1919 [5], which was also proposed earlier by Goldstein in 1886 [6], and neutron (by Chadwick in 1932) [7] confirmed the hypothesis that nucleus was made up of protons and neutrons. Thus by early 30's the basic understanding of matter sub-structure was confined to electrons, protons and neutrons.

However the compactness of nucleus (1 fm=10^{-15} m) was an issue because several positive charged protons can't be confined into such a small nucleus due to electrostatic repulsive force. Stability of the nuclei gave rise to the idea of "strong force" which is strong enough to overcome the electrostatic repulsive force among protons and bind them inside the nucleus. In 1927 Dirac combined the theory of relativity and quantum mechanics into a single theory called 'quantum field theory' (QFT) [8]. With this proposition, he also predicted the existence of 'antimatter' particles [9] [10], each of which has the same mass but opposite charge as its corresponding matter particle. In 1932 the positron (anti-electron) was discovered by Anderson [11], confirming the anti-matter theory proposed by Dirac. Around the same time, Pauli, while studying the β decay problem, proposed the existence of an unobserved neutral particle, with spin 1/2 and having a very small mass compared to the proton (no more than 1% of proton mass) [12] to explain the mass-energy and momentum conservation. Enrico Fermi carried forward Pauli's idea and developed the theory of beta decay. Fermi named these particles as neutrino [13]. The process was explained by a new type of interaction called as "weak interaction". In 1940s, Feynman, Schwinger, and Tomonaga, developed quantum electrodynamics (QED) [14] [15] [16], which explained electromagnetic phenomena at a basic level in terms of the exchange of photons. The QED was tested experimentally with great success. Till now the big picture

evolving from all these studies was that the description of particles needs a quantum field theory which somehow incorporates all the three interactions: strong, electromagnetic and weak.

The unification of the electromagnetic and weak interactions - Electroweak [17] using the gauge group $SU(2)_L \otimes SU(1)_Y$, proposed by Glashow, Salam and Weinberg in mid 1960's, was one of the major breakthrough in physical sciences in last century. The Quantum Chromo Dynamics (QCD) [18] is the theory of strong interaction among the coloured quarks and gluons which is based on the symmetry group $SU(3)_C$. Combining Electroweak and QCD provides the unified framework which takes into account the three fundamental forces of nature. It is known as the standard model (SM) which is the most consistent theory of fundamental particle and their interactions. This theory being purturbative [18] and renormalizable [19] at very high energies provides an excellent description of these interactions at quantum level. The theory has been scrutinized in great detail at various high energy experiments during the last four decades and till date no experimental evidence is found against its predictions.

Spontaneous electroweak symmetry breaking (EWSB) via Higgs mechanism is one of the key aspects of the SM which was first proposed by Englert, Brout, Higgs, Guralnik, Hagen and Kibble [20]. After the discovery of week neutral current at the Gargamelle experiment [21] in early 1970's and intermediate vector bosons (W^+, W^- and Z^0) at CERN [22] in early 1980's, probing EWSB became the centre of attraction of particle physicists and the search for the Higgs boson took the center stage among the EHEP experiments across the globe. In 1970's and 1980's considerable understanding of the expected properties of Higgs boson was developed both within the SM framework and its (supersymmetric and non supersymmetric) extensions. At the end of 1980's, basic properties of Higgs boson, its main production mechanisms in hadron and lepton colliders and principle decay modes were well known. Search for Higgs boson was central objective of LEP which failed to find it but put a very strong limit on the mass of the SM Higgs boson, $M_H > 114.4$ GeV [23], ruling out broad low mass Higss region, while indirect experimental measurements using precise electroweak data set an upper limit of 144 GeV [24]. In 1995, the top quark was discovered at the Tevatron [25] [26]. With the determination of the top mass [27], most of the SM parameters are now well known except that we still do not have any idea about the Higgs. Experimental evidence of the Higgs boson is very important for the consistency of the SM theory.

There is an old saying "Theory Guides and Experiment Decides". With all these experimental advancements, large effort has also been devoted on the theoretical front in detailed study of all the major production and decay processes of Higgs boson at colliders. For all major Higgs production processes, next-to-leading order radiative corrections were

calculated. For some processes like gluon-gluon fusion and Higgs-Strahlung at hadron colliders, the radiative corrections to cross-sections have been calculated even for up to next-to-next-to-leading order for strong interaction part and for next-to-leading order for electroweak part [28]. In addition, for various Higgs signals and backgrounds, parton level analysis and Monte Carlo simulation, taking into account the experimental environment of Tevatron and LHC has been done.

Finding this last missing link of the SM, the Higgs boson, and studying its properties is one of the highest priority at the Tevatron and is also the central objective of the CERN Large Hadron Collider physics programme.

1.2 General Aspects

The SM is the most profound theory of elementary particles and their interactions. It is a non-abelian gauge theory based on $SU(2)_L \otimes U(1)_Y \otimes SU(3)_C$ symmetry group. Elementary particles consist of fermions, consisting of quarks and leptons, which are the basic building block of the universe, and gauge bosons which are mediators of their interactions.

1.2.1 Fundamental Interactions

There are four fundamental interactions in nature - strong, electromagnetic, weak and gravitational. Weak and electromagnetic interactions have been unified into a single "Electroweak theory" and the theory of strong and electroweak interactions have been incorporated into the SM. The dynamics of these interactions is described by gauge theories in which the Lagrangian is invariant under gauge transformations. These transformations form a symmetry group, called gauge group, whose generator leads to the corresponding vector fields, the gauge fields. If symmetry group is non-commutative, gauge theory is called non-abelian. The quanta of gauge fields are called gauge bosons.

Quantum Electrodynamics is an abelian gauge theory with symmetry group $U(1)_{EM}$ having electromagnetic gauge field and the photon as gauge boson. The weak interactions are described by $SU(2)_L$ gauge group. The electroweak theory predicts that at very high energy there are four massless vector bosons with symmetry group $SU(2)_L \otimes U(1)_Y$. But the short range of weak force indicates that it is mediated by massive particles, implying the underlying gauge symmetry of electroweak group is spontaneously broken to $U(1)_{EM}$ group of electromagnetic interactions via some mechanism, providing mass to three weak gauge bosons W^+, W^- and Z^0. The fourth gauge boson, the photon remains massless. The mechanism responsible for massive weak gauge bosons is known as Higgs mechanism.

Quantum Chromodynamics is the non-abelian gauge theory which describes strong interactions between quarks by the symmetry group $SU(3)_C$ of "color" charge. By convention, the color charge can be "red", "blue" or "green". The interactions between quarks are mediated by gluons which also carry color charge, and therefore participate in strong interactions. The quarks and gluons together constitute the hadrons. The main aspect of QCD is "asymptotic freedom", which means at very high energies quarks and gluons interact very weekly. Another important aspect of QCD is "color confinement", which means there is always force between quarks however far they are so they can never be isolated singularly. This is the reason quarks confine themselves as color neutral combination of baryons and mesons and we have only eight types of gluons. As we have discussed above, QCD and QED have important differences. First, in QED there is only one type of charge but in QCD we have three type of color charge. Another difference is that in QED the photon does not carry any charge so they can not interact with each other but in QCD gluons do carry color charge so they can interact with each other via strong interaction.

The gravitational interaction is forty orders of magnitude weaker than the strong interaction and is not included in the mathematical formalism of the SM. It is believed to be mediated via a massless boson "graviton", but its experimental evidence has not been found yet.

Basic properties of gauge bosons have been summarized into Table 1.1 [29].

Force	Gauge Boson	Charge	Spin	Mass (GeV/c^2)	Range	Rel. Strength
Strong	Gluon (g)	0	1	0	$10^{-15}m$	1
EM	Photon(γ)	0	1	0	∞	1/137
Weak	$W^{\pm}$	±1	1	80.423 ± 0.039	$10^{-18}m$	10^{-5}
	Z^0	0	1	91.188 ± 0.002		
Gravity	Graviton (G)	0	2	0	∞	10^{-38}

Table 1.1: Fundamental forces and gauge bosons and their properties: for strong force mediators are gluons; for electromagnetic force, photons; for weak force, $W^{\pm}$ and Z^0 and for gravity, graviton.

1.2.2 Fundamental Particles

In the SM, we have basically two types of fundamental particles. Matter particles, described as spin 1/2 fermions and force carriers, described as spin 1 gauge bosons. The gauge bosons has been already described in Section 1.2.1.

Fermions consist of quarks and leptons. There are six flavors of leptons forming three generations. These are: electron (muon) [tau] family, consisting of the electron,

e, (muon, μ) [tau, τ] and electron neutrino, ν_e, (muon neutrino, ν_μ) [tau neutrino, ν_τ]. Electron, muon and tau are charged particles. They interact via electromagnetic and weak interactions. Neutrinos are chargeless and interact through weak interactions only. In the SM neutrinos are considered as massless but experimental evidence indicates that they have masses, although quite small [29].

Quarks also come in six flavors known as - up (u), down (d), charm (c) , strange (s), top (t) and bottom (b). They carry fractional charge - either $+\frac{2}{3}$e or $-\frac{1}{3}$e, where e is the charge of the electron. Quarks participates in strong, electromagnetic as well as weak interactions. Basic features of $fermions$ has been summarized in Table 1.2 [29].

Gen	Leptons (spin=$\frac{1}{2}$)			Quarks (spin=$\frac{1}{2}$)		
	Flavors	Charge	Mass (MeV)	Flavors	Charge	Mass (MeV)
1	e	-1	0.511	u	$+2/3$	$1.5-4.5$
	ν_e	0	$< 3\times10^{-6}$	d	$-1/3$	$5-8.5$
2	μ	-1	105.7	c	$+2/3$	$(1.0-1.4)\times10^3$
	ν_μ	0	< 0.19	s	$-1/3$	$80-155$
3	τ	-1	1777	t	$+2/3$	$(172.0\pm4.3)\times10^3$
	ν_τ	0	< 18.2	b	$-1/3$	$(4.0-4.5)\times10^3$

Table 1.2: Three generations of elementary particles.

Most of the matter we are familiar with are made of first generations of leptons and quarks. Thus we have twelve elementary particles. In addition, for every particle in Table 1.2, there is a corresponding anti-particle which has the same mass and spin but opposite charge. For example, the positron (e^+) and electron anti-neutrino ($\overline{\nu}_e$) are the anti-particles of electron (e^-) and electron neutrino (ν_e), respectively. Similarly $\overline{u}$ is the anti-particle of u.

Thus taking into account the color charge of quarks, most of the visible matter of universe is made of these 48 fundamental particles. Hadrons consist of mesons, which are made of quark and anti-quark pairs, and baryons, which are made of quarks or anti-quarks triplets.

1.3 Mathematical Formulation

In this chapter we are going to describe about the mathematical formulation of the SM. Gauge theories, Fermionic fields and the SM Lagrangian formalism will be discussed in detail.

1.3.1 Gauge Theories

A gauge transformation is a local group transformation. A gauge theory requires the introduction of "gauge fields", spin - 1 bosons which mediates the corresponding force, to keep the Lagrangian invariant under a gauge transformation.

Free matter particles can be described by a Dirac field $\psi(x)$ whose Lagrangian can be written as

$$\mathcal{L}_\psi = \overline{\psi}(i\gamma^\mu\partial_\mu - m)\psi, \tag{1.1}$$

where γ^μ are 4x4 matrices. Now we define a gauge transformation as

$$\psi \rightarrow \psi' = U(x)\psi(x) = e^{-i\alpha(x)}\psi(x), \tag{1.2}$$

$$\overline{\psi} \rightarrow \overline{\psi}' = \overline{\psi}(x)U^\dagger(x) = \overline{\psi}(x)e^{i\alpha(x)}. \tag{1.3}$$

On applying this transformation, the new Lagrangian will be

$$\mathcal{L}_\psi \rightarrow \ \mathcal{L}'_\psi = \mathcal{L}_\psi + \overline{\psi}\gamma_\mu\psi\partial^\mu\alpha(x) \tag{1.4}$$

and not invariant. Now if we introduce a gauge field A_μ through the minimal coupling

$$D_\mu = \partial_\mu + ieA_\mu, \tag{1.5}$$

and transform A_μ as

$$A_\mu \rightarrow A'_\mu = A_\mu + \frac{1}{e}\partial_\mu\alpha(x), \tag{1.6}$$

the new Lagrangian can be written as

$$\begin{aligned}
\mathcal{L}_\psi \rightarrow \ \mathcal{L}'_\psi &= \overline{\psi}'(i\gamma^\mu D_\mu - m)\psi' \\
&= \overline{\psi}e^{+i\alpha(x)}[i\gamma^\mu(\partial_\mu + ieA'_\mu) - m]e^{-i\alpha(x)}\psi \\
&= \overline{\psi}e^{+i\alpha(x)}[i\gamma^\mu\partial_\mu - e\gamma^\mu(A_\mu + \tfrac{1}{e}\partial_\mu\alpha(x)) - m]e^{-i\alpha(x)}\psi \\
&= \overline{\psi}[i\gamma^\mu\partial_\mu - m]\psi - e\overline{\psi}\gamma^\mu\psi A_\mu \\
&= \mathcal{L}_\psi - e\overline{\psi}\gamma^\mu\psi A_\mu
\end{aligned} \tag{1.7}$$

which is invariant under the gauge transformation in Equation 1.4.

Imposing invariance under local gauge transformations $U(1)$ on the kinetic energy term of free fermion Lagrangian results in coupling between ψ and A_μ, given by the term $e\overline{\psi}\gamma^\mu\psi A_\mu$. An additional kinetic energy term which is invariant under transformation

$U(1)$ can be written as

$$\mathcal{L}_{K.E.} = -\frac{1}{4}F_{\mu\nu}F^{\mu\nu}, \tag{1.8}$$

where $F_{\mu\nu} = \partial_\mu A_\mu - \partial_\nu A_\nu$, is the electromagnetic strength tensor. Adding this invariant kinetic energy term to Equation 1.7 results in the Lagrangian for quantum electrodynamics

$$\mathcal{L}_\psi = \overline{\psi}[i\gamma^\mu\partial_\mu - m]\psi - e\overline{\psi}\gamma^\mu\psi A_\mu - \frac{1}{4}F_{\mu\nu}F^{\mu\nu}. \tag{1.9}$$

Since $m^2 A_\mu A^\mu$ is not invariant under gauge transformation, massive vector bosons can not be described by imposing gauge invariance. Similarly various symmetry groups gives different interactions. Strong interactions are attributed to $SU(3)_C$ symmetry group whereas weak interactions are based on symmetry group $SU(2)_L$.

1.3.2 Fermionic fields

Dirac spinors can be written as $u(p,s)$ and $v(p,s) = i\gamma_2 v^*(p,s)$, which are eigenstates of γ_5 matrix. We can define chirality projectors P_L and P_R as

$$P_L = \frac{1-\gamma_5}{2}, \qquad\qquad P_R = \frac{1+\gamma_5}{2}, \tag{1.10}$$

where P_L and P_R satisfy the following properties: $P_L^2 = P_L$, $P_R^2 = P_R$ and $P_L P_R = 0$. Now the left-handed and right-handed fermionic components of a generic field ψ can be written as $\psi_L = P_L\psi$ and $\psi_R = P_R\psi$. For conjugate fermionic field we have $\overline{\psi}_L{=}\psi P_R$ and $\overline{\psi}_R{=}\psi P_L$. In terms of chiral states, the electromagnetic current shows a vector structure as we have

$$\overline{\psi}\gamma_\mu\psi = \overline{\psi}_R\gamma_\mu\psi_R + \overline{\psi}_L\gamma_\mu\psi_L, \tag{1.11}$$

while fermionic weak current can be written as vector minus axial-vector (V-A) term having only left-handed fermionic states

$$\overline{\psi}_L\gamma_\mu\psi_L = \overline{\psi}P_R\gamma_\mu P_L\psi = \overline{\psi}\gamma_\mu P_L^2\psi = \overline{\psi}\gamma_\mu P_L\psi = \frac{1}{2}\overline{\psi}\gamma_\mu(1-\gamma_5)\psi. \tag{1.12}$$

For a particle of spin $\vec{\mathcal{S}}$ and momentum $\vec{p}$, helicity can be written as $\vec{\mathcal{S}}\cdot\frac{\vec{p}}{|p|}$, which is the projection of particle spin $\vec{\mathcal{S}}$ in the direction of its momentum $\hat{p}$. Since eigenvalues of spin with respect to momentum direction is discrete, helicity eigenvalues are also discrete. At very high energies, i.e. massless particles, helicity is equivalent to the chirality and therefore the three families of quarks and leptons can be introduced via left as well as

right chiral fermionic fields

$$\psi_{Li}^{lepton} = P_L(\nu_i, l_i) \qquad \psi_{Li}^{lepton} = P_L(u_i, d_i) \tag{1.13}$$

$$\psi_{Ri}^{lepton} = P_R(\nu_i, l_i) \qquad \psi_{Ri}^{lepton} = P_R(u_i, d_i) \tag{1.14}$$

and they interact under $SU(2)_L$. Only left handed fermion participate in the weak interaction.

1.3.3 Standard Model Lagrangian

The unification of electromagnetic and weak interactions was done by Glashow-Salam-Weinberg model which is based on $SU(2)_L \otimes U(1)_Y$ group where L refers to weak isospin and Y to leptonic hypercharge. The symmetry group for QED - $U(1)_Q$ which is an abelian gauge group, is subset of $SU(2)_L \otimes U(1)_Y$. The gauge boson of this latter group is photon which is neutral and the generator is electric charge - Q. For the group $U(1)_Y$, Q is replaced by leptonic hypercharge. Weak isospin and leptonic hypercharge are related to electric charge Q by the Gell-Mann-Nishijima equation [30]

$$Q = T_3 + \frac{Y}{2}, \tag{1.15}$$

where T_3 is the third component of weak isospin of $SU(2)_L$.

There are four gauge bosons for the symmetry group $SU(2)_L \otimes U(1)_Y$. Three generators corresponding to the group $SU(2)_L$ - W_μ^1, W_μ^2 and W_μ^3 with coupling constant g, and a neutral field B_μ related to $U(1)_Y$ with coupling constant g'. The coupling constants g and g' are related to electromagnetic charge via weak mixing angle $e = g' \cos\theta_W = g \sin\theta_W$ where $\sin^2\theta_W$=0.2223(21). The charged gauge bosons, $W^\pm$, can be written as linear combinations of W_μ^1 and W_μ^2 while photon and another charged weak boson Z^0 are mixture of W_μ^3 and B_μ:

$$W^\pm = \frac{1}{\sqrt{2}}(W_\mu^1 \mp W_\mu^2), \tag{1.16}$$

$$Z^0 = -B_\mu \sin\theta_W + W_\mu^3 \cos\theta_W, \tag{1.17}$$

$$A_\mu = B_\mu \cos\theta_W + W_\mu^3 \sin\theta_W, \tag{1.18}$$

The strength tensors for these gauge bosons are

$$W_{\mu\nu}^i = \partial_\mu W_\nu^i - \partial_\nu W_\mu^i, \qquad B_\mu\nu = \partial_\mu B_\nu - \partial_\mu B_\nu. \tag{1.19}$$

The free Lagrangian for the gauge fields can be expressed as

$$\mathcal{L} = -\frac{1}{4}W^i_{\mu\nu}W^{i\mu\nu} - \frac{1}{4}B_{\mu\nu}B^{\mu\nu}. \tag{1.20}$$

The SM Lagrangian density can be written as

$$\mathcal{L}_{SM} = \mathcal{L}_{fermion} + \mathcal{L}_{Yang-Mills} + \mathcal{L}_{Yukawa} + \mathcal{L}_{Higgs}, \tag{1.21}$$

$\mathcal{L}_{fermion}$ is the kinetic term of fermionic field Ψ and their interactions with gauge bosons. It is represented as

$$\mathcal{L}_{fermion} = \overline{\Psi}_L i\gamma^\mu D_\mu \Psi_L + \overline{\Psi}_R i\gamma^\mu D_\mu \Psi_R, \tag{1.22}$$

with

$$D_\mu = \partial_\mu + i\frac{g}{2}T^i W^i_\mu + i\frac{g'}{2}YB_\mu \tag{1.23}$$

where T_i is weak isospin component.
$\mathcal{L}_{Yang-Mills}$ terms indicates the self interaction and kinetic energy terms of the gauge bosons associated with local symmetry groups:

$$\mathcal{L}_{Yang-Mills} = -\frac{1}{4}G^{\mu\nu}_j G^j_{\mu\nu} - \frac{1}{4}F^{\mu\nu}_i F^i_{\mu\nu} - \frac{1}{4}B^{\mu\nu}B_{\mu\nu}. \tag{1.24}$$

Within this framework, we can not have massive gauge bosons since a mass term of the form $m_A^2 A^\mu A_\mu$ is not invariant under the gauge transformation. Same is true for fermionic masses which does not preserve the local gauge invariance. But from the results of various collider experiments we know that fermions do have mass as well $W^\pm$ and Z^0 are massive gauge bosons so there must be a mechanism which provide mass to the gauge bosons. Based on the earlier work of Goldstone, Anderson and Nambu, in 1964 three group of physicists, Francois Englert and Robert Brout; Peter Higgs; and Gerald Guralnik, C. R. Hagen, and Tom Kibble, proposed a mechanism which provide mass to bosons in non-abelian gauge theories, which is known in SM as Higgs mechanism [20]. $\mathcal{L}_{Higgs}$ is the subject of the discussion in the next section.

1.4 Higgs Mechanism

In the Glashow-Salam-Weinberg theory of electroweak interactions, gauge invariance of symmetry group breaks because of finite masses of $W^\pm$ and Z^0. In 1967 Salam and Weinberg, independently, proposed the theory of spontaneous symmetry breaking and

Higgs mechanism [17] which gives mass to weak bosons and also preserve the gauge invariance making theory renormalizable, which was proved later in 1971 by 't Hooft [19]. We can write a complex scalar doublet as,

$$\Phi = \begin{pmatrix} \phi^+ \\ \phi^0 \end{pmatrix} \tag{1.25}$$

which has weak isospin $I = 1/2$ and hypercharge $Y = 1$. Its Lagrangian contains a kinetic and a potential term

$$\mathcal{L} = (D_\mu \Phi)^\dagger (D_\mu \Phi) - V(\Phi^\dagger \Phi) \tag{1.26}$$

where the potential is given by

$$V(\Phi^\dagger \Phi) = \mu^2 \Phi^\dagger \Phi + \lambda (\Phi^\dagger \Phi)^2. \tag{1.27}$$

This potential is $SU(2)_L$ invariant. It is an even function of the scalar field, V(ϕ) = V(-ϕ), so the Lagrangian is invariant under parity transformation $\phi \rightarrow -\phi$. For simplicity we indicate ϕ^0 as ϕ in the rest of the section.

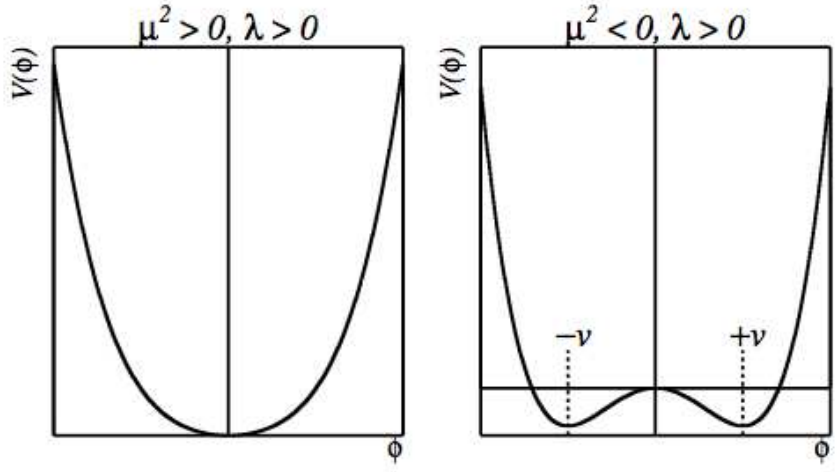

Figure 1.1: Higgs Potential V(ϕ), v is vacuum expectation value.

When the potential V(ϕ) is at minima, the system will be at the lowest energy state. The parameter μ^2 can be positive or negative depending on minimum of the potential V(ϕ). Considering the case μ^2 is positive, the minimum of potential occurs at

$$\langle \phi \rangle_0 \ = 0 \tag{1.28}$$

which is a trivial minima. The parity transformation is also maintained. This Lagrangian describes theory of QED with a massless photon and a charge scalar field Φ which has mass μ.

Now lets consider the case when μ^2 is negative. In this case a non trivial minimum of potential occurs at

$$\langle\phi\rangle_0 \;=\; \pm\sqrt{\frac{-\mu^2}{|\lambda|}} = \pm\frac{v}{\sqrt{2}}, \tag{1.29}$$

where v is known as the vacuum expectation value which corresponds to degenerate ground state of Φ. Now assume the true vacuum state for neutral component of Φ as

$$\langle\phi\rangle_0 \;= \begin{pmatrix} 0 \\ \frac{v}{\sqrt{2}} \end{pmatrix} \tag{1.30}$$

Thus by choosing a specific minima symmetry of Higgs potential is spontaneously broken. It is called "spontaneous symmetry breaking". Now to preserve the electromagnetic symmetry in order to conserve electric charge, the electroweak symmetry group must break as

$$SU(2)_L \otimes U(1)_Y \rightarrow U(1)_{EM}. \tag{1.31}$$

With this broken symmetry, group $U(1)_{EM}$ represents the symmetry of vacuum and its gauge field, the photon, remain massless. Expanding scalar field $\Phi(x)$ around this ground state under a unitary $SU(2)$ gauge transformation gives

$$\phi^0 \;= \frac{v + h(x)}{\sqrt{2}}, \tag{1.32}$$

where $h(x)$ is a real field and corresponds to a massive scalar particle, Higgs Boson. The Higgs field associated mass will be

$$M_H = \sqrt{-2\mu^2}, \tag{1.33}$$

Now expanding the Lagrangian around the minimum gives mass term of W, Z boson while retaining photon as massless. The resulting masses of the electroweak bosons are

$$m_W = \frac{gv}{2}, \tag{1.34}$$

$$m_Z = \frac{gv}{2\cos\theta_W}. \tag{1.35}$$

M_W and M_Z has been measured in hadron colliders so the value of vacuum expectation value of Higgs boson, v, is known. It can also be determined from muon decay experiments and is expressed in terms of Fermi coupling constant G_F as

$$v = (\sqrt{2}G_F)^{-1/2} = 246 \text{ GeV}. \tag{1.36}$$

Therefore although the SM predicts about existence of Higgs boson but being μ^2 priori unknown, it does not tell anything about the Higgs mass.

Fermions masses are predicted in the SM via Yukawa coupling to Higgs doublet field Φ:

$$\mathcal{L}_{Yukawa} = -f_l \overline{L} \Phi R - f_l \overline{R} \Phi^\dagger L, \tag{1.37}$$

where f_l ($l = e, \mu, \tau$) are coupling constants of leptons and Higgs field. With properly chosen transformation of Higgs boson under symmetry group $SU(2)_L \otimes U(1)_Y$, the Yukawa coupling is gauge invariant. Once the Higgs field get a vacuum expectation value, these couplings produce leptonic mass as

$$m_l = \frac{f_l v}{\sqrt{2}}, \tag{1.38}$$

which indicates that leptonic mass is proportional to their couplings to Higgs boson. Similarly quarks mass comes as

$$m_u = \frac{f_u v}{\sqrt{2}}, \tag{1.39}$$

$$m_d = \frac{f_d v}{\sqrt{2}}. \tag{1.40}$$

1.5 Higgs Boson Phenomenology

The Higgs boson is the only missing link of the SM. Although the SM predicts with considerable certainty the existence of Higgs boson, it does not give clear picture about its mass profile. There is no experimental confirmation of existence of Higgs till date. Various limits on possible mass of Higgs boson has been set by direct measurements (LEP, Tevatron) and indirect precision measurements.

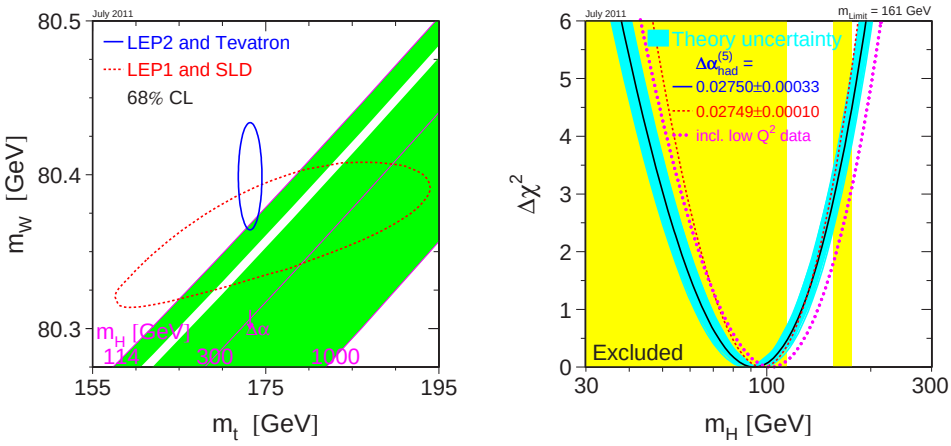

(a) (b)

Figure 1.2: Limits on m_H set by electroweak precision measurements. (a) Regions of allowed Higgs mass consistent with the W and top mass measurements. Red dotted curve shows the limit from the indirect measurements of LEP-I and SLD while blue solid curve shows the direct measurements from Tevatron and LEP-II experiments. Limits are plotted at 68% confidence level. (b) Goodness of electroweak precision data fit i.e. $\delta\chi^2 = \chi^2 - \chi^2_{min}$ versus m_H. The line shows fit using all available data and blue band shows theoretical uncertainity estimate. The yellow shaded region shows mass range excluded by direct searches at LEP and Tevatron [31].

1.5.1 Direct and Indirect Searches

Direct searches for Higgs boson have been performed with no success yet. The LEP experiments performed the search for Higgs boson primarily in $e^-e^+ \rightarrow HZ$ channel but no evidence was found. So they did place a lower limit on its mass $m_H > 114.4$ GeV [23] at 95% C.L., thus excluding a large low mass region. The Tevatron Electroweak Working Group has excluded the mass ranges 156 GeV $< m_H <$ 177 GeV [32] at 95% C.L by combining the CDF and DØ data.

Quantum correction effects of Higgs mass on heavy electroweak observables (W/Z bosons) and on top quarks can be used to set an upper limit on its mass. The Higgs boson couples to top quark and W bosons through higher order loop corrections. The W mass corrections has quadratic dependence on the mass of top quark whereas logarithmic dependence on Higgs mass. A global fit to electroweak observable parameters, like mass, cross-section and coupling between gauge bosons, measured in various collider experiments gives $m_H = 87^{+35}_{-26}$ GeV at 68% confidence level or $m_H < 157$ GeV at 95% C.L. without taking direct limit of LEP into account while it will be $m_H < 186$ GeV at 95% C.L. if we also consider direct limit from LEP [33]. These limit curves has been shown in

Figure 1.2(a), where the blue (red) contour is 68% CL interval wherein top and W mass are expected to lie from various collider experiments. Here the green band describes the functional dependance of top and W mass for a given value of Higgs mass.

Combining various direct as well indirect measurements, the current best estimate on constraints of Higgs mass comes as 114.4 GeV $< m_H <$ 186 GeV which is also the region where Tevatron has best sensitivity for finding the Higgs boson. Major efforts are going on at both the Tevatron experiments, the CDF and DØ, for discovery (or exclusion) of Higgs boson in low (most sensitive around $m_H = 115$ GeV) as well high mass regions (most sensitive around $m_H = 160$ GeV).

1.5.2 Higgs Production and Decay

At the Tevatron, Higgs are produced mainly via two important processes. Most dominant production mechanism is the "gluon fusion"($gg \rightarrow H$) through a top loop. Another important mechanism is the "Higgs-strahlung", commonly known as "associated production", where quark and anti-quark pair fuse to produce a virtual EW boson ($W^{\pm}, Z$) which eventually decays into a real EW boson and Higgs. In addition we also have small contribution from "vector boson fusion" and "$t\bar{t}H$" production. The main production process of Higgs boson at the Tevatron are summarized in Figure 1.3.

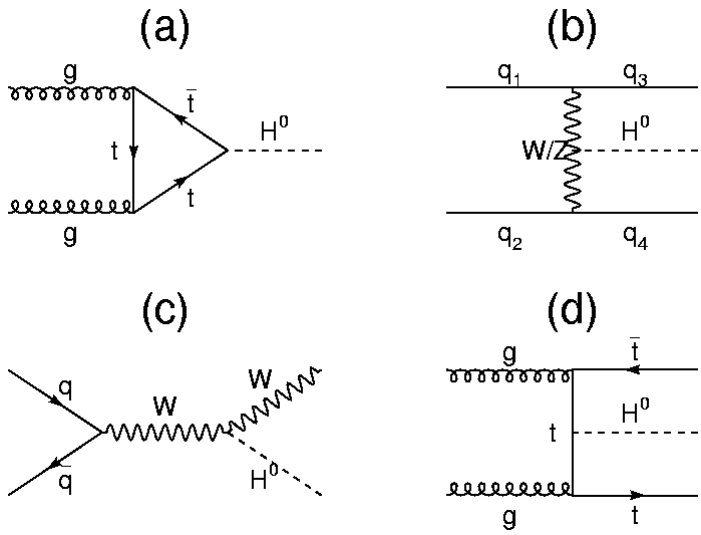

Figure 1.3: Various Higgs production processes at Tevatron (a) gluon gluon fusion, (b) vector boson fusion, (c) Higgs-strahlung production, and (d) $t\bar{t}H$ production.

On the basis of production cross-section and decay sensitivity, Tevatron Higgs search programme can be classified into two broad regions. The "gluon fusion" has higher production rate and favors a heavy Higgs, which decays primarily to W^+W^- pair which

eventually decays into lepton pairs. A light Higgs boson ($\leq$ 135 GeV) decay predominantly to $b\bar{b}$ [Figure 1.4(b)] because it couples to quarks and b-quark being heaviest in this energy range. In low mass region direct search for Higgs is extremely difficult due to overwhelming multijet backgrounds coming from other processes having same final states. Therefore we look for associated production of Higgs with Z/W where Z/W mainly decay leptonically and thus one get rid of most of the multijet and other SM backgrounds and get better description of the signal. Although cross-section of these processes are small, they have clean signature.

The main low mass Higgs boson search channels at the Tevatron are $WH \rightarrow \ell\nu b\bar{b}$, $ZH \rightarrow \ell\ell b\bar{b}$ and $ZH \rightarrow \nu\nu b\bar{b}$. There cross-sections are shown as function of Higgs mass in Figure 1.4(a).

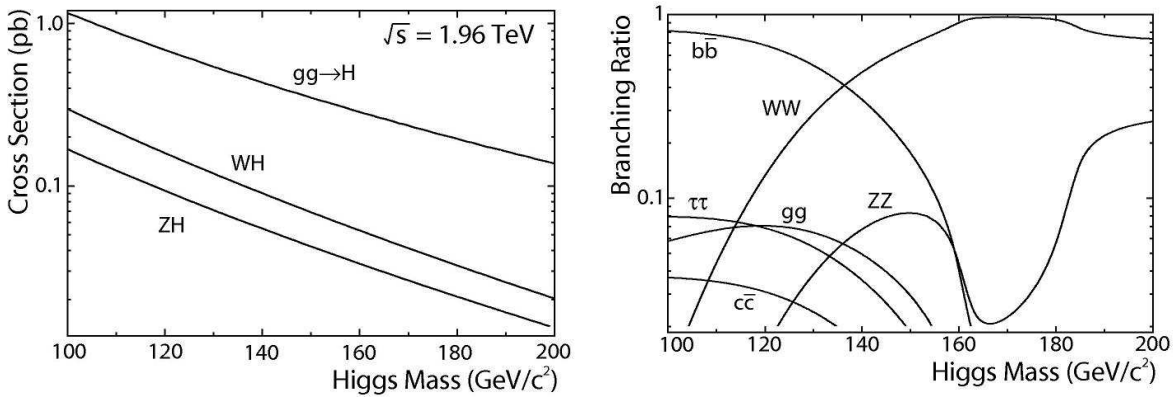

(a) (b)

Figure 1.4: Summary of (a) production cross-section as function of Higgs mass and (b) branching ratio as function of Higgs mass, for Higgs boson at the Tevatron [34].

1.5.3 Higgs Search in ZH Channel

Due to higher branching ratio of $Z \rightarrow \nu\bar{\nu}$ ($\sim$20%) the associated ZH production in $p\bar{p}$ collisions, with $H \rightarrow b\bar{b}$ and $Z \rightarrow \nu\bar{\nu}$, is one of the most sensitive channel for the low mass Higgs production at the Fermilab Tevatron [35]. It is also very challenging at hadron colliders due to absence of any visible lepton which results in overwhelming multijet background. This dissertion presents a search strategy for Higgs boson in this particular channel.

The final state considered in this analysis is a pair of acoplanar b jets from the Higgs decay, with large missing transverse energy ($\not\!\!E_T$) due to neutrinos from the invisible decay of Z, indicated by energy imbalance in the detector. The search is therefore also sensitive

to the WH channel $(W \to \ell\nu)(H \to b\bar{b})$ when the charged lepton is not detected. The main backgrounds arise from $(W/Z)b\bar{b}$, (W/Z)+(non-b jets) due to flavor misidentification (mistagging), top quark production e.g., $t\bar{t} \to \ell\nu bq\bar{q}'\bar{b}$ and $t(q)\bar{b} \to \ell\nu b(q)\bar{b}$, diboson production such as $(W \to q\bar{q}')(Z \to \nu\bar{\nu})$ or $(Z \to b\bar{b})(Z \to \nu\bar{\nu})$, and from multijet events produced via the strong interaction, with real-b or mistagged light parton jets and large $\not\!\!E_T$ resulting from fluctuations in measurement of jet energies.

Proper discrimination of signal from backgrounds is essential for finding Higgs. A kinematic selection is first applied to reject the bulk of multijet events. The two jets expected from the Higgs boson decay are next required to be tagged as b jets, using a neural network b-tagging algorithm. Finally, discrimination between the signal and the remaining backgrounds is achieved by means of a boosted decision tree (BDT) technique. The output of BDT is used to set an upper limit on cross-section times branching ratio for ZH production process as a function of Higgs mass.

1.6 Future Prospects

The Tevatron is performing well and both the experiments are expected to acquire up to 10 fb^{-1} data by the end of September 2011. The Tevatron has recently excluded Higgs mass range of 156 GeV $< m_H <$ 177 GeV as shown in Figure 1.5 [32].

Sensitivity to Higgs search at Tevatron is growing very rapidly. With current combination, for $m_H = 115$ GeV it is 1.17 times the SM cross-section whereas for $m_H = 165$ GeV it is 0.48 times the SM cross-section [32]. With increasing luminosity and improving analysis techniques discovery of Higgs boson is still within the reach of the Tevatron and both the experiments, the CDF and DØ are trying their best to achieve it. The LHC has also started delivering data but neither the ATLAS [36] nor the CMS experiment has reported sighting of Higgs boson. At LHC, search for associated production of Higgs boson will be extremely difficult due to higher QCD backgrounds until a reasonably large dataset is accumulated. Therefore Tevatron remains the best place to search for Higgs boson in immediate future.

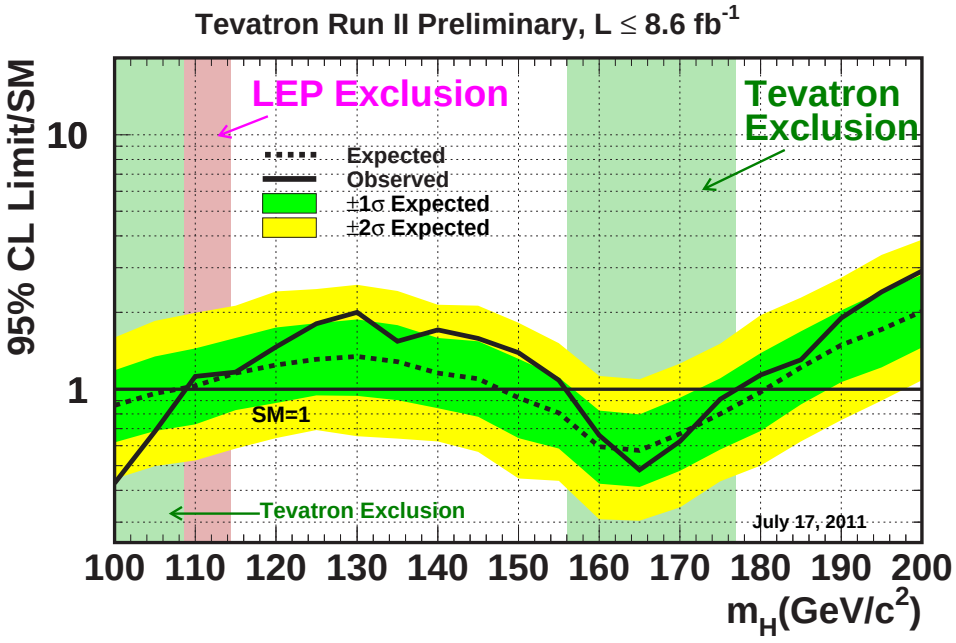

Figure 1.5: Combined CDF and DØ 95% C.L. upper limis on Standard Model Higgs boson production as a ratio to SM expectation. The expected limit and 1 and 2 standard deviation bands around the median value are derived from the background prediction assuming no signal production [32].

Chapter 2

The DØ Detector

Till recently, the Tevatron was the world's highest energy particle accelerator. It is situated at Fermi National Accelerator Laboratory (Fermilab) in Batavia, Illinois, USA. The Large Hadron Collider (LHC) at CERN, which became operational in early 2010 superceded it in energy, but, LHC is a proton proton collider whereas Tevatron is a proton anti-proton collider, thus providing a unique insight into matter anti-matter interaction at very high energy. The Tevatron is a synchrotron that accelerates counter rotating beams of protons and anti-protons up to energies of 0.98 TeV in a ring of 6.28 KM circumference. These beams collide at the center of two large particle detectors - the CDF and DØ, producing center of mass energy $\sqrt{s} = 1.96$ TeV at their interaction points. The detectors measures debris of collision and thus gives information about the underlying physics processes initiated by the $p\bar{p}$ interactions.

Initially, the Tevatron operated at a center-of-mass energy of 1.8 TeV. The first major breakthrough at the Tevatron came in 1995 with the discovery of the "top quark" by both of these experiments. After operating for a year after the top discovery, in 1996, the first phase of the Tevatron physics programme - known as Run I, ended and both the detectors as well as the accelerator went through a major upgrade. In 2001, a new phase of Tevatron physics programme, known as Run II, started with increased center of mass energy of 1.96 TeV and an ever increasing peak luminosity. The Tevatron performance has enhanced significantly over the years and Fermilab plans to keep it operating until September 2011 which will result in more than 10 fb^{-1} of data, recorded by both the experiments.

In Run II, both detectors were upgraded to optimally utilize the physics potential of increased luminosity of the Tevatron. Probing the Higgs boson, the last missing link in the SM, was one of the top most objectives of the Tevatron Run II physics programme. Tevatron has recently excluded the Higgs mass range of 156 GeV to 177 GeV at 95% CL [32]. Probing low mass Higgs, which is strongly favoured by the theory, will be

difficult at LHC due to high QCD background. So the Tevatron is still a favoured place to detect low mass Higgs boson.

This thesis is an attempt towards search of a low mass Higgs, in data collected from 2002-2009 using the DØ detector. The Tevatron accelerator complex, DØ detector and their various sub-system will be described in this chapter.

2.1 The Fermilab Accelerator Complex

A chain of accelerators are employed at Fermilab to produce one of the world's most energetic particle beams. A schematic description of various accelerator stages of complex has been given in the Figure 2.1

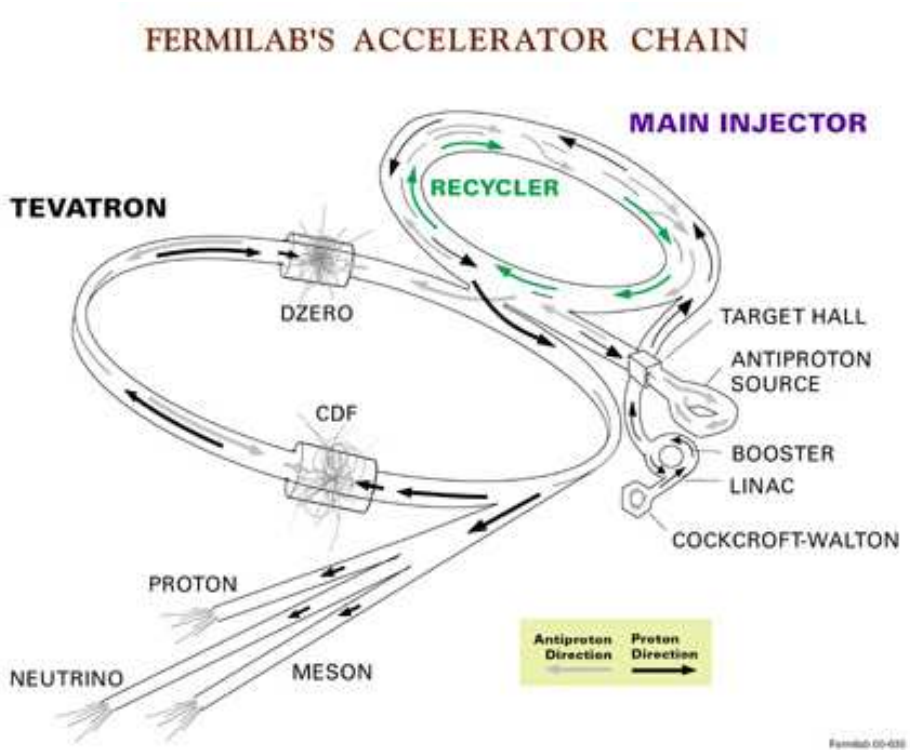

Figure 2.1: Fermilab Accelerator Complex

The first stage of acceleration, known as pre-acceleration, is done in Crockroft-Walton generator. It involves a proton beam originating as hydrogen gas which is ionized to H^- ions by a Magnetron source. These negative ions are then accelerated to 750 KeV using a positive electrostatic field. These H^- ions are further accelerated to 400 MeV using LINAC, a linear accelerator which is about 150 m in length consisting of several Radio Frequency (RF) cavities. The H^- ions are passed through a carbon foil which strips off the electrons, resulting in H^+ ions which is proton. Protons are then injected into the

Booster, which is a synchrotron ring of ≈478 m circumference and uses dipole magnets to bend the proton beams in a circular path. The proton beam passes through the Booster about 20,000 times, picking energy from RF cavities in each revolution. The proton beam is accelerated to 8 GeV before leaving the Booster. From Booster, the proton beam is injected into the Main Injector, which is a synchrotron, 3 KM in circumference. It accelerates the proton beam upto an energy of either 120 GeV or 150 GeV. The 150 GeV proton beam is injected into the Tevatron, while the 120 GeV bunches are delivered to the anti-proton facility.

For production of anti-protons, 120 GeV protons from the Main Injector are collided on a nickel target. About 20 anti-protons are produced for every million protons hitting the target. The anti-protons are transferred to the Debuncher, which is a 520 m long triangular storage ring. Since the proton beam from Main Injector is bunched, so are the anti-protons coming off the target. The Debuncher removes this bunch structure and reduces the transverse momentum profile of the anti-protons. Next, the anti-protons are transferred to the Accumulator, another 8 GeV storage ring, where they are further cooled and focused using Stochastic Cooling technique. The anti-protons can be stored here for sufficient time so that large number can be accumulated. These anti-protons at 8 GeV are sent back to Main Injector where they are further accelerated to 150 GeV before being injected into the Tevatron.

The final stage of acceleration takes place in the Tevatron. It uses a state of the art cryogenic cooling system which provides liquid helium to cool the superconducting magnets upto 4.6° K, which produces fields of up to 4 Tesla. When accelerator complex is ready for beam injection (it is also called beginning of store), 36 bunches of protons and anti protons each are injected from Main Injector into the Tevatron. These beams are further accelerated by the Tevatron in two oppositely rotating directions in the same beam pipe, to a final energy of 980 GeV. After accelerating the two beams to 980 GeV energy, they are squeezed into high density beam using low beta quadrupole focusing magnets. The beam halos (protons and anti-protons in irregular orbits far from the beam center) are scraped away with collimators. These high density beams are then brought into head on collisions at a center-of-mass energy of 1.96 TeV at time intervals of 396 ns at two points on the Tevatron ring, known as interaction regions. The CDF and DØ detectors are located at these two interaction regions to record the debris of collisions. The beam interaction region has a 3D-Gaussian shape with a width of ≈30 cm along the beam-axis (the "z" direction), and ≈30 μm in the transverse directions.

The Tevatron operating parameters are listed in Table 2.1 and the bunch structures for Run I and Run II are shown in Figure 2.2. In Run I, the accelerator delivered 6 bunches of protons and anti-protons ("6×6" bunches) with a crossing every 3500 ns, but, after the

accelerator upgrade, the accelerator complex now delivers 36 bunches of protons and 36 bunches of anti-protons ("36×36" bunches) in the collider separated into 3 super bunches, each having 12 bunches separated by 396 ns. The major upgrades in Tevatron for Run II which resulted in increase in center of mass energy and peak luminosity includes the construction of the Main Injector and the Anti-proton Recycler. Both the CDF and DØ detectors were upgraded to cope with the new smaller bunch crossing time.

Parameters	Run I	Run II
Energy (GeV)	900	980
Bunches	6	36
Protons/bunch	2.3×10^{11}	2.7×10^{11}
Anti-protons/bunch	0.55×10^{11}	0.3×10^{11}
Total Anti-protons	3.3×10^{11}	11×10^{11}
Anti-proton production rate (/hr)	6.0×10^{10}	20×10^{10}
Typical Luminosity ($cm^{-2}s^{-1}$)	$\sim 1.6 \times 10^{31}$	$\simeq 2 \times 10^{32}$
Integrated Luminosity (pb^{-1}/week)	∼3.2	∼62.5
Bunch-spacing (ns)	∼3500	396
Interactions/crossing (@ 50 mb)	2-3	2-3

Table 2.1: Tevatron operating parameters in Run I and Run II. Run I is the period of operation from 1992 to 1996 and Run II is the period of operation which started in 2002 and is still in progress.

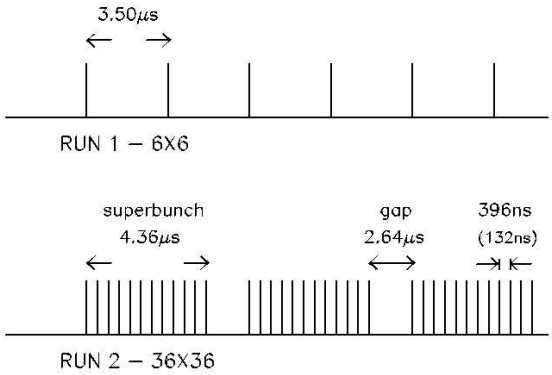

Figure 2.2: Tevatron bunch scheme for Run I (top) and Run II (bottom).

2.2 Luminosity and Cross-Sections

In collider physics, processes are usually expressed in terms of cross-section, σ, which is a measure of the interaction probability per unit flux. The flux corresponds to the

size of colliding beams and numbers of particles in it and is referred to as luminosity, $\mathcal{L}$. The luminosity depends on the number of bunches, number of particle in each bunch, revolution frequency and the area of the beams. The luminosity is given as:

$$\mathcal{L} = \frac{f_{rev} B N_p N_{\overline{p}}}{2\pi(\rho_p^2 + \rho_{\overline{p}}^2)} F(\rho_l/\beta^*), \tag{2.1}$$

where f_{rev} is the revolution frequency, B is the number of bunches per beam, $N_{p(\overline{p})}$ is the number of protons (anti-protons) per bunch, $\rho_{p(\overline{p})}$ is the transverse beam size of the proton (anti-proton) beam, and F is a form factor depending on the bunch length (ρ_l) and the beta function at the interaction point (β^*). Thus luminosity is proportional to the product of the number of particles in each beam passing through a unit area per unit time and is expressed in units of $cm^{-2}s^{-1}$. The cross-section is expressed in units of barn where 1barn$\equiv 10^{-24}$ cm^2.

The rate of interaction of any given process is given as

$$R = \sigma\mathcal{L}, \tag{2.2}$$

The number of any particular interaction N, occurring in collisions over a given period of time is given by

$$N = \sigma \int \mathcal{L} dt \tag{2.3}$$

Where $\int \mathcal{L}dt$ is the luminosity integrated over time and referred as the integrated luminosity, and is measured in units of inverse barns. For a particular interaction, the cross-section is fixed for a given center-of-mass energy and fixed accelerator parameters. Usually for the rare processes that occur at the Tevatron energy, cross-sections are of the order of pico-barns (pb), or $\equiv 10^{-36}$ cm^2, therefore integrated luminosity is measured in inverse pico-barns (pb^{-1}). For example, a certain process having a cross-section of 1 pb is expected to occur 100 times during the delivery of 100 pb^{-1} integrated luminosity.

The production cross section for a given process can also be given as

$$\sigma = \frac{dN/dt}{\mathcal{L}}, \tag{2.4}$$

The instantaneous luminosity delivered by the Tevatron is usually of the order of $\approx 10^{32} cm^2 s^{-1}$. In Figure 2.3 we show the instantaneous luminosity as a function of time for a typical store. Usually the store begins at a high luminosity $\approx 3 * 10^{32} cm^2 s^{-1}$ and decay exponentially. Stores are usually terminated when luminosity goes down to $\approx 0.6 * 10^{32} cm^2 s^{-1}$.

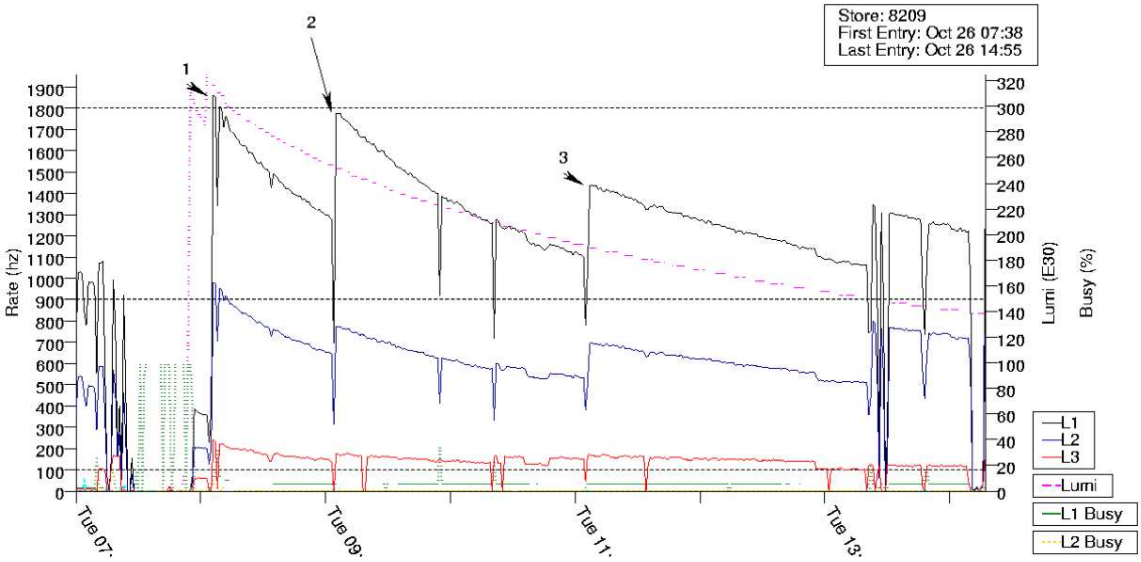

Figure 2.3: A typical data taking store shown here. Dashed line shows initial luminosity 3 $*10^{30} cm^2 s^{-1}$ in the beginning. Solid lines are Level1, Level2, Level3 triggers output rates. A typical run is from 4 to 8 hrs. Runs are changed to change the set of triggers to account for the changed luminosity.

Figure 2.4 shows the delivered and recorded luminosity by DØ from April 2002 to January 2010 . Due to detector and recording rate limitations, recorded luminosity is always slightly lower than the delivered luminosity. The DØ data acquisition system has an overall efficiency greater than 90%.

2.3 Particle Detection at Collider Detectors

In Tevetron, only those $p\overline{p}$ interactions which results in large momentum transfer between constituent particles, tearing apart original protons and anti-protons into partons (quarks and gluons), are useful for probing the standard model physics. Partons of proton and anti-proton exchange force carrier bosons to create a hard scattering process. The fragments of proton and anti-proton does not get much transverse momentum and thus passes along the beam-line, but ejected partons enter into the detector. These hard scattering interactions produces various SM (and possibly beyond SM) particles such as W, Z bosons as well as the top quark. Most of them are unstable and thus decay further into semi-stable lighter particles such as muons, electrons, photons, neutrinos etc. which live long enough to reach the detector and can be measured.

A typical particle detector for high energy hadron collider consist of three main components : the tracking system, the calorimeter and the muon system.

The detectors closest to the interaction point are the tracking detectors. They have finer segmentation and are usually within a magnetic field. Fine segmentation ensures

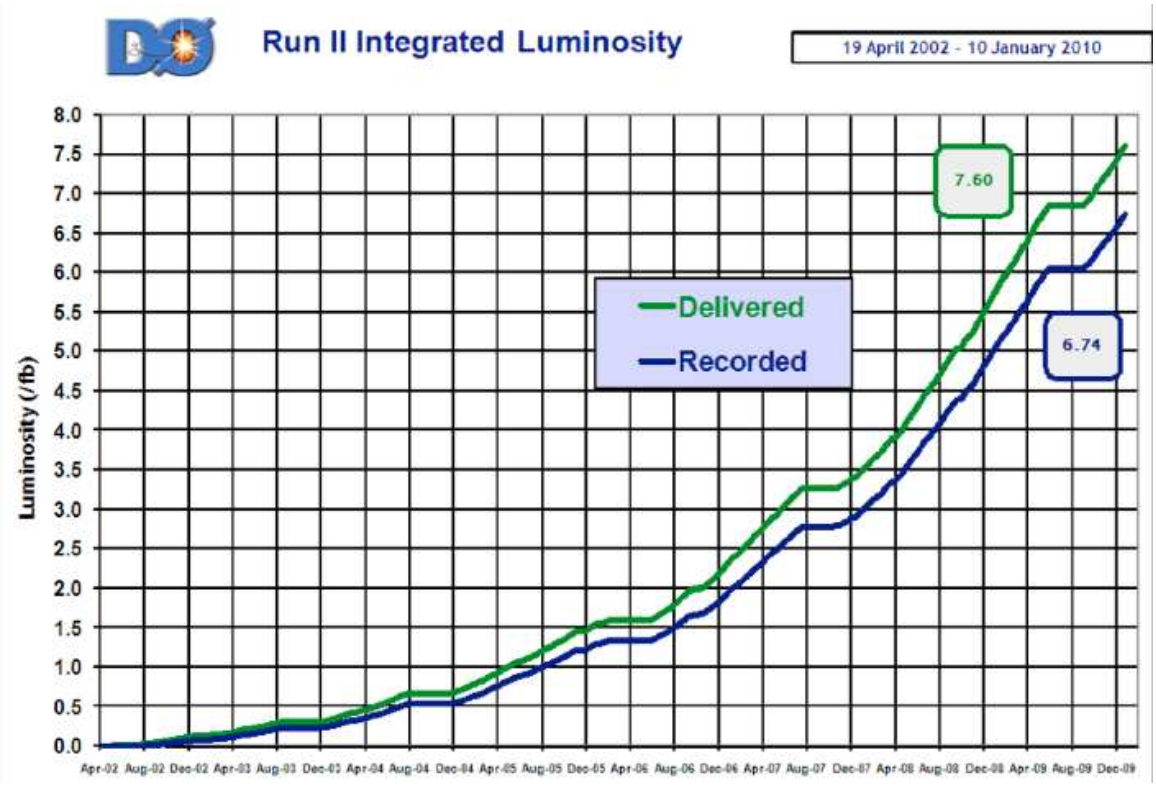

Figure 2.4: Total integrated luminosity, delivered and recorded by the DØ experiment from April 2002 to January 2010.

reconstruction of the three-dimensional trajectories (tracks) of the charged particles passing through them with considerable accuracy and at the same time, the magnetic field helps in measurement of their charge and momenta by measuring their bend. A light (low Z) material is used for the construction of the tracking detectors and to minimize scattering and energy loss of charged particles. Thus, the tracking system is very crucial in identifying leptons. Modern tracking detectors consist of mainly two parts: an inner high resolution silicon vertex detector, to provide precise primary and secondary vertex determination, and a larger outer tracking system, to provide efficient track pattern recognition and improved momentum resolution.

The tracking system is surrounded by the calorimeters which measures the energy of most of the particles that crosses the tracking system. Calorimeters are made of dense (high Z) materials so that the full energy of most incident particles can be absorbed within it and the energy deposited can be measured. A particle passing through a dense material produces a shower of secondary particles. By studying the shower profile one can get an idea of an incident particle. The shower size can be used for the determination of the particle energy, whereas the shower shapes differentiate between various particle types such as electrons, photons and hadrons. Heavier the particle, more deeper will be

its shower profile.

The muons being a minimum ionizing particle escape through the calorimeter, so we have additional tracking detectors (muon chambers with toroidal magnetic field) to identify them, generally known as the muon system. The muon system forms the outermost part of the detector and is located just outside the calorimeter. It is designed to measure the trajectory hence momentum and charge of the muon.

The neutrinos escape the detector and can't be measured directly. So their presence is inferred from an imbalance in the total transverse energy measured by the calorimeter, denoted by $\not\!\!E_T$. The quarks and gluons which are produced in hard scattering has a very short lifetime before they undergo hadronization. This process produces a jet of particles, each traveling in the same direction as of the initial quark or gluon. These jets are detected by measuring their shower profile in the calorimeter.

2.4 Overview of the DØ Detector in Run II

The DØ detector [37][38] is a general purpose nearly-hermetic particle detector, designed to study interactions originating from $p\overline{p}$ collisions at $\sqrt{s} = 1.96$ TeV at the Fermilab Tevatron Collider.

The detector is designed to measure the momenta and energy of final states containing photons, leptons, jets, and neutrinos from various processes originating from $p\overline{p}$ collisions. It is optimized to study large transverse momenta (high-p_T) phenomena. The detector went through various upgrades, retaining high efficiency of measurements for high-p_T processes, at the same time extending its physics reach to low-p_T processes, as well as to B-physics.

The upgraded Run II detector has been described in the next section. The main motivation for the Run II upgrade of the DØ detector was two fold. First, the detailed study of known physics processes such as precision study of the top quark, W and Z bosons to provide sensitive tests of the standard model, and next, the search for the Higgs boson and processes beyond the SM such as supersymmetry and large extra dimensions.

2.5 The DØ Detector Components

Figure 2.5 shows the schematic side view of the Run II DØ detector [38]. The DØ detector has undergone significant upgrades for Run II, which is designed to enhance its capabilities from Run I and to accommodate the reduced bunch timing from 3.5 μs in Run I to 396 ns in Run II. The upgraded DØ detector consists of three primary detector systems as we move from inside to outside : inner trackers, calorimeters, and muon

systems, all symmetric about the Tevatron beam line. The inner tracking system has been completely replaced, and sits inside a 2 Tesla magnetic field provided by a superconducting solenoid. The calorimeter itself remains unchanged, although the readout electronics has been completely replaced. Preshower detector has been added between the solenoid and the calorimeter to provide electron identification and to compensate for the energy loss in the solenoid. A new 3-level trigger system and data acquisition system are used to handle the high event rate.

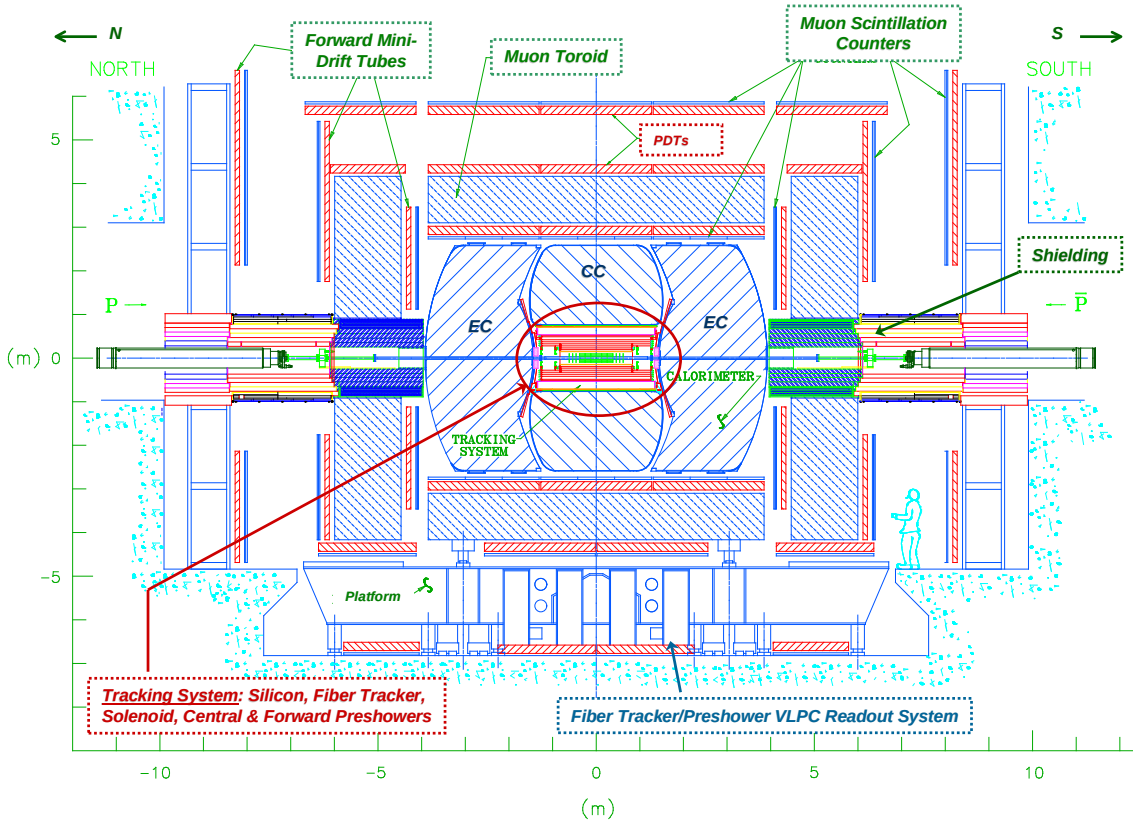

Figure 2.5: Side view of the DØ detector [38].

The tracking system consists of a Silicon Microstrip Tracker (SMT) and a Scintillating Central Fiber Tracker (CFT) enclosed within a 2 Tesla superconducting solenoid magnet. The tracking system is surrounded by two scintillator based Central (CPS) and Forward (FPS) Preshower detectors to provide electron identification and to compensate for energy losses in the solenoid. The calorimeter is made of four sampling Uranium-liquid Argon cryostats : a central cryostat covering the region $|\eta|<1.1$, two forward cryostats extending the coverage to $|\eta| \sim 4.2$ and the Inter Cryostat Detector (ICD) to cover the overlapping pseudorapidity region $1.1 < |\eta| < 1.4$. The muon system consists of a central and a forward scintillating based tracking detector, a toroidal magnet (1.8 Tesla) and special shielding material surrounding the accelerator beam pipe. The purpose of the shielding

material is to reduce the presence of non-muon background particles originating from the beam halo and proton-antiproton fragments interacting with the beam pipe and the calorimeter.

These major subsystems are supported by other subsystems like a trigger and data acquisition (DAQ) system which select events which are interesting to be written on tape, data storage system, luminosity monitoring system, radiation monitoring and other control and monitoring systems for efficient operation of data acquisition without compromising safety of the detector system.

The next subsections describes various subsystems in detail as well as the detector coordinate system. An extensive description of the DØ detector can be found in [37][38].

2.5.1 Coordinate System and Kinematic Quantities

The DØ uses a right-handed cartesian coordinate system (x, y, z) with the center (0,0,0) at the center of the detector. Figure 2.6 shows the coordinate system used in DØ . The $+x-$axis is a vector pointing radially outwards from the center of the Tevatron ring, the $+y-$axis direction is vertically upwards and the $+z-$axis direction is along the proton beam direction in the detector.

The DØ exhibits roughly cylindrical symmetry and particle collisions do not have any preferred direction in the $x-y$ plane. A cylindrical coordinate system (r,θ,ϕ) symmetric with z=0 axis can also be used. The polar angle, θ, is defined such that $\theta = 0$ lies along the beam pipe in the $+z$ direction while $\theta = \pi/2$ is perpendicular to the beam pipe. It is defined as:

$$\theta = cot^{-1}(z/r), r = \sqrt{x^2 + y^2}. \tag{2.5}$$

The azimuthal angle, ϕ, is defined such that $\phi = 0$ points away from the center of the Tevatron ring (also the positive $x-$axis). The upward direction, $\phi = \pi/2$, defines the positive $y-$axis.

$$\begin{aligned} \phi &= tan^{-1}(y/x), x > 0, y > 0 & (2.6)\\ &= tan^{-1}(y/x) + \pi, x < 0 & (2.7)\\ &= tan^{-1}(y/x) + 2\pi, x > 0, y < 0 & (2.8) \end{aligned}$$

Polar angle θ is often replaced by another kinematic variable - the rapidity, y, because the multiplicity of high energy particles (dN/dy) is invariant under Lorentz transforma-

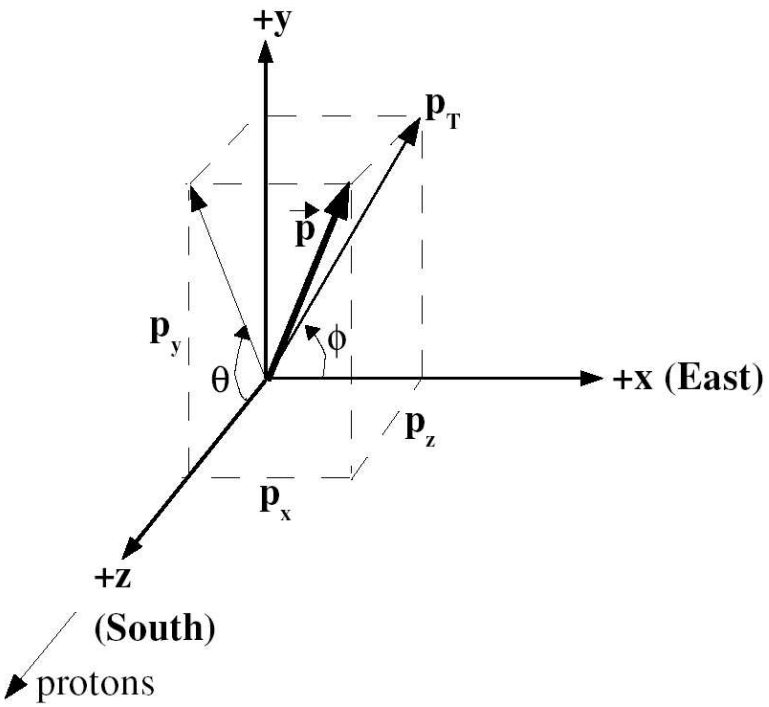

Figure 2.6: Diagram of p_T in the DØ coordinate system.

tions along the $z-$axis. The rapidity is defined as

$$y = \frac{1}{2} \ln \left(\frac{E + p_z}{E - p_z} \right). \tag{2.9}$$

where E is the particle energy and p_z is the particle momentum along the z-axis. But the quantity most frequently used for all practical purposes is the pseudo-rapidity, η, defined as

$$\eta = -\ln \tan \left(\frac{\theta}{2} \right). \tag{2.10}$$

which approximates the true rapidity y for finite angles in the limit that $m/E \to 0$. It has to be noted here that in $p\bar{p}$ collider experiments like DØ, the dimensions of the beam along the x and y axis tend to be very small, but along the z-axis where the actual collision takes place the size of beam is not as limited. Because of this, the primary interaction point has a Gaussian distribution in the z axis with mean at $z = 0$ and $\sigma_z = 28$ cm. As a result of this beam structure, there is another useful variable, the detector pseudo-rapidity, η_d. This pseudo-rapidity is computed with respect to an interaction point whose position is at $z = 0$. Because the real interaction point's position is distributed around $z = 0$, η (also called the "physics" pseudo-rapidity) and η_d may be different. The "physics" η of

a particle is determined by θ of the particle as measured from the interaction point or primary vertex.

A difference between two directions (ϕ_1, η_1) and (ϕ_2, η_2) is often expressed in terms of ΔR distance defined as follows:

$$\Delta R = \sqrt{\Delta\phi^2 + \Delta\eta^2} \quad (2.11)$$

$$\Delta\phi = min(|\phi_1 - \phi_2|, 2\pi - |\phi_1 - \phi_2|) \quad (2.12)$$

$$\Delta\eta = |\eta_1 - \eta_2|. \quad (2.13)$$

Since the parton-parton collisions do not occur at fixed $\sqrt{\hat{s}}$ and since a significant fraction of energy escapes the detector as the nucleon remnants carry it away down the uninstrumented beam pipe, the longitudinal boost of hard scatter particles is very difficult to measure. However, these particles can still be studied by applying conservation of energy and momentum in the transverse plane. We use some variables defined in transverse plane to exploit this aspect of hadron collders

- $E_T = E \sin\theta$: Transverse energy.
- $p_T = p \sin\theta = \sqrt{p_x^2 + p_y^2}$: Transverse momentum as shown in Figure 2.6.
- $\not\!\!E_T$: Missing transverse energy, or energy imbalance in the transverse plane.

2.5.2 Central Tracking System

A good tracking system and hence the ability of vertex reconstruction is essential for almost all physics studies at hadron colliders. The central tracking system consists of two subsystems : the Silicon Microstrip Tracker (SMT) and the Central Fiber Tracker (CFT), surrounded by the Tevatron beam line on inner side and a superconducting solenoid magnet, providing a 2 Tesla magnetic field parallel to the beam line, on outer side. Figure 2.7 depicts the tracking system. In combination with the magnetic field, the trackers are designed to perform the following goals :

- Charged particle detection upto $|\eta| \leq 3$.
- Charged particle momentum measurement : The solenoidal field causes electrically charged particles to follow a curved path, with the curvature inversely proportional to the particle's momentum. That is, a particle with momentum p and non-zero charge q travels in a helix with radius r given by

$$r = \frac{p_T}{qB}$$

in a solenoidal field of strength B along the z direction. This allows for precise measurements of momentum and determination of the particle's charge.

- The tracking detectors provide a means to measure the hard-scatter vertex and any secondary vertices produced by the decay of short-lived particles and thus play an important role in heavy flavor identification.

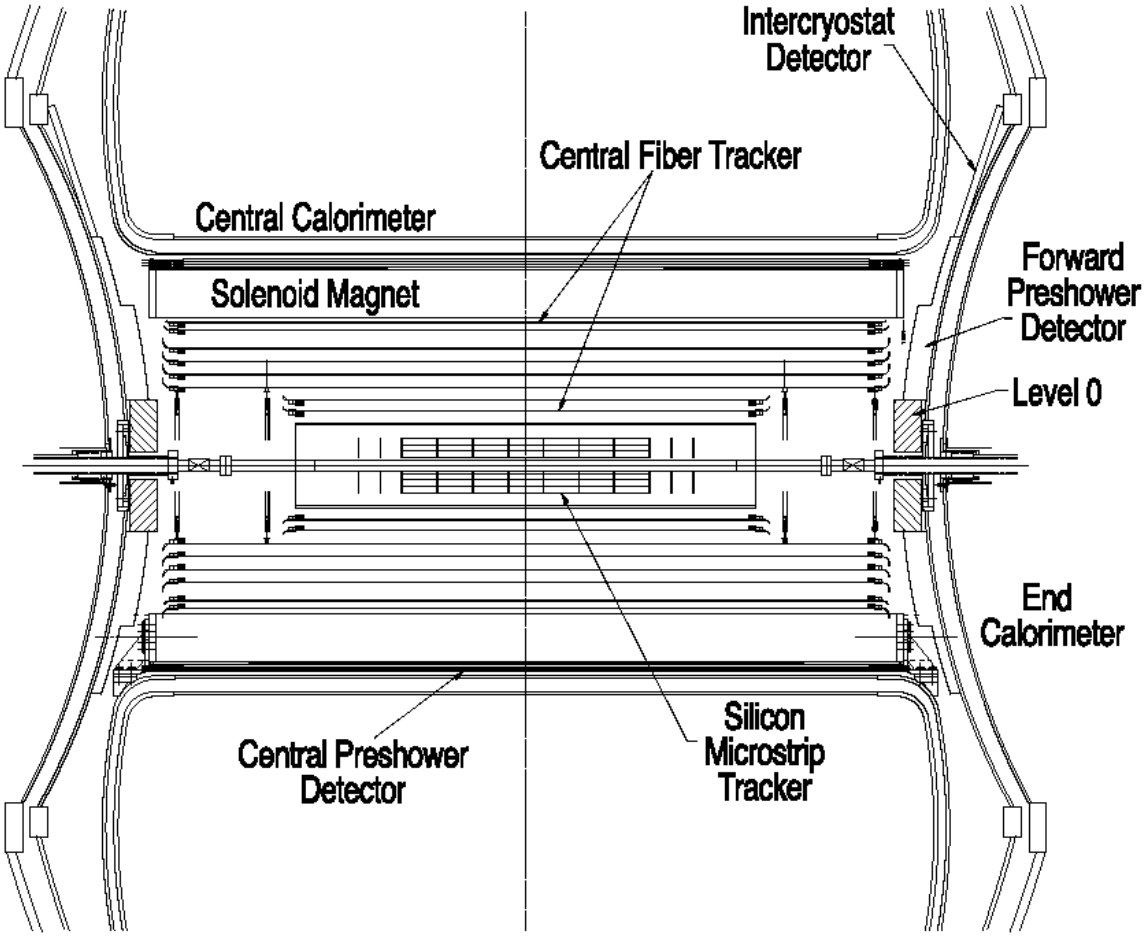

Figure 2.7: The DØ tracking system [38].

2.5.2.1 Silicon Microstrip Tracker (SMT)

The Silicon Microstrip Tracker (SMT) [39] is the center piece of the DØ tracking system and is the first detector which particles coming from the collision encounter. It is designed for providing high-resolution measurements of the paths of charged particles leaving the interaction region, finding the primary interaction vertex as well as reconstructing the secondary decay vertices of short-lived bottom hadrons. It uses silicon sensors(wafers)

having readout strips placed at a distance ("pitch") of 50 to 135 μm of each other depending on location in the SMT. The readout strips are made of p^+ doped silicon on one side and n^+ doped silicon on another side of sensor. A bias voltage is applied across the sensor to deplete the charge carriers from bulk. When a charge particle travels across the silicon, extra charge carriers are created which results in an electrical signal at the nearest readout strips. Hits from several sensors are combined to reconstruct trajectory of the traversing charged particles. The design of the SMT was driven by the length of the interaction region which is extended, with a $\sigma_z \sim 28$ cm. Since the tracks coming from the interaction region should penetrate sensors predominantly perpendicularly, therefore to minimize multiple scattering and to get the most precise measurements, a special design of SMT system was adopted, having sensors parallel and perpendicular to beam directions. Parallel sensors are arranged into concentric layers forming six units, called as barrel which measures primarily the $r-\phi$ coordinate. Perpendicular sensors are arranged into interspersed disks, twelve smaller "F disks" and two bigger "H disks", providing $r-z$ as well as $r-\phi$ measurements. The SMT system provides tracking coverage up to $|\eta|$ <3. The high η particles are reconstructed in three dimensions by the disks, and particles at small η are primarily reconstructed by the barrels. A schematic of the SMT geometry is shown in the Figure 2.8.

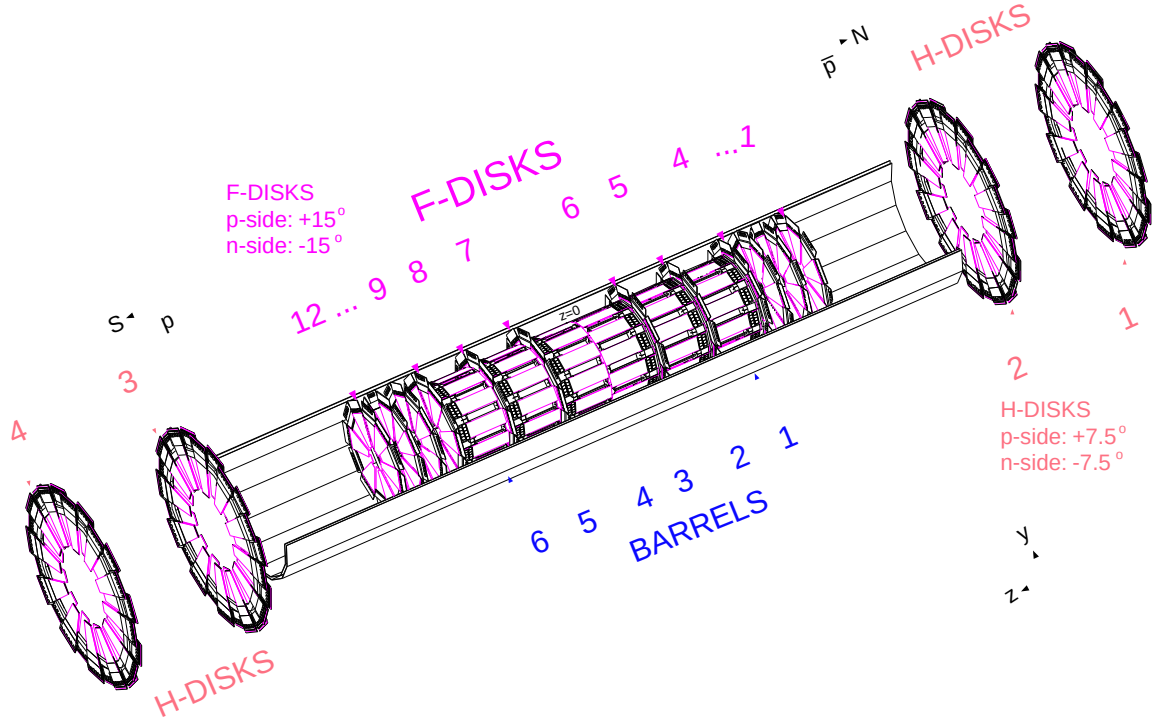

Figure 2.8: DØ Run II Silicon Microstrip Tracker detector.

The six barrels are made up of four concentric layers of single and double-sided silicon

wafers, allowing for $r-\phi$ measurements of central tracks. Layer 2 and 4 of barrels have double-side wafers, having strips and readouts on both sides, with a stereo angle of 2° while layer 1 and 3 have single sided wafers, glued back to back, with stereo angle of 90°. Barrel detector covers radius of 2.7 cm $< r <$ 10.5 cm providing coverage to $|\eta| \leq 2.4$ region.

At the extreme end of each barrel along z axis, there are smaller disks, referred to as F-disks which are made of 12 overlapping, double-sided silicon wedges, at stereo angle of 30°. Two larger disks, referred to as H-disks, which provides tracking at high η, are made of 16 overlapping, single-sides silicon wedges positioned back to back with stereo angle of 15°. The F-disks and H-disks together provide $r-z$ and $r-\phi$ tracking coverage out to $|\eta| \sim 3$.

In initial design there were 4 H-disks but during 2006 upgrade two outermost H-disk were removed and a new layer of silicon, known as "Layer Zero" was installed between the beam pipe and first layer of barrel. This new layer was added to overcome the problem of radiation exposure which changes the impurity concentration of silicon wafers resulting in enhanced bias voltage which is required to deplete the wafer upto a point where silicon wafers can not be used anymore. It was anticipated that radiation damage of Layer-1 may degrade the b-tagging efficiency but till now there is no indication of lost channels due to radiation damage. Layer-0 will ensure good tracking capability even if part of the SMT becomes inefficient due to radiation damage. Besides it is also closer to interaction points thus providing better secondary vertex tagging.

2.5.2.2 Central Fiber Tracker

The SMT is surrounded by scintillating central fiber tracker (CFT)[40]. The CFT together with the silicon detector enables track reconstruction and momentum measurement of all charged particles within the range of $|\eta| < 2.4$. Combined hit information from the two tracking systems enhances the overall tracking efficiency. The fiber tracker provides fast "Level 1" track triggering within the given $|\eta|$ range.

The detector consists of scintillating fibers which are mounted on eight concentric carbon fiber barrels, with radii from 20 to 52 cm from the center of the beam pipe. The outer six barrels are 2.5 m long while the two inner ones are only 1.7 m long to accommodate the silicon H-disks. Each cylinder has a doublet layer of scintillating fibers. One is oriented parallel to the beam line (axial fibers) which provide $r-\phi$ measurements and the other holds an offset at alternating angles of $\pm 3^0$ (stereo fibers) which provides $r-z$ measurements. Each fiber consists of a 835 μm polystyrene core that is doped with fluorescing molecules. Surrounding the core are two 15 μm layers of cladding (acrylic and fluoro-acrylic), increasing the light-collection efficiency. The fiber scintillates in the

yellow-green part of the visible spectrum, with a peak emission wavelength near 530 nm. The CFT contains 76,800 fibers. It covers more radial distance than the SMT, hence it gives better measurement of curvature in 2 Tesla magnetic field which is used for a more precise measurement of the p_T of charged particles.

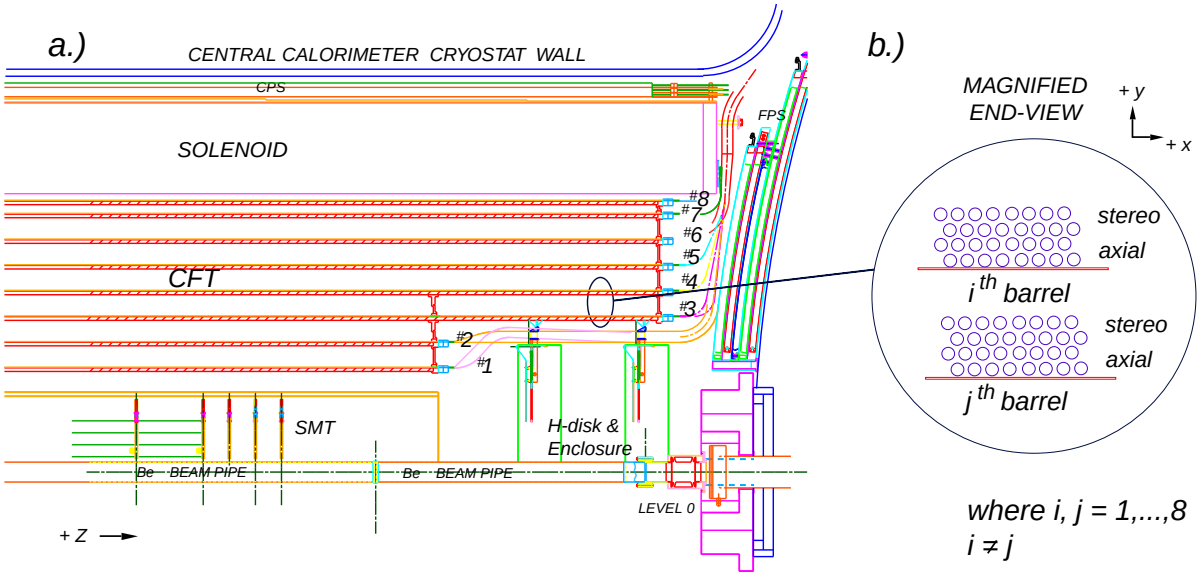

Figure 2.9: (a) A quarter r-z view of the CFT detector showing the nested eight barrel design. (b) A magnified r-ϕ end view of the two doublet layer configuration for two different barrels.

As charged particles traverse through the fibers, scintillation light is produced which travels their length in both directions. The fibers, which range in length from 166 cm for the innermost cylinder to 257 cm for the outermost cylinder, have an aluminum mirror coating at one end to reflect photons back into the fiber so that scintillating light is collected at only one end of the fiber which is coupled to clear fibers which guides the scintillation light to a solid-state silicon device called a Visible Light Photon Counter (VLPC) which convert the light signal into electrical signal. The VLPC's are silicon based avalanche photodetectors which are capable of detecting single photon. They have fast response time, excellent quantum efficiency($> 75\%$) and a high gain (22000-65000 electrons produced per photon).

At $\eta_d = 0$, the transverse momentum resolution for the DØ tracking system can be parameterized as $\sigma_{p_T}/p_T = \sqrt{0.0015^2 + (0.0014 p_T)^2}$ [40].

2.5.3 Calorimeter System

The calorimeter detector is one of the most important part of any detector system. It is designed to accurately measure the energy of the electromagnetic (EM) and hadronic

(HAD) objects that enter it. It also assists in the identification of electrons, photons and jets as well as infer the presence of non-interacting particles (neutrinos) from the missing transverse momentum imbalance. Energy measurement is made by measuring showering profile of incident particles which induce interactions while passing through the active material of the calorimeter, creating showers of secondary particles which lose energy through ionization, excitation etc. A fully contained showering process gives measurement of a particle's total energy.

The EM and HAD objects shower differently in the calorimeter. For EM objects (electrons and photons) there are two dominant process through which they lose their energy: pair production ($\gamma \rightarrow e^+e^-$) and bremsstrahlung ($e \rightarrow e\gamma$). Successive occurrence of these two processes results into an EM shower. For each successive occurrence the number of secondary particles increases while the average energy per particle decreases. The energy of original EM objects (E_0) can be reconstructed by collecting and measuring the energy of all of these secondary particles. Since the energy of the original particle drops exponentially :

$$E(x) = E_0 e^{-x/X_0} \tag{2.14}$$

where x is the distance traveled and X_0 is the radiation length of the material through which the particle passed. The X_0 is defined both as the mean distance a high-energy electron loses all but $1/e$ of its energy to bremsstrahlung, and as 7/9 of the mean free path for pair production by a high-energy photon. For uranium, X_0 is approximately 3.2 mm [29].

The hadrons interact with the uranium nuclei via the strong force and these interactions also produce secondary particles, mostly neutral and charged pions (π^0 and $\pi^\pm$). About a third of the secondary particles produced in these interactions are neutral pions (π^0's), which decay primarily to photons which interact electromagnetically. Other secondary particles (like charged pions ($\pi^\pm$)) tend to interact strongly. So hadronic showers tend to be larger and develop over longer distances. The hadronic counterpart to radiation length X_0 is the nuclear interaction length (λ_0). For uranium, λ_0 is about 10.5 cm [29]. Thus we need two type of calorimeters: Electromagnetic (EM) and Hadronic (HAD). Although hadronic showers are dominated by nuclear interactions, they also contain EM shower components. So while determining the hadronic shower, EM part has to be accounted differently. Because of its nature, a hadronic shower tends to be of larger than the EM ones.

The EM calorimeter is the inner of the two calorimeters and encloses the region closer to the interaction point, while the hadronic calorimeter covers the outer region of the detector. The calorimeter design is optimized for both types of showers, but still some

difficulties are there affecting the energy measurement of showers. Since hadronic showers are dominated by nuclei interactions, only fraction of energy comes in the form of visible energy. Also the EM component of the hadronic shower fluctuates in energy. These two drawbacks results in a electromagnetic and hadronic response ratio (e/h) which is not unity. For a better calorimeter performance, attempts have been made to make e/h as close to unity as possible by means of compensation. The main idea was to use uranium as the absorber material; this would contribute an additional , i.e., compensating signal due to nuclear fission caused by nuclear excitations. The DØ calorimeter is a nearly compensating calorimeter.

From the construction point of view there are two types of calorimeters:

- Homogeneous calorimeter
- Sampling calorimeter

In homogeneous calorimeters both the function of absorption and signal creation is carried by the same material, typically a pure or doped heavy crystal (like NaI or CsI), or a composite material (like lead glass). It is usually difficult to grow and machine large homogeneous crystals, but in recent times many large experiments have used such crystal detectors.

In sampling calorimeter, the absorption and signal creation materials are different. The absorber material is inactive and interspersed with layers of signal-producing material (active), typically liquid or solid scintillator. Inactive materials typically used are copper, lead, uranium etc. The ratio of energy loss in active and inactive material typically is of the order of 1:10. If the sampling of a signal contains adequate detail of the absorption process, the original phenomenon can be inferred from it, allowing the reconstruction of the energy dissipation profile during shower development.

2.5.4 DØ Calorimeter

The DØ calorimeter [37] is a sampling calorimeter with fine segmentation in which the sampling layers (made of an active material) are interspersed with the layers of an absorber material. In the active material, the shower development of the incident particles is periodically sampled via ionization. Calorimeter is segmented in the transverse and longitudinal shower directions to measure the shower profile (the width of shower as function of depth in calorimeter). The segmentation also helps in determining the direction of the incident particles. The shower profile together with information from tracking system, can be used for the identification of various particles such as leptons (using $\frac{E}{p}$) and photons (absence of associated charge particle tracks). Muons are minimum ionizing particle (MIP) so they can be easily identified with MIP signal in the calorimeter. Since the

colliding partons initially do not have any energy in transverse plane, transverse energy of non-interacting particles can be reconstructed from the energy balance of hermetically closed calorimeter.

The DØ calorimeter uses liquid Argon (LAr) as active medium and ^{238}U, stainless steel/copper plates as absorber materials. LAr is an ideal active material due to the following reasons. It provides uniform gain over the entire calorimeter thus one has stable response over time from different channels. Due to its nature the calorimeter can be easily segmented into readout cells. It is also radiation hard and easy to calibrate. Uranium was chosen as absorber material due to its high density which allows for a compact detector that contains almost all shower energy while reducing the cost. Because of the operating convenience calorimeter is divided into 3 parts. The central calorimeter (CC) and two end calorimeters (EC-North and EC-South). Each of the three modules (CC, EC-North and EC-South), is placed inside a separate cryostat, which is a vessel containing the calorimeter and the cryogenics to maintain the liquid argon at a constant temperature. The central calorimeter covers $|\eta| < 1.2$ region while the endcap calorimeters (EC-North and EC-South) extends the coverage upto $|\eta| < 4.2$ region. There is also an inner cryostat detector (ICD) between the central and endcap cryostates to improve the jet energy and missing energy resolution by reducing the uninstrumented regions. The ICD covers the region $1.1 < |\eta| < 1.4$. The schematic diagram of calorimeter is shown in Figure 2.10. The CC weighs about 330 tons; each of the EC modules weighs about 240 tons. The calorimeter modules themselves are further segmented into three distinct sections.

- Electromagnetic (EM) section with relatively thin uranium absorber plates.
- Fine-Hadronic (FH) with thick uranium plates.
- Coarse-Hadronic (CH) with thick copper or stainless steel plates.

2.5.4.1 Electromagnetic Calorimeter

The EM objects because of their interaction properties tend to decay over a shorter distance resulting in smaller shower profile. Therefore the innermost layers of both the CC and EC are the electromagnetic layers. The electromagnetic calorimeter is arranged in four readout layers - EM1 through EM4 and is roughly 21 radiation length deep. These layers extend radially in the central region and along the z direction in the endcap region. Each layer uses 3(4) mm thick uranium (^{238}U) absorber plates in the CC (EC). In the central region, EM calorimeter has a transverse segmentation of $\Delta\eta \times \Delta\phi = 0.1 \times 0.1$ in all layers except the third. The third layer (EM3) is designed to receive the maximum of EM showers and hence is segmented into finer cells with $\Delta\eta \times \Delta\phi$=0.05 $\times$ 0.05, resulting

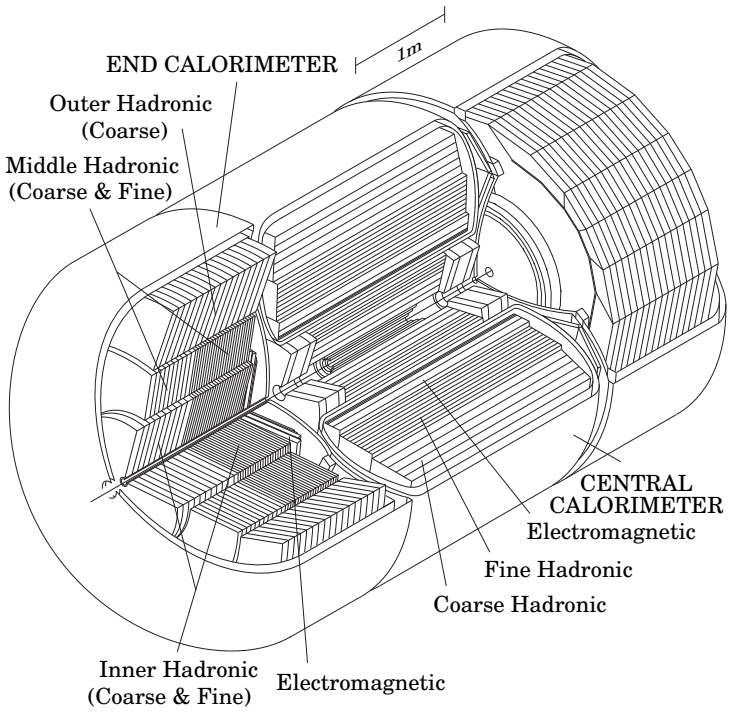

Figure 2.10: Overall view of the DØ calorimeter system [38].

in a more precise location of the EM shower centroid. This fine segmentation gives the azimuthal position resolution for electrons with energy above 50 GeV close to 2.5 mm. In the endcap regions, the segmentation is 0.1×0.1 except for $|\eta| > 3.2$, where the segmentation is increased to 0.2×0.2 because of smaller size of the pad.

2.5.4.2 Hadronic Calorimeter

Since hadrons give deeper shower profile in calorimeter therefore hadronic calorimeter comes after the EM calorimeter in both the CC and EC cryostats and is of typically 7-9 interaction length deep. The transverse segmentation of all hadronic modules is around 0.1×0.1. It consists of 3 (4) fine hadronic layers (FH) in CC (EC). The fine hadronic layers uses 6 mm thicker uranium absorbers. The coarse hadronic layer uses 46.5 mm thick copper (CC) or stainless steel (EC) absorbers. While the central region has one CH layer, the endcap regions has three CH layers.

The calorimeter layer depths in terms of their radiation (X_0) and nuclear interaction (λ_0) lengths are summarized in the Table 2.2 .

From the readout point of view each layer represents a discrete set of readout cells. These readout cells (one from each layer) are grouped radially along the outward direction (approximate direction of a shower development) to form a $\Delta\eta \times \Delta\phi = 0.2 \times 0.2$ readout geometry referred to as a tower. The readout tower geometry is shown in Figure 2.11.

	EM (X_0)				**FH** (λ_0)				**CH** (λ_0)		
	EM1	EM2	EM3	EM4	FH1	FH2	FH3	FH4	CH1	CH2	CH3
CC	2	2	7	10	1.3	1.0	0.9		3		
EC	0.3	2.6	7.9	9.3	1.2	1.2	1.2	1.2	3	3	3

Table 2.2: Layer depths for ECAL and HCAL given in X_0 and λ_0 respectively.

This is a "pseudo-projective" geometry. The term "pseudo-projective" refers to the fact that the centers of cells of increasing shower depth lie on the rays projecting from the center of the detector, but the cell boundaries are aligned perpendicular to the absorber plates.

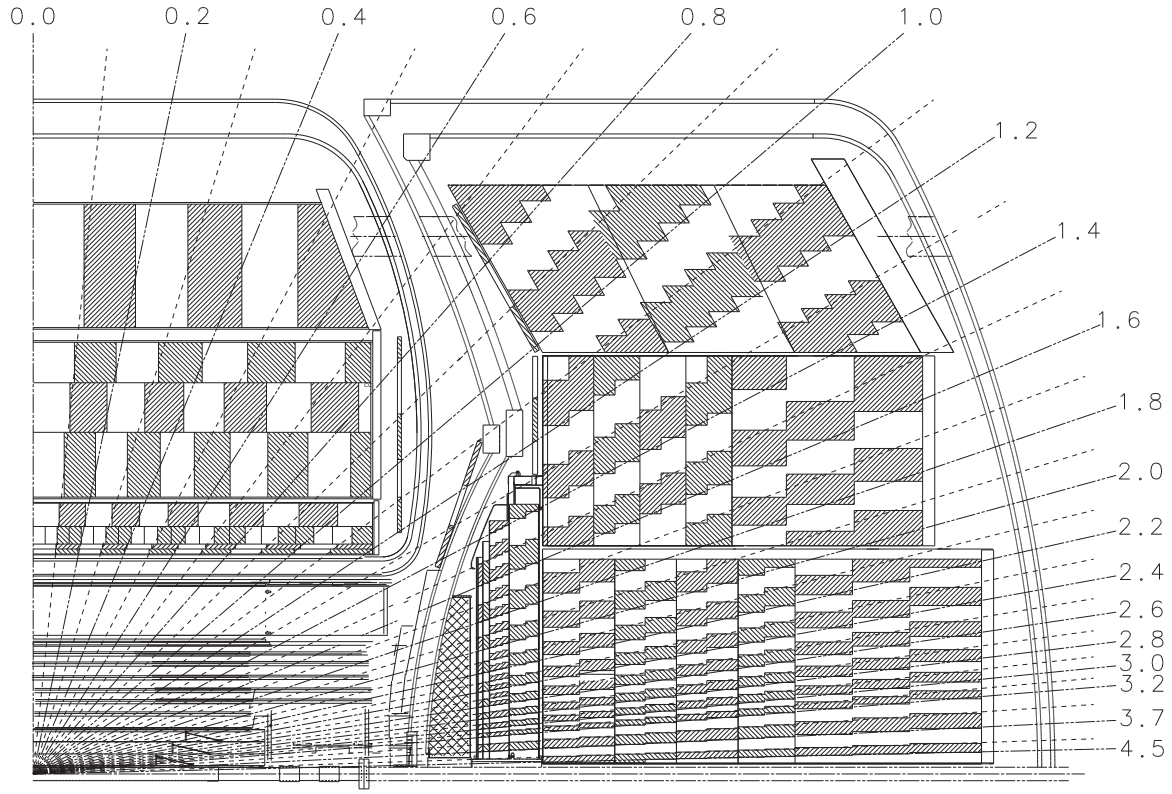

Figure 2.11: A quarter of the calorimeter in the $r-z$ plane of the detector showing the tower geometry.

A typical calorimeter readout cell is a combination made of absorber material, LAr active material and signal board. It is combination of several adjacent unit cells. A calorimeter unit cell is shown in Figure 2.12. The signal boards are made of copper readout pad sandwiched by two 0.5 mm thick G10 insulator. The outer surfaces of the boards facing the LAr are coated with a highly resistive carbon-loaded epoxy. An electric field is established by applying a positive high voltage of 2.0-2.5 KeV between the resistive surfaces of the signal boards and the grounded absorber. The inner surface of G10 is

uncoated while outer surface is coated with copper. A particle entering the calorimeter showers inside the absorber plate which results in secondary particles which ionizes the argon atoms. The ionization electrons drift toward the signal boards inducing a signal on the copper pad. The gap between the absorber plates is 2.3 mm, and the electron drift time across the gap is about 450 ns which is quite challenging from the perspective of charge signal integration since the bunch crossing interval in Run II is 396 ns. The readout electronics samples the charge on the pad, converting it to an analog signal proportional to the ionization energy recorded. Sometimes observed signal from a unit cell is very small so signals from several boards in the same eta and phi regions are grouped together in depth to form a readout cell.

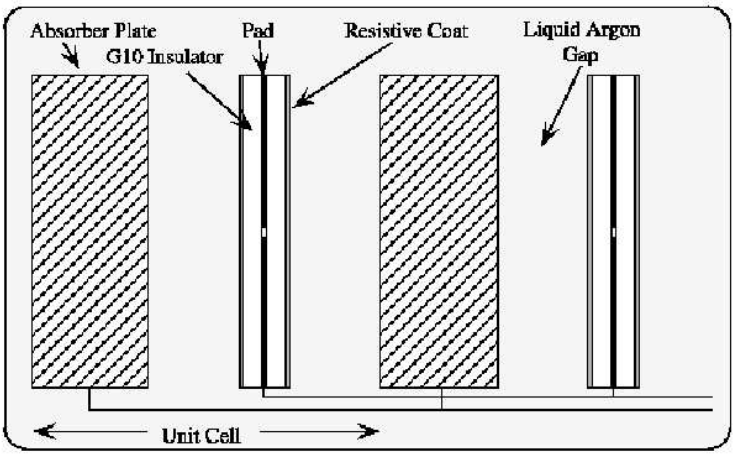

Figure 2.12: Unit Cell in the Calorimeter.

The transverse sizes of the cells were chosen to be comparable to the transverse sizes of the showers : ΔR ~0.2 for EM showers and ΔR ~0.5 for hadronic showers. A finer segmentation helps in measuring the shape of electrons and jets. Longitudinal subdivision within the EM, fine hadronic and coarse hadronic sections also helps, since the longitudinal shower profiles can distinguish EM objects and hadronic jets.

2.5.4.3 Intercryostat and Massless Gaps Detectors

We also have an uninstrumented region between the central and endcap cryostats ($1.1 < |\eta_d| < 1.4$) as seen in Figure 2.10. Materials in this region (support structure for cryostat walls, cabling) can lead to unaccounted shower development, degrading the jet resolution. To minimize the effect of uninstrumented region on shower formation, scintillator detectors were mounted on the endcap cryostat walls facing the gap. Intercryostat detector (ICD) consists of 384 scintillator tiles of the same size as the calorimeter cells ($\Delta\eta\times\Delta\phi$=0.1×0.1), which are read out by photomultiplier tubes. Massless Gap detectors are made of a

sampling LAr layer and are installed in the gap region to make further measurements of shower formation. These detectors compensate for the uninstrumented region resulting in better energy resolution for central and endcap calorimeter regions.

2.5.4.4 Calorimeter Electronics

In Run II, the higher instantaneous luminosity of the Tevatron collider with shorter bunch crossing interval of 396 ns (compared to the Run I bunch crossing interval of 3.5 μs) forced a faster readout time. At the same time, a low-noise performance and minimal channel-to-channel variations must be maintained, to prevent any degradation to the calorimeter's performance [45] [46]. A schematic of the calorimeter readout chain is shown in Figure 2.13 [47].

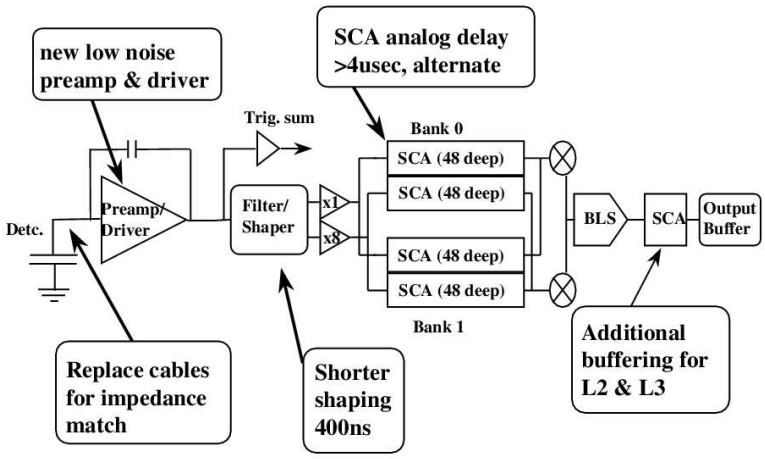

Figure 2.13: Schematic diagram of the calorimeter readout chain.

The signal from each calorimeter readout cell is triangular in shape with a very fast rise time and a decay time of 400 ns. Each signal is taken to a feedthrough port via 30 Ω resistive coaxial cables. The feed-through boards reorganize signal from the module-structure scheme to the physics scheme in which the readout channels are arranged in pseudo-projective η-ϕ towers.

The preamplifiers integrate the charge produced in the calorimeter cells producing proportional voltages. The output signal from the preamplifier is approximately a step function with a rise time of 430 ns (the drift time in the liquid argon gap) and a longer decay time constant of 15 μs.

The readout electronics of the DØ calorimeter is composed of 12 crates containing 12 ADC cards. Each card contains 384 channels which are distributed on 8 BLS cards, each treating the signals of 4 towers with 12 longitudinal depths each. All three calorimeter

cryostats together contain a total of $12 \times 12 \times (8 \times 4 \times 12) = 12 \times 12 \times 384 = 55296$ channels.

2.5.4.5 Calorimeter Performance

The performance of the DØ calorimeter has been tested extensively in test beams as well as during Run I. Its response to electrons and pions with energies between 10 GeV and 150 GeV was found to be linear to within 0.5%. The energy resolution can be described as arising from three major sources. The first is the noise term that has a fixed value, independent of the observed signal. The second is the sampling term which reflects statistical fluctuations in the energy deposited in the argon and therefore scales like the square root of the signal size. The third is the constant term, which reflects how well the response of different parts of the detector are equalized, in other words, how well we understand and calibrate the entire calorimeter. It therefore scales linearly with signal size, assuming the energy is distributed over approximately the same number of readout cells, independent of energy. The energy resolution is thus described using the following functional form:

$$\frac{\sigma_E}{E} = \sqrt{\left(\frac{N}{E}\right)^2 + \left(\frac{S}{\sqrt{E}}\right)^2 + C^2} \tag{2.15}$$

where N, S and C are the noise, sampling, and constant terms, respectively. The energy resolution was measured to be [48]

$$\left(\frac{\sigma_E}{E}\right)^2 = (0.03\%)^2 + \left(\frac{15\%}{E}\right)^2, for\ electrons \tag{2.16}$$

$$\left(\frac{\sigma_E}{E}\right)^2 = (4.0\%)^2 + \left(\frac{45\%}{E}\right)^2, for\ pions. \tag{2.17}$$

$$\tag{2.18}$$

In Run II, the resolutions are expected to be slightly worse because of extra material between the beam pipe and the calorimeter due to added preshower.

2.5.5 Muon System

The Muon system act as muon identification detector and measures its charge and momentum. It is made of proportional and mini drift tube detectors, scintillators and toroidal magnets, providing coverage upto $|\eta| < 2$. Muons are minimum ionizing particle hence they do not lose much energy via bremsstrahlung i.e, they do not readily initiate electromagnetic showers. Muon losses energy mainly via ionization and excitation of the

detector media, which are low energy-loss absorption processes. Thus muons with energy thresholds (∼3.5-5.0 GeV) for various rapidity passes the calorimeter and therefore muon system is typically the outermost part of the detector located outside the calorimeter and is well protected from the debris from the hadronic and electromagnetic showers by the thick calorimeter material. In Run II addition of 2 Tesla magnetic field in the central region along with the tracking system provides additional sensitivity for muon identification. We veto muons in this analysis so only a brief description of muon system will be given here. A more complete description can be found in [37][38].

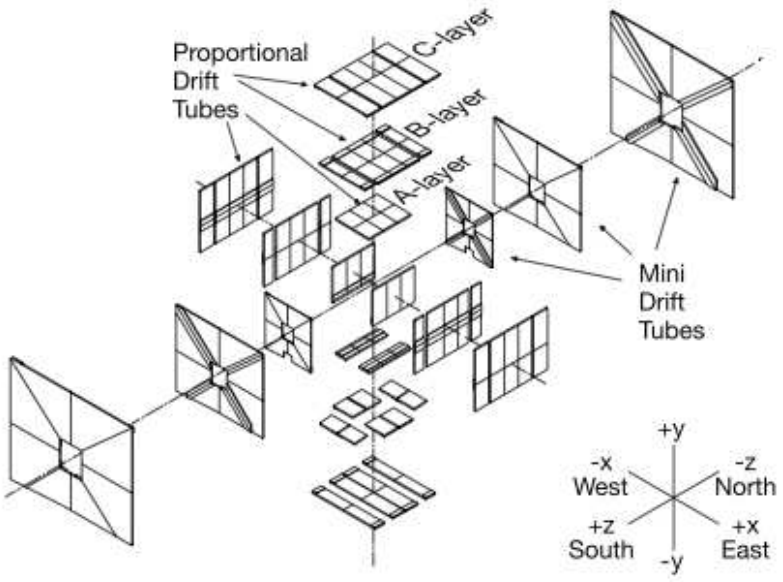

Figure 2.14: Exploded view of muon wire chambers.

The muon system can be divided into 3 main regions. The central muon system providing coverage upto $|\eta| < 1$ and forward muon systems providing coverage in $1 < |\eta| < 2$. Each section consist of 3 detection layers of drift tubes, labeled as A, B and C, with A layer situated just outside the calorimeter. Solid-iron magnet generating a toroidal field of 1.8 T is located between A and B layers. Timing and triggering information in each layer is provided by the scintillators. The central muon system uses Proportional Drift Tubes (PDT) whereas the forward muon system uses Mini Drift Tubes (MDT). A layer has 4 planes of drift tubes while B and C layers have 3 planes of drift tubes. The PDTs are 10.1 cm wide and 5.5 cm tall and have a maximum drift time of 500μs. The MDT cells have cross-section of 9.4 x 9.4 mm^2 with maximum drift time of 60 ns.

The scintillator counters are used to trigger muons and to provide accurate timing information of muon hits in drift chambers for track reconstruction. The central muon

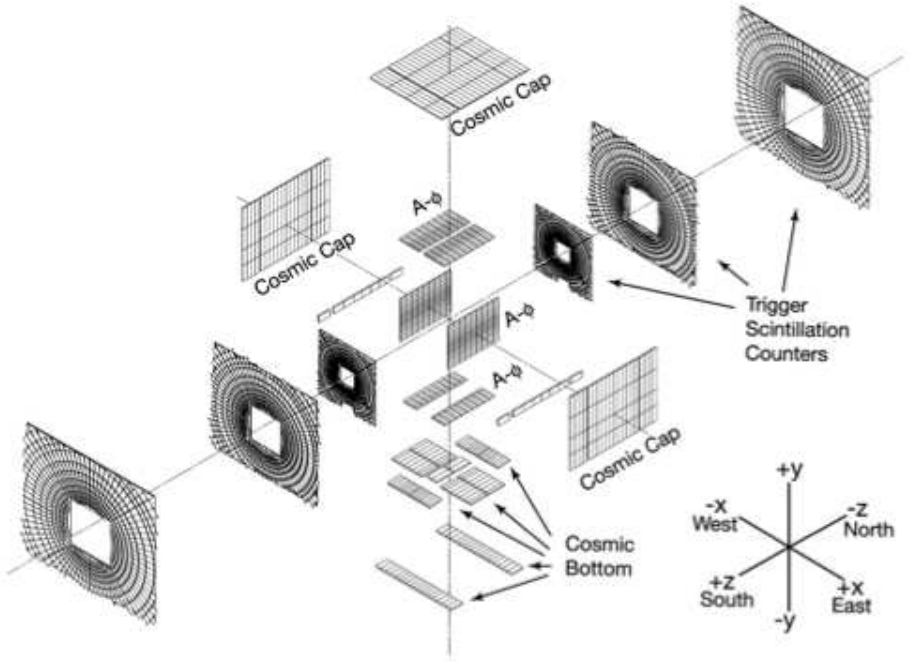

Figure 2.15: Exploded view of muon scintillator detectors.

system has 2 layers of scintillator counters, one in front of Layer A and other after Layer C. Forward muon system has 3 layers of scintillator counters. Two of them are located in front of layers A and C and third one is located behind layer C.

The muon system is stable over time to the order of 1%. Both drift tubes PDTs and MDTs have coordinate resolution of ≈1 mm whereas scintillator counters have a time resolution of ≈2μs. For muons upto 100 GeV, momentum resolution is dominated by central tracking system. Rest of the sensitivity in momentum resolution comes from the muon system. The momentum resolution for the central muon system is $\sigma(p) = 0.36(p - 3.1)/p + 0.03\%$ whereas for forward muon system it is ≈20%.

2.6 Luminosity Monitor

The luminosity monitor (LM) is used to measure the Tevatron luminosity in DØ interaction region by detecting inelastic $p\overline{p}$ collisions. Two arrays of 24 plastic scintillator counters located at $z = \pm 140$ cm, along with photo multiplier tubes (PMT) are used for this purpose. The plastic scintillators are 15 cm long and cover the pseudorapidity range $2.7 < |\eta| < 4.4$. Signal from each of them are read by PMTs. The LM is also used for measuring beam halo rates. It can also be used for a fast measurement of z coordinate of the interaction vertex.

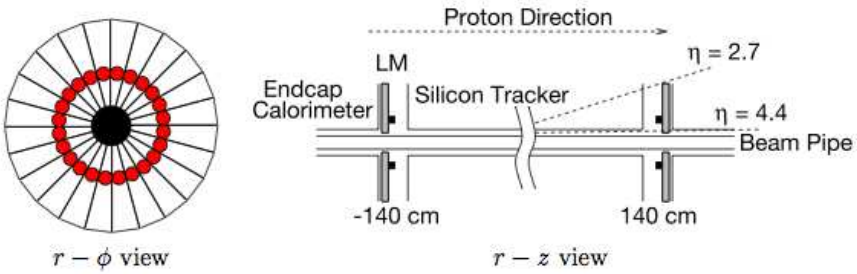

Figure 2.16: Both luminosity detectors (shown in left) are located between SMT and forward calorimeter (right) at $z = \pm 140$ cm.

To measure the luminosity accurately, the LM detectors on both ends need to be fired and background from beam halo must be suppressed from $p\overline{p}$ interactions. This is achieved by requiring z coordinate (z_0) of interaction vertex within 100 cm of the detector center. The vertex coordinate is calculated as

$$z_v = \frac{c}{2}(t_- - t_+) \tag{2.19}$$

where $t_\pm$ is the time of flight measurements of particles hitting the LM detector at $z = \pm 140$ cm.

The luminosity is measured by using average number of inelastic collisions N_{LM} per beam crossing measured by the LM.

$$\mathcal{L} = \frac{f \int \mathcal{L}_{\mathcal{LM}}}{\sigma_{LM}} \tag{2.20}$$

where f is beam crossing frequency and σ_{LM} is effective cross-section of inelastic collisions which also takes into account the efficiency and acceptance of LM detector. The σ_{LM} is proportional to inelastic cross-section $\sigma_{inelastic}(1.96 \text{ TeV}) = 60.7 \pm 2.4$ mb which is used by both the CDF and DØ collaborations for RunII.

In 2005, new VME readout electronics for LM detectors was installed which has a large dynamic range and is fully incorporated into the DØ data acquisition system, providing timing information and pulse height for each channel for every beam crossing. The data taken with new readout electronics has improved the determination of absolute scale of luminosity measurement at the DØ .

The luminosity is measured over short periods of times (60 sec), which is called luminosity blocks. Choice of such a short period is motivated by the fact that effective luminosity will be almost constant during each luminosity block, thus minimizing any uncertainty on the measurement of luminosity due to the width of time duration. It also helps in minimizing loss of data due to bad electronics of any detector sub-system. We

can reject only the bad luminosity blocks thus maintaining high data taking efficiency.

2.7 Trigger and Data Acquisition (DAQ) System

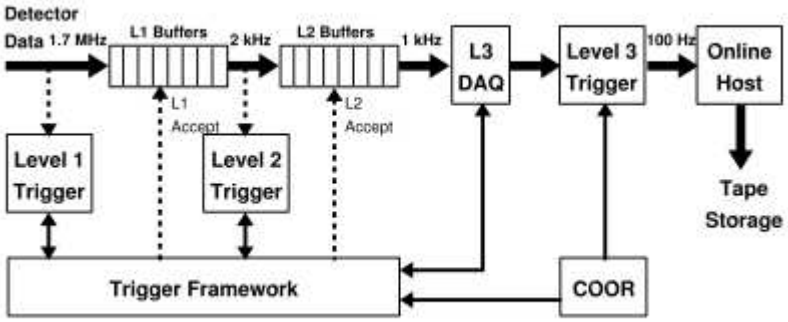

Figure 2.17: The DØ trigger scheme with typical trigger rates.

The circulating proton-antiproton beams give rise to bunch crossing at a rate of 1.7 MHz. During these, collisions can occur at the center of the DØ detector, which is called an event. Not all the events coming from collisions are useful and hence we record only those events on tape which is of considerable physics interest. Also from storage point of view, it is not beneficial to record all the events. To suppress uninteresting events (termed as backgrounds) and to identify and record interesting events (termed as signal), a 3 stage event triggering system is used. It passes only those events which matches a predefined set of patterns which is characteristics of physics process of interests. The 3 stages are Level 1 (L1), Level 2 (L2), and Level 3 (L3) triggers as shown in Figure 2.17 [38]. At each trigger level a fast reconstruction algorithm is used to compute physical meaningful terms like energy deposition, number of leptons, jets, tracks based on which decision to pass or reject the events are taken. Each trigger level is increasingly more complex than the previous, which creates a filtering system to maximize the signal to background ratio within event rate constraint. The 3 layered trigger system reduces the 1.7 MHz input at L1 to 100 Hz at the L3 output. Figure 2.17 shows maximum output rates for various trigger systems.

The trigger system is deeply integrated with the data readout. Events which passes L1 and L2 trigger levels are fully digitized and all the data from individual subdetectors are transferred to L3. L1 and L2 buffers minimize the experimental deadtimes by providing a FIFO storage to hold events data which are awaiting a L2 or L3 decision. The COOR (main run control and algorithm configuration) system provides the complete coordination

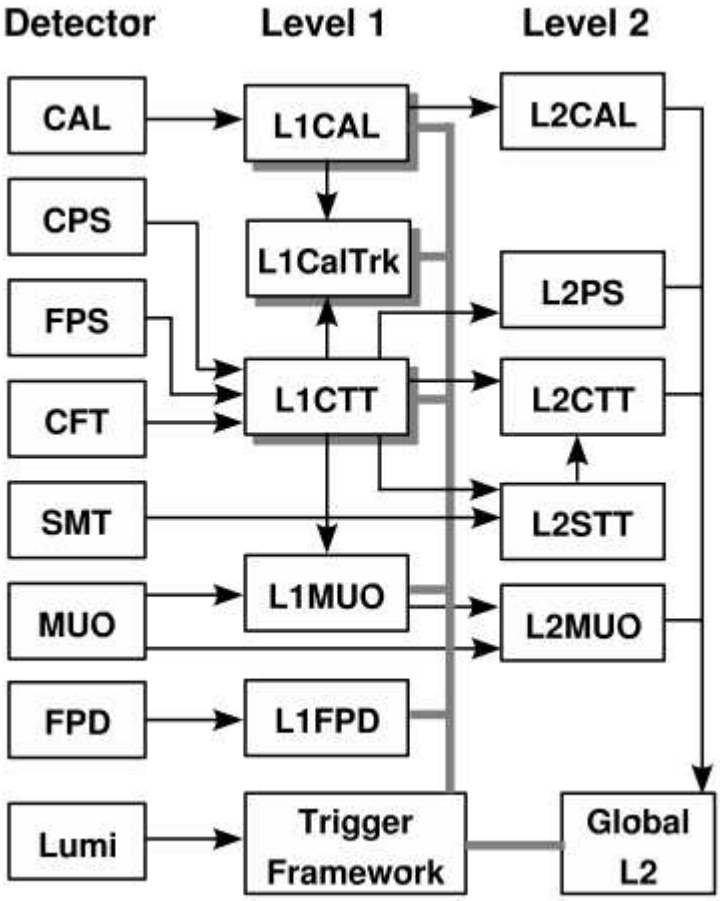

Figure 2.18: DØ L1 and L2 trigger system with data pathway (arrow).

and control of the triggering and various data taking stages. The COOR interacts directly with L1 and L2 triggering through trigger framework and to L3 through DAQ supervising system. The COOR receives all the request from users for data taking operation.

Most of the events are thrown out at the L1 level [49] because it has to make a decision on every beam crossing to determine which events should proceed in the trigger chain. The L1 decision is based on the raw detector information and simple algorithms in Field Programmable Gate Arrays (FPGA's) on specialized microprocessors. Condensed information from the calorimeter, preshower, CFT, and muon detectors is processed in parallel to make a preliminary triggering decision about each event. The L2 trigger [50] receives the information from L1 output and correlates the different pieces of information from the subdetectors to construct basic physics objects i.e. electrons, muons, tracks and jets. A block diagram for L1 and L2 level trigger system is shown in Figure 2.18

When the L2 trigger system accepts an event, it is passed to the L3/Data Acquisition (DAQ) system. L3 is a software based selection system running in a farm of parallel

commercial processors [51]. At this point, the full detector information is obtained from the subdetector readout crates (ROCs). This event information is then routed to one of ∼125 Linux PC's in the L3 farm. Each PC processes the data with an identical copy of a filtering software package, reconstructing refined physics objects and applying sophisticated algorithms to arrive at a final trigger decision. The L3 system provides a trigger decision at an accept rate of around 50 Hz. The selected events are stored on a robotic tape accessible for offline event reconstruction.

Chapter 3

Data and MonteCarlo Samples

3.1 Data

In this analysis we have used the data [52] recorded by the DØ detector between March-2002 and June-2009, corresponding to trigger versions v12 to v16. This set of data was collected using dedicated triggers, selecting events with acoplanar jets and a large imbalance in transverse momentum, defined as missing energy deposited in the DØ calorimeter. After applying data quality requirements, which removes contaminated data due to non functioning electronics of the calorimeter, we get a total integrated luminosity of 5.17 fb^{-1}.

The data collected during 2002-2005, using pre-v15 trigger versions is called as RunIIa, whereas the data collected using trigger versions v15 or higher is called as RunIIb. The total integrated luminosity corresponding to each trigger version is given in Table 3.1.

Trigger list – –	Trigger Name	Delivered Luminosity pb^{-1}	Recorded Luminosity pb^{-1}	Good Data Luminosity pb^{-1}
v12.10–v12.40	MHT30_3CJT5	277.3	250.1	227.6
v13.00–v14.00	JT1_ACO_MHT_HT	463.9	425.4	378.5
v14.00–v15.00	JT1_ACO_MHT_HT	415.2	394.0	339.2
Total Run IIa –		1156.4	1069.5	945.3
v15.00–v15.20	JT1_ACO_MHT_HT	321.0	250.5	209.2
v15.20–v16.00	JT1_MHTACO	1615.3	1535.3	1409.2
v16.00–v17.00	JT1_MHTACO	2942.2	2823.0	2600.9
Total Run IIb		4878.5	4608.8	4219.3

Table 3.1: Different triggers used to collect data for $ZH \rightarrow \nu\bar{\nu}b\bar{b}$ physics during RunIIa and RunIIb and the corresponding integrated luminosity.

3.2 Trigger Terms

3.2.1 RunIIa Triggers

In this analysis, the final state consists of $2b$ jets arising from the decay of Higgs boson and large $\not\!\!E_T$ from the invisible decay of Z boson. Thus we require triggers which can only pass set of events having di-jets and large $\not\!\!E_T$. For RunIIa data analysis two di-jet + $\not\!\!E_T$ trigger terms, `MHT30_3CJT5` and `JT1_ACO_MHT_HT` are used. The trigger contents are described in Table 3.2, using the following definitions:

- CJT(X, Y, Z): requires at least X towers, with $E_T \geq$ Y GeV and $|\eta| <$ Z. Trigger towers from ICD and MG are not taken into account.
- MHT is the vector sum of p_T of jets above a given threshold.
- HT is the scalar sum of p_T of jets above a given threshold.
- v14a runs from trigger list v14.00 to v14.79.
- v14b runs from trigger list v14.80 to v14.99.

			MHT30_3CJT5	JT1_ACO_MHT_HT		
			v12	v13	v14a	v14b
L1	CJT(3, 5, 3.2)		X	X	X	X
	CJT(3, 4, 2.4)				X	X
	CJT(1, 7, 1.8)					X
L2	MHT $>$ 20 GeV	($E_T^{jet} >$ 10 GeV)	X	X	X	X
	$\Delta\phi(jet_1, jet_2) < 168.75°$	($E_T^{jet} >$ 10 GeV)		X		
	$\Delta\phi(jet_1, jet_2) < 168.75°$	($E_T^{jet} >$ 5 GeV)			X	X
L3	MHT $>$ 30 GeV	($E_T^{jet} >$ 9 GeV)	X	X	X	X
	HT $>$ 50 GeV	($E_T^{jet} >$ 9 GeV)		X	X	X
	$\Delta\phi(jet_1, jet_2) < 170°$	($E_T^{jet} >$ 9 GeV)		X	X	X
	$25° < \Delta\phi(jets, MHT)_{min}$	($E_T^{jet} >$ 9 GeV)			X	X

Table 3.2: Contents of jet+$\not\!\!E_T$ triggers used to select p17 data sample.

3.2.2 RunIIb Triggers

For RunIIb data analysis, three set of triggers based on jets + $\not\!\!E_T$ were derived for the v15 trigger list, corresponding to topologies: mono-, di- and multi-jet + $\not\!\!E_T$. To enhance the ZH signal efficiency at L1 we select events with mono-, di- or multi-jet, to increase the acceptance of di-jet+$\not\!\!E_T$ events. In the v15 trigger list we do not have any single trigger which can fulfill all the three conditions so we use three separate triggers which

have common L2 and L3 but different L1 requirement.Two sets of three triggers were used in RunIIb:

For trigger versions v15.00 to v15.19, we use set of three triggers MJ_ACO_MHT_HT, JT1_ACO_MHT_HT and JT2_ACO_MHT_HT. Events passing any of these triggers were selected. These triggers have the following selection criteria:

- At L1, CSWMET(24) x CSWJT(1,30,3.2) (L1 monojet)
  OR CSWMET(24) x CSWJT(1,20,2.4) x CSWJT(2,8,2.4) x ACOKILL (L1 dijet)
  OR CSWJT(1,30,2.4) x CSWJT(2,15,2.4) x CSWJT(3,8,3.2) (L1 multijet)
  where an event must have:
  - A L1Cal2b missing transverse energy above X to pass CSWMET(X).
  - At least N L1 jets with an E_T greater than Y GeV in $|\eta| < Z$ to pass CSWJT(N,Y,Z).
  - All pairs of jets, which have an E_T between 8 and 20 GeV, not back to back in ϕ to pass ACOKILL i.e. jets should not be in the same plane with respect to beam axis.

- At L2, at least one jet with $E_T > 20$ GeV and $|\eta| < 2.4$; $\not\!\!H_T > 20$ GeV, calculated from all L2 jets in the event (with $E_T > 10$ GeV); $H_T > 35$ GeV, computed from all L2 jets (with $E_T > 6$ GeV and $|\eta| < 2.6$); and the acoplanarity between the two leading jets smaller than 168.75°.

- At L3, at least one jet with $E_T > 9$ GeV, H_T greater than 50 GeV, $\not\!\!H_T$ above 30 GeV, the acoplanarity between the two leading jets smaller than 170°, and the minimum $\Delta\phi$ angle between all the jets and the $\not\!\!H_T$ greater than 25°.

For trigger version v15.20 or higher, we use set of triggers MJ_MET, JT1_MET and JT2_MET. It has the same L1 and L2 criteria as used in trigger version v15.00 to v15.19 but a different L3 condition that requires:

- At least two jets with $E_T > 9$ GeV, $\not\!\!H_T$ above 25 GeV, $\not\!\!E_T$ above 25 GeV, the acoplanarity between the two leading jets smaller than 170° and the minimum $\Delta\phi$ angle between all the jets and the $\not\!\!H_T$ greater than 25°.

3.3 Monte Carlo Samples

Monte Carlo (MC) simulation techniques can be used to simulate various physics processes at the hadron colliders. The role of MC simulation is to mimic what happens in

the detector after the collision of elementary particles to understand experimental conditions i.e. tracking of particles through various detectors and their responses to various particles, so that image of an event can be reconstructed which is not the same as real event but close to it. By comparing simulation with real data, physics results can be interpreted. Monte Carlo simulation is a two step processes - first events are generated using various event generators and then these generated events are processed through detector simulation packages. Event generators perform calculations of the matrix elements for a large set of multi-parton processes for various interactions at leading order (LO) or next-to-leading order (NLO) or even next-to-next-to-leading order (NNLO), and in most cases it incorporates full spin correlations. In proton anti-proton collisions, parton distribution functions (PDFs) gives distribution of colliding quarks and gluons. Simulation techniques also incorporates initial and final state parton showers and hadronization processes. Simulated events must be processed through detector simulation package, which takes into account the detailed geometry of the detector and material distribution. A proper understanding of various SM processes depend on how well the simulated events match with the recorded data.

For this analysis we have used events generated with simulation packages ALPGEN [53], PYTHIA [54], CompHEP [55] or their combination. PYTHIA contains theory and models for various physics processes such as soft and hard interactions, initial and final state parton showers, parton distributions, multiple interactions, fragmentation and decay. For DØ physics simulation, jet hadronization and gluon radiation by initial or final state partons is also incorporated in PYTHIA. ALPGEN is a leading order generator for multi-parton hard processes and is used with PYTHIA to simulate heavy flavor processes. CompHEP is used for automatic calculation of elementary particle decays and collision processes at the lowest order of perturbation theory. MCFM (Monte Carlo for FemtoBarn processes) [56] calculates cross-sections for various femto-barn level processes.

For simulation, the PYTHIA version v6.409 [54] and the CTEQ6L1 [57] LO PDF set are used. All samples of W/Z+jets and $t\bar{t}$ processes were generated with ALPGEN v2.11 [53] interfaced with PYTHIA for the simulation of initial and final state radiation, and for jet hadronization. The inclusive di-boson MC samples were produced with PYTHIA. The single top samples were produced with CompHEP [55], interfaced with PYTHIA. The $WH \to l\nu b\bar{b}$ and $ZH \to \nu\bar{\nu}b\bar{b}$ signal sample were simulated with PYTHIA at mass difference of 5 GE for Higgs boson mass from 100 GeV to 150 GeV.

All the generated MC samples are listed in Tables 3.3, 3.4, 3.5 and 3.6. The cross-sections for some of the processes are slightly different for RunIIa and RunIIb due to different generators used. For simulating RunIIa conditions ALPGEN was not used, while for RunIIb ALPGEN was used to simulate V+Jets and $t\bar{t}$ processes and therefore

Mode	RunIIa		RunIIb	
	σ (pb)	# of events	σ (pb)	# of events
HZ$\nu\nu$bb_100	0.02709	194019	0.02709	246338
WH-lν2b_100	0.07528	194715	0.07528	320322
HZ$\nu\nu$bb_105	0.02278	193664	0.02278	235674
WH-lν2b_105	0.06271	193580	0.06271	293813
HZ$\nu\nu$bb_110	0.01899	197002	0.01899	320404
WH-lν2b_110	0.05183	199080	0.05183	316140
HZ$\nu\nu$bb_115	0.01563	199410	0.01563	235102
WH-lν2b_115	0.04225	196937	0.04225	279087
HZ$\nu\nu$bb_120	0.01256	193438	0.01256	328845
WH-lν2b_120	0.03368	194764	0.03368	321634
HZ$\nu\nu$bb_125	0.00983	198352	0.00983	133884
WH-lν2b_125	0.02611	193882	0.02611	278550
HZ$\nu\nu$bb_130	0.00742	208463	0.00742	318507
WH-lν2b_130	0.01956	193045	0.01956	553407
HZ$\nu\nu$bb_135	0.00537	192930	0.00537	133537
WH-lν2b_135	0.01404	193795	0.01404	470211
HZ$\nu\nu$bb_140	0.00372	192663	0.00372	319374
WH-lν2b_140	0.00964	197155	0.00964	495718
HZ$\nu\nu$bb_145	0.00243	193353	0.00243	133832
WH-lν2b_145	0.00626	195850	0.00626	446339
HZ$\nu\nu$bb_150	0.00148	197067	0.00148	331022
WH-lν2b_150	0.00377	194676	0.00377	320201

Table 3.3: Signal MC samples with cross sections. The number of events is calculated after applying the data quality cuts and removal of duplicate events.

Mode	RunIIa		RunIIb	
	σ (pb)	# of events	σ (pb)	# of events
w0lp	4520	12526514	4510	46404567
w1lp	1280	9425157	1280	19898756
w2lp	304	4285002	304	18087996
w3lp	72.7	3535816	72.6	3754272
w4lp	16.8	2493506	16.8	2602738
w5lp	5.08	780938	5.15	2044335
w2c0lp	23.3	1205996	24.5	934253
w2c1lp	13.9	740093	13.5	738709
w2c2lp	5.57	342472	5.50	554236
w2c3lp	2.40	446288	2.53	469900
w2b0lp	9.30	1372108	9.37	1104413
w2b1lp	4.14	666553	4.30	782487
w2b2lp	1.58	248702	1.57	523717
w2b3lp	0.763	276900	0.724	412747
WZ $\rightarrow$ any	3.25	590647	3.25	632296
WW $\rightarrow$ any	11.6	2457974	11.6	709879
ZZ $\rightarrow$ any	1.33	590647	1.33	540273
tb-eνbb	0.112	290262	0.112	247517
tb-$\mu\nu$bb	0.110	287994	0.110	225286
tb-$\tau\nu$bb	0.117	287991	0.117	248722
tqb-eνbqb	0.243	289325	0.243	272573
tqb-$\mu\nu$bqb	0.239	288444	0.239	273354
tqb-$\tau\nu$bqb	0.254	289106	0.254	246552
t+t+0lp-2b+4lp_excl	1.40	771121	1.42	793267
t+t+1lp-2b+5lp_excl	0.582	487256	0.576	456317
t+t+2lp-2b+6lp_incl	0.281	188451	0.281	277912
t+t+0lp-lν+2b+2lp_excl	1.4	771271	1.4	777068
t+t+1lp-lν+2b+3lp_excl	0.589	492647	0.577	457782
t+t+2lp-lν+2b+4lp_incl	0.284	289289	0.267	321166
t+t+0lp-2l+2ν+2b+0lp_excl	0.349	1516107	0.352	749642
t+t+1lp-2l+2ν+2b+1lp_excl	0.147	963057	0.142	452177
t+t+2lp-2l+2ν+2b+2lp_incl	0.072	258903	0.0678	281453

Table 3.4: Background MC samples with cross sections (W+jets background is calculated without K-factors). For W+jets samples, only leptonic W decays are simulated. The number of events is calculated after applying the data quality cuts and removal of duplicate events.

Mode	RunIIa		RunIIb	
	σ (pb)	# of events	σ (pb)	# of events
z+0lp-$\mu\mu$+0lp_m15-75_excl	336	533270	344	1726264
z+1lp-$\mu\mu$+1lp_m15-75_excl	39.7	429859	40.1	570408
z+2lp-$\mu\mu$+2lp_m15-75_excl	9.92	162803	9.87	275077
z+3lp-$\mu\mu$+3lp_m15-75_incl	2.81	78219	2.84	267966
z+0lp-$\mu\mu$+0lp_m75-130_excl	132	2894120	134	1514055
z+1lp-$\mu\mu$+1lp_m75-130_excl	40.6	1917640	41.4	604493
z+2lp-$\mu\mu$+2lp_m75-130_excl	9.81	956045	9.91	400558
z+3lp-$\mu\mu$+3lp_m75-130_incl	3.06	934623	3.25	146250
z+0lp-$\mu\mu$+0lp_m130-250_excl	0.881	473275	0.887	351275
z+1lp-$\mu\mu$+1lp_m130-250_excl	0.347	369868	0.359	170242
z+2lp-$\mu\mu$+2lp_m130-250_excl	0.096	266045	0.0984	160267
z+3lp-$\mu\mu$+3lp_m130-250_incl	0.0349	249232	0.0335	141929
z+0lp-$\tau\tau$+0lp_m15-75_excl	337	534038	338	1532702
z+1lp-$\tau\tau$+1lp_m15-75_excl	39.9	428065	39.9	528075
z+2lp-$\tau\tau$+2lp_m15-75_excl	9.94	163473	10.0	279564
z+3lp-$\tau\tau$+3lp_m15-75_incl	2.78	77433	2.77	278238
z+0lp-$\tau\tau$+0lp_m75-130_excl	133	2848048	131	1516656
z+1lp-$\tau\tau$+1lp_m75-130_excl	40.6	1881530	40.3	562760
z+2lp-$\tau\tau$+2lp_m75-130_excl	10.0	864222	9.99	274324
z+3lp-$\tau\tau$+3lp_m75-130_incl	3.18	828424	3.10	173657
z+0lp-$\tau\tau$+0lp_m130-250_excl	0.885	281921	0.922	358601
z+1lp-$\tau\tau$+1lp_m130-250_excl	0.340	183371	0.375	171211
z+2lp-$\tau\tau$+2lp_m130-250_excl	0.0993	86752	0.0972	162320
z+3lp-$\tau\tau$+3lp_m130-250_incl	0.0322	83736	0.0362	157799
z+0lp-$\nu\nu$+0lp_excl	809	1921328	805	2308113
z+1lp-$\nu\nu$+1lp_excl	242	1856981	246	2449272
z+2lp-$\nu\nu$+2lp_excl	62.7	883662	61.0	590022
z+3lp-$\nu\nu$+3lp_excl	15.4	248300	14.1	166856
z+4lp-$\nu\nu$+4lp_excl	3.16	81974	3.28	82479
z+5lp-$\nu\nu$+5lp_incl	0.990	38273	0.936	38872

Table 3.5: Z + light flavor MC samples with cross sections (without K-factors). The number of events is calculated after applying the data quality cuts and removal of duplicate events.

Mode	RunIIa		RunIIb	
	σ (pb)	# of events	σ (pb)	# of events
z+cc+0lp-cc+$\mu\mu$+0lp_m15-75_excl	4.14	196941	4.14	180580
z+cc+1lp-cc+$\mu\mu$+1lp_m15-75_excl	1.12	100243	0.953	93093
z+cc+2lp-cc+$\mu\mu$+2lp_m15-75_incl	0.374	97406	0.343	95436
z+cc+0lp-cc+$\mu\mu$+0lp_m75-130_excl	0.931	193789	0.932	193928
z+cc+1lp-cc+$\mu\mu$+1lp_m75-130_excl	0.504	101903	0.548	92744
z+cc+2lp-cc+$\mu\mu$+2lp_m75-130_incl	0.293	50563	0.281	51277
z+cc+0lp-cc+$\mu\mu$+0lp_m130-250_excl	0.00745	96075	0.00756	79493
z+cc+1lp-cc+$\mu\mu$+1lp_m130-250_excl	0.00460	47913	0.00439	45857
z+cc+2lp-cc+$\mu\mu$+2lp_m130-250_incl	0.00278	48783	0.00283	47946
z+cc+0lp-cc+$\tau\tau$+0lp_m15-75_excl	4.13	201925	4.11	180024
z+cc+1lp-cc+$\tau\tau$+1lp_m15-75_excl	1.02	95266	1.05	181402
z+cc+2lp-cc+$\tau\tau$+2lp_m15-75_incl	0.352	98947	0.382	179172
z+cc+0lp-cc+$\tau\tau$+0lp_m75-130_excl	0.907	196058	0.898	260243
z+cc+1lp-cc+$\tau\tau$+1lp_m75-130_excl	0.505	97060	0.488	100802
z+cc+2lp-cc+$\tau\tau$+2lp_m75-130_incl	0.277	48058	0.298	50711
z+cc+0lp-cc+$\tau\tau$+0lp_m130-250_excl	0.00746	96318	0.00743	91957
z+cc+1lp-cc+$\tau\tau$+1lp_m130-250_excl	0.00452	48303	0.00441	48814
z+cc+2lp-cc+$\tau\tau$+2lp_m130-250_incl	0.00274	47683	0.0025	46629
z+cc+0lp-cc+$\nu\nu$+0lp_excl	5.03	202417	5.61	376456
z+cc+1lp-cc+$\nu\nu$+1lp_excl	2.82	96503	3.00	199012
z+cc+2lp-cc+$\nu\nu$+2lp_incl	1.71	50589	1.64	96147
z+bb+0lp-bb+$\mu\mu$+0lp_m15-75_excl	0.514	257157	0.509	182875
z+bb+1lp-bb+$\mu\mu$+1lp_m15-75_excl	0.188	96233	0.199	85812
z+bb+2lp-bb+$\mu\mu$+2lp_m15-75_incl	0.0782	90920	0.0784	80002
z+bb+0lp-bb+$\mu\mu$+0lp_m75-130_excl	0.404	189897	0.424	205628
z+bb+1lp-bb+$\mu\mu$+1lp_m75-130_excl	0.187	94139	0.195	96232
z+bb+2lp-bb+$\mu\mu$+2lp_m75-130_incl	0.105	45458	0.099	44893
z+bb+0lp-bb+$\mu\mu$+0lp_m130-250_excl	0.00341	103161	0.00340	88816
z+bb+1lp-bb+$\mu\mu$+1lp_m130-250_excl	0.00174	45837	0.00184	44058
z+bb+2lp-bb+$\mu\mu$+2lp_m130-250_incl	0.00096	43026	0.000884	41268
z+bb+0lp-bb+$\tau\tau$+0lp_m15-75_excl	0.532	195605	0.510	182703
z+bb+1lp-bb+$\tau\tau$+1lp_m15-75_excl	0.194	89648	0.189	89263
z+bb+2lp-bb+$\tau\tau$+2lp_m15-75_incl	0.0805	92887	0.0801	80755
z+bb+0lp-bb+$\tau\tau$+0lp_m75-130_excl	0.410	197668	0.424	192733
z+bb+1lp-bb+$\tau\tau$+1lp_m75-130_excl	0.191	96265	0.197	98185
z+bb+2lp-bb+$\tau\tau$+2lp_m75-130_incl	0.0946	45393	0.104	43850
z+bb+0lp-bb+$\tau\tau$+0lp_m130-250_excl	0.00353	102378	0.00340	87909
z+bb+1lp-bb+$\tau\tau$+1lp_m130-250_excl	0.00172	46112	0.00171	44571
z+bb+2lp-bb+$\tau\tau$+2lp_m130-250_incl	0.00095	43428	0.00103	41018
z+bb+0lp-bb+$\nu\nu$+0lp_excl	2.47	388118	2.52	367482
z+bb+1lp-bb+$\nu\nu$+1lp_excl	1.25	190191	1.14	171942
z+bb+2lp-bb+$\nu\nu$+2lp_incl	0.654	88683	0.617	82829

Table 3.6: Z + heavy flavor MC samples with cross sections (without K-factors). The number of events is calculated after applying the data quality cuts and removal of duplicate events.

their cross-sections are different. For the signal, diboson and single top samples, the cross-sections for RunIIa and RunIIb are same because event generators did not change during the time period.

All simulated events have been processed through the DØ detector simulation d0gstar [58] based on the detailed detector material simulation package GEANT [59], the electronics simulation d0sim [60] and the reconstruction software d0reco [61]. Real zero bias events have been overlaid in the MC production. As the distribution in instantaneous luminosity of these zero bias events is different from those in our analysis data set, the MC events have been re-weighted in luminosity in order to match the data. Since real zero-bias events are overlaid on the MC, we use the same data quality criteria that we use in data to remove contaminated events coming from bad electronics of the calorimeter. In addition several other corrections are applied. They are described below.

3.3.1 Cross Section Correction

The cross sections for (W/Z)+jets used in the analysis are the ALPGEN leading-log cross sections, corrected with a "k factor" to match the inclusive W/Z cross sections calculated at the next-to-next-to-leading order (NNLO) [63]. The heavy flavor fractions are also corrected by the ratio of heavy to light NLO k' factors obtained using MCFM [56]. The di-boson production cross sections are calculated with MCFM, and the cross sections for top-pair and single-top are taken from Ref. [64]. Signal (WH and ZH) production cross sections are from Ref. [65]. A summary of the different k and k' factors is shown in Table 3.7.

Process	$k * k'$	Process	$k * k'$
$W(\to l\nu)$ + light flavors	1.3	$Z(\to ll, \to \nu\nu)$ + light flavors	1.3
$W(\to l\nu)$ + cc	1.3*1.47	$Z(\to ll, \to \nu\nu)$ + cc	1.3*1.67
$W(\to l\nu)$ + bb	1.3*1.47	$Z(\to ll, \to \nu\nu)$ + bb	1.3*1.52
$W(\to l\nu)$ + c	1.3*1.42		
$t\bar{t} \to$ any decay	1.43	WW	1.0
single top$\to l\nu b$ (s-channel)	0.99	WZ	1.06
single top$\to l\nu b$ (t-channel)	0.99	ZZ	1.03

Table 3.7: k- and k'-factors used for RunIIa and RunIIb Monte Carlos

3.3.2 Heavy Flavor skimming

The ALPGEN samples have been produced in exclusive bins of light (i.e. gluons or u, d and s quarks) parton multiplicity except for the highest bin obtained in an inclusive way, i.e it includes higher multiplicities as well. All ALPGEN W/Z+jets samples have

undergone a process of heavy-flavor (HF) skimming; that is, events containing heavy-flavored partons generated by PYTHIA in the region of phase space where they are also generated by ALPGEN in the hard process, have been removed in order to avoid double counting of heavy flavor production.

3.3.3 Jet Shifting Smearing and Removing (JSSR)

To account for differences in energy scale, resolution, reconstruction and identification efficiency between data and simulation, MC jets are shifted and smeared and possibly removed [66] using the standard JSSR processor. We however turn off the shifting for quark dominated final states (double and single top, dibosons, and signal). The energy changes resulting from this processor are then propagated to the $\not\!\!E_T$.

3.3.4 Z and W p_T reweighting

Jet multiplicity dependent Zp_T [67] and Wp_T [68] reweighting is applied on V+jets samples. If a jet is matched to a generator level lepton from a Wor Z decay, it is not counted as jet (using the "Lepton Veto" option).

3.4 Monte Carlo Trigger Parametrization

For MC we use trigger parametrization to match the trigger conditions used in data. Using simulated jets we calculate properties of an event at L1, L2 and L3 levels.

3.4.1 RunIIa parametrization

For L1 parametrization, we calculate the probability of the number of trigger towers fired by jet for three different E_T thresholds and η ranges in $W \rightarrow \mu\nu$ + 1 jet events. These probabilities are measured as a function of corrected p_T of the jet and by setting the z coordinate of the primary vertex to zero. There may be some L1 towers above E_T threshold without being matched to a jet. Simulation also takes into account these noisy towers. To get the number of noisy towers, simulation draws random number using the distributions of numbers of unmatched L1 towers.

These probabilities are validated in an independent $W \rightarrow \mu\nu$ + 2 jets sample. Simulation is applied on data events and compared to true L1 decision. As shown in Fig 3.1, the simulation reproduces the L1 trigger decision very well.

For higher level triggers, parametrization is done using simulated jets with $p_T >$ 15 GeV which are smeared and corrected for resolution effects to match the data. The

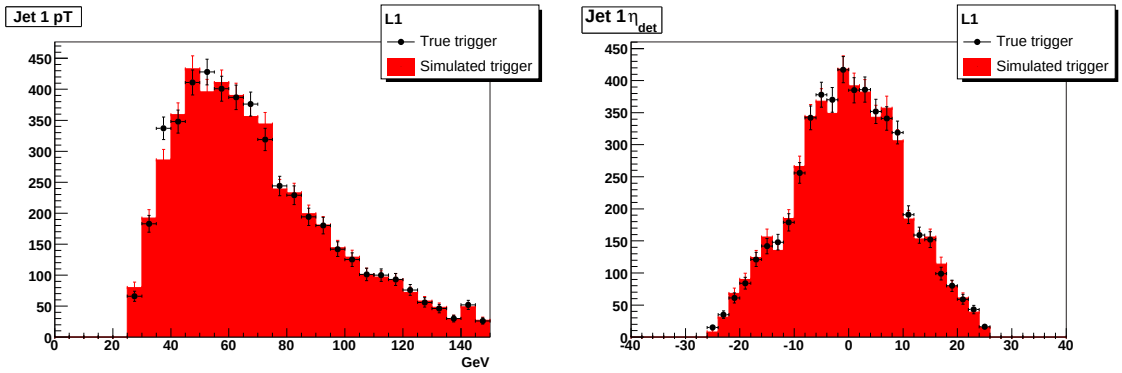

Figure 3.1: Distribution for p_T (left) and η (right) of the leading jet for W$\rightarrow \mu\nu$ + 2 jets events for L1 jet + $\not\!\!E_T$ triggers (black points) and the simulation (red histogram).

probability of reconstruction of each jet and its equivalent energy at L2/L3 levels are calculated using efficiency and resolution of L2 and L3 jets compared to jets in data events passing jet + $\not\!\!E_T$ triggers which has same L1 requirements as used in this analysis. Resolution functions are derived from the matched offline and L2/L3 jets, divided into p_T bins and for CC and EC regions separately, by fitting ratio of offline jet P_T to matched online jet P_T to a Gaussian.

At L2, offline jet p_T is corrected to remove the coarse hadronic fraction and vertex of jets are set at origin. Fig 3.2 shows the distributions comparing simulated and true L2 decision for events passing the L1 condition and we find a good agreement.

At L3, only those reconstructed jets are used which matches its L3 value via a cut $\Delta R < 0.5$. The offline energy of jets is corrected to L3 value by using $p_T^{offline}/p_T^{online}$ Gaussian fit. Fig 3.3 describe the agreement seen at L3 level.

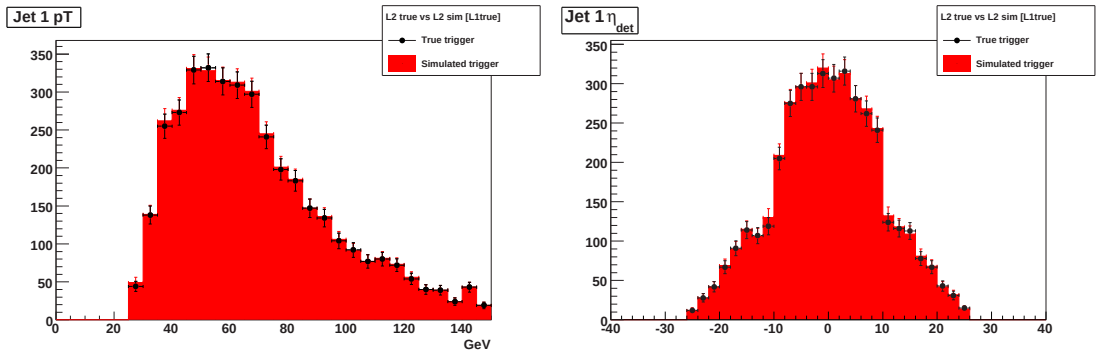

Figure 3.2: Distribution for p_T (left) and η (right) of the leading jet for W$\rightarrow \mu\nu$ events after L2 jet + $\not\!\!E_T$ trigger (black points) and the simulation of this L2 (red histogram), for the events which have passed the true L1.

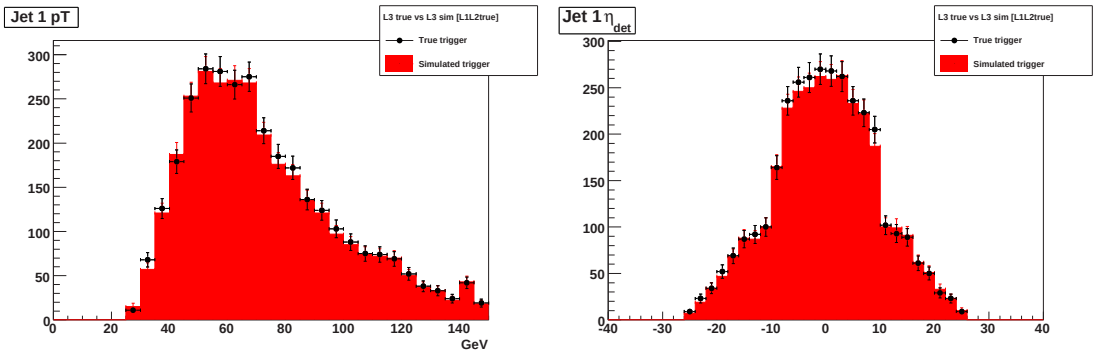

Figure 3.3: Distribution for p_T (left) and η (right) of the leading jet for W$\rightarrow \mu\nu$ events for L3 jet + $\not\!\!E_T$ trigger (black points) and the simulation of this L3 (red histogram), for the events which have passed the true L1 and L2.

After L1, L2 and L3 we find a nice agreement which is seen in the Fig 3.4

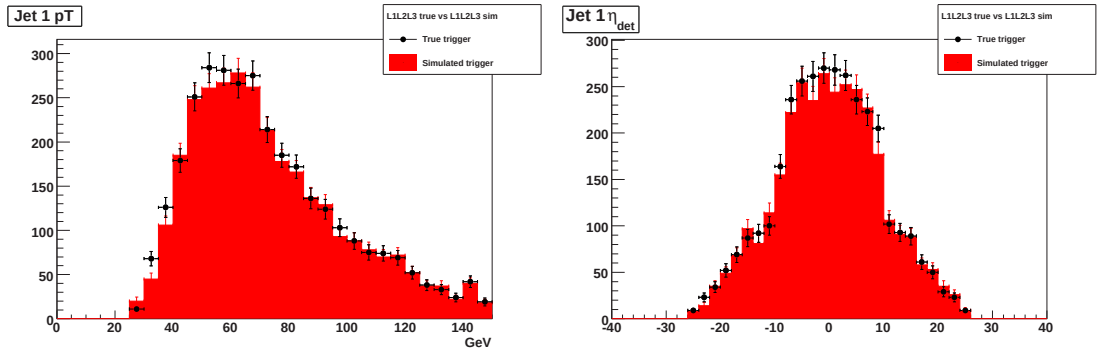

Figure 3.4: Distribution for P_T (left) and η (right) of the leading jet for W$\rightarrow \mu\nu$ events for L1, L2 and L3 jet + $\not\!\!E_T$ trigger (black points) and the simulation of the this (red histogram), for the events which have passed the true L1, L2 and L3.

3.4.2 RunIIb parametrization

During RunIIb upgrade, the L1 calorimeter trigger was upgraded for selection of EM objects, jets and building of $\not\!\!E_T$ variable at L1. Response of L1 is parametrized on data sample. Probability of firing L1 jet CSWJT(X,Y,Z) trigger towers and then L1 MET CSWMET(X,Y,Z) towers is calculated. The jet turn-on requirement is calculated using Z$\rightarrow \mu\mu$ + 1 jet sample which is parametrized as a function of modified offline jet p_T and by setting the z coordinate of the primary vertex to zero to better approximate L1 jet energy. The $\not\!\!E_T$ turn-on is calculated by building a L1 like offline $\not\!\!E_T$. Fluctuations in the jet energy measurement may produce fake $\not\!\!E_T$ resulting in correlation between jet and $\not\!\!E_T$ requirement. To absorb most of the correlation $\not\!\!E_T$ L1 turn-on is computed

after calculating jet L1 turn-on. The $\not\!\!E_T$ L1 turn-on from MC events is also shifted and smeared to match the data level because of the difference in calorimeter calibration for data and simulation. Combining all these turn-ons gives the probability for each event to pass L1 requirement. This parametrization is validated on W$\rightarrow \mu\nu$ events collected from single muon triggers. The EM objects which can fire jet trigger tower at L1 are also parametrized in similar manner. Figure 3.5 shows the agreement of simulated and true L1 decision.

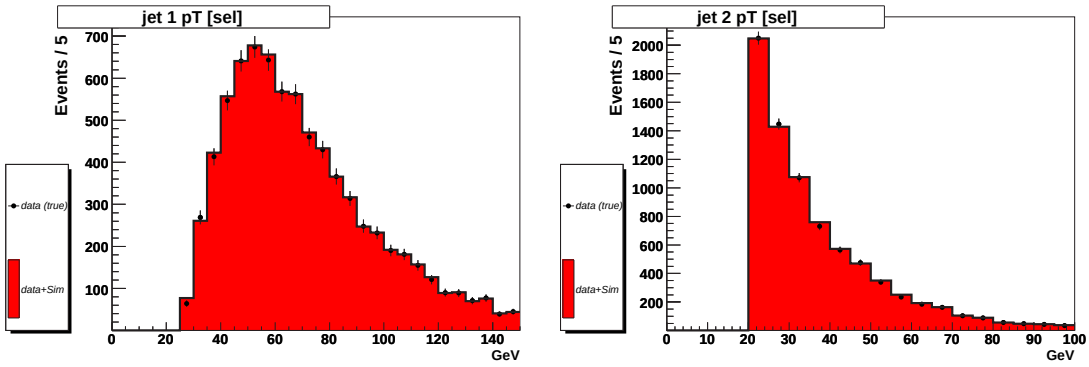

Figure 3.5: Distribution for leading jet p_T (left) and sub-leading jet p_T (right) for events which fulfill L1 trigger conditions (black points) and for those which fulfill L1 parameterization conditions (red histogram) for $W \rightarrow e\nu$ events.

In W$\rightarrow \mu\nu$ events, used to parametrize the triggers, the L2 efficiency is found to be 98.9% for events passing the L1, so we do not parametrized it and set it to be 100% efficient. The error thus performed is well within the trigger systematic uncertainities.

At L3, jet terms can be simulated in similar manner as done for RunIIa. The $\not\!\!E_T$ L3 terms can be simulated for events which pass the jet terms and also in addition some minimal analysis cuts. Same procedure is applied for EM objects too which improves the agreement between true and simulated L3. Fig 3.6 shows the agreement after L1, L2, and L3 level.

3.4.3 Systematic uncertainty on trigger parametrization

There are two main sources of uncertainties. They are:

- the precision with which the trigger decisions are parametrized in the data and
- the precision with which the parametrization of trigger decisions are adapted into the simulation

These uncertainties are evaluated with the same samples which are being used for the validation of parametrization. The first uncertainty is calculated by applying the trigger

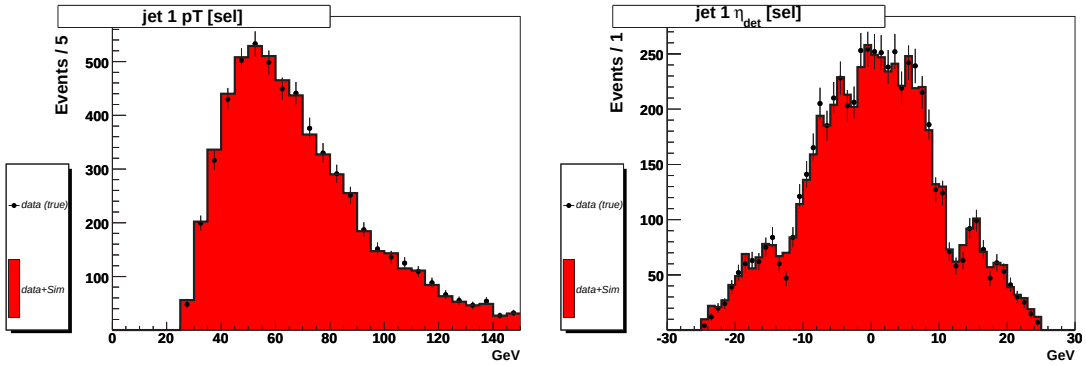

Figure 3.6: Distribution for leading jet P_T (left) and detector η (right) for $W \rightarrow e\nu$ events which fulfill L1, L2 and L3 trigger conditions (black points) and simulation for this (red histogram) for the events which pass true L1, l2 and L3.

simulation on data and comparing it with true decision using the invariant mass distribution. The ratio is fitted with a polynomial and a constant, which is assigned as systematic uncertainty. The second uncertainty is calculated with a sample which has relatively better data/MC agreement by performing bin by bin re-weightings on the jet and $\not\!\!E_T$ related variables. When the MC fully reproduces the data, we apply trigger simulation to the MC and to the data. The ratio of resulting shape is fitted by a constant which is assigned as systematic uncertainty. Both the uncertainties are added in quadrature.

Chapter 4

Object Identification

After passing through the DAQ system events get written on the tape as raw data, in form of objects like calorimeter clusters, tracks, etc. This raw data passes through an offline event reconstruction algorithm. Physics objects which characterize the final state topology of the analysis such as jets, tracks, leptons, photons and $\not\!\!E_T$ etc. are reconstructed using this offline reconstruction algorithm. Simulated events (MC) are also processed through the same offline reconstruction algorithm to get final objects for the analysis. This analysis relies heavily on jets and $\not\!\!E_T$ reconstruction, both of which are reconstructed using objects found in the calorimeter. The present chapter describes the algorithms to reconstruct these objects.

4.1 Jets

4.1.1 Jet Finding Algorithm

Jets are defined as clusters of energy or particles deposited in the calorimeter and is produced by hadronization of quarks and gluons. In DØ, jets are reconstructed via an "Improved Legacy Cone Algorithm" [69]. This specific cone algorithm has three major steps: clustering, addition of midpoints and merging and splitting of cones. The algorithm can be carried out using either energy depositions in the detector, leading to "detector jet", or using MC particles, leading to "particle jet". The jet is enclosed within a cone in $\eta \otimes \phi$ plane with a radius R, which is invariant under boosts along the z-axis. Axis of cone coincides with the jet direction, defined by the E_T weighted centroid of particles within the cone.

The first step in jet reconstruction algorithm is determining the number of "seeds" for the cone, which corresponds to most energetic particles in the event. Calorimeter towers exceeding a certain threshold energy (typically few hundred MeV) are used as seeds.

A calorimeter tower consists of all the calorimeter cells which has same eta, phi(η, ϕ) coordinate covering an area of $\Delta\eta \otimes \Delta\phi = 0.1 \otimes 0.1$ in $\eta - \phi$ plane. Since the EM shower peaks in the third layer of the EM calorimeter for CC region, the particle density is high, hence we use cells of segmentation $0.05 \otimes 0.05$ in $\Delta\eta \otimes \Delta\phi$ to further increase the resolution. For each of the seed cone, E_T weighted centroids are calculated which are used as centerers of new cones. Iteration continues until the cone axis matches with the E_T weighted centroid. Thus we get stable cones or jets which are called *protojets*.

In principle, area of the cone size created by a parton emerging from hard collision should contain trajectories of all the particles originating from that parton and reconstructed jet energy should correspond to original parton's energy but seed base cone algorithm faces some problem in reconstruction of jets due to algorithmic limitations. An ideal jet reconstruction algorithm must be "collinear safe" and "infrared safe". Saying more specifically, an ideal algorithm should be independent of detector performance and cell specifications. Any algorithm should find same solutions independent of boosts in longitudinal direction. There should not be much luminosity dependence and kinematic properties of jets must be taken into account through proper calibration.

Collinear safety problem arises when energy of a particle is shared among various calorimeter towers. It is also affected by E_T ordering of the seeds. When particle energy is distributed among several calorimeter towers [Figure 4.1(a)], none of the towers passes the requirement to become a seed for cone algorithm even if original particle do satisfy the criteria to become a jet. Also if we consider seeds in order of decreasing energy, there may be case if energy of most energetic particle is split in different seeds, a new cone appears and a different particle acts as new seed [Figure 4.1(b)]. In this case cone algorithm will not be able to reconstruct all the particles in a jet. To overcome the collinearity problem, in DØ we use seed threshold of $E_T > 1$ GeV. With this requirement cone algorithm was found to be collinear safe for jets with $p_T > 20$ GeV.

Another serious concern about the cone algorithm is infrared safety [Figure 4.1(c)]. It arises because only those towers are considered which have seed energy greater than the threshold limit. Thus one is not taking into account the scenario when two particles with one of them radiating a soft gluon are merged into a single cone and their energy is less than the threshold. So instead of having one jet, cone algorithm reconstructs two jets. Therefore a jet algorithm which only takes into account seed towers with minimum threshold are not infrared safe. To fix this problem of seed based cone algorithm, each calorimeter tower should be treated as seed. But for a large calorimeter such as DØ the computing effort will be enormous. Better efficiency can be achieved by using a minimum threshold limit i.e. selecting only towers passing seed cut as starting point for initial jet cones. Infrared sensitivity of cone based algorithm can be removed by adding a starting

point for the clustering at a mid point position of two proto jets which are separated by less than $\Delta R < 2.0$ x R_{cone}.

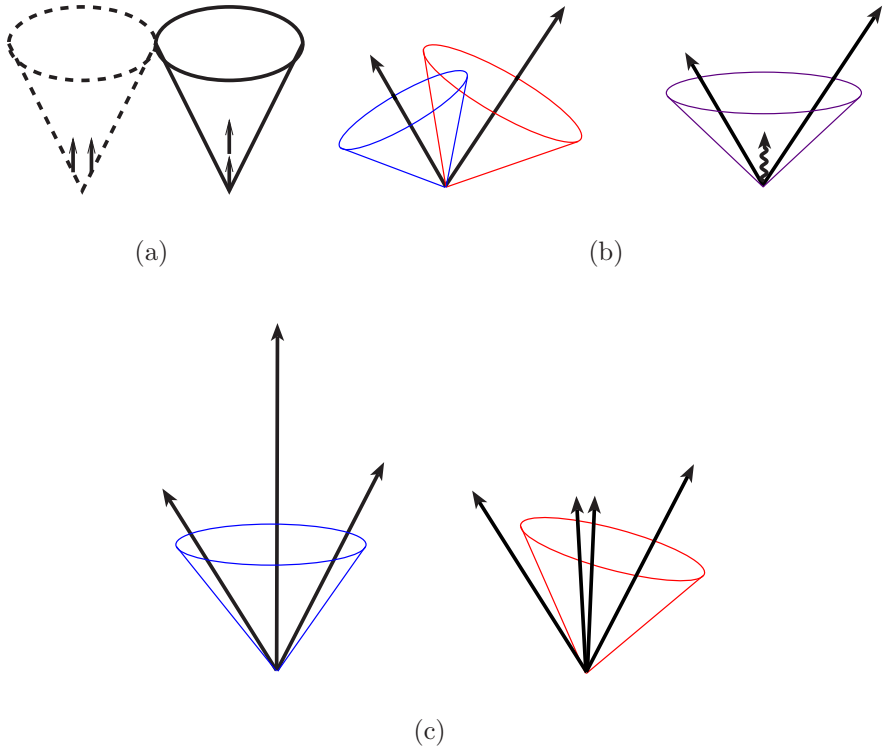

Figure 4.1: (a) Seed collinear sensitivity, (b) E_T ordering sensitivity, and (c) Infrared sensitivity

The final step in the jet finding algorithm is recombination or splitting of proto jets. Two proto jets may belong to the same source and need to be recombined or they may have common calorimeter towers and need to be split. To overcome this problem, proto jets are arranged in descending order of transverse energy E_T and are tested for calorimeter towers which are shared with other proto jets. Proto jets that share one or more towers are merged if the shared E_T is larger than a given fraction f of the total energy of the lowest energy jet. If the shared E_T is smaller than f, the shared towers are assigned to the nearest proto jet. In both cases cones are recalculated. Iteration continues with newly obtained proto jets until there are no more proto jets with overlapping calorimeter towers. Those are called final proto jets. When all the jets are final, jets below a certain E_T threshold are discarded. Table 4.1 summarize the cone jet algorithm specifications used for this analysis.

cone size R_{cone}	0.5
seed threshold p_T	1.0 GeV
split merge fraction f	0.5
jet threshhold E_T	8 GeV

Table 4.1: Cone Jet Algorithm Specifications

4.1.2 Noise Reduction

An algorithm called T42 (T42 = Threshold 4 - 2 σ) is used to suppress jets arising due to calorimetric noise. This algorithm rejects calorimeter cells which has less than 4σ energy above threshold, or with less than 2σ if there is an adjacent cell that has at least 4σ energy above the threshold. About 30% of the cells in an event are rejected by this algorithm. In central region of the calorimeter ($|\eta| < 3.2$) the number of rejected cells corresponds to expected number of noisy cells, while in the forward region of the calorimeter number of rejected cells is higher due to pile-up effects, which accumulate close to the beampipe. The T42 algorithm is applied before jet clustering.

4.1.3 Jet Energy Scale

So far we have seen how jets are being reconstructed from calorimeter towers. Each identified jet has a measured energy E_{meas}, which is the sum of all energy in calorimeter cells above certain threshold, within cone of size ΔR around the jet axis. The measured jet energy E_{meas} is different from the energy of initial parton that produces the jet due to theoretical and experimental limitations and therefore a calibration is needed. This is done using Jet Energy Scale (JES) correction.

The parametrization relating measured jet energy E_{meas} to original parton energy E_{corr} can be expressed in the form

$$E_{corr} = \frac{E_{meas} - O}{R \times S} \tag{4.1}$$

where O is the offset energy, R is the calorimeter response and S is the showering correction.

The energy offset term O, represents the additional energy in the calorimeter cells within the cone due to underlying events (multiple parton interactions and beam remnants), energy pile-up or noise from the calorimeter. The magnitude of offset correction is determined from "minimum bias" events, by triggering on events based on luminosity detector only, with no other trigger requirements. The value of O depends on η as well

as on the number of primary vertices.

The calorimeter response R depends strongly on partons specification or calorimeter region due to inhomogeneous instrumentation, dead material and non-linear response to particle energies. The value of R is measured by examination of QCD Compton events such as $qg \rightarrow q\gamma$. Photon has only EM energy which can be precisely reconstructed due to accurate EM scale calibration using $Z \rightarrow e^+e^-$ peak. Jet energies are calibrated by requiring transverse energy balance in photon+jet events where q and γ are back to back. This is the largest relative correction.

The showering correction S accounts for the escaped energy of the original parton from the cone, due to interaction of low energetic, charged hadrons with magnetic field. It is measured from jet energy profiles.

The JES correction and uncertainty on it depends on p_T of initial parton as well as on η. Since the jet energies differs in data and MC, a different MC JES is applied in simulated events. The total systematic uncertainty for the JES correction can be represented as quadratic sum of statistical and systematic errors on both data and MC.

$$\sigma_{JES} = \sqrt{\sigma^2_{data,stat} + \sigma^2_{data,syst} + \sigma^2_{MC,stat} + \sigma^2_{MC,syst}} \tag{4.2}$$

4.1.4 Jet Energy Resolution

Jet Energy Resolution (JER) is determined from di-jet event samples where both jets are back to back ($|\delta\phi - \pi| < 5^\circ$). Different samples are selected using set of dedicated di-jet triggers JT_8TT, JT_15TT, JT_25TT, JT_45TT, JT_65TT, JT_95TT, JT_125TT [70].

The sample is split in bins of 20 GeV of the average momentum of the two jet system $p_T = \frac{1}{2}(p_T^{jet1} + p_T^{jet2})$. This binning reduces jet p_T smearing related effects. The momentum asymmetry is given as:

$$|A| = \frac{|p_T^{jet1} - p_T^{jet2}|}{p_T^{jet1} + p_T^{jet2}} \tag{4.3}$$

Jet p_T resolution is related to asymmetry resolution σ_A, obtained by Gaussian fit of A with mean value set to zero. If both jets are in same p_T bin, resolution can be written as

$$\frac{\sigma_{p_T}}{p_T} = \sqrt{2}.\sigma_A \tag{4.4}$$

In case only one jet is in the rapidity bin and other jet is in some larger reference region, then the resolution can be expressed as:

$$\frac{\sigma_{p_T}}{p_T} = \sqrt{4\sigma_A^2 - 2\sigma^2_{A_{ref}}} \tag{4.5}$$

where $\sigma_{A_{ref}}$ is the resolution on the asymmetry for that other reference region.

The resolution is fitted using this formula

$$\frac{\sigma_{p_T}}{p_T} = \sqrt{(\frac{N}{p_T})^2 + (\frac{S}{\sqrt{p}_T})^2 + C^2} \tag{4.6}$$

where N, S and C are contributions from noise, statistical sampling fluctuations and calibration errors, respectively.

4.2 Missing Transverse Energy

Some of the particles produced in $p\bar{p}$ collision may not interact with the detector material or have very small interaction cross-section. For example the neutrinos do not leave any trace in the detector or sometimes leptons go undetected. In hadron colliders, energy and momentum are conserved in the transverse plane only. The information about missing particles can be accessed indirectly by calculating missing energy in the transverse plane which is called missing transverse energy - $\not\!\!E_T$. The $\not\!\!E_T$ is a vector quantity and calculated for each event as negative sum of the transverse energy contents of all calorimeter cells with energy content of at least 100 MeV above the threshold. In each cell vertex z-component is reconstructed to calculate polar angle, which is eventually used in calculating transverse energy component of that cell. Reconstructed muon momentum for visible muons in the event is also added to the visible calorimeter energy. Corrections to Jet Energy scale, noise suppression by T42 algorithm are used in $\not\!\!E_T$ calculation. A detailed description of $\not\!\!E_T$ calculation can be found in [71] [72].

4.3 Tracks

Tracks are reconstructed using hits in the tracking detector. We use two hit finding algorithm for track reconstruction and another algorithm for propagating the track reconstruction through full detector which gives parameters for potential track candidates.

The first track finding algorithm start with search of tracks starting from seeds of three SMT or CFT hits [73] [74]. These seed tracks are then propagated through the SMT and CFT detectors and at each layer a new seed track is created for every hit within predicted trajectory. The second algorithm uses Hough transform to find tracks [75]. By default both track finding algorithms are run and all the candidate tracks found by both these algorithms are ranked by quality criteria. The tracks passing minimum quality criteria are fitted using third algorithm which is based on Kalman Track Fitter. Fitting process is

the final step in track determination and it takes into account the energy loss, variations in the magnetic field and multiple scattering [76] [77].

4.4 Track Jets

Other than the particle jets (from MC particles) or detector jets (from energy deposits), we can cluster a jet from tracks too. The DØ track jet reconstruction technique is based on finding tracks within cone size $\Delta R < 0.5$ of a seed track. The tracks must have at least 2 SMT hits. The seed tracks should have $p_T > 1$ GeV. The track jets consists of at least 2 tracks with $p_T > 0.5$ GeV. Matching of track jets to calorimeter jets ensures that the jets are coming from real energy deposit in the calorimeter and not due to calorimeter noises (e.g. bad electronics).

4.5 Leptons

Lepton veto reduces lots of backgrounds in this analysis coming from decay of top, W and Z bosons having lepton in the final states. Electrons are identified after qualifying following criteria:

- Candidate track with $p_T > 8$ GeV
- Electron likelihood > 0.2, where likelihood is calculated using 7 kinematic variables.
- EM fraction of calorimeter energy over total energy $f_{EM} = E_{EM}/E_{Total} > 0.9$.
- Isolation fraction $f_{iso} > E_{Total}(0.4) - E_{EM}(0.2)/E_{EM}(0.2) > 0.2$, where $E_{Total}(0.4)$ and $E_{EM}(0.2)$ are the energies contained inside cone of size 0.4 and 0.2 in R, for total deposited energy and EM section alone, respectively.

Muons are identified after qualifying following criteria:

- Centrally matched tracks with $p_T > 8$ GeV and $\chi^2/d.o.f < 4$ from the fit of the track arc to the detector hits.
- Hits in 3 muon segment (From A and BC layers).
- No cosmic origin.

Lepton criteria is selected so that analysis remains statistically independent from other DØ Higgs search channels having leptons in the final state. By considering this we ensure avoiding overlapping events during combination across different channels.

4.6 Vertices

Vertices play an important role in finding the parent particles of decay products and thus it can be exploited to get the decay process which creates final state particles. There are two types of vertices which can be useful in this context. Primary vertices, which corresponds to hard scatter in the event and secondary vertices, which corresponds to decays of long lived particles.

4.6.1 Primary Vertices

Production vertices of particles can be reconstructed by extrapolating all the tracks passing a quality criteria to point of common origin along the z-axis. The Adaptive Primary Vertex algorithm [78] is used in DØ to find primary vertices. To remove the contribution of tracks from long lived decay particles to the primary vertex, the track errors are reweighted according to their χ^2 distribution to the vertex. Tracks which belongs to same primary vertex are fitted using the Kalman Filter algorithm and all the tracks in the fitting are initially assigned a weight of one. In following iterations, tracks are weighted according to its χ^2 distance to the fitted vertex. These steps get repeated until weights converge.

Finally to separate primary vertex from the vertices of overlayed min-bias events, a probabilistic approach is used [79], which takes into account the fact that tracks from the min-bias events have smaller transverse momenta and assign a probability to each such vertex coming from min-bias events.

4.6.2 Secondary Vertices

Decay of long lived particles lead to secondary vertices which are removed from the primary vertex. A two-pass algorithm [80] is used to find secondary vertices. First pass uses a very tight criteria to find vertices. In second pass we use looser criteria to optimize the selection efficiency. Both first and second pass uses Kalman Fitter algorithm.

4.7 b-tagging

Since the final state topology in low mass Higgs searches consists of 2 b-tagged jets, b-tagging becomes very crucial and can be exploited to optimize Higgs sensitivity. Since b-quarks are long lived, bottom hadrons often travel some distance from point of production before decaying and in this process they produce charged tracks which are displaced from the primary vertex position resulting in secondary vertices. Also b-quarks are sufficiently

heavier than other quarks, thus it produces massive B hadrons which can be easily located among other jet structures. Since b-tagging relies heavily on tracking variables while reconstructed jets are calorimeter based objects therefore secondary vertices are searched on within the track jets. First all vertices having 2 displaced tracks are considered and then tracks are added to these vertices with an algorithm that takes into account the increase of χ^2 value of the vertex fit caused by the addition of new tracks.

Presence of high mass secondary vertices having displaced tracks is used for identifying the reconstructed jets that correspond to b-quark decay. The process is called b-tagging. In DØ several b-tagging algorithm have been developed. Among them important ones are:

- **Jet Lifetime Impact Parameter (JLIP) tagger:** It combines all track impact parameters to calculate the probability that all tracks in a jet originated from a primary vertex.
- **Counting Signed Impact Parameter (CSIP) tagger:** It counts the number of tracks in a jet with a large impact parameter significance with respect to primary vertex.
- **Secondary Vertex Tagger (SVT):** It uses tracks with large impact parameter significance to reconstruct secondary vertices.

The output of all these algorithms are fed into a more powerful artificial neural network (NN) tagger which is trained using large number of simulated QCD $b\bar{b}$ and QCD light jet events, output of which gives a very strong discrimination power for b jets than any of the input variables as shown in Figure 4.2

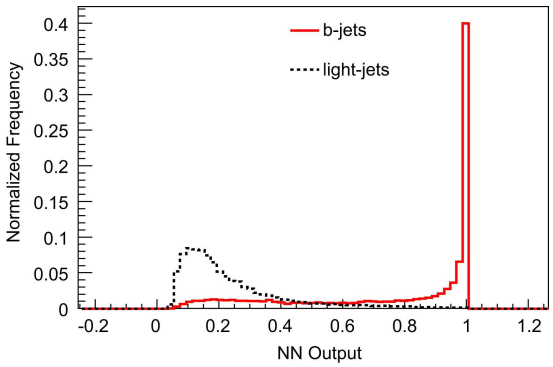

Figure 4.2: NN tagger output for QCD light jets MC (dashed lines) versus QCD $b\bar{b}$ MC (solid line), normalized to unit area.

The NN tagger combines the following 7 input variables:

- Decay length significance of the secondary vertex selected by NN tagger. If more than one secondary vertices are present in the track jet, tagger selects one with the highest decay length significance.
- Weighted combination of the impact parameter significances of all the tracks in the jet as calculated by CSIP algorithm.
- JLIP probability that all the tracks in the jet originated from the primary vertex.
- χ^2/d.o.f of the fit constraining all the tracks in the jet to the selected secondary vertex.
- Number of tracks used by SVT algorithm to reconstruct secondary vertex.
- Invariant mass of the tracks of the selected secondary vertex.
- Number of secondary vertices found by the SVT algorithm within a cone of $\Delta R < 0.5$ around the jet.

4.8 Taggability and Tag Rate Function (TRFs)

In order to be considered for b-tagging, jets must be taggable, i.e. it must match a track jet within a distance $\Delta R < 0.5$. Taggability requirement must be fulfilled because all b-tagging algorithm relies heavily on the tracks and vertices present in the track jets. It also indicates the efficiency of the tagging algorithm.

The efficiency of the NN tagger was measured in data by applying direct tagging in a sample with jets containing muons i.e. jets either pass or fail NN output cut. In MC due to over estimated performance, we apply corrections at tagging level. When measuring the performance in data, Tag Rate Functions (TRFs) and Scale Factors (SFs) are derived. TRFs gives the probability to tag b-jets, c-jets in MC as well as the Fake Tag Rates - which is the probability to tag a jet not coming from heavy quarks. SFs are determined between data and MC to accurately reproduce the data performance in MC. These functions are parametrized in terms of p_T and η of jets. Based on the cut of NN tagger output 12 operating point are defined. In this analysis we use two operating points:

- **Loose:** with a NN output cut at 0.45
- **Tight:** with a NN output cut at 0.85

Chapter 5

Analysis

5.1 preselection

In the first stage of analysis we apply a cut based preselction criteria to minimize the overwhelming multijet background and at same time retaining high efficiency for signal. In the second stage we apply selection criteria which uses a set of kinematic and topological cuts with a neural network based b-tagging algorithm to enhance the signal sensitivity. Finally, separation between signal and remaining background is achieved by means of a Boosted Decision Tree (BDT) technique. The analysis is optimized for search of Higgs boson in the mass range of 100 - 150 GeV, with m_H=115 GeV chosen as the reference point. After basic data quality and trigger selection we apply the following cuts for preselection.

The primary vertex (PV) must be reconstructed within the acceptance of the silicon vertex detector ($|z_{\mathrm{PV}}| < 40$ cm, where z is measured from the center of the detector along the beam direction), and at least three charged particle tracks have to originate from that vertex. Only jets with $p_T > 15$ GeV within $|\eta| < 3.2$ are considered in the analysis, and are ordered in decreasing p_T. There must be at least two taggable jets in the event, and the missing transverse energy is required to be greater than 20 GeV. Finally, there must be no bad jets in the event with $p_T > 15$ GeV, not considering those for which the only bad-jet criterion is EM fraction $> 95\%$ The numbers of events after each cut for the MC signal samples and the observed data events can be seen in Tables 5.1 and 5.2.
After this preselection, additional criteria are used to define four distinct samples:

- a signal sample (Sec. 5.2) used to search for Higgs boson signal. Here, further topological criteria are applied to reduce the multijet background, among which a tighter cut on the $\not\!\!E_T$ is required. In addition, a veto on isolated leptons [81] is applied to reduce the background from $W \to \ell\nu$+jets;

- an electroweak control sample (Sec. 5.3), enriched in $(W \to \mu\nu)$+jets events, where the jet system has a topology similar to that of the signal sample, and used to validate the SM background simulation. The selection is similar to the one used for the signal sample, except that the veto on isolated muons is reversed;
- a "MJ-model" sample, dominated by multijet events, and used to model the multijet background in the signal sample. This sample is selected in the same way as the signal sample, except for the very last topological selection criterion that is reversed;
- a large multijet control sample (Sec. 5.4), used to validate this modeling procedure. Here, the topological selection criteria are sufficiently relaxed to lead to a sample largely dominated by multijet events.

5.1.1 Signal Selection

The signal sample is selected as follows:

- The highest p_T good jet in the event has to be taggable.
- Exactly two or three taggable jets with $p_T > 20$ GeV and $|\eta| < 2.5$.
- Acoplanarity $\Delta\phi(\text{jet}_1, \text{jet}_2) < 165°$ (The two leading taggable jets must not be back-to-back in the plane transverse to the beam direction.)
- $\not\!\!E_T > 40\ GeV$ (To reduce the large multijet background which are low $\not\!\!E_T$ events)
- $\not\!\!E_T$ Significance > 5. The "missing E_T significance" $\mathcal{S}$ variable takes into account the resolution of jet energies to assess the significance of the observed $\not\!\!E_T$ relative to expected fluctuations in measured jet energies. Larger the $\mathcal{S}$, it is more likely that the observed $\not\!\!E_T$ is not due to such fluctuations. $\not\!\!E_T$ Significance is calculated using the standard DØ algorithm [82], with jet energy resolutions updated as implemented in the JSSR processor, and unclustered energy smeared in the simulation. The distribution of missing E_T significance in the electroweak control sample (see Section 5.3) without the $\mathcal{S} > 5$ cut is shown in Figure. 5.1.
- Veto on isolated electrons and muons as described in section 5.1.3. (This cut is designed to reduce the background from $(W \to \ell\nu)$+jets.)
- $\mathcal{D} < \pi/2$, where $\mathcal{D} = \Delta\phi(\not\!\!E_T, \not\!\!p_T)$. For signal, the missing track-p_T, $\not\!\!p_T$, defined as the opposite of the vectorial sum of the charged particle transverse momenta, is expected to point in a direction similar to that of $\not\!\!E_T$. This is not expected in multijet events, in which the $\not\!\!E_T$ originates mainly from mismeasurements of jet energies.

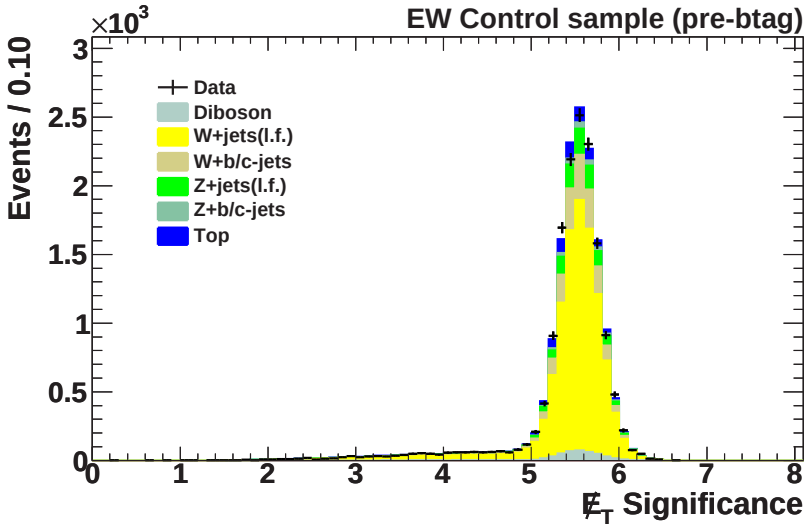

Figure 5.1: Missing E_T significance in the electroweak control sample.

In all of the following, any "dijet" quantity, such as dijet invariant mass, dijet acoplanarity, dijet ΔR, is calculated using the two leading taggable jets.

5.1.2 Additional cuts in Run IIa

In Run IIa our triggers do not have a $\not\!\!E_T$ requirement at L1. In addition, in a large part of the Run IIa triggers (v12 & v13) the $25^\circ < \Delta\phi(jets, MHT)_{min}$ (where MHT is scalar sum of p_T of all jets) cut is absent at L3. These two missing trigger conditions create significant differences between the p17 and p20 part of the analysis. Especially, they enhance significantly the relative multijet contribution in Run IIa (compared to Run IIb).

In order to reduce these differences between the p17 and p20 part of the analysis and to be able to have the same final Decision Tree treatment in the two samples we apply two additional cuts in p17:

- Uncorrected $\not\!\!E_T$ (without the CH part of the calorimeter) > 30 GeV
- $\not\!\!E_T(GeV) > -40 \times \min \Delta\phi(\not\!\!E_T, \text{jets}) + 80$ (MET triangle cut)

which were found to be closest to the trigger conditions. The effect of these two cuts is illustrated in Figure.5.2.

5.1.3 Lepton Veto

To ensure orthogonality to other low mass Higgs search channels, we veto on events that contain isolated leptons [81] with the following definitions.

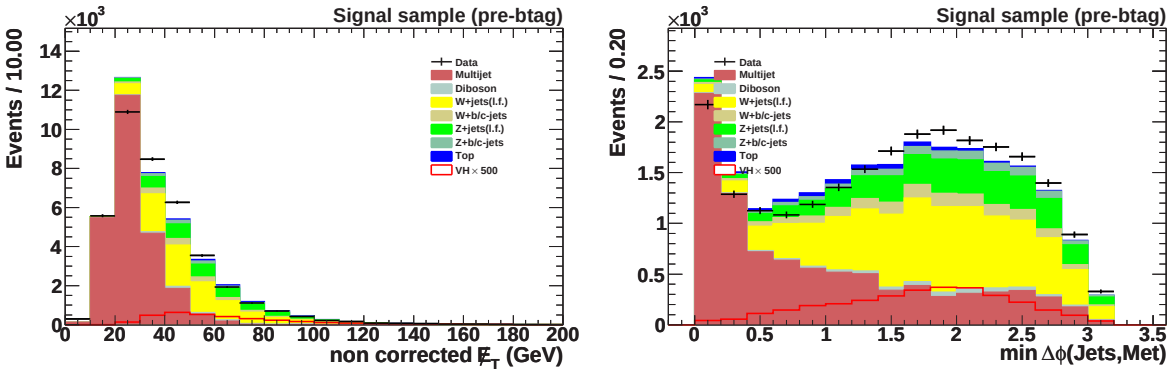

Figure 5.2: The left plot is the uncorrected $\not\!\!E_T$in p17 before the additional p17 cuts were applied. The right plot is the min $\Delta\phi(\not\!\!E_T, \text{jets})$ after the uncorrected $\not\!\!E_T$cut was applied.

Electrons:

- medium selection criteria within $|\eta_{det}| < 1.1$
- tight selection criteria within $1.5 < |\eta_{det}| < 2.5$
- $p_T > 15$ GeV

Muons:

- tight selection criteria
- $|\eta_{det}| < 2.0$
- $p_T > 15$ GeV

The efficiencies of lepton identification are used during the vetoing process. For electrons and muons with $\mathrm{p_T} > 15GeV$, momenta are smeared in the simulation in order to reproduced the momentum resolution in data.

5.1.4 $\not\!\!E_T$ Significance

Significance of measured $\not\!\!E_T$ for each event, based on its resolution can be evaluated using a probabilistic method. The $\not\!\!E_T$ significance method was first developed in RunI. In RunII it was optimized by incorporating underlying event algorithm. It provides a measure of purity of $\not\!\!E_T$, thus discriminating true $\not\!\!E_T$ events from the events with fake $\not\!\!E_T$ coming from the mismeasuremnt of jet energy scale.

The missing transverse energy resolution of an event can be determined by variety of effects e.g. the energy resolution of jets, muons and electrons, vertex location, unclustered

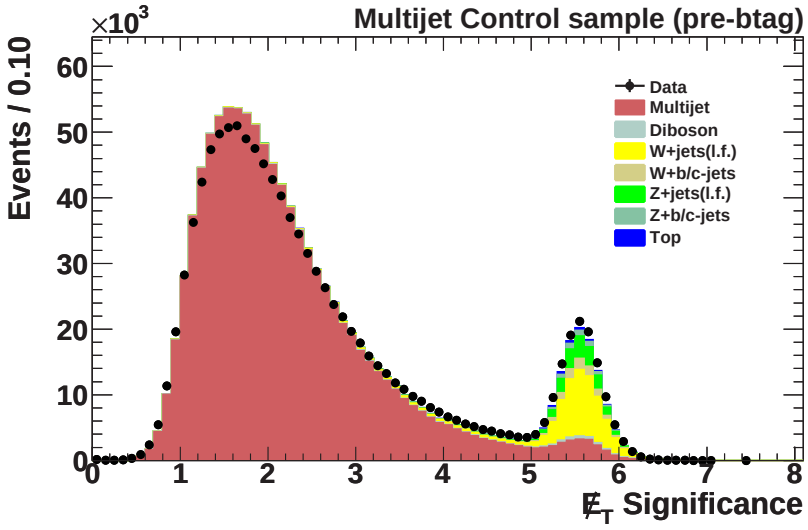

Figure 5.3: Missing E_T significance in the multijet control sample.

energy deposits and electronic noises in the calorimeter. A probability distribution for the $\not\!\!E_T$ is computed using the energy resolution of physics objects in an event which indicates the likelihood that measured $\not\!\!E_T$ is consistent with a resolution fluctuation of the measured object in that direction. Also for computational convenience, probability densities of energy of individual physics objects is presumed to be Gaussian distribution. The objects considered are

- **Unclustered Energy:** Unclustered energy is deposited in calorimeter due to presence of soft jets, warm and noisy regions due to electronic problem and out of cone energy.
- **Jets:** The jet energy resolution is calculated from the p_T momentum imbalance in back-to-back di-jet events parametrized as a function of jet E_T in four different η regions. For RunIIb, the latest updated jet resolutions are used.
- **Leptons:** Resolution of EM objects is derived from MC simulation.

Taking all these resolution parameters into account a probability S is calculated which is used for discriminating real and fake $\not\!\!E_T$, which is referred as $\not\!\!E_T$ significance. Figure 5.3 shows the distribution of $\not\!\!E_T$ significance in multijet control sample. This sample is dominated by instrumental background which is concentrated and peaks at the lower S value. The simulated physical processes having real $\not\!\!E_T$ peaks at higher significance value. Thus by applying a cut on S one can reject most of the events with fake $\not\!\!E_T$ while maintaining high signal acceptance by lowering the $\not\!\!E_T$ cut.

Selection	Data			ZH MC ($115 GeV$)			WH MC ($115 GeV$)		
	Events	Rel.(%)	Abs.(%)	Events	Rel.(%)	Abs.(%)	Events	Rel.(%)	Abs.(%)
NP Skim	58058784	100.00	100.00	199410	100.00	100.00	196937	100.00	100.00
Bad runs & LBNs	49059725	84.50	84.50	198842	99.72	99.72	196264	99.66	99.66
Event quality	43160619	87.98	74.34	192848	96.99	96.71	190154	96.89	96.56
First PVz $\leq$ 40cm	36465706	84.49	62.81	171726	89.05	86.12	169379	89.07	86.01
First PV has $\geq$ 3 tracks	36240684	99.38	62.42	171476	99.85	85.99	169247	99.92	85.94
Trigger	14522989	40.07	25.01	–	–	–	–	–	–
$N_{\text{good}_{\text{jets}}} \geq 2$	10844094	74.67	18.68	121888	71.08	61.12	122845	72.58	62.38
Trigger simulation	–	–	–	59330	48.68	29.75	54484	44.35	27.67
$\not\!\!E_T \geq 20$ GeV	7820144	72.11	13.47	59238	99.84	29.71	52290	95.97	26.55
At least two taggable jets	6084447	77.80	10.48	55378	93.48	27.77	48427	92.61	24.59
Veto on bad jets	5976873	98.23	10.29	55231	99.73	27.70	48000	98.12	24.37

Table 5.1: Cut-flow for p17 pre-selection. (Generated number of MC events for the signal, scale factors not applied.)

Selection	Data			ZH MC (115GeV)			WH MC (115GeV)		
	Events	Rel.(%)	Abs.(%)	Events	Rel.(%)	Abs.(%)	Events	Rel.(%)	Abs.(%)
NP Skim	117982762	100.00	100.00	235102	100.00	100.00	279087	100.00	100.00
Bad runs & LBNs	104717299	88.76	88.76	234613	99.79	99.79	278125	99.66	99.66
Event quality	96411187	92.07	81.72	227265	96.87	96.67	269387	96.86	96.52
First PVz $\leq$ 40cm	87081921	90.32	73.81	203180	89.40	86.42	240840	89.40	86.30
First PV has $\geq$ 3 tracks	83480876	95.86	70.76	200176	98.52	85.14	238597	99.07	85.49
Trigger	21969133	26.32	18.62	–	–	–	–	–	–
$N_{\mathrm{confirmed_{jets}}} \geq 2$	8212140	37.38	6.96	134134	67.01	57.05	161633	67.74	57.91
Trigger simulation	–	–	–	67974	50.68	28.91	64957	40.19	23.27
$\not{E}_T \geq 20$ GeV	6275319	76.42	5.32	67959	99.98	28.91	64007	98.54	22.93
At least two taggable jets	5306614	84.56	4.50	63989	94.16	27.22	59999	93.74	21.50
Veto on bad jets	5154074	97.12	4.37	63770	99.66	27.12	59398	98.99	21.28

Table 5.2: Cut-flow for p20 pre-selection. (Generated number of MC events for the signal, scale factors not applied.)

5.1.5 Sideband and MJ-model Sample

The variable $\mathcal{D}$ is used to define the "signal sideband". It is selected in the same way as the signal sample, except that the previous requirement $\mathcal{D} < \pi/2$ is now inverted. To define the multijet model (MJ-model), the small contribution from SM processes in that $\mathcal{D} > \pi/2$ sideband is subtracted, and the resulting sample is used to model the multijet background in the signal sample, i.e., in the $\mathcal{D} < \pi/2$ region. The MJ-model sample is normalized such that, after adding contributions from the SM backgrounds in the signal sample, the expected number of events is identical to the number observed in the signal sample. A MJ-model sample is constructed for the multijet control sample (Sec. 5.4) using the same procedure.

5.1.6 Cut Flows

The number of events after each cut for the MC signal samples and the observed data events for p17 and p20 can be seen in Tables 5.3 and 5.4, respectively.

5.1.7 *b*-Tagging

We have used the standard DØ Neural Network *b*-tagging algorithm [83]. We perform *b*-tagging on the two leading taggable jets selected using the analysis cuts. Using simulated samples we studied various *b*-tagging combinations for the two jets, to determine the optimum *b*-tagging strategy:

- Both leading jets pass the Loose 3 (L3) tagging point (L3-L3)
- Both leading jets pass the Very Tight (VT) tagging point (VT-VT)
- Exactly one of the 2 leading jets pass the L3 tagging point (L3 only)
- Exactly one of the 2 leading jets pass the VT tagging point (VT only)
- Both leading jets pass the L3 tagging point, and one of them also passes the VT tagging point (asymmetric tagging) (VT-L3)
- Both leading jets fail the L3 tagging point (no *b*-tags)

and concluded that the VT-L3 asymmetric tag is the optimal combination. To increase the sensitivity we also define an orthogonal single-tag sample, in which one of the two jets has a VT tag, while the other fails the L3 tag (VT-not L3 combination). In the following, we will often simply call tight and loose the VT and L3 *b*-tagging operating points, respectively, whereas a jet failing a particular tag such as L3 will be refered as !L3.

Selection	Data			ZH MC (115GeV)			WH MC (115GeV)		
	Events	Rel.(%)	Abs.(%)	Events	Rel.(%)	Abs.(%)	Events	Rel.(%)	Abs.(%)
Pre-selection	5976873	–	–	21.55	–	–	51.24	–	–
Leading good jet taggable	5606933	93.81	92.15	21.24	98.56	98.34	49.59	96.76	95.99
Veto on $N_{\text{taggable}_{\text{j}}\text{ets}} \leq 3$	5278555	94.14	86.75	20.54	96.70	95.10	47.71	96.21	92.36
$\Delta\phi(\text{jet}_1, \text{jet}_2) \leq 165°$	3917075	74.21	64.38	20.03	97.52	92.74	44.99	94.31	87.10
$\not\!\!E_T \geq 40GeV$	301064	7.68	4.95	19.40	96.87	89.83	39.47	87.73	76.41
Uncorrected $\not\!\!E_T \geq 30GeV$	110091	36.57	1.81	18.59	95.82	86.08	36.52	92.54	70.71
$\not\!\!E_T$vs min $\Delta\phi(\not\!\!E_T, \text{jets})$	42915	38.98	0.71	18.13	97.50	83.93	34.16	93.53	66.13
MET Significance ≥ 5	32122	74.85	0.53	18.13	100.00	83.93	33.38	97.72	64.63
Isolated muon veto	28403	88.42	0.47	17.92	98.84	82.95	25.29	75.75	48.96
Isolated electron veto	25319	89.14	0.42	17.92	99.99	82.95	21.11	83.49	40.87
$\Delta\phi(\not\!\!E_T, \not\!\!p_T^{\text{trk}}) < \pi/2$	20349	80.37	0.33	17.82	99.48	82.52	18.64	88.31	36.09

Table 5.3: Cut-flow for p17 selection. (All scale factors applied for the signal, with an integrated luminosity of 5.2 fb^{-1})

Selection	Data			ZH MC (115GeV)			WH MC (115GeV)		
	Events	Rel.(%)	Abs.(%)	Events	Rel.(%)	Abs.(%)	Events	Rel.(%)	Abs.(%)
Pre-selection	5154074	–	–	21.41	–	–	45.54	–	–
Leading good jet taggable	4708570	91.35	88.73	20.96	97.88	97.49	43.85	96.28	95.33
Veto on $N_{\text{taggable}_\text{j}\text{ets}} \leq 3$	4500563	95.58	84.81	20.36	97.16	94.72	42.62	97.20	92.66
$\Delta\phi(\text{jet}_1, \text{jet}_2) \leq 165°$	3773698	83.85	71.11	20.16	98.99	93.77	40.48	94.97	88.00
$\not{E}_T \geq 40GeV$	747581	19.81	14.09	19.79	98.18	92.06	37.05	91.52	80.54
MET Significance ≥ 5	156639	20.95	2.95	18.47	93.33	85.92	32.99	89.07	71.74
Isolated muon veto	139920	89.33	2.64	18.47	99.99	85.92	25.76	78.05	55.99
Isolated electron veto	128223	91.64	2.42	18.47	99.99	85.91	21.74	84.41	47.27
$\Delta\phi(\not{E}_T, \not{p}_T^{\text{trk}}) < \pi/2$	100526	78.40	1.89	17.96	97.24	83.54	18.81	86.52	40.90

Table 5.4: Cut-flow for p20 selection (All scale factors applied for the signal, with an integrated luminosity of 5.2 fb^{-1})

In the simulated samples direct tagging is applied, and the events are weighted according to the relevant data/MC scale factors provided by the b-ID group. In addition to these regular scale factors, we need anti-tag scale factors, e.g., for the !L3 jet in the single-tag (VT-!L3) sample. We use this example to explain how such an anti-tag scale factor is calculated.

In the equations below N_{all} refers to all events that have at least one VT tag. N_{loose} refers to these events that have an additional L3 tag.

$$N_{!loose} = N_{all} - N_{loose}$$

The probability of finding a loose tag is

$$P_{loose} = \frac{N_{loose}}{N_{all}}$$

which is the Tag Rate Function (TRF). Therefore

$$\frac{N_{!loose}}{N_{all}} = 1 - \frac{N_{loose}}{N_{all}}$$

$$P_{!loose} = 1 - P_{loose} \tag{5.1}$$

The scale factor for a loose tag is

$$S_{loose} = \frac{P^{Data}_{loose}}{P^{MC}_{loose}} \tag{5.2}$$

Using equations (5.1) and (5.2):

$$S_{!loose} = \frac{P^{Data}_{!loose}}{P^{MC}_{!loose}} = \frac{1 - P^{Data}_{loose}}{1 - P^{MC}_{loose}} = \frac{1 - P^{MC}_{loose} S_{loose}}{1 - P^{MC}_{loose}}$$

$$S_{!loose} = \frac{1 - TRF^{MC}_{loose} S_{loose}}{1 - TRF^{MC}_{loose}}$$

Similarly, the scale factor for a jet that is not-tight tagged

$$S_{!tight} = \frac{1 - TRF^{MC}_{tight} S_{tight}}{1 - TRF^{MC}_{tight}},$$

and for jets that are loose-not-tight tagged

$$S_{loose!tight} = \frac{TRF^{MC}_{loose} S_{loose} - TRF^{MC}_{tight} S_{tight}}{TRF^{MC}_{loose} - TRF^{MC}_{tight}}.$$

The weight given to an event with two tight tags is

$$S_{tight}(jet1)S_{tight}(jet2).$$

For an event where the first jet is tightly tagged, and the second is only loosely tagged, the weight is

$$S_{tight}(jet1)S_{loose!tight}(jet2)$$

and similarly if it is the second jet that is tightly tagged.

For an event where the first jet is tightly tagged and the second not loosely tagged, the weight is

$$S_{tight}(jet1)S_{!loose}(jet2)$$

and similarly if it is the second jet that is tightly tagged.

For an event where neither jet is tightly tagged, the weight is

$$S_{!tight}(jet1)S_{!tight}(jet2).$$

These are all the b-tagging weights that we will need. We verified that, within precision, the sum of event yields from the 0-tag, 1-tag exclusive, and 2-tag weighted events is equal to the total initial yield.

To check how well the b-ID Neural Network (NN) output is modelled by the simulation, a bin-by-bin reweighting was performed. The bin boundaries are defined by the twelve b-ID supported working points (WP). The weight, similar to $S_{loose!tight}$ shown above, represents the WP_i-not-WP_{i+1} scale factor, where WP_i and WP_{i+1} are the working points just below and just above the NN output of the jet, respectively:

$$S_{WP_i!WP_{i+1}} = \frac{TRF^{MC}_{WP_i} S_{WP_i} - TRF^{MC}_{WP_{i+1}} S_{WP_{i+1}}}{TRF^{MC}_{WP_i} - TRF^{MC}_{WP_{i+1}}}.$$

Distributions of such reweighted NN outputs are shown in Fig. 5.4 for the signal, electroweak-control and multijet-control samples (Secs. 5.2 and 5.3).

Direct tagging is also applied in the MJ-model sample and a dedicated procedure is used for the L3-VT asymmetric tag, as explained below.

After applying the L3-VT asymmetric tag in the events used to model the multijet background, the statistics are strongly reduced and the results degraded by the corresponding statistical uncertainties. We solve this problem by applying a tagging rate factor. We verified that for this particular set of events, once a VT tag is applied, a L3 tag in the other jet does not change the event topology (see Figures. 5.5 and 5.6 for the signal-sample sideband, and Figures. 5.7 and 5.8 for the multijet-control-sample side-

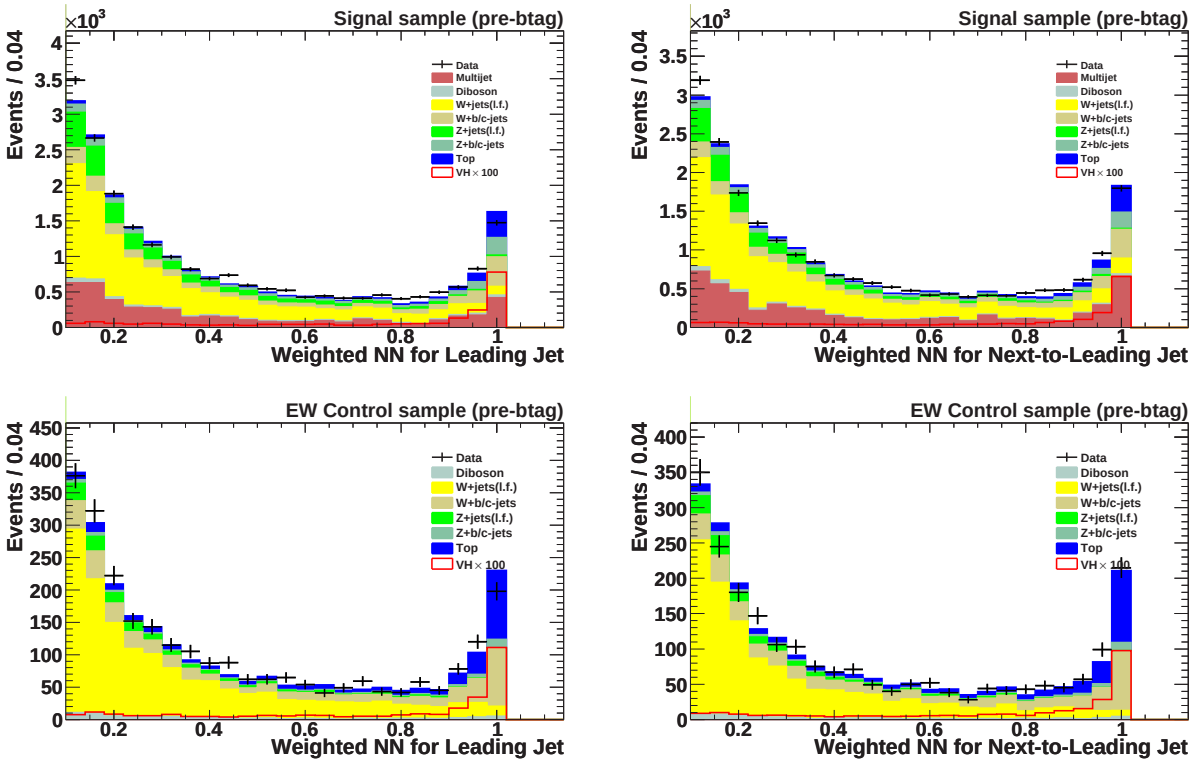

Figure 5.4: The reweighted b-ID NN output distributions in the signal and electroweak-control samples.

band). Therefore, for the multijet modeling in the L3-VT asymmetric tag, we actually use an inclusive VT tag multiplied by a tagging rate factor of 0.15 for p17 data and 0.17 for p20 data. These tagging rate factors were derived in the signal-sample sideband. They are used in the following plots, but the final multijet normalization in the double-tagged signal samples will be derived from the multijet decision tree outputs (Sec. 5.6). Note that these tagging rate factors are not related to the post- to pre-tag normalization ratios applied to the multijet model, as explained in Section 5.2.

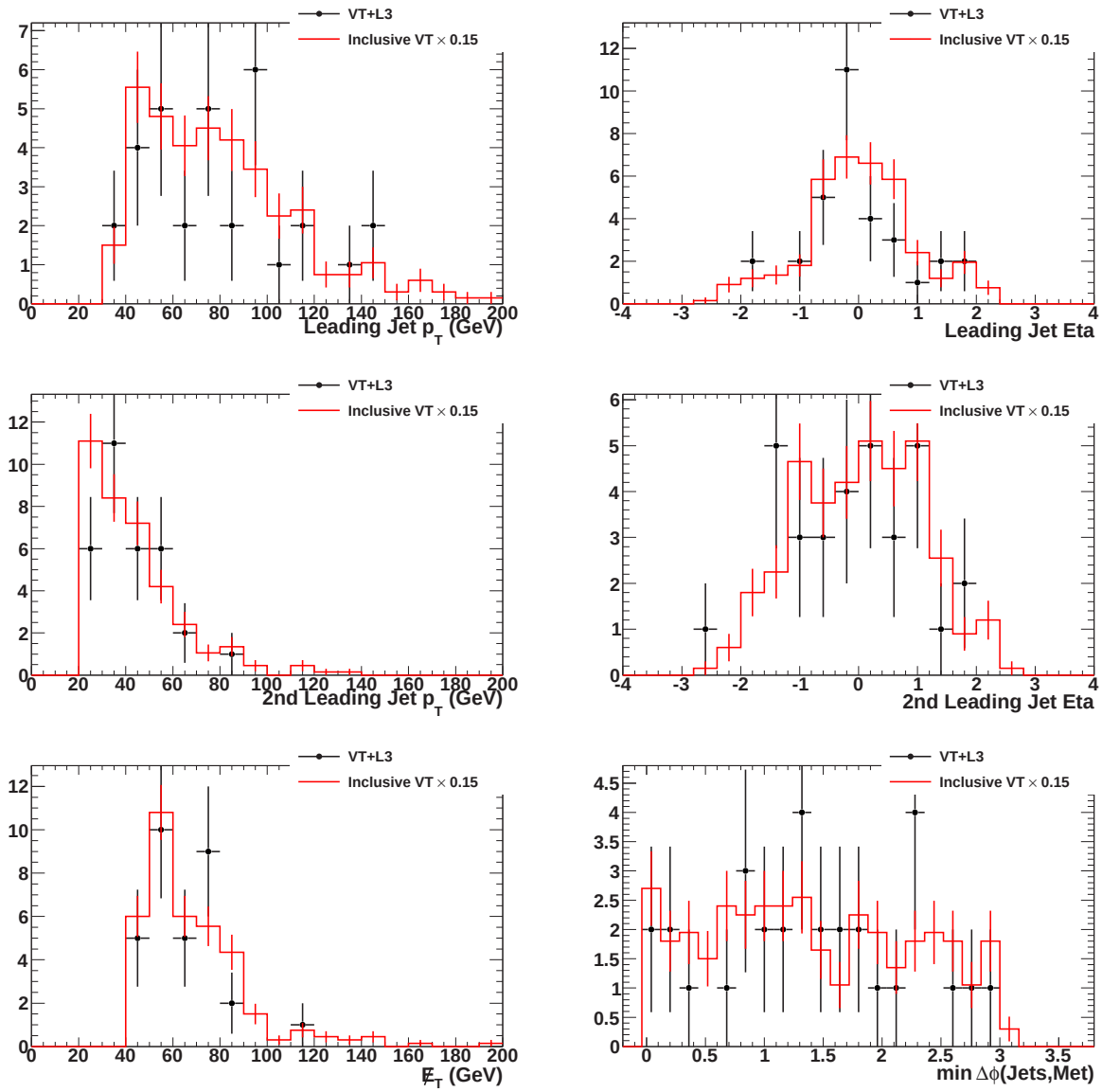

Figure 5.5: p17 data - Jet and $\not\!\!E_T$ distributions after L3-VT asymmetric tag compared to inclusive VT tag in the signal sample sideband.

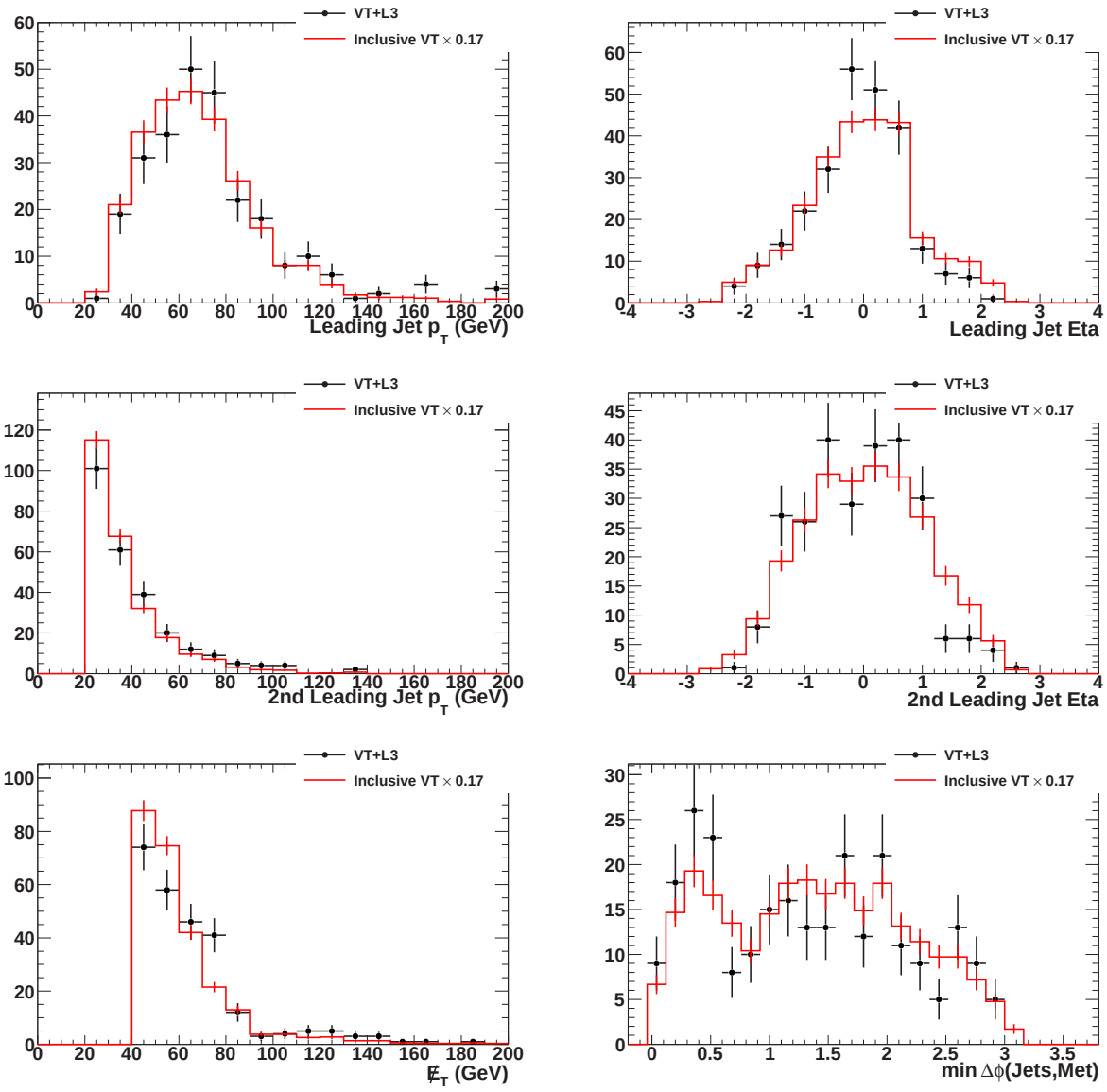

Figure 5.6: p20 data - Jet and $\not\!\!E_T$ distributions after L3-VT asymmetric tag compared to inclusive VT tag in the signal sample sideband.

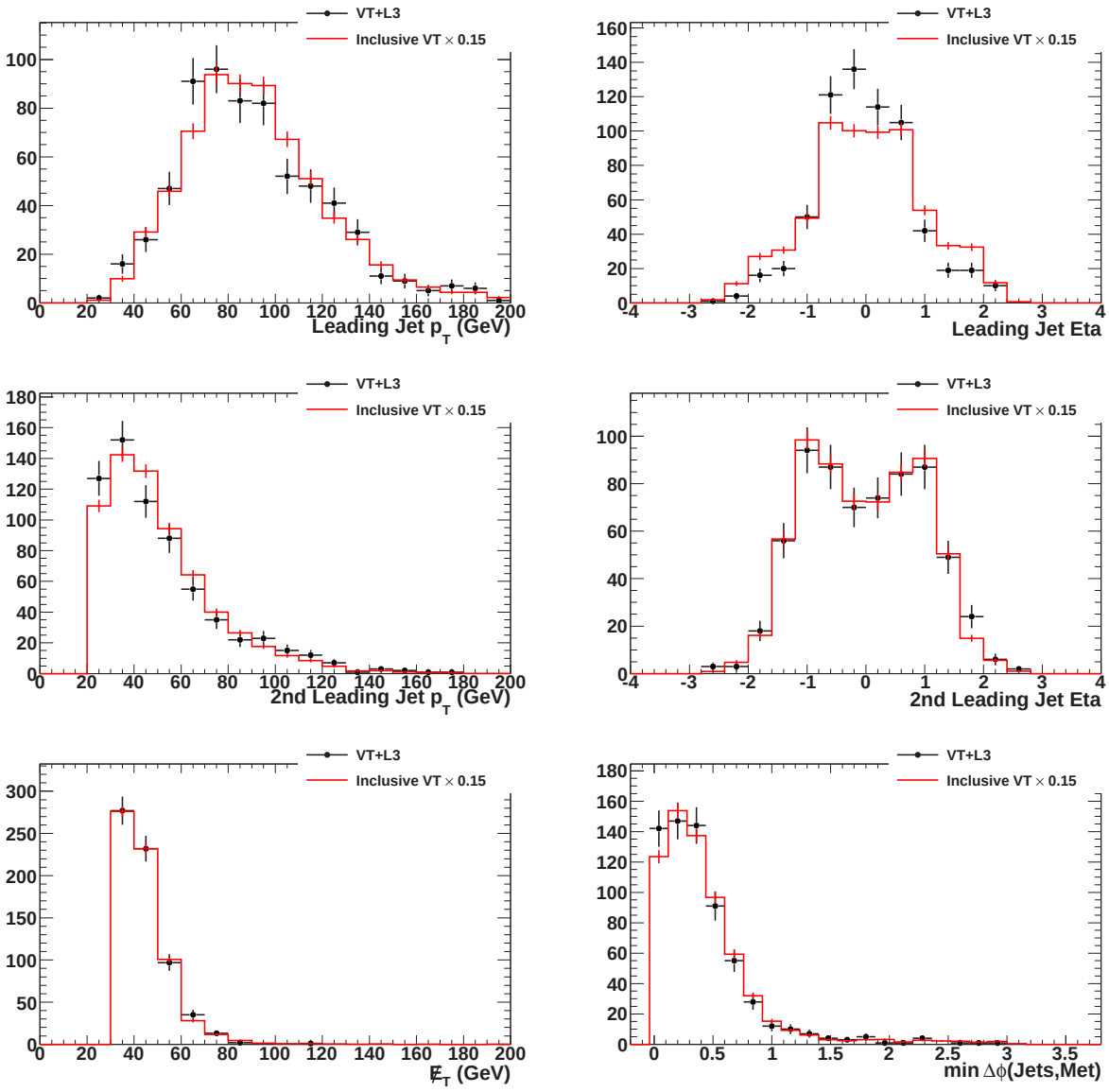

Figure 5.7: p17 data - Jet and $\not\!\!E_T$ distributions after L3-VT asymmetric tag compared to inclusive VT tag in the multijet control sample sideband.

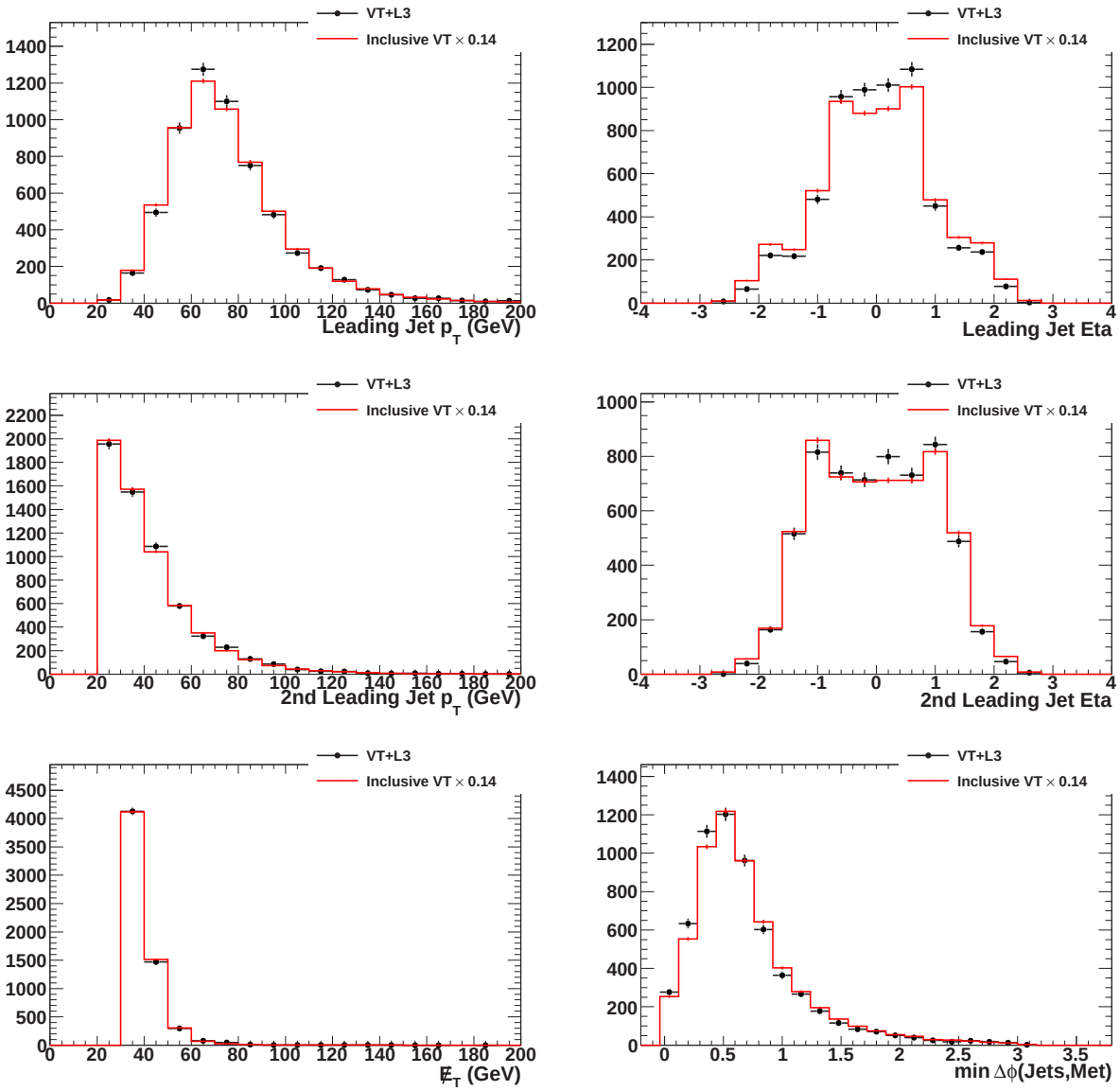

Figure 5.8: p20 data - Jet and $\not\!\!E_T$ distributions after L3-VT asymmetric tag compared to inclusive VT tag in the multijet control sample sideband.

5.2 Signal Sample

The signal sample (also called analysis sample) is selected as described in Sec. 5.1.1. The normalization and heavy-flavor scale factor determined in Sec. 5.3 are applied to the (W/Z)+jets simulation. The MJ-model sample is normalized at pretag level as explained in Sec. 5.1.5, with normalization factors of 2.98 in p17 and 1.82 in p20.

To obtain the normalization of the MJ-model in the signal sample after b-tagging, the pre-tag normalization factor is multiplied by the ratio of post- to pre-tag normalizations of the MJ-model in the multijet control sample, separately for single-exclusive and asymmetric-double b tagging. These ratios are 0.98 and 1.07 in p17, and 1.08 and 1.10 in p20.

One variable we plot and use in the multivariate analysis is the "recoil subtracted dijet $\mathrm{p}_\perp$". It is closely related to a similar variable defined in DØ 's $ZZ \to ll\nu\nu$ result [84]. In the transverse plane we define a dijet thrust axis, which is the transverse momenta of the leading minus the next-to-leading jet. The dijet transverse momentum is then decomposed into parallel and perpendicular components with respect to this thrust axis. We keep only the transverse component "dijet $\mathrm{p}_\perp$" which is robust against jet resolution effects so it gives a good discrimination against multijet events which have high $\not\!\!E_T$ due to jet mismeasurements. A recoil activity correction is further defined either using the jet-uncorrected $\not\!\!E_T$ or the remaining jets in the event ($p_T > 15$ GeV and $|\eta| < 3.2$). We choose the one with the largest projected magnitude in the hemisphere opposite to the thrust axis, i.e. the one that minimizes the "dijet $\mathrm{p}_\perp$". The recoil activity is enhanced with a factor of two to account for the underestimation of the true recoil energy.

At later stage, in this analysis we also use the number of isolated tracks. A track is called isolated if it has a $p_T > 5$ GeV, fulfills certain quality criteria and there is no other track with $p_T > 0.5$ GeV in the hollow-cone of $0.06 < \Delta R < 0.3$ around this track. This definition of isolated tracks was devised in [85], where it was optimized for a similar jets+$\not\!\!E_T$ final state to reject $(W \to \ell\nu)$+jets events with unidentified leptons. The track quality criteria used for this definition are described in that note.

The numbers of events observed and expected from the various background sources are given in Table 5.5 before b tagging, for an exclusive VT tag, and for an asymmetric VT-L3 double tag. There is agreement between numbers of events expected and observed in the b-tagged samples, once the systematic uncertainties reported in Section 6.3 are taken into account.

Plots of various variable distributions before b-tagging can be seen in Figures. 5.9-5.11. For one tight tag sample it is shown in Figures. 5.12-5.14, whereas for double asymmetric (L3-VT) tag, in Figures. 5.15-5.17. Overall, there is good agreement between the observed data and expected background, both before and after b-tagging.

Sample	Before b-tagging	1 VT and 1 !L3 tag	1 VT and 1 L3 tag
ZH (115GeV)	17.72 ± 0.09	5.44 ± 0.05	5.69 ± 0.05
WH (115GeV)	18.55 ± 0.15	5.81 ± 0.08	5.83 ± 0.07
W+jets	55502.19 ± 134.53	1311.11 ± 24.43	135.63 ± 10.13
W+b/c jets	9101.85 ± 45.65	1252.06 ± 14.66	411.10 ± 8.28
Z+jets	17785.05 ± 130.62	211.43 ± 17.11	8.67 ± 2.70
Z+b/c jets	4621.03 ± 36.15	700.67 ± 11.43	256.46 ± 6.33
top	2407.71 ± 5.98	814.58 ± 3.35	427.18 ± 2.13
di-boson	2309.04 ± 15.10	125.59 ± 3.39	42.48 ± 1.70
Total Physics	91726.88 ± 197.02	4415.44 ± 35.47	1281.54 ± 15.04
Instr. Bgrd	29148.12 ± 376.90	2254.98 ± 100.72	397.70 ± 20.36
Total Bgrd	120875.00 ± 425.29	6670.42 ± 106.78	1679.24 ± 25.31
Observed	120875.00	6853.00	1581.00

Table 5.5: Number of events after applying all analysis cuts and after b-tagging using different combinations of L3 and VeryTight NN operation points. Errors are statistical only.

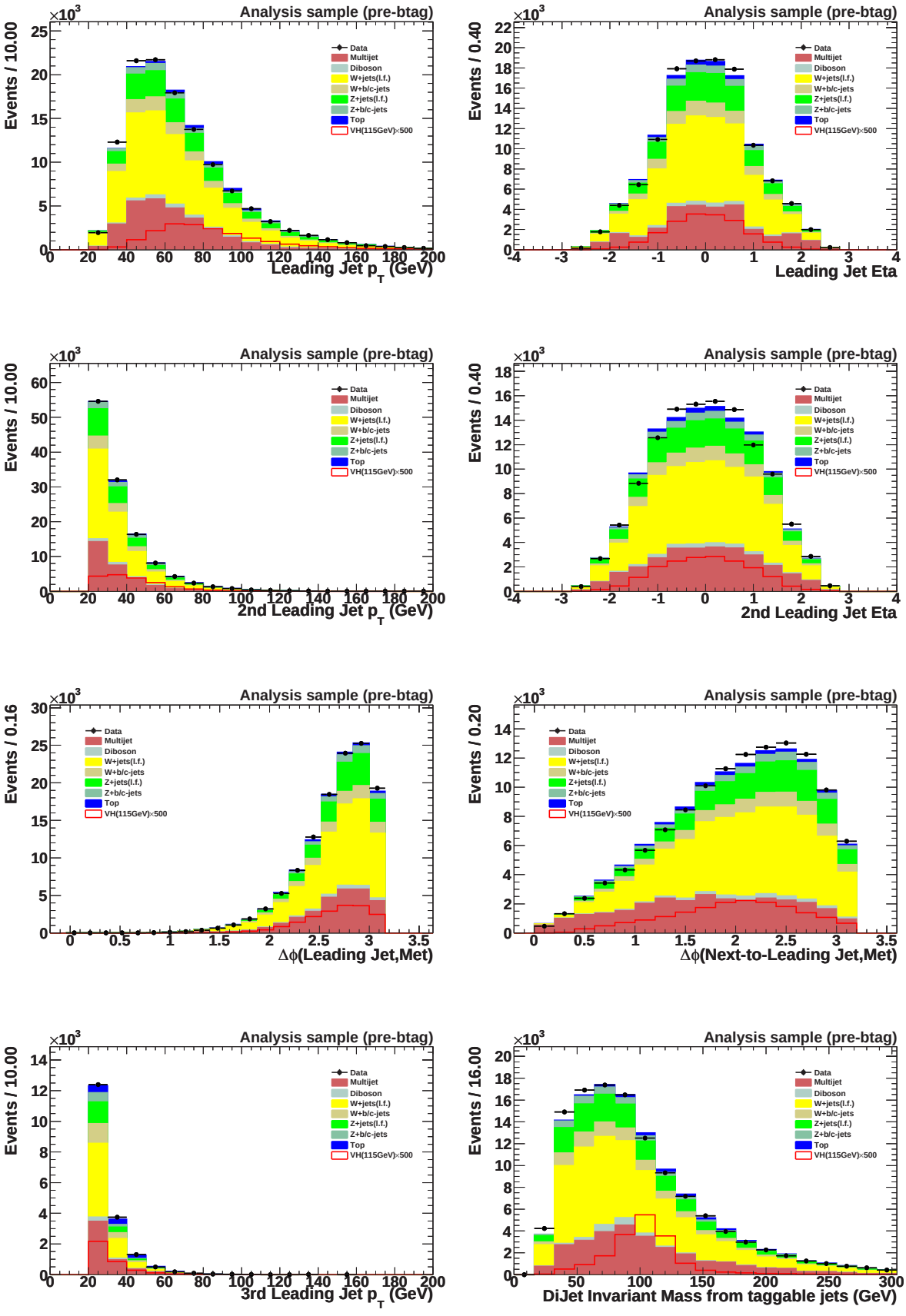

Figure 5.9: Signal sample before b-tagging

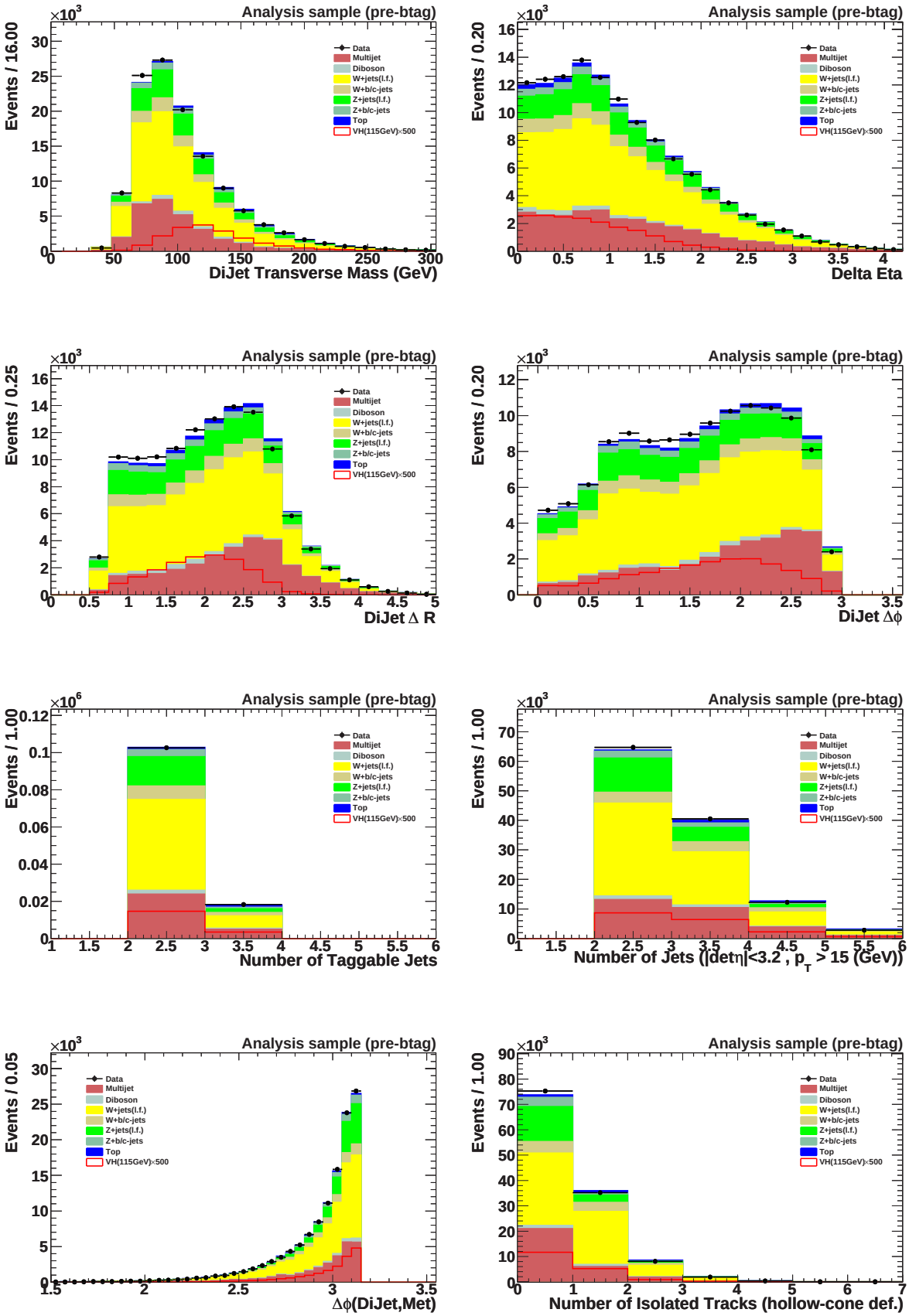

Figure 5.10: Signal sample before b-tagging

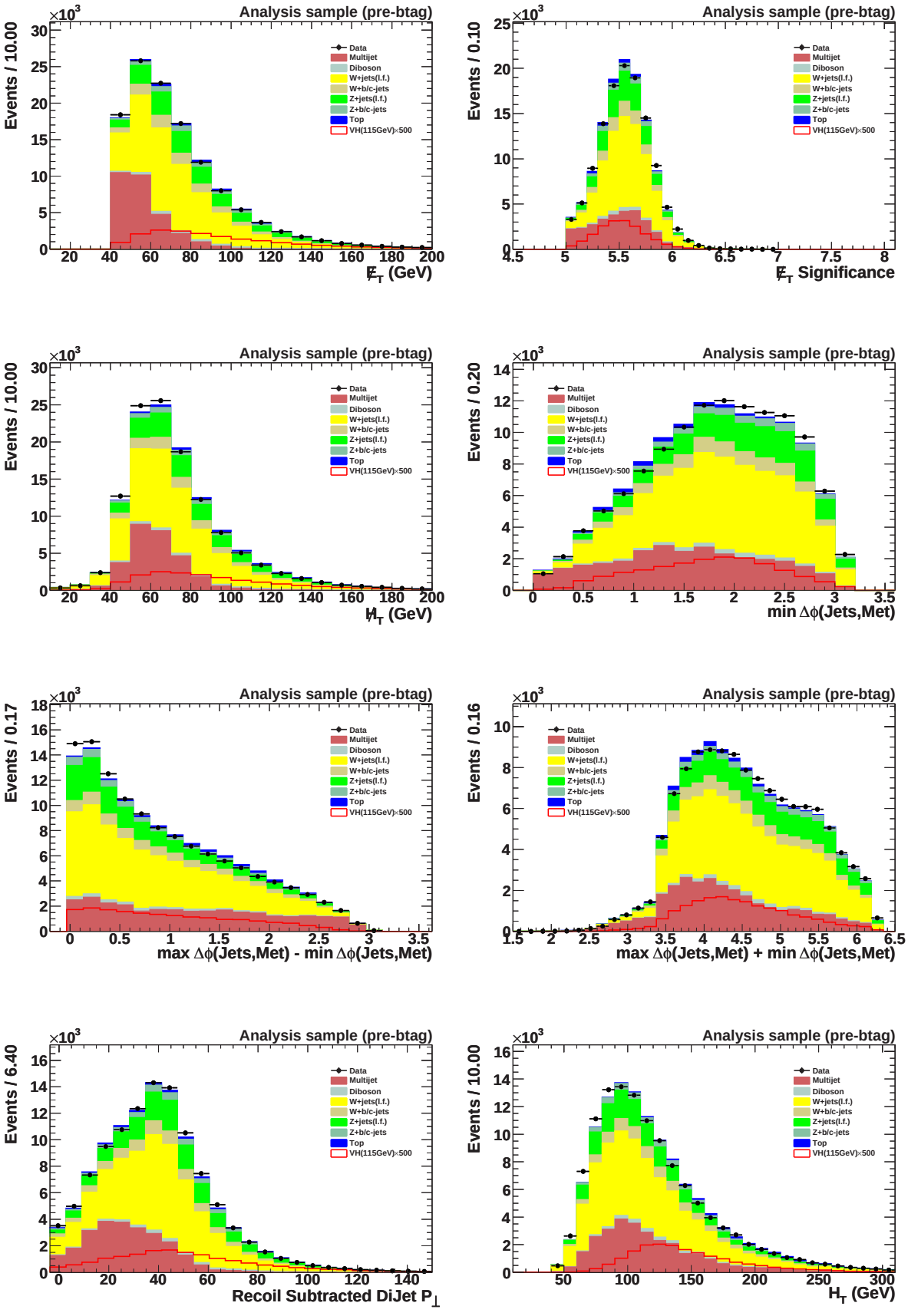

Figure 5.11: Signal sample before *b*-tagging

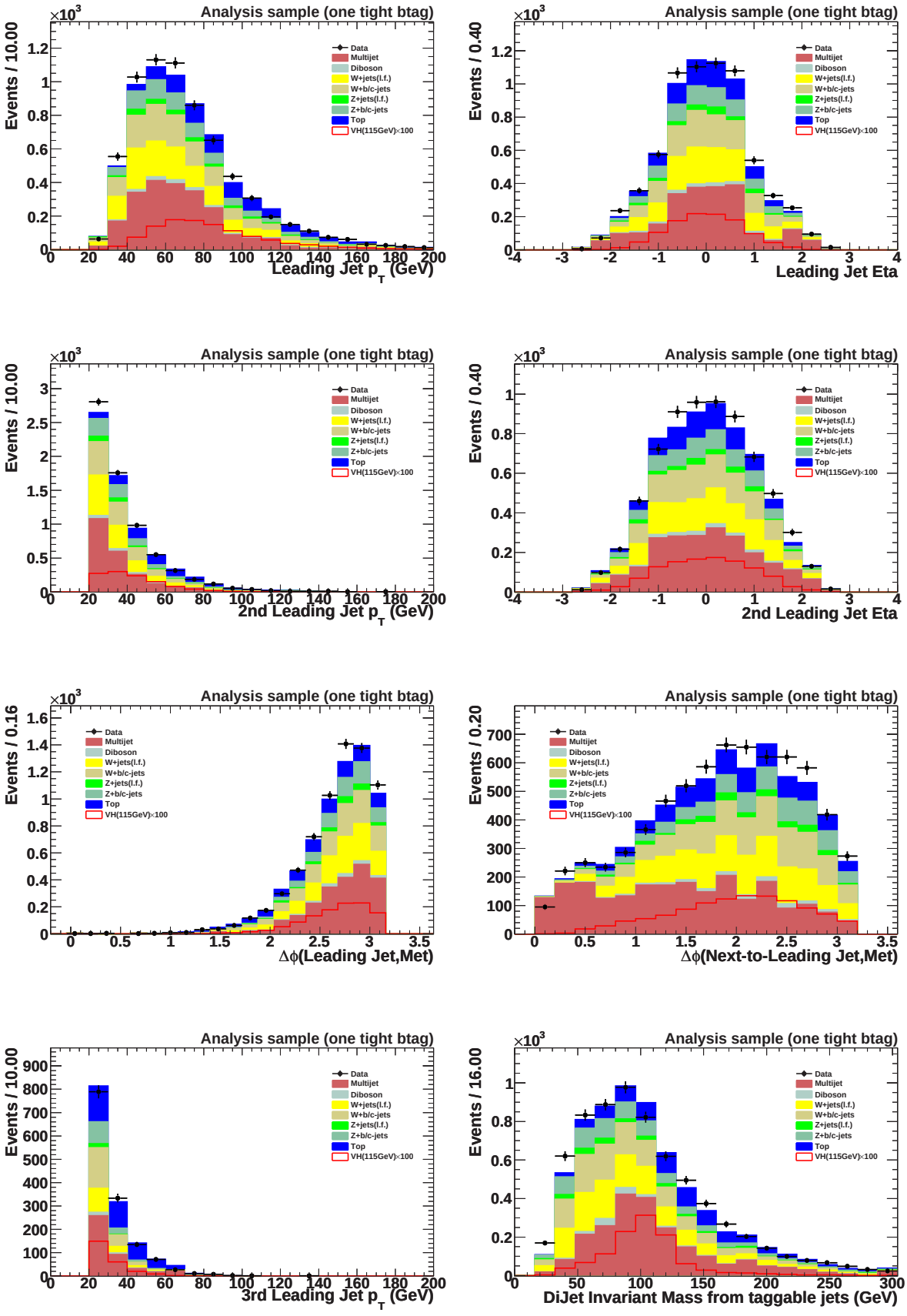

Figure 5.12: Signal sample with one tight b-tag

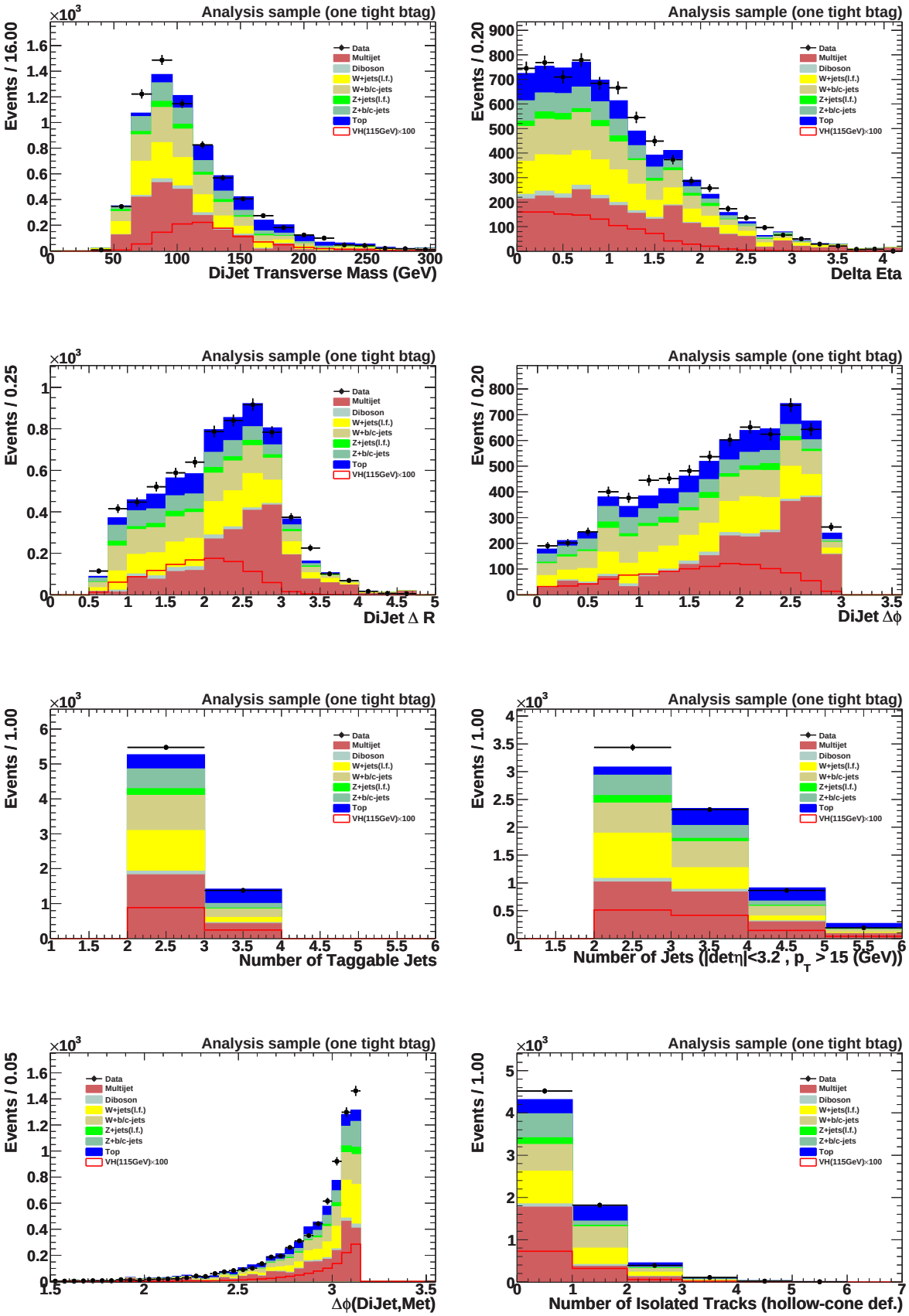

Figure 5.13: Signal sample with one tight b-tag

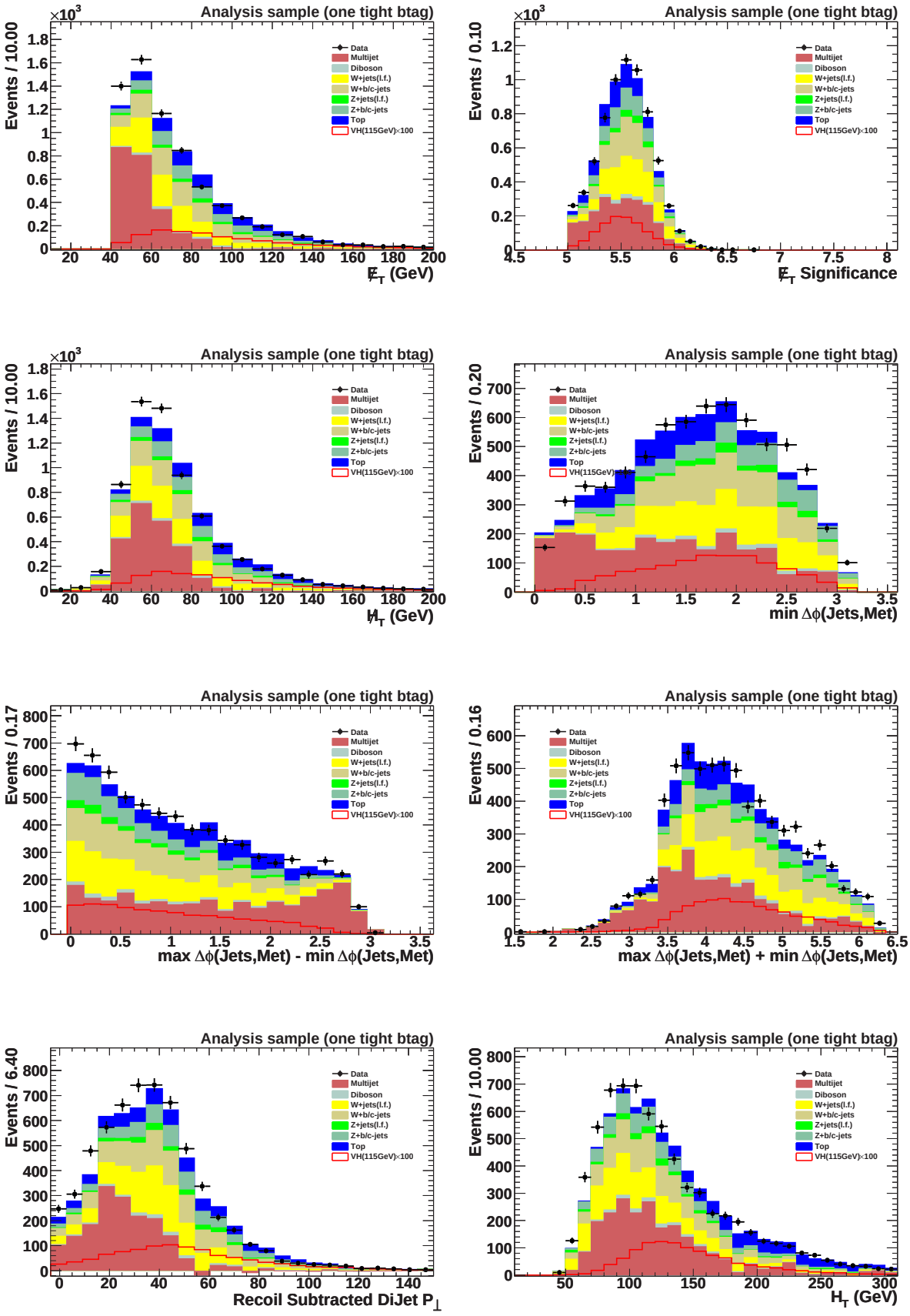

Figure 5.14: Signal sample with one tight b-tag

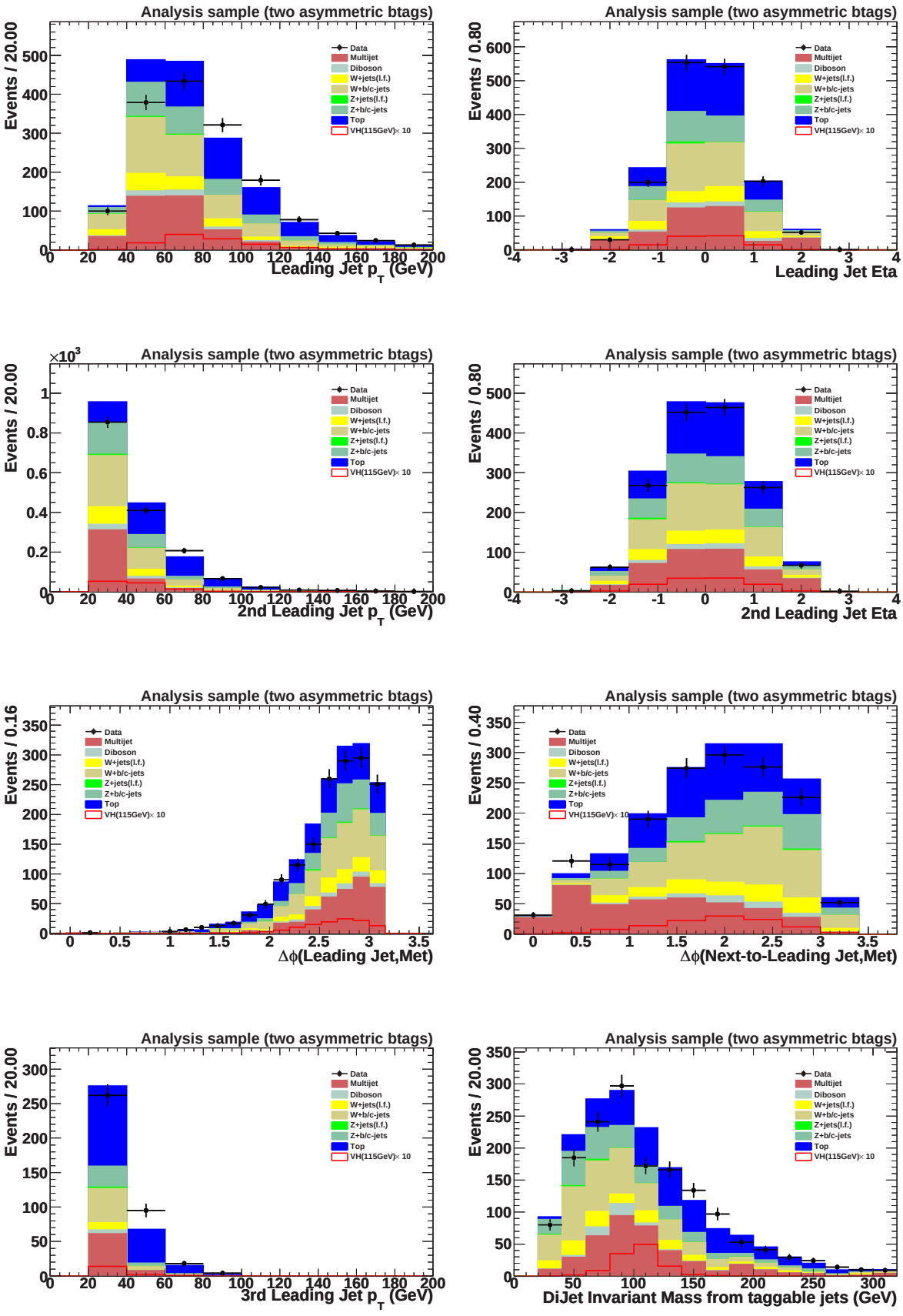

Figure 5.15: Signal sample with one tight and one loose b-tag

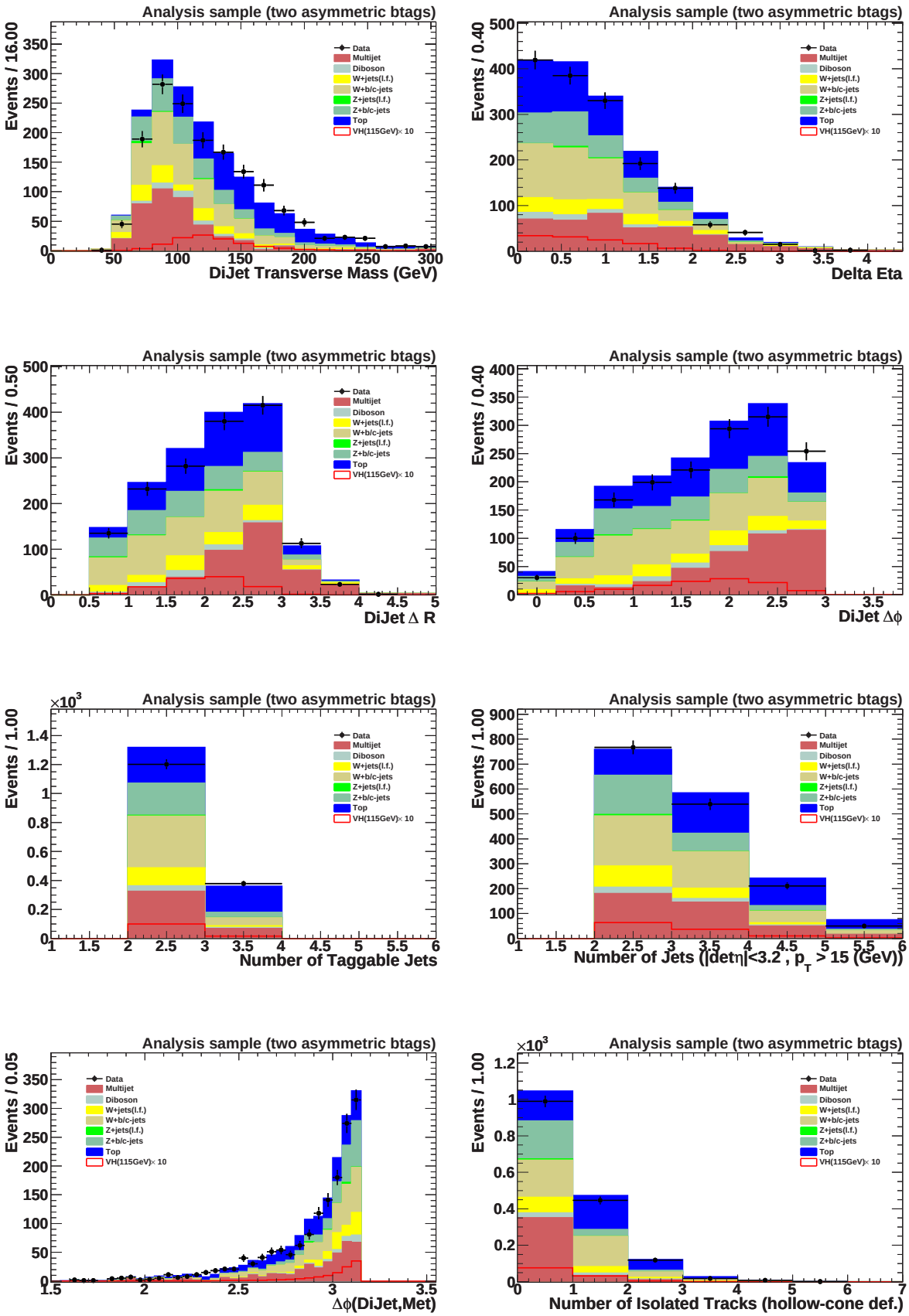

Figure 5.16: Signal sample with one tight and one loose b-tag

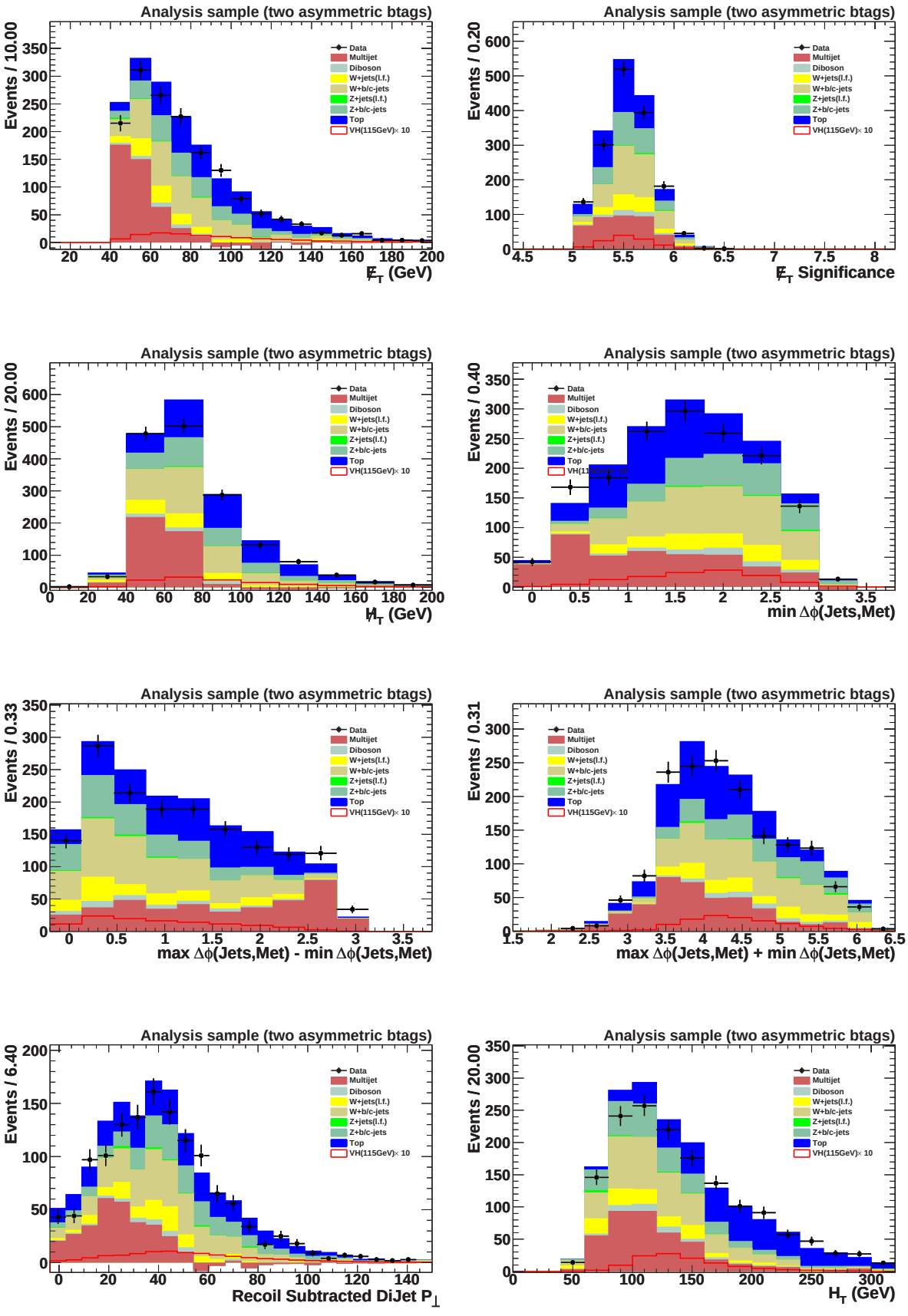

Figure 5.17: Signal sample with one tight and one loose b-tag

5.3 Electroweak Control Sample

A W+jets sample is used to test our MC modeling of the electroweak (EW) backgrounds, the trigger simulation and the b-tagging performance. This sample is orthogonal to our signal sample, but has similar event topology, and is virtually void of instrumental background.

We require the presence of a tight isolated muon by reversing the muon veto in the basic selection ($\mathrm{p_T} > 15\ GeV, |\eta| < 2$). The muon track information is removed from all variables to simulate the event topology of our signal sample. In this sample we apply the analysis cuts used in the signal sample and in addition we cut on the tight muon-corrected $\not\!\!E_T > 20\ GeV$ and require that the transverse mass of the W candidate is greater than 30 GeV. These additional cuts are used to remove all the remaining multijet contribution from this sample, and it has been verified that the multijet background is less than 1%. After all cuts prior to b-tagging are applied, we cross check the V+jets normalization in this sample. We find a very good agreement with a priori normalization, as the additional scale factor measured in this sample is 1.00 in p17 and 0.98 in p20. For the final V+jets normalization of the full data set we use the luminosity-weighted average value of 0.98.

5.3.1 Empirical HF Scale Factor

Due to the large uncertainties on the HF k-factors obtained with MCFM, in this analysis we apply an additional HF scale factor S_HF. This factor can be determined in the zero-tag, one-tag and two-tag samples separately. We do this with a formula taken from [86].

Every sample can be split into two orthogonal samples: the tagged sample (denoted as superscript $'$) and the anti-tagged sample (denoted by superscript $''$), and for the heavy flavor scale factor one gets:

$$\mathrm{S\_HF} = \frac{(\mathrm{Data}' - \mathrm{X}') * \mathrm{W}'' - (\mathrm{Data}'' - \mathrm{X}'') * \mathrm{W}'}{(\mathrm{Data}'' - \mathrm{X}'') * \mathrm{B}' - (\mathrm{Data}' - \mathrm{X}') * \mathrm{B}''} \tag{5.3}$$

where W (B) is the number of events in the (W/Z)+nlp ($(W/Z)bb$+nlp and $(W/Z)cc$+nlp) sample (where nlp being the number of light partons) and X denotes the number of events in MC background samples other than (W/Z)+jets (i.e., double and single top, and dibosons).

The values we obtain in our combined p17-p20 EW control sample for the three different tagging points are summarized in Table.5.6. They are consistent within statistical errors, and we use the value 1.09 from the 0-tag sample, which has the smallest uncertainty. This implies a small renormalization of the inclusive (W/Z)+jets MC by a factor 0.99. The S_HF values obtained from the 0-tag samples in p17 and p20 separately are

0.95 ± 0.22 and 1.12 ± 0.11, consistent within their statistical uncertainties.

Zero b-tag sample	1.09 ± 0.10
One VT b-tag sample	1.09 ± 0.12
Two (VT,L3) b-tags sample	1.10 ± 0.19

Table 5.6: S_HF factors obtained from the various b-tag samples.

This value of 1.09 for S_HF is used in all the following plots, and also in the training of the physics decision trees (Secs. 5.5 and 5.6). In the derivation of the final results, however, we let the limit setting procedure adjust independently the parameters on which S_HF depends (e.g., cross sections, b-tagging efficiencies).

The numbers of events observed and expected from the various background sources are given in Table 5.7 before b tagging, for an exclusive VT tag, and for an asymmetric VT-L3 double tag.

Plots of various variable distributions before b-tagging can be seen in Figures. 5.18-5.20. For one tight tag sample it is shown in Figures. 5.21-5.23, whereas for double tag (L3-VT) tag in Figures. 5.24-5.26. Overall, there is good agreement between the observed data and the expected background, both before and after b-tagging.

Sample	Before b-tagging	1 VT tag	1 L3 and 1 VT tag
ZH (115GeV)	0.00 ± 0.00	0.00 ± 0.00	0.00 ± 0.00
WH (115GeV)	5.23 ± 0.06	1.61 ± 0.03	1.76 ± 0.03
W+jets	9468.70 ± 36.77	142.87 ± 5.49	12.59 ± 2.20
W+b/c jets	1826.69 ± 15.39	269.10 ± 5.02	92.74 ± 3.07
Z+jets	1023.03 ± 12.91	7.15 ± 1.19	1.50 ± 0.75
Z+b/c jets	255.35 ± 3.64	39.37 ± 1.11	14.15 ± 0.62
top	669.72 ± 2.26	226.44 ± 1.27	138.18 ± 0.83
di-boson	410.50 ± 5.06	20.89 ± 1.06	5.87 ± 0.44
Total Bgrd	13654.00 ± 42.42	705.81 ± 7.79	265.03 ± 4.01
Observed	13654.00	705.00	266.00

Table 5.7: Number of events after applying all analysis cuts including requiring the transverse mass of the W candidate to be greater than 30 GeVand after b-tagging using different combinations of L3 and VeryTight NN operation points in the Electroweak control sample. Errors are statistical only.

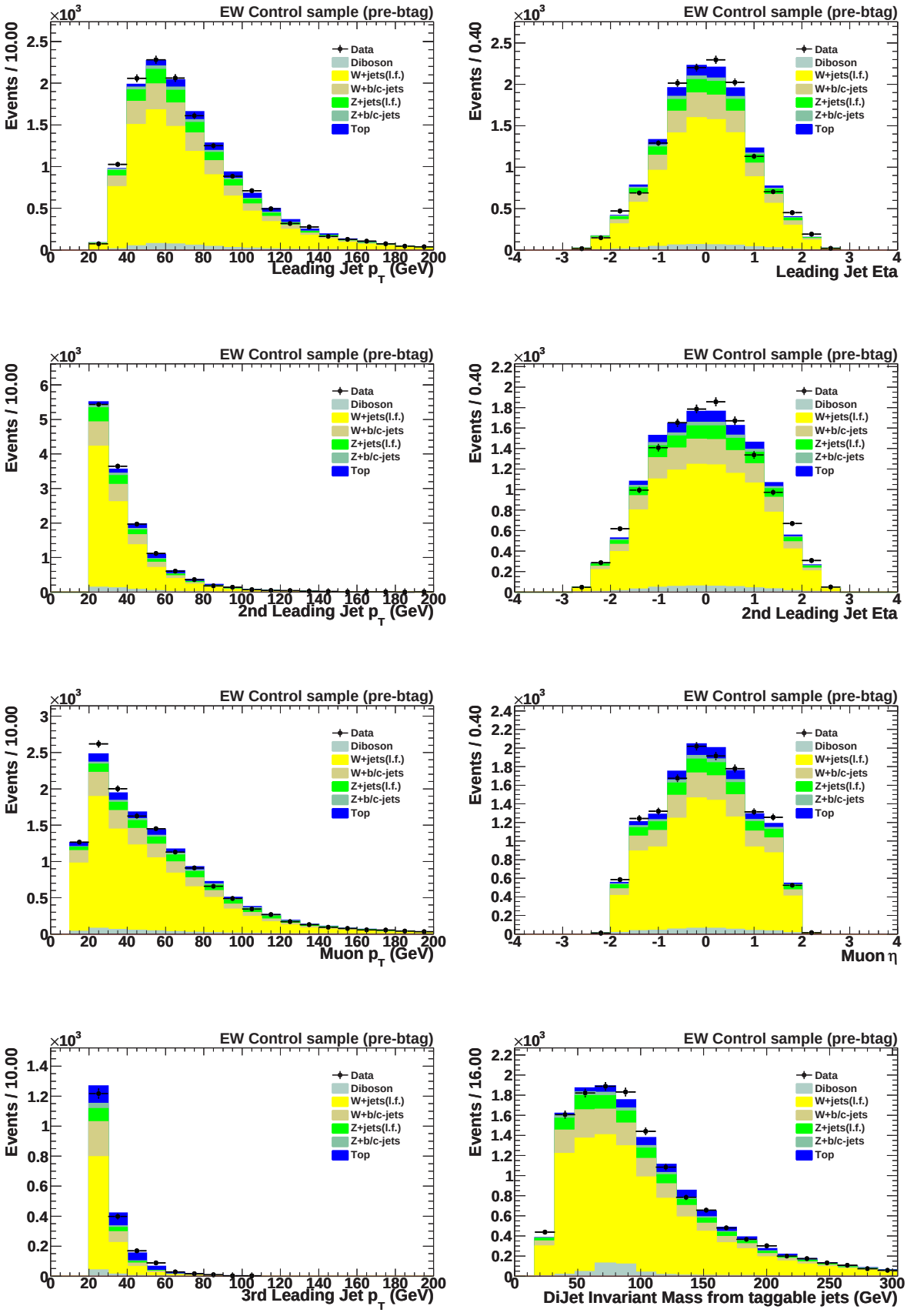

Figure 5.18: Electroweak control sample before *b*-tagging

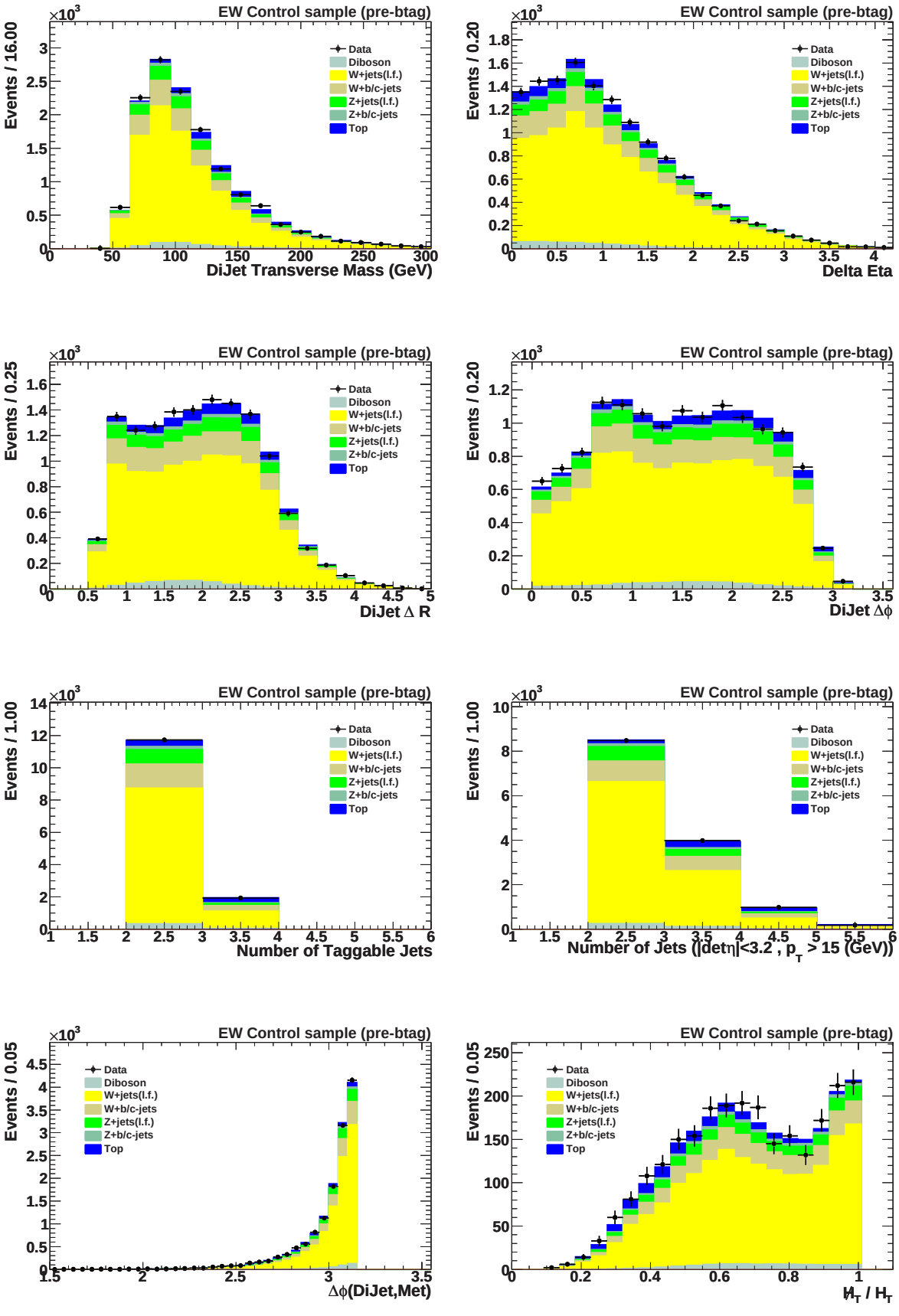

Figure 5.19: Electroweak control sample before b-tagging

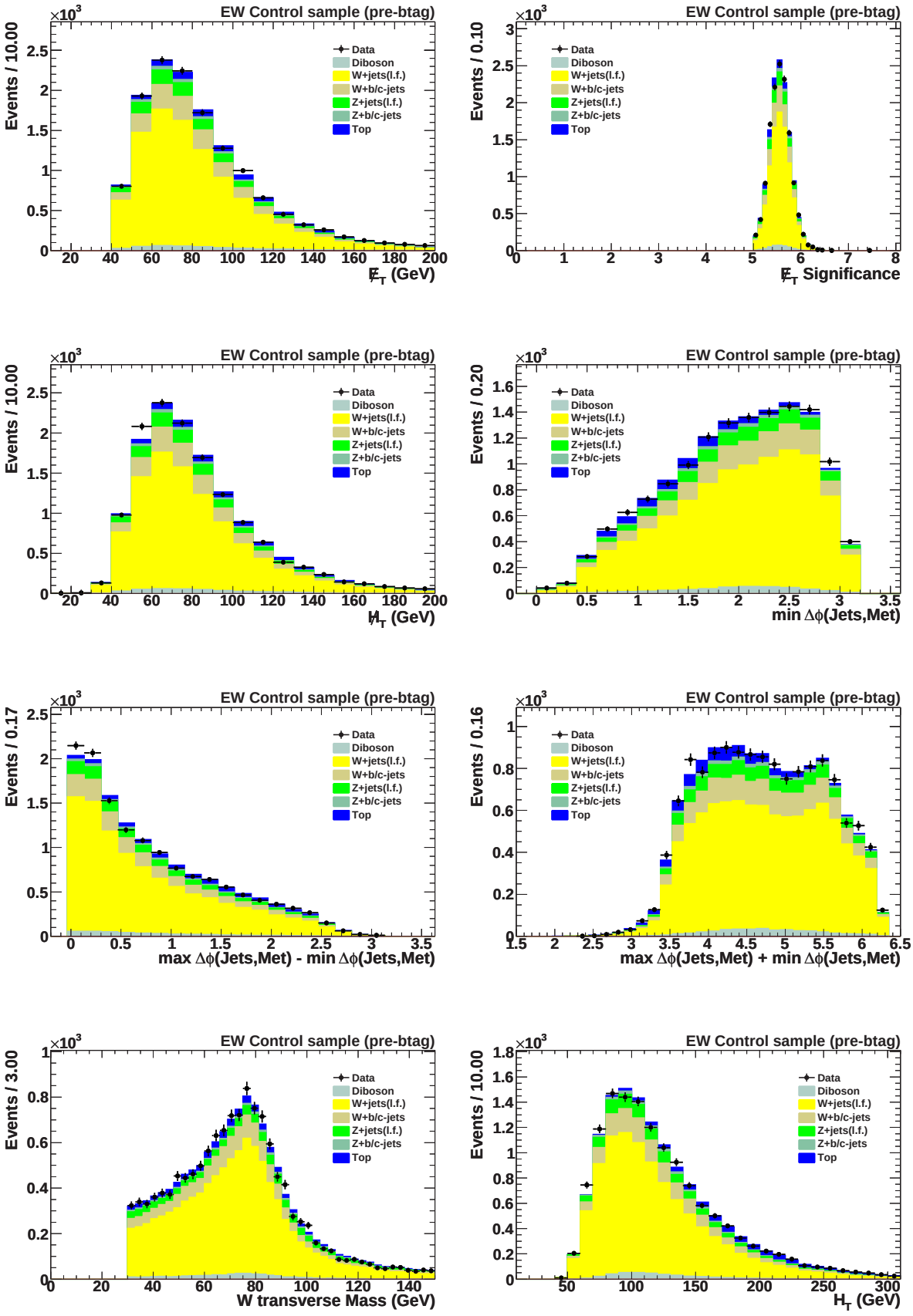

Figure 5.20: Electroweak control sample before b-tagging

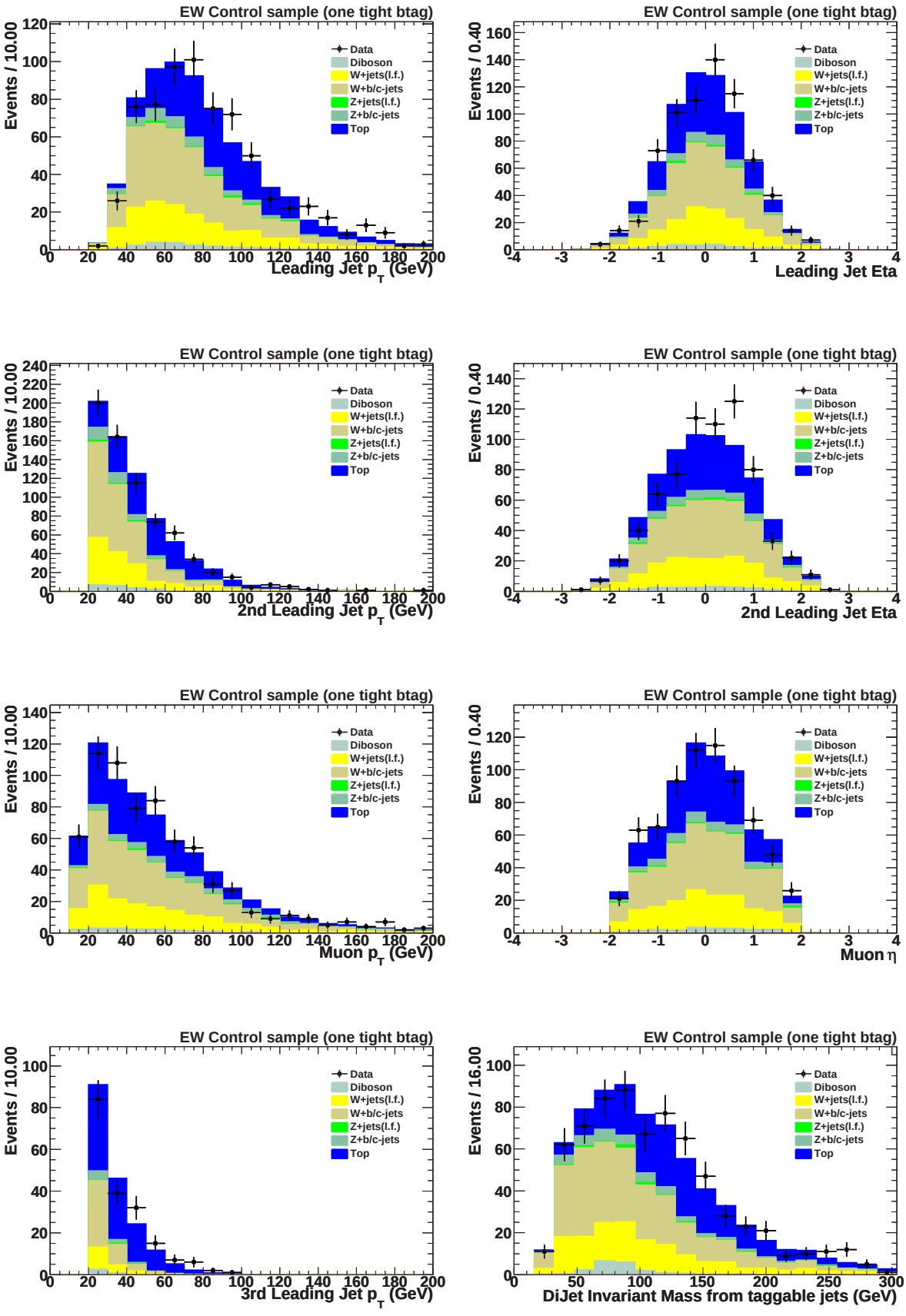

Figure 5.21: Electroweak control sample with one tight b-tag

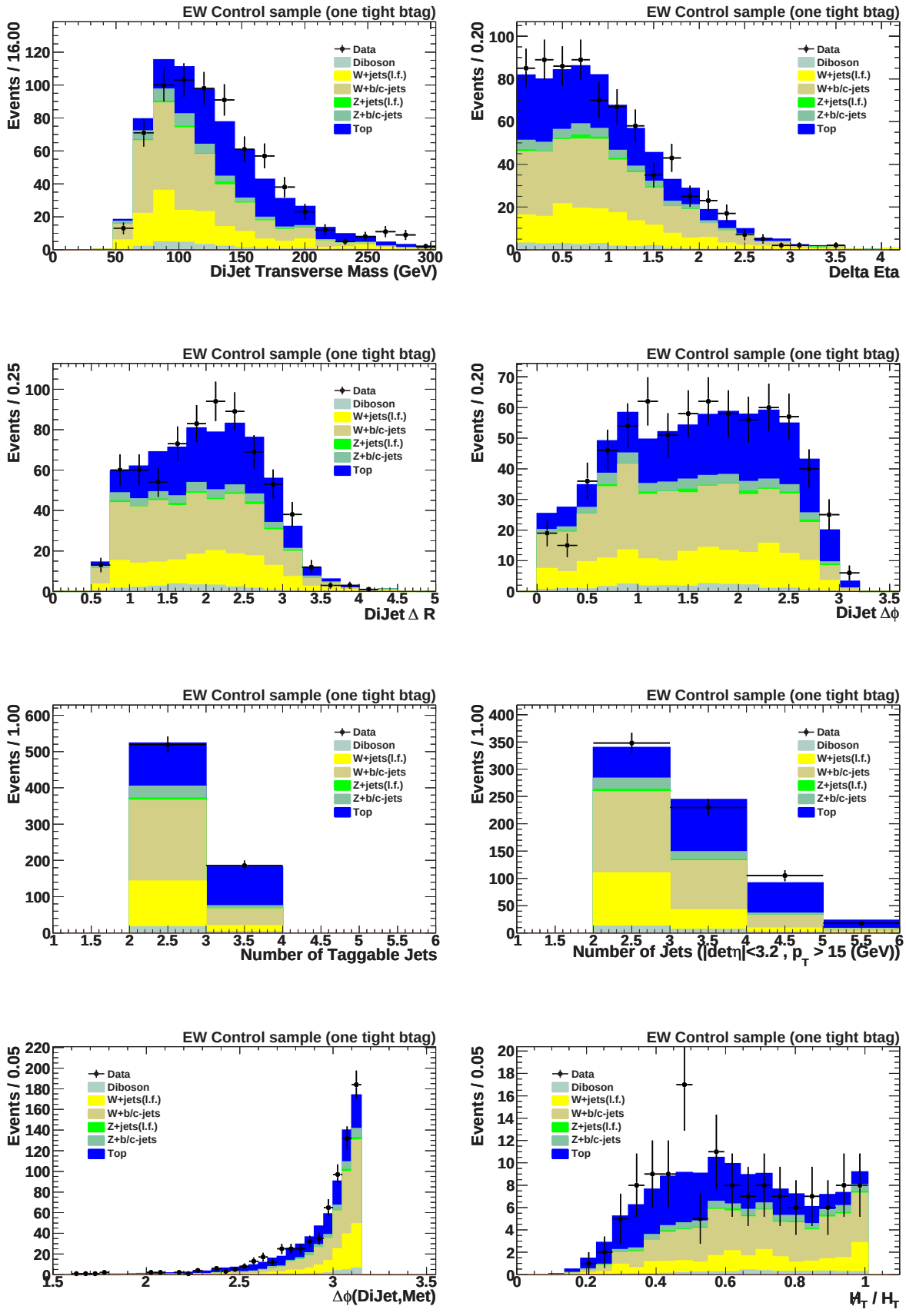

Figure 5.22: Electroweak control sample with one tight b-tag

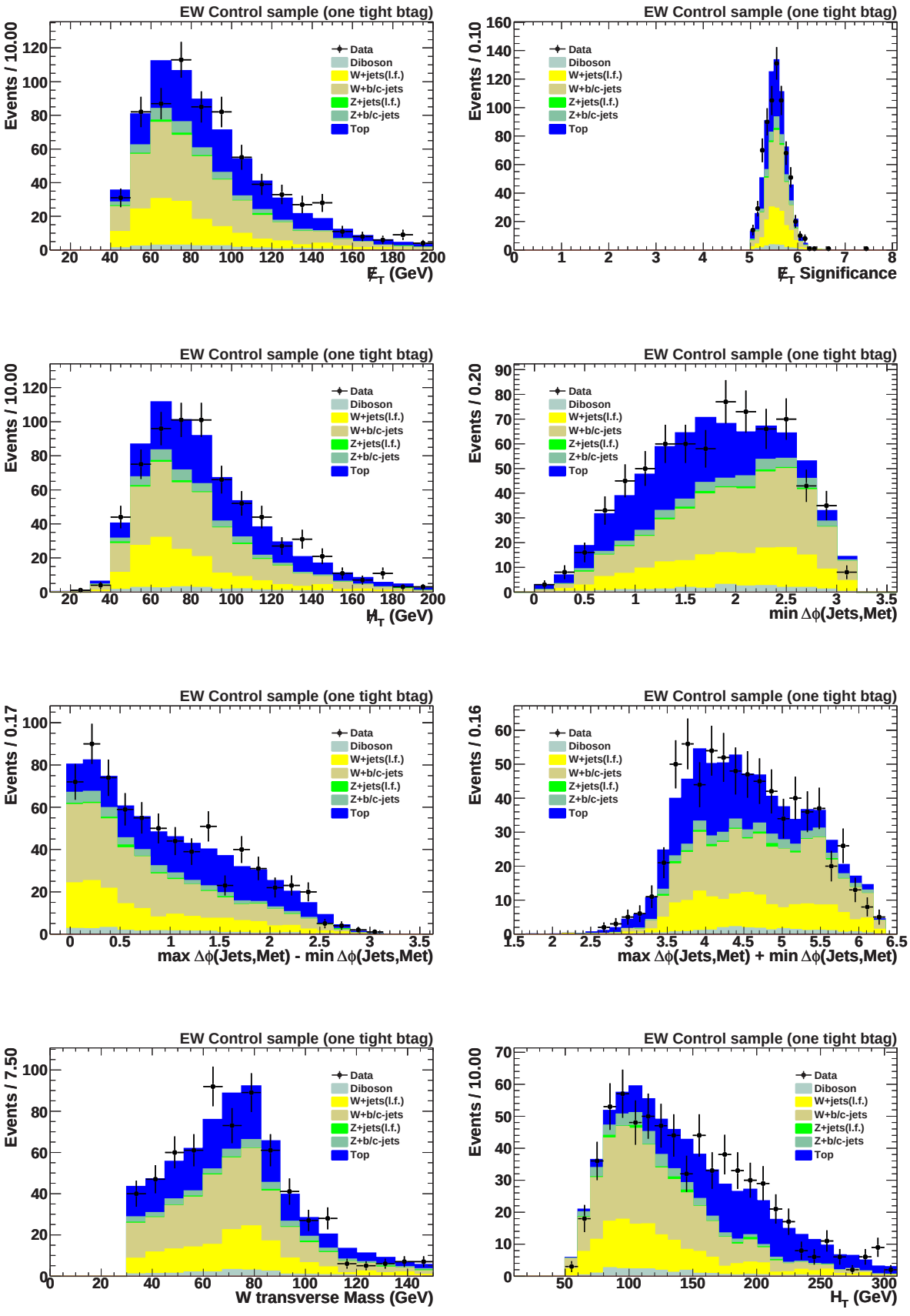

Figure 5.23: Electroweak control sample with one tight b-tag

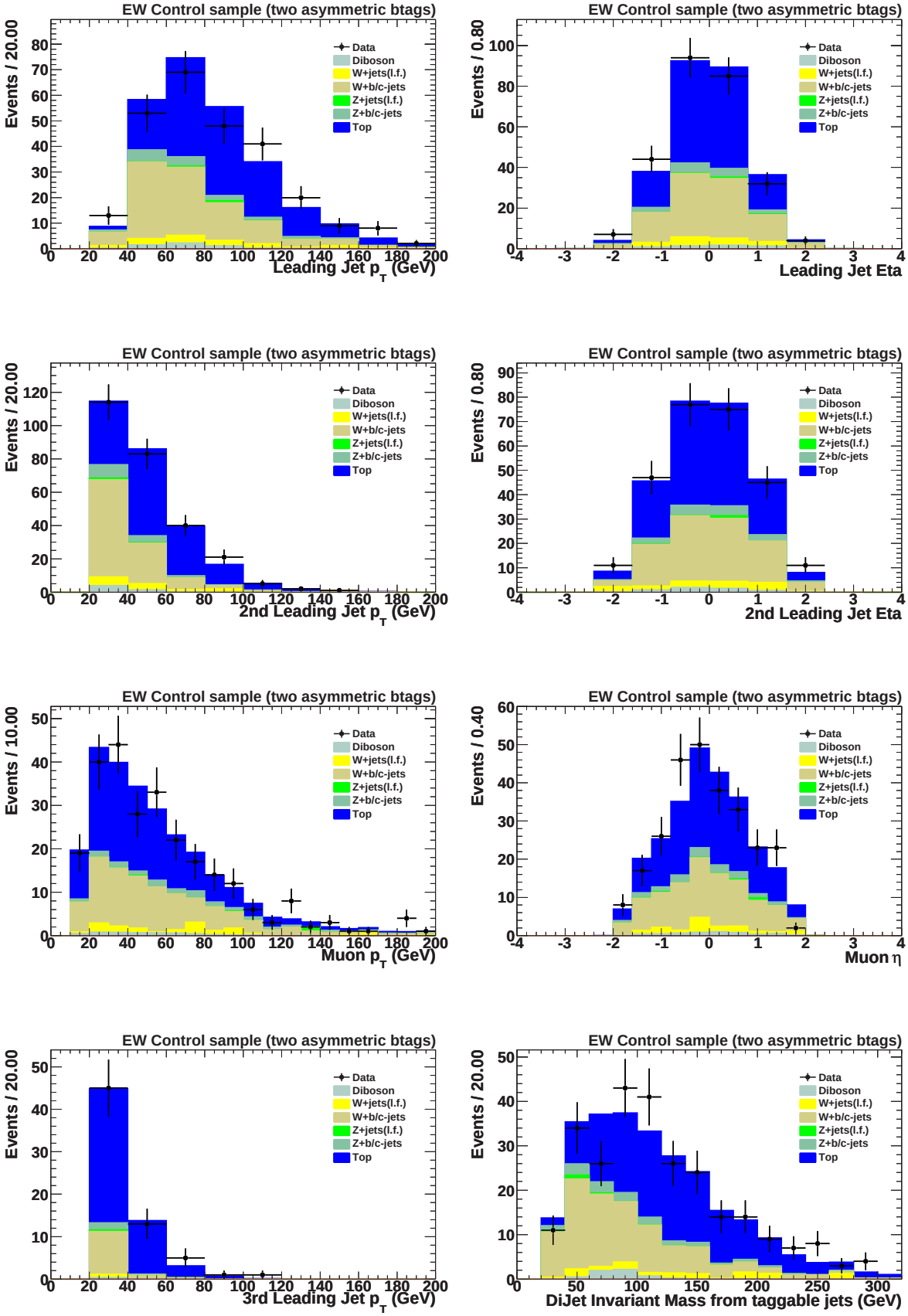

Figure 5.24: Electroweak control sample with one tight and one loose b-tag

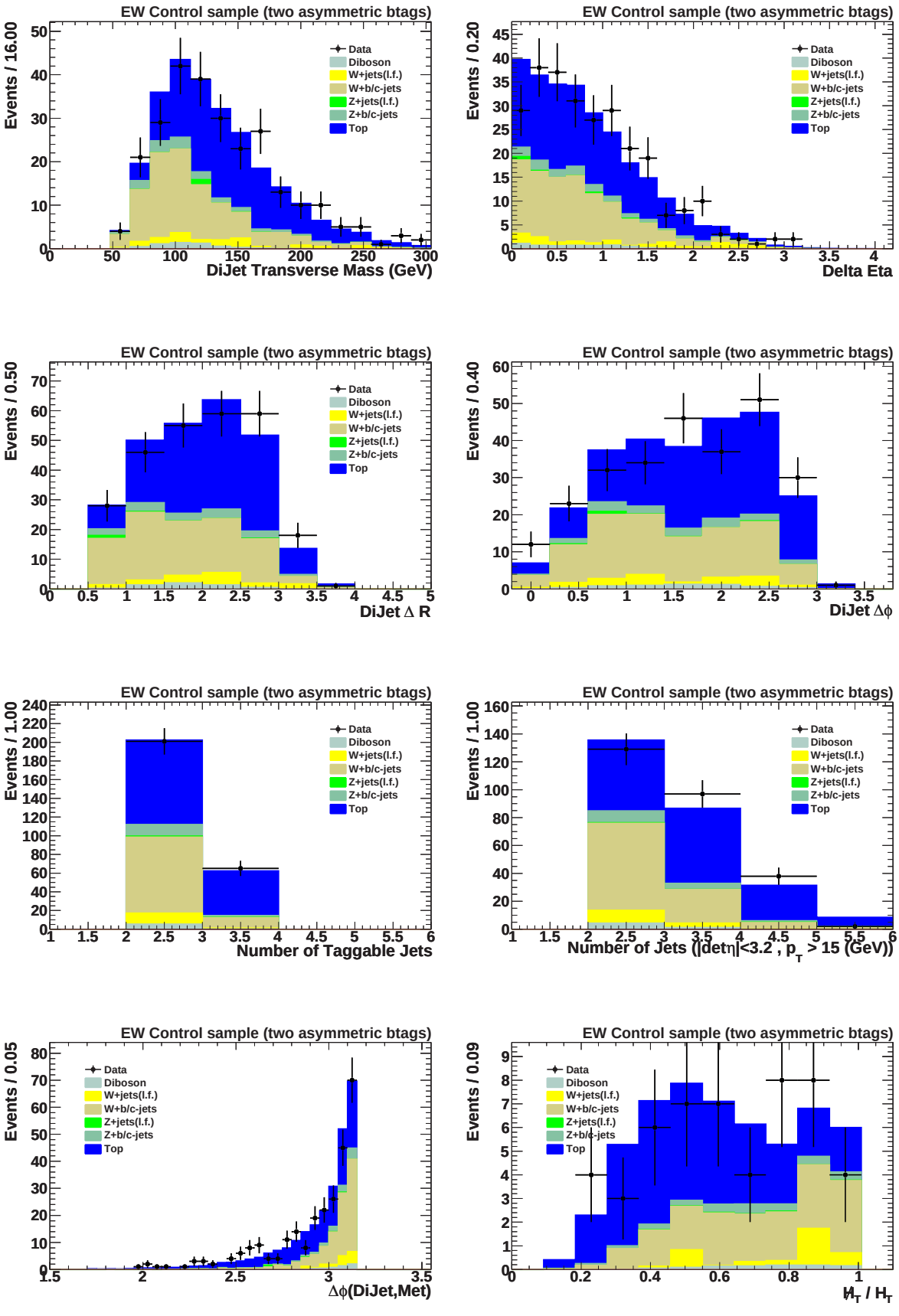

Figure 5.25: Electroweak control sample with one tight and one loose b-tag

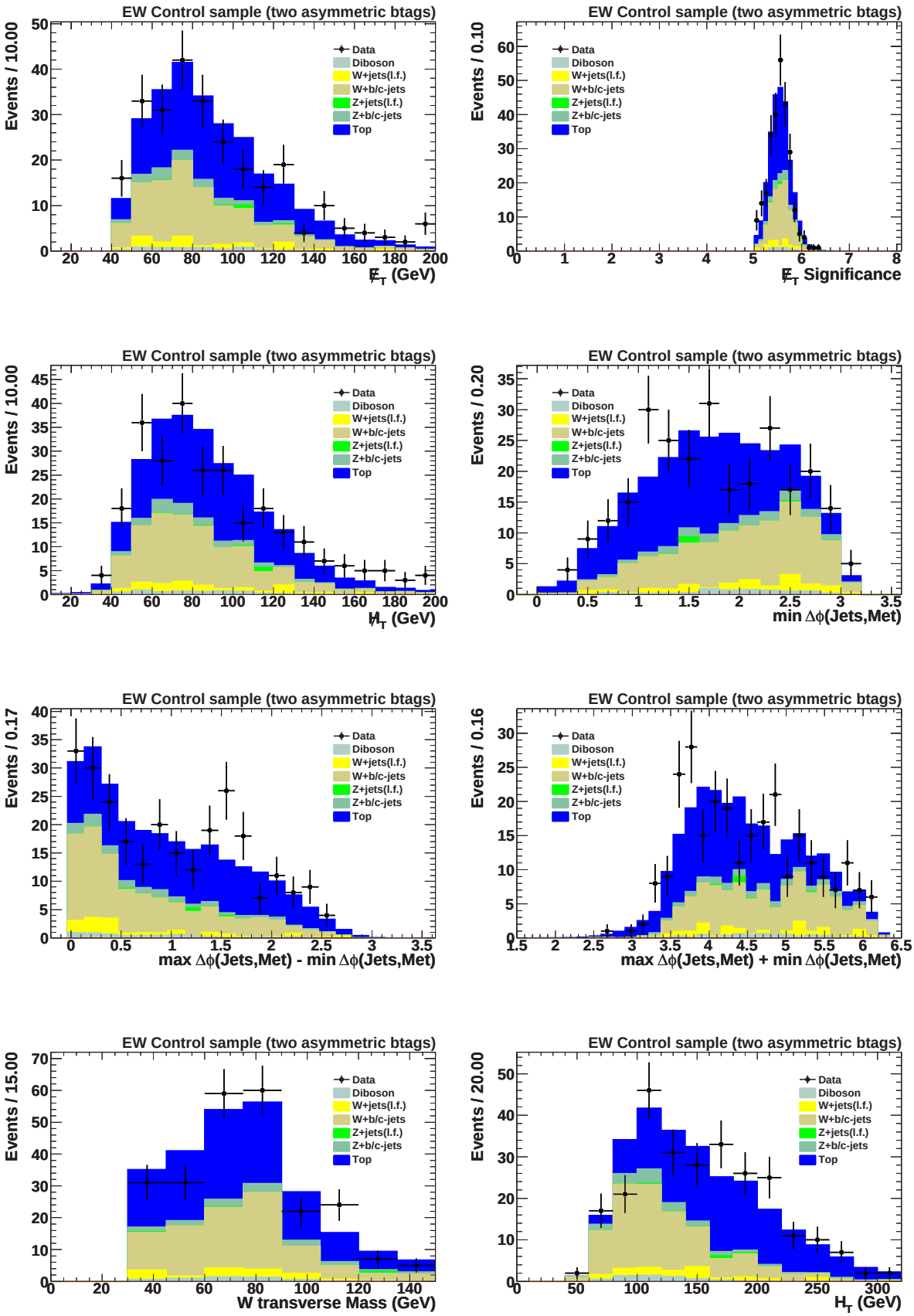

Figure 5.26: Electroweak control sample with one tight and one loose b-tag

5.4 Multijet Control Sample

As described in Section 5.1.5, the variable $\mathcal{D} = \Delta\phi(\not\!\!E_T, \not\!\!p_T^{\rm trk})$ is used to define a sample dominated by the multijet background. It is selected in the same way as the signal sample, except that the cut $\mathcal{D} < \pi/2$ is now inverted, we call this our signal sideband. The $\not\!\!p_T^{\rm trk}$ is computed only with tracks that originate from the primary vertex within distance of closest approaches (dca) rdca < 2 mm and zdca < 5 mm and have a $p_T \leq 400$ GeV. The latter cut is used to reject fake tracks, as most tracks with a very high p_T are fake. After SM background subtraction, the signal sideband is used as the multijet-model in the signal sample, i.e., in the $\mathcal{D} < \pi/2$ region. The distribution of $\mathcal{D}$ after applying all selection cuts, before b-tagging, is plotted in Figure 5.27. The multijet-model sample is normalized such that, after adding the SM background contribution, the number of events expected is equal to the number of events observed in the signal sample with $\mathcal{D} < \pi/2$.

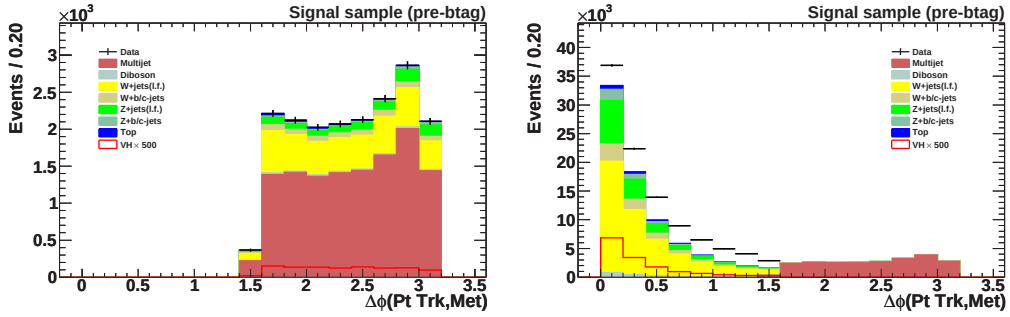

Figure 5.27: The left plot shows details of the signal sideband: below the SM contributions, the events used to model the multijet background (MJ-model sample) are shown in majenta. The right plot shows those same MJ-model events, in majenta, for $\mathcal{D} > \pi/2$, with the SM contributions removed; here the MJ-model normalization is adjusted such that the MJ-model compensates the difference between data and SM contributions seen for $\mathcal{D} < \pi/2$ (data shown as black points, SM contributions as colored histograms).

To test this multijet-background modeling procedure, we define a multijet control sample which is largely enhanced in multijet events. This sample is selected in the same way as the signal sample, but the $\not\!\!E_T$ cut is relaxed from 40 to 30 GeV and other cuts specifically designed to reject multijet events are dropped. These are the $\not\!\!E_T$ triangle cut for Run IIa 5.1.2, and the cut $\mathcal{S} > 5$ on the $\not\!\!E_T$ significance. A multijet-model sample is then defined in the same way as for the signal sample, and compared with the multijet control sample in the $\mathcal{D} < \pi/2$ region.

To further suppress events in our multijet-model samples with such nature we compare the leading jet p_T measured with the calorimeter and the tracking in the multijet control sample. These two dimensional distributions are plotted for the $\mathcal{D} < \pi/2$ and $\mathcal{D} > \pi/2$ regions in 5.28. As can be seen in these plots, the events from our multijet-model

have more events with small Jet p_T^{trk}. To reject events from our multijet-model sample with missing tracks we apply a further cut in this sample, only keeping events with $3.0 * LJTrkPt + 20 > LJetPt$ where $LJTrkPt$ is the track p_T of the leading jet (vectorial sum of tracks in the jet) and $LJetPt$ is the jet p_T measured with the calorimeter.

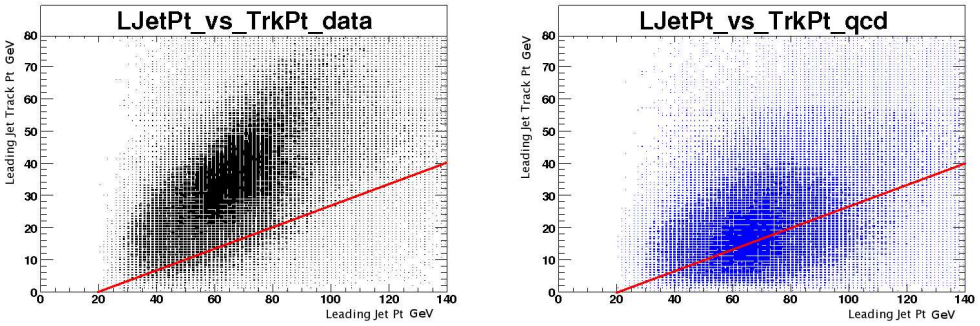

Figure 5.28: Signal like (black) and multijet events (blue) in the leading jet p_T vs. leading jet track p_T plane (p17). Red line shows the triangle cut on the 2-D plane.

All calorimeter related variables in the multijet control sample are very well described by our multijet model, as shown before b tagging in 5.30-5.32. The normalization factors for the multijet model are 1.54 and 1.27 for p17 and p20, respectively.

There are some remaining biases in the tracking related distributions. These have an effect on the b-tagging efficiency mainly for the leading jet as can be seen in the reweighted b-tagging NN output Figure 5.29 as discussed in Sec. 5.1.7. Semi-leptonic decays will also result in a different normalization for the pretagged and b-tagged samples since these events have intrinsic $\not\!\!E_T$ aligned with the jets. For these reasons, the multijet-model sample has to be derived and normalized for each b-tagging point separately. The normalization factors in the multijet control sample are 1.51 and 1.65 for p17 with single and double tag, respectively, and 1.37 and 1.39 for p20. Plots for the single tag and double tag multijet control sample are shown in Figures.5.35-5.37.

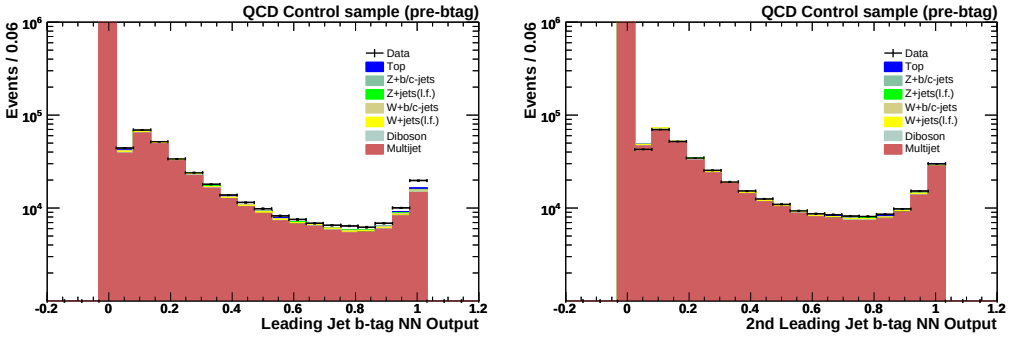

Figure 5.29: Leading and next-to-leading jet b-tag NN distributions in the multijet dominated sample.

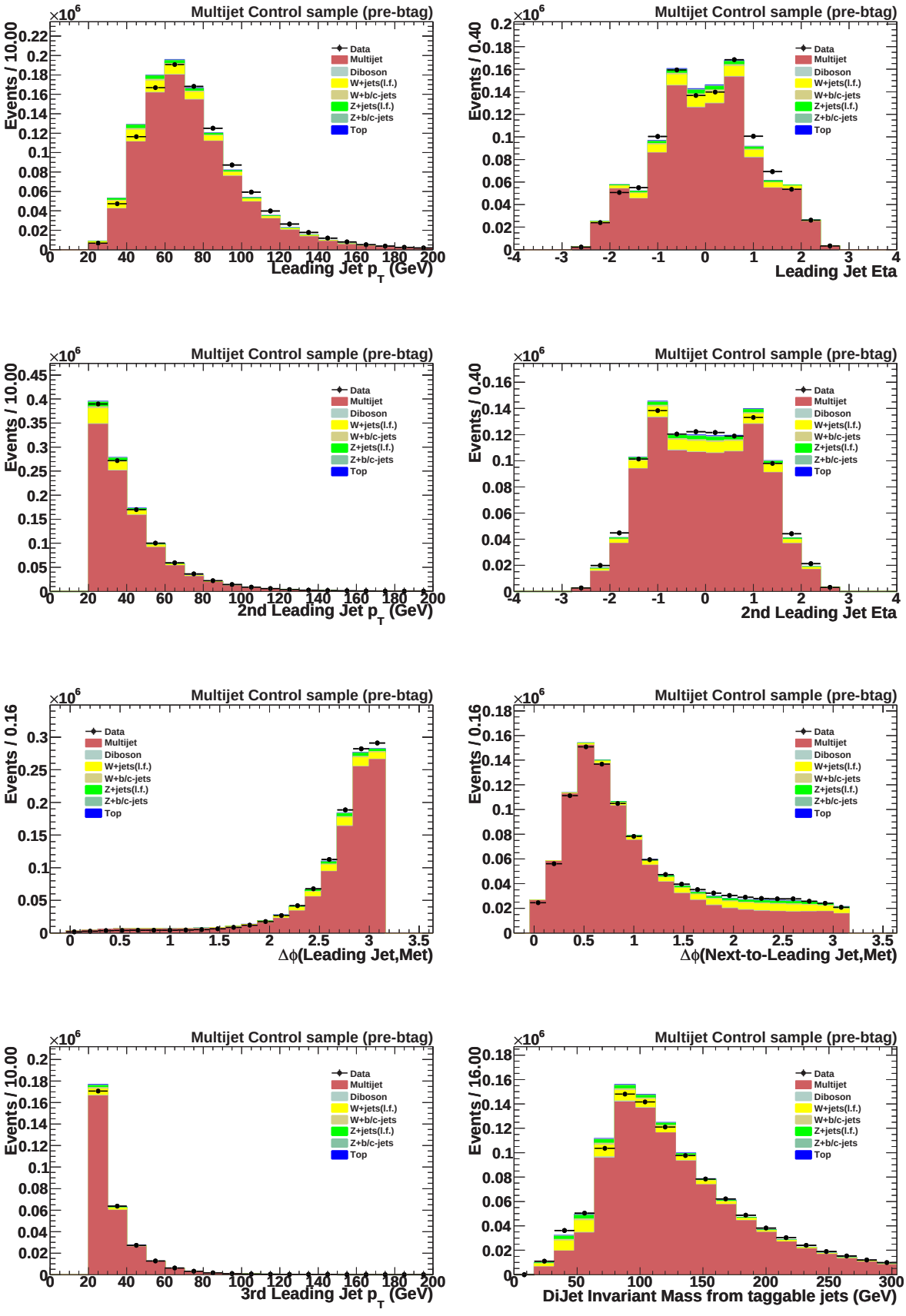

Figure 5.30: Multijet control sample before b-tagging

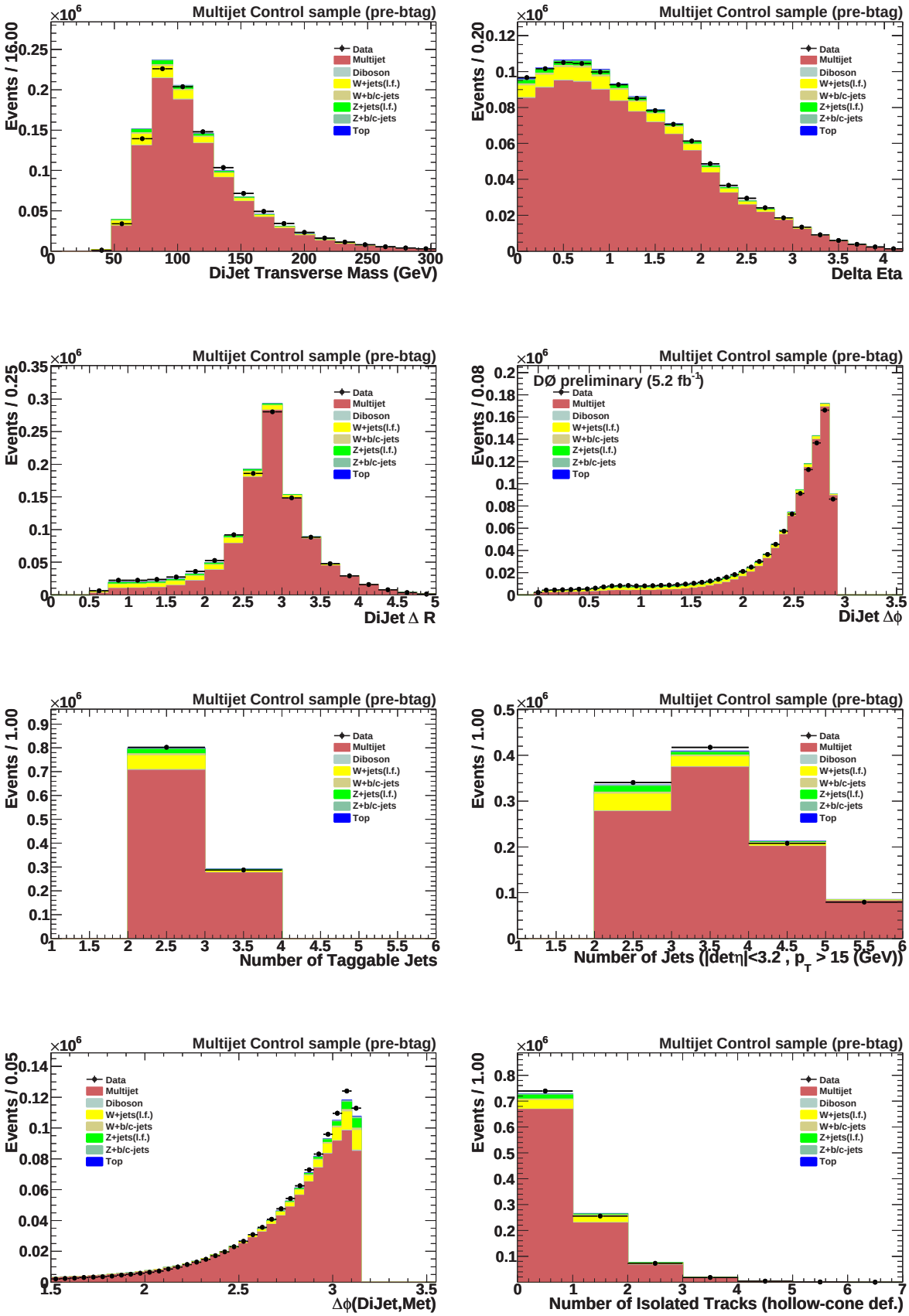

Figure 5.31: Multijet control sample before b-tagging

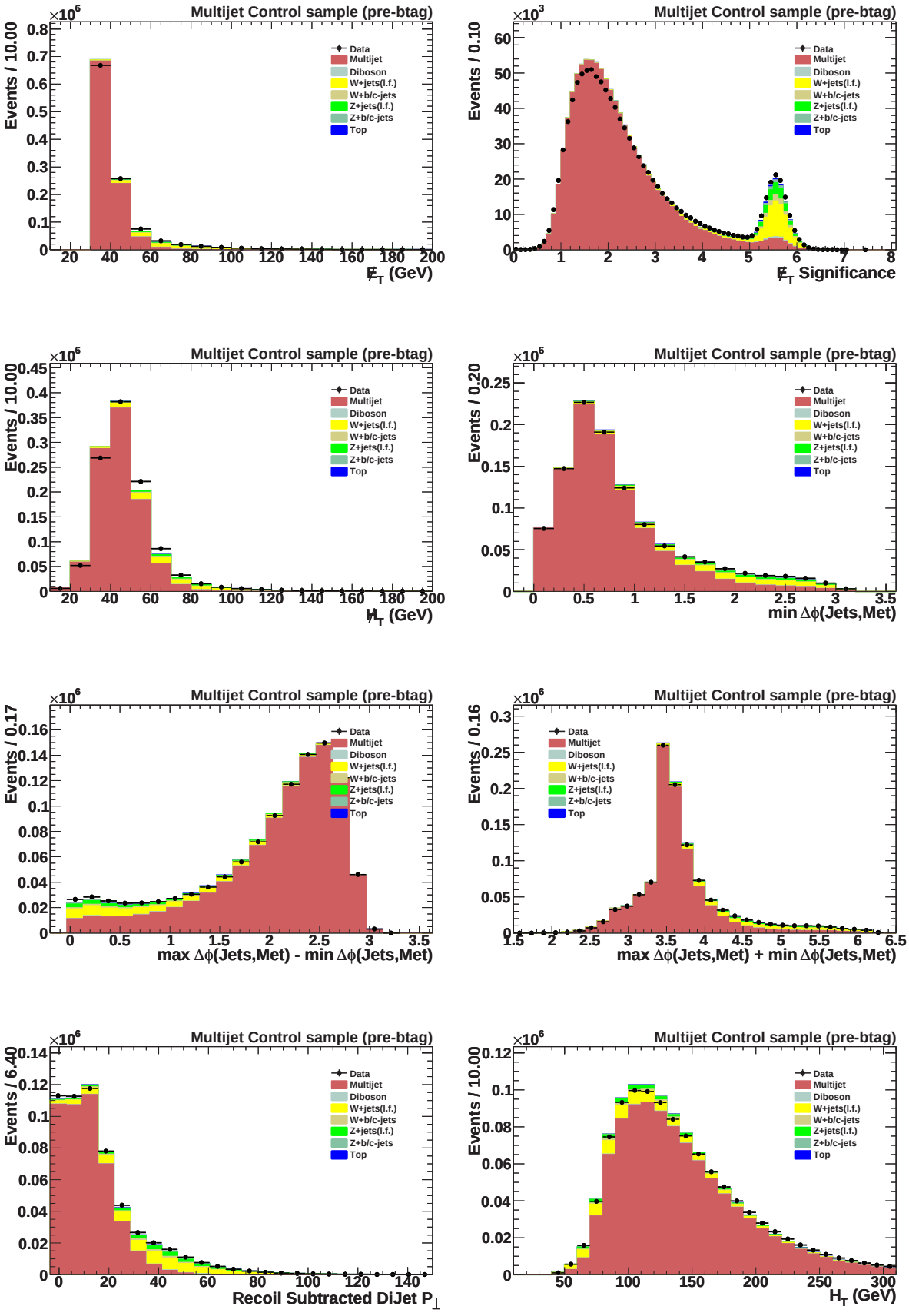

Figure 5.32: Multijet control sample before *b*-tagging

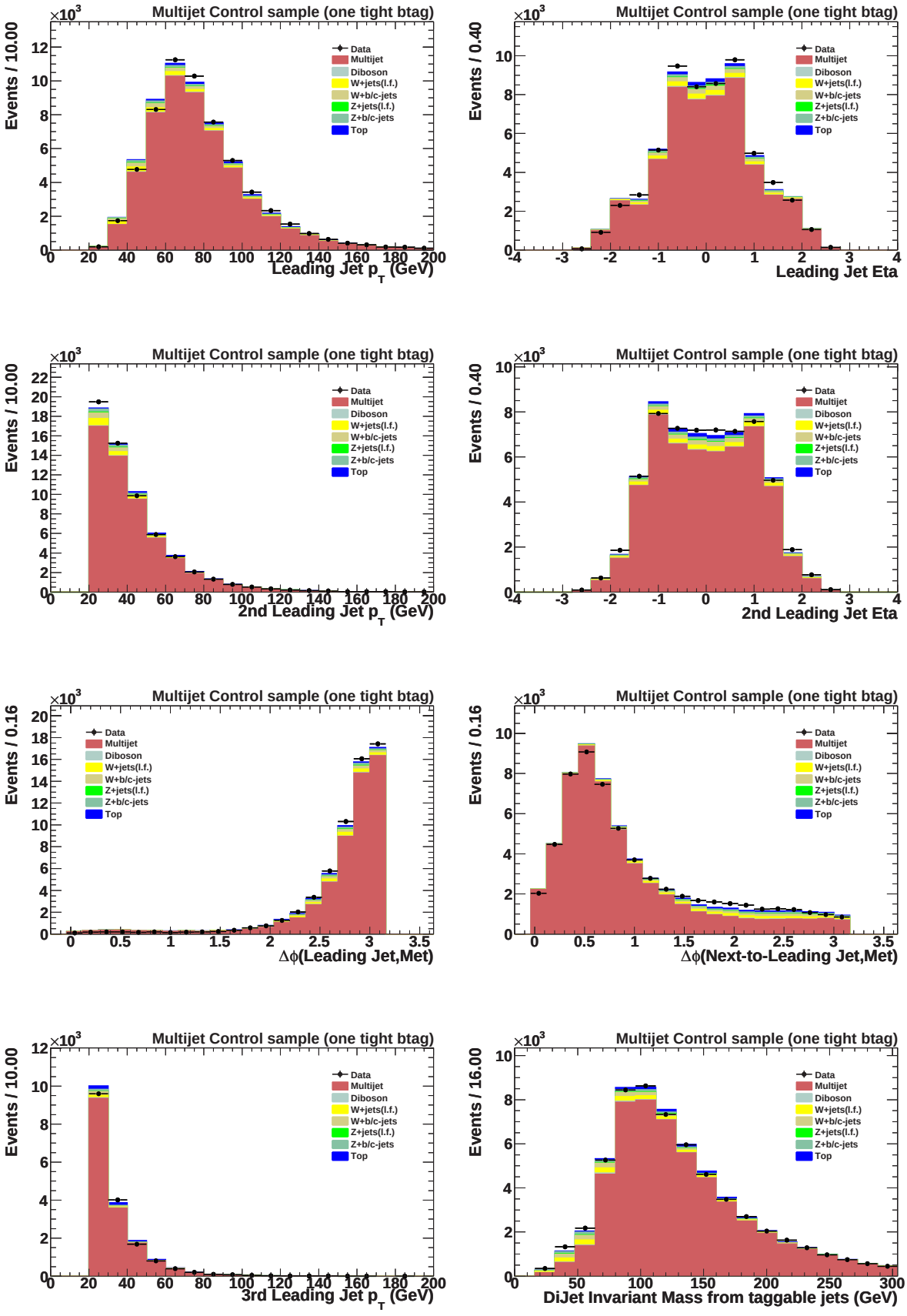

Figure 5.33: Multijet control sample with one tight b-tag

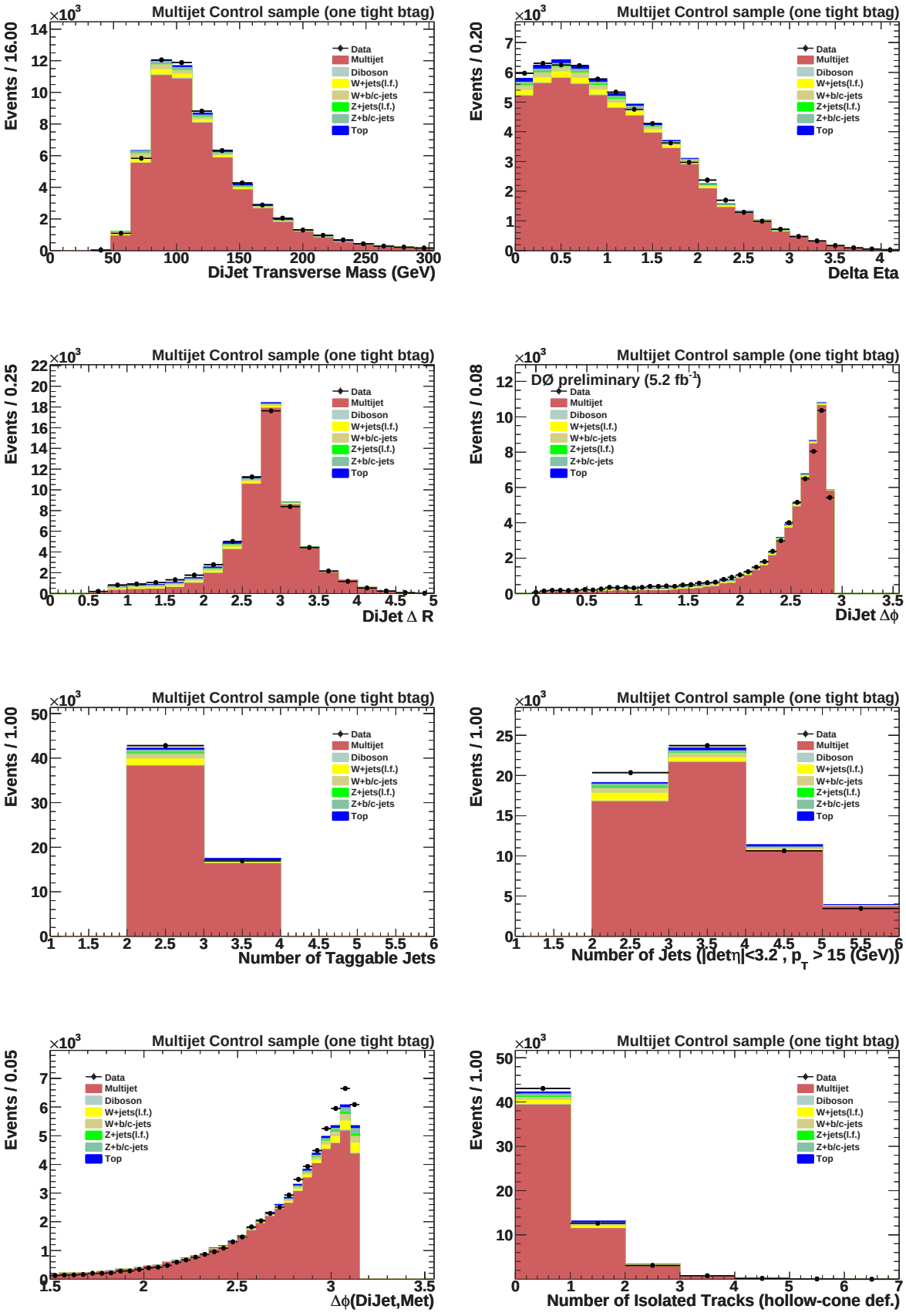

Figure 5.34: Multijet control sample with one tight b-tag

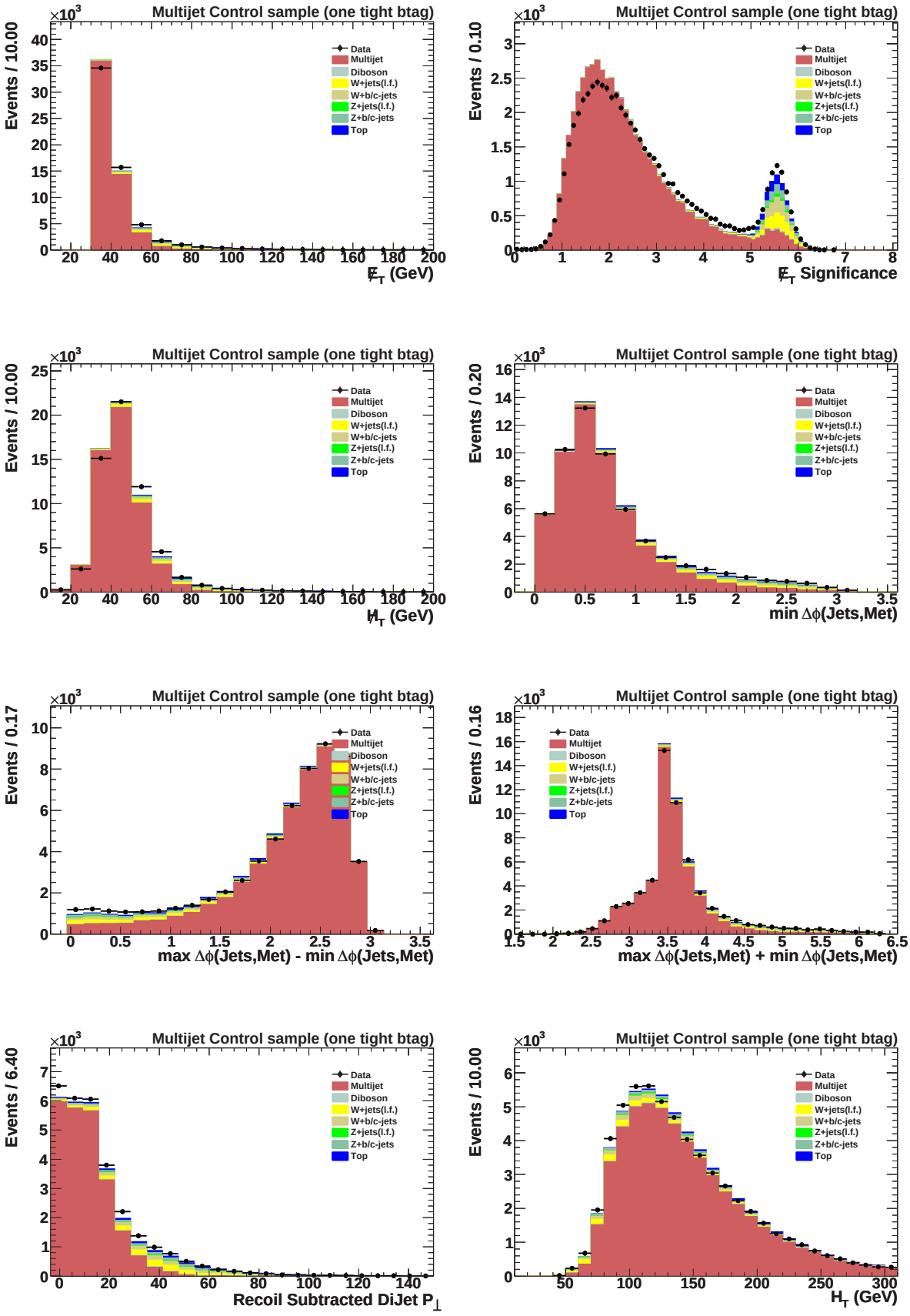

Figure 5.35: Multijet control sample with one tight b-tag

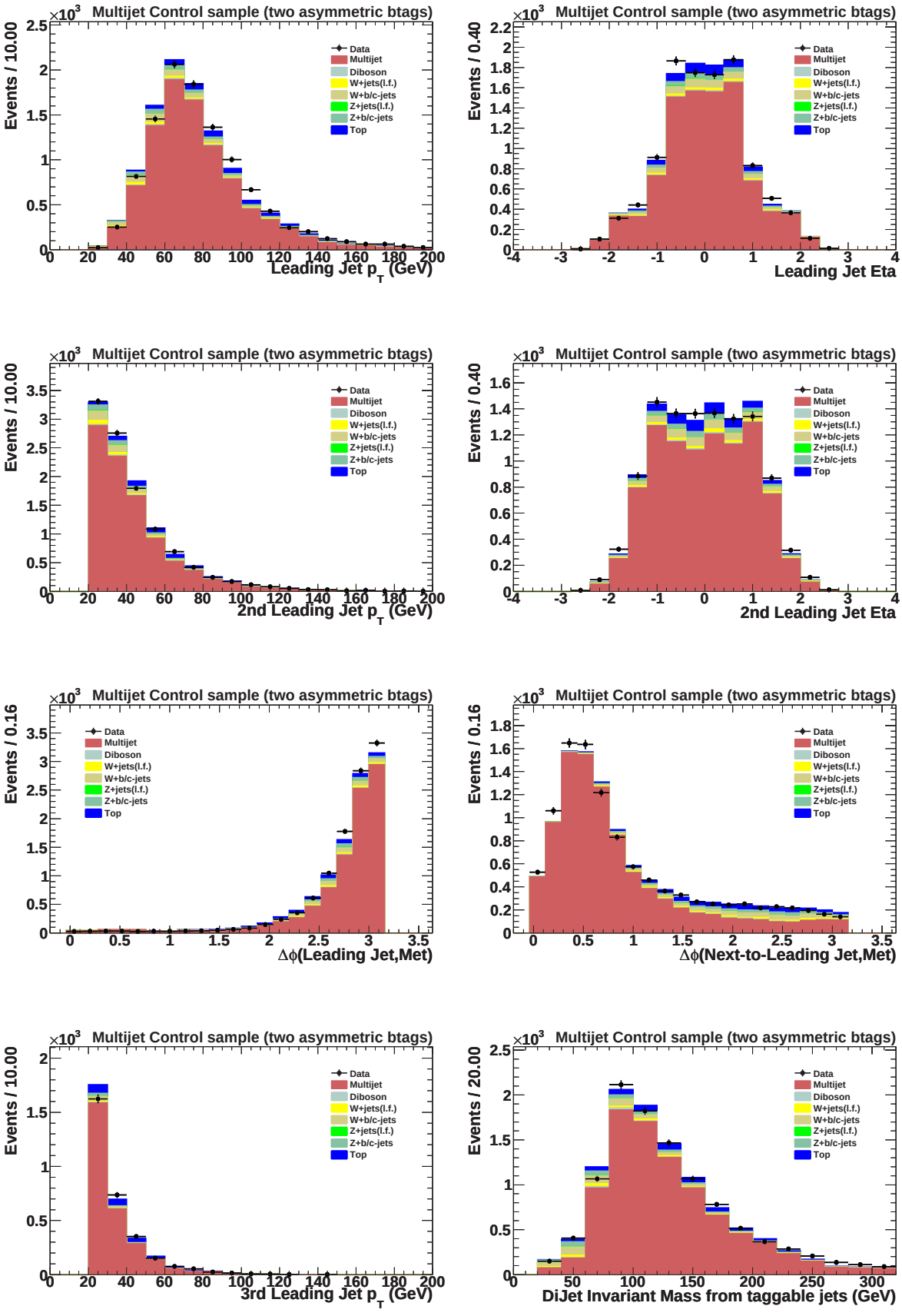

Figure 5.36: Multijet control sample with one tight and one loose b-tag

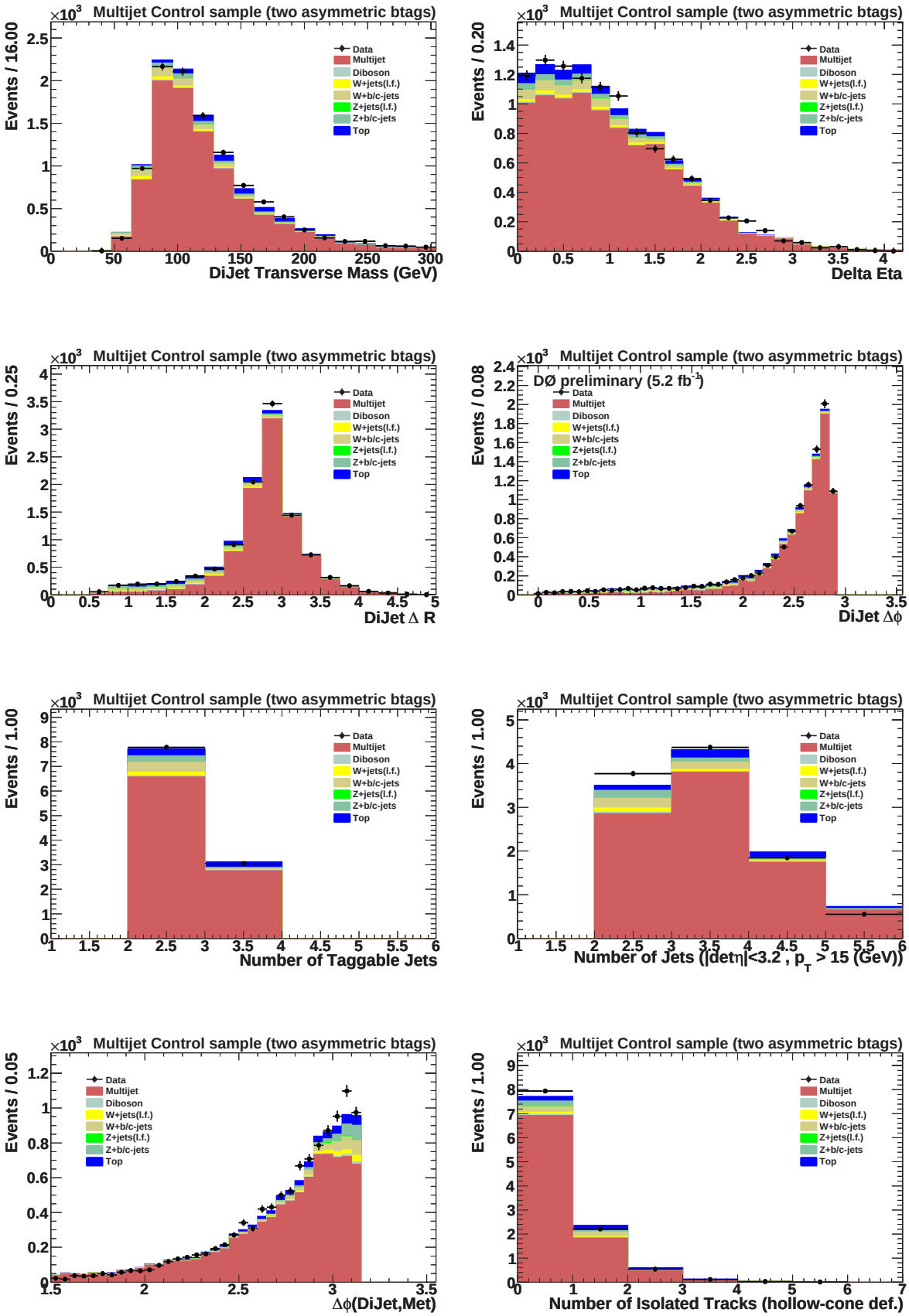

Figure 5.37: Multijet control sample with one tight and one loose b-tag

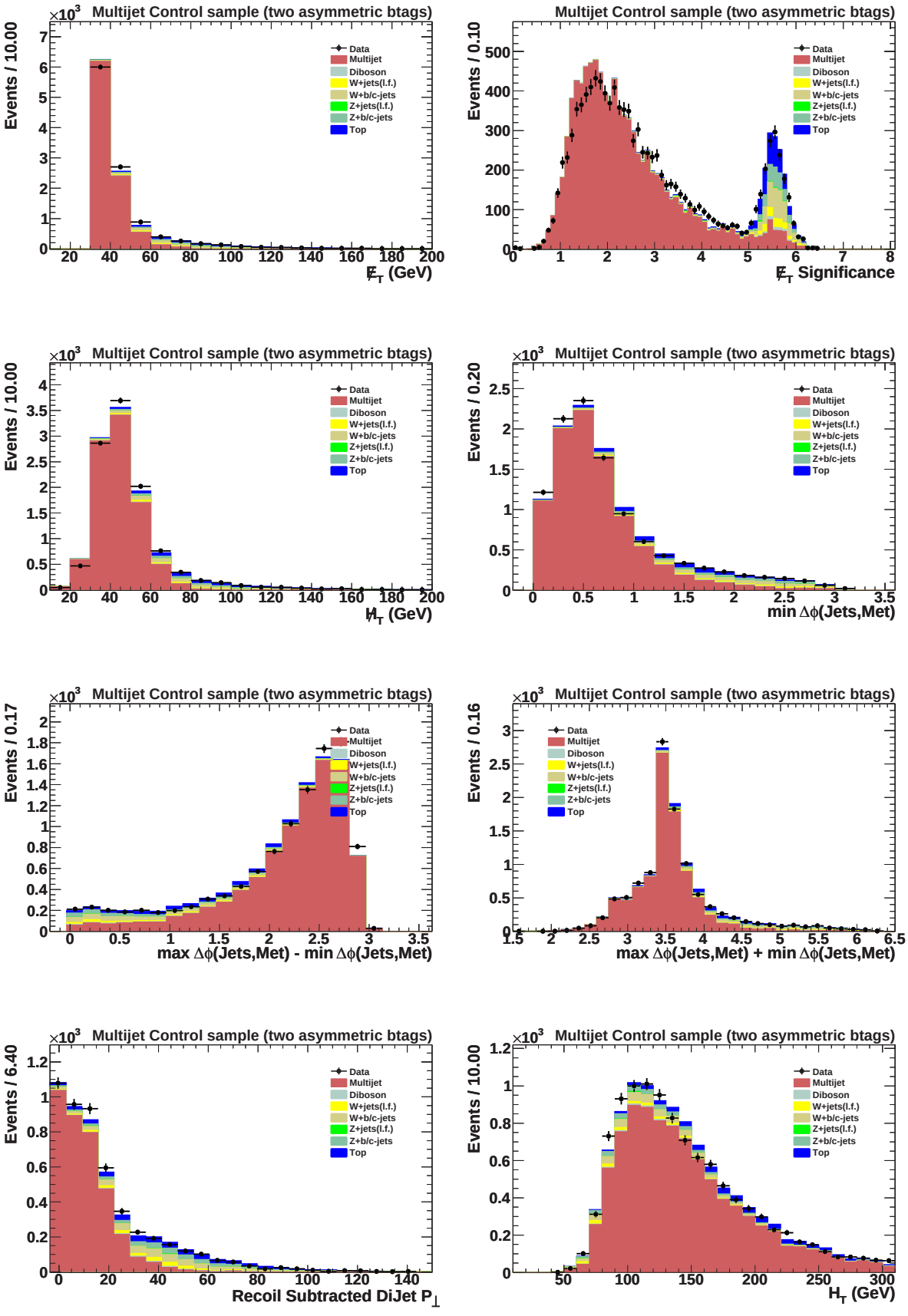

Figure 5.38: Multijet control sample with one tight and one loose b-tag

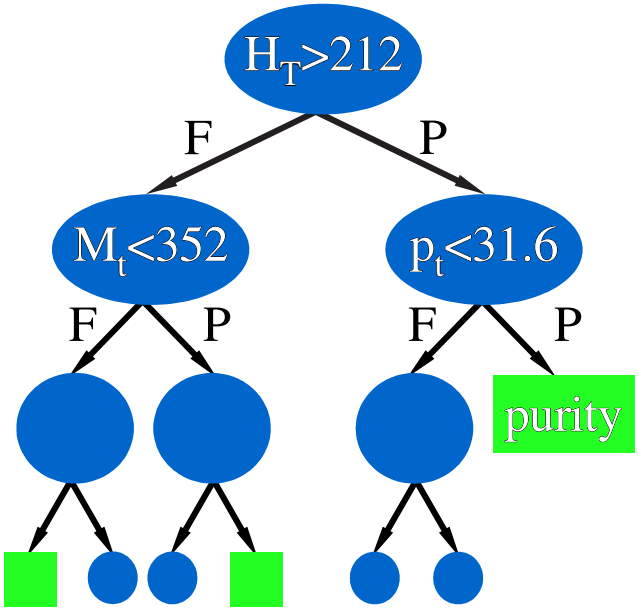

Figure 5.39: A schematic example of a Decision Tree. Nodes are shown in blue, with their associated splitting test; terminal nodes (leaves) are in green.

5.5 Decision Trees

5.5.1 Introduction

Decision trees are a machine learning technique [87] not (yet) commonly used in high energy physics. In DØ, the technique was pioneered by the single top analysis group [88, 89]. The goal is to extend a simple cut-based analysis into a multivariate technique by continuing to analyze events that fail a particular criterion. The following description is largely based on [90].

5.5.2 Tree Construction

Mathematically, decision trees are rooted binary trees. An example is shown in Figure 5.39. Consider a training sample made of known signal and background events: they form the root node of the tree. Given a list of variables x_i, all events are sorted in turn according to each variable. For each x_i the splitting value that gives the best separation of the events into two child nodes – one with mostly signal events, the other with mostly background events – is found. The variable and split value giving the best separation are selected and two new nodes are created, one corresponding to events satisfying the split criterion (labeled P for passed in 5.39), the other containing events that failed it (labeled F). The algorithm is then applied recursively to the two child nodes. The splitting stops if the number of available events falls below 100 or no splitting is found which improves the

separation of signal and background. In this case the node is called a leaf. The training continues until every node is a leaf. Each leaf is assigned the purity value p=s/(s+b), where s (b) is the weighted sum of signal (background) events in the leaf. A leaf is labeled signal if the purity is larger than 0.5, background otherwise. The Gini factor is used as the splitting criterion (see [89, 91] for more details).

5.5.3 Boosting

A very powerful technique to improve the performance of any weak classifier (anything that does better than random guessing) called boosting, was introduced about a decade ago. We use the same boosting algorithm as the single top quark search called adaptive boosting, known in the literature as AdaBoost [92].

The basic principle of boosted decision trees is to train a tree T_n, check which events are misclassified by T_n, increase the weight of misclassified events and train a tree T_{n+1} on the re-weighted sample. The weight of tree T_n is calculated according to

$$\alpha_n = \beta \times \ln \frac{1-\epsilon_n}{\epsilon_n} \tag{5.4}$$

where β is the boost parameter which determines the strength of classification and ϵ_n is the sum of weights of the misclassified events. The weight of each misclassified event is increased by the factor e^{α_n} before training the tree T_{n+1}. This makes T_{n+1} work harder on difficult events to classify them properly. This is repeated N times, where N is the total number of boosting cycles. The final boosted decision tree output for event i is the weighed average of the different tree outputs:

$$D(x_i) = \frac{1}{\sum_{n=0}^{N} \alpha_n} \sum_{n=0}^{N} \alpha_n D_n(x_i). \tag{5.5}$$

5.5.4 The Sets of Three Decision Trees

For this round of the analysis, we use sets of three decision trees, for each Higgs boson mass. In each set, a first tree ("multijet DT") is trained to separate V+H signal from multijet background. This tree is trained at pre-tag level on the multijet-model for the signal sample, and applied to the pre-tagged and tagged signal samples. Two other trees ("Physics DT") are trained to separate V+H from top, V+jets, and diboson backgrounds, one at the single-tag level, and the other at the double-tag level. The various backgrounds are weighted according to their expected contributions.

All background samples are divided into three samples. Training is done on one third of the available MC statistics. To assess the purity of the leaves another third of the MC is used. The last third is used to verify that the third sample used for the purity determination is not biased. We remove the third of the events used in the training from further use. The signal samples are divided into four, with one sample used in the multijet training, one sample used in the Physics training, and the other two used for testing and deriving the results.

In practice, each decision tree is doubled, one for Run IIa, and one for Run IIb. In the following, results and distributions are shown for the full Run IIa + Run IIb data set, combining the Run IIa and Run IIb DT outputs as appropriate.

5.5.5 Optimizing the Boost Parameters

The main parameters to tune in the boosting process are the number of boosting cycles (N) and the boost parameter β.

We explored β parameters from 0.02 to 0.2, and boosting cycles from 0 (no boosting) up to 16 (high boosting) for Run IIb, double tagged sample, as shown in Figure 5.40.

For the decision trees used in this analysis, it was found that the expected limit on the SM Higgs cross section improves up to 10 boosts, after which no further improvement is seen. The best expected limits are obtained with $0.08 < \beta < 0.12$. As a result of these studies, $\beta = 0.1$ with 10 boosts is used for all trees and all Higgs boson masses.

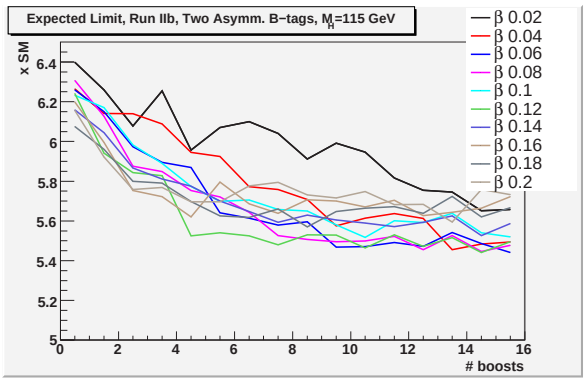

Figure 5.40: Optimization of DT boosting parameters β (Ada) and boost cycles N. The plot shows the expected limit (as a factor of the Standard Model cross section) for a Higgs mass of 115 GeV in the Run IIb, double tagged sample.

5.6 The Multijet and Physics Decision Trees

The variables used in the multijet decision tree are given in Table 5.8. The ranking of these variables in terms of discriminating power in the multijet DT is shown in Tables 5.9 and 5.10.

The final results are obtained using the Physics Decision Tree outputs, after a cut on the multijet DT. The multijet DT cut was optimized on the expected cross-section limit, together with the $\not\!\!E_T$ significance cut, by performing a scan with various cuts. The result of this scan is shown in Figure 5.41, with the optimal value of 0.6 being chosen. The default approach is to train the Physics DT before cutting on the multijet DT. It was verified that no improvement is obtained by training the Physics DT on samples with the multijet DT cut applied.

leading jet p_T	second jet p_T
third jet p_T	Number of taggable jets
Number of good jets	$\Delta R(\text{jet}_1, \text{jet}_2)$
$\Delta\eta(\text{jet}_1, \text{jet}_2)$	$\Delta\phi(\text{jet}_1, \text{jet}_2)$
$\not\!\!E_T$ significance	$\Delta\phi(\not\!\!E_T, \text{dijet system})$
$\Delta\phi(\not\!\!E_T, \text{jet}_1)$	$\Delta\phi(\not\!\!E_T, \text{jet}_2)$
$\min \Delta\phi(\not\!\!E_T, \text{jet}_\text{i})$	dijet mass
H_T	$\not\!\!H_T$
$\not\!\!E_T$	$\not\!\!H_T / \sqrt{H_T}$
$\max \Delta\phi(\not\!\!E_T, \text{jet}_\text{i}) + \min \Delta\phi(\not\!\!E_T, \text{jet}_\text{i})$	$\max \Delta\phi(\not\!\!E_T, \text{jet}_\text{i}) - \min \Delta\phi(\not\!\!E_T, \text{jet}_\text{i})$
No. Isol. tracks	Transverse mass
recoil subtracted dijet $P_\perp$	

Table 5.8: Variables used as input to the Decision Trees.

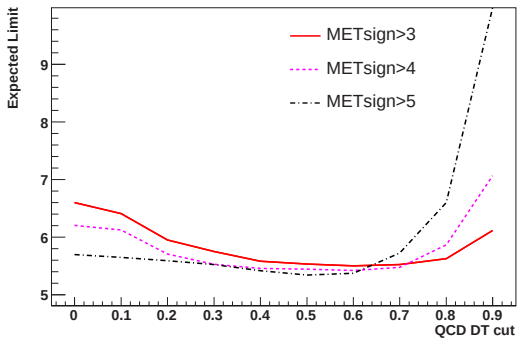

S

Figure 5.41: Optimization of the cut on the multijet Decision Tree. The plot shows the expected limit from the Physics DT output for different cuts on the multijet DT, for a Higgs mass of 115 GeV in the Run IIb, double tagged sample.

$\not\!\!E_T$
dijet mass
No. Isol. tracks
$\not\!\!E_T$ significance
recoil subtracted dijet $P_\perp$
$\Delta\eta(\mathrm{jet}_1, \mathrm{jet}_2)$
Transverse mass
$\not\!\!H_T$
$\not\!\!H_T$/ H_T
$\min \Delta\phi(\not\!\!E_T, \mathrm{jet_i})$
$\Delta\phi(\not\!\!E_T, \text{dijet system})$
$\Delta R(\mathrm{jet}_1, \mathrm{jet}_2)$
$\max \Delta\phi(\not\!\!E_T, \mathrm{jet_i}) + \min \Delta\phi(\not\!\!E_T, \mathrm{jet_i})$
H_T
$\Delta\phi(\not\!\!E_T, \mathrm{jet}_1)$
$\max \Delta\phi(\not\!\!E_T, \mathrm{jet_i}) - \min \Delta\phi(\not\!\!E_T, \mathrm{jet_i})$
second jet p_T
third jet p_T
leading jet p_T
$\Delta\phi(\not\!\!E_T, \mathrm{jet}_2)$
Number of good jets
$\Delta\phi(\mathrm{jet}_1, \mathrm{jet}_2)$
Number of taggable jets

Table 5.9: Ranking of variables in terms of discriminating power in the multijet DT in Run IIa.

$\not\!\!E_T$
dijet mass
Transverse mass
$\not\!\!E_T$ significance
No. Isol. tracks
$\Delta R(\text{jet}_1, \text{jet}_2)$
$\not\!\!H_T$
$\not\!\!H_T$/ H_T
H_T
$\Delta\eta(\text{jet}_1, \text{jet}_2)$
$\Delta\phi(\not\!\!E_T, \text{dijet system})$
second jet p_T
recoil subtracted dijet $P_\perp$
$\min \Delta\phi(\not\!\!E_T, \text{jet}_\text{i})$
$\Delta\phi(\not\!\!E_T, \text{jet}_1)$
$\max \Delta\phi(\not\!\!E_T, \text{jet}_\text{i}) + \min \Delta\phi(\not\!\!E_T, \text{jet}_\text{i})$
$\max \Delta\phi(\not\!\!E_T, \text{jet}_\text{i}) - \min \Delta\phi(\not\!\!E_T, \text{jet}_\text{i})$
$\Delta\phi(\not\!\!E_T, \text{jet}_2)$
$\Delta\phi(\text{jet}_1, \text{jet}_2)$
leading jet p_T
Number of good jets
third jet p_T
Number of taggable jets

Table 5.10: Ranking of variables in terms of discriminating power in the multijet DT in Run IIb.

Figure 5.42 and Figure 5.43 shows the multijet DT output distribution for all Higgs boson masses at the pre-tag level. In these plots one can see for all the Higgs mass points good agreement between data (shown in black points) and estimated backgrounds (shown in histograms) has been achieved. Also good separation between signal (shown as red line, peaks around 1) and multijet background (shown as magenta histogram, peaks around 0) has been achieved.

5.6.1 Signal Sample After Multijet DT Cut

Kinematic-variable distributions after the cut at 0.6 on the multijet DT output are shown here for a Higgs boson mass of 115 GeV. Distributions before b-tagging can be seen in Figures. 5.44-5.46. Plots for a sample with one tight b-tag is shown in Figures. 5.47-5.49, and after double asymmetric (L3-VT) tagging in Figures. 5.50-5.52. Overall, there is good agreement between the observed data and the expected background, both before and after b-tagging. One can clearly see after the cut, multijet background (shown in magenta histogram) is negligible. Compared to previous versions of this analysis, an effort was made to lower the $\not\!\!E_T$ cut. It can however be seen that, after the cut on the multijet-DT output, the benefit is minimal.

The numbers of events observed and expected from the various background sources are given in Table 5.11 after applying the cut at 0.6 on the multijet DT output and before b-tagging, for an exclusive VT tag, and for an asymmetric VT-L3 double tag. The effect of the cut on the multijet-DT output can be seen by comparing with Table 5.5.

The variables used in the Physics decision trees are the same as for the multijet DT. The ranking of these variables in terms of discriminating power in the physics DTs is shown in Tables 5.12 to 5.15.

The physics DT output distributions are shown in Figs. 5.53-5.54 and Figs. 5.55-5.56 for the single and double tag signal samples, respectively. Here also one can see clear separation between signal (shown as red line) and remaining SM backgrounds (shown as histograms) is achieved. Good agreement between data (black points) and estimated backgrounds (histograms).

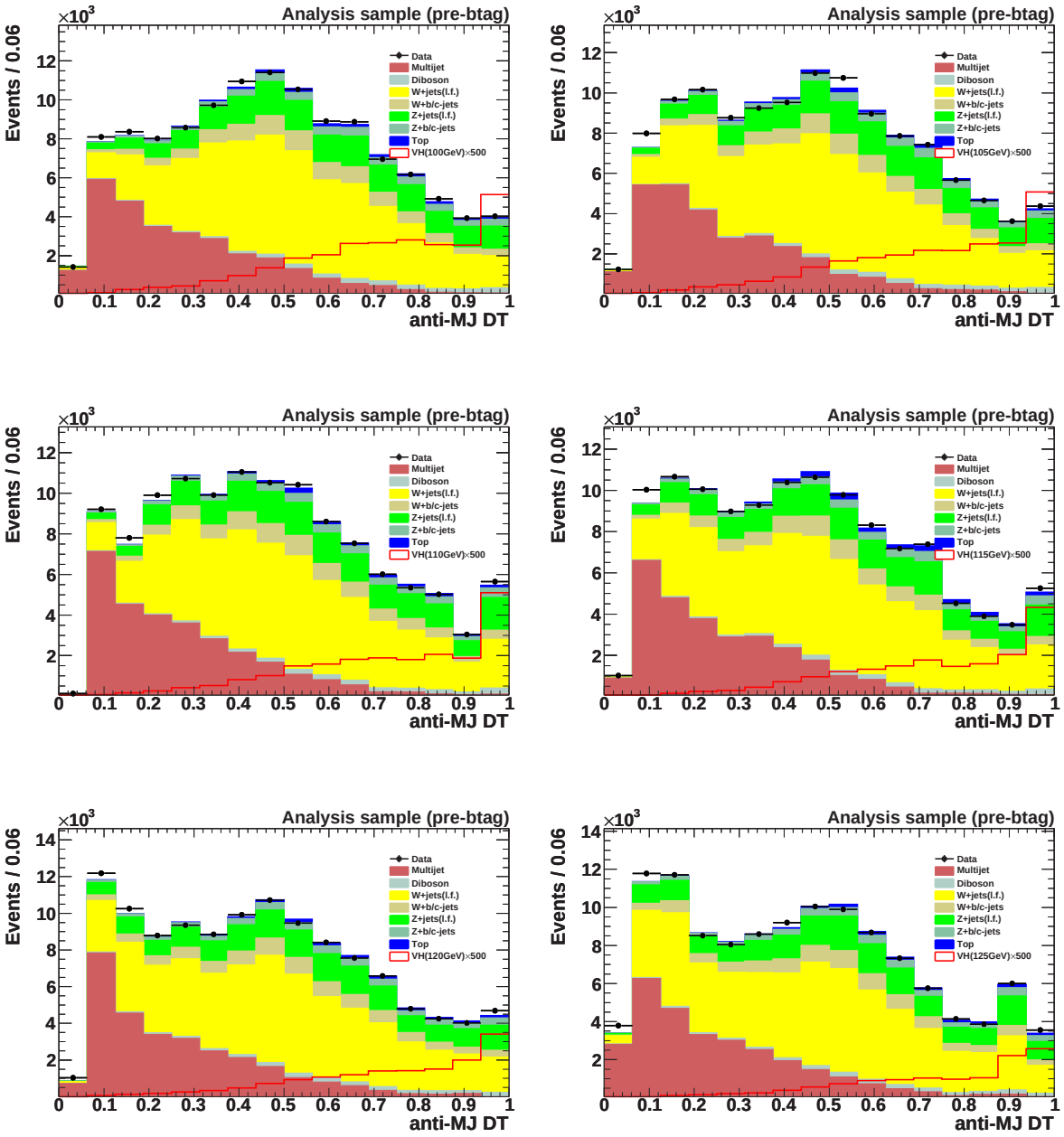

Figure 5.42: Multijet DT distribution for different Higgs masses (100-125 GeV) at the pretag level.

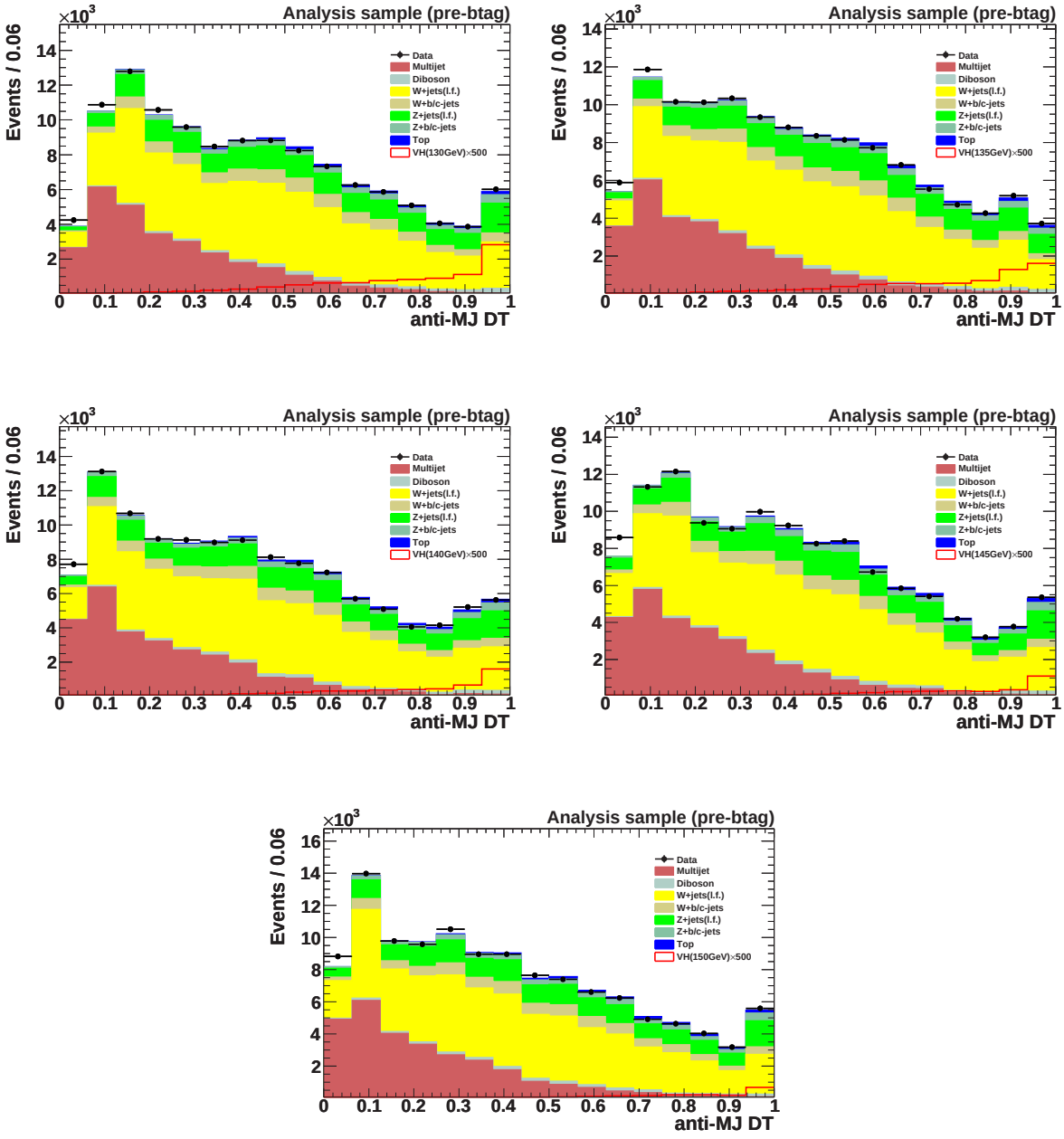

Figure 5.43: Multijet DT distribution for different Higgs masses (130-150 GeV) at the pretag level.

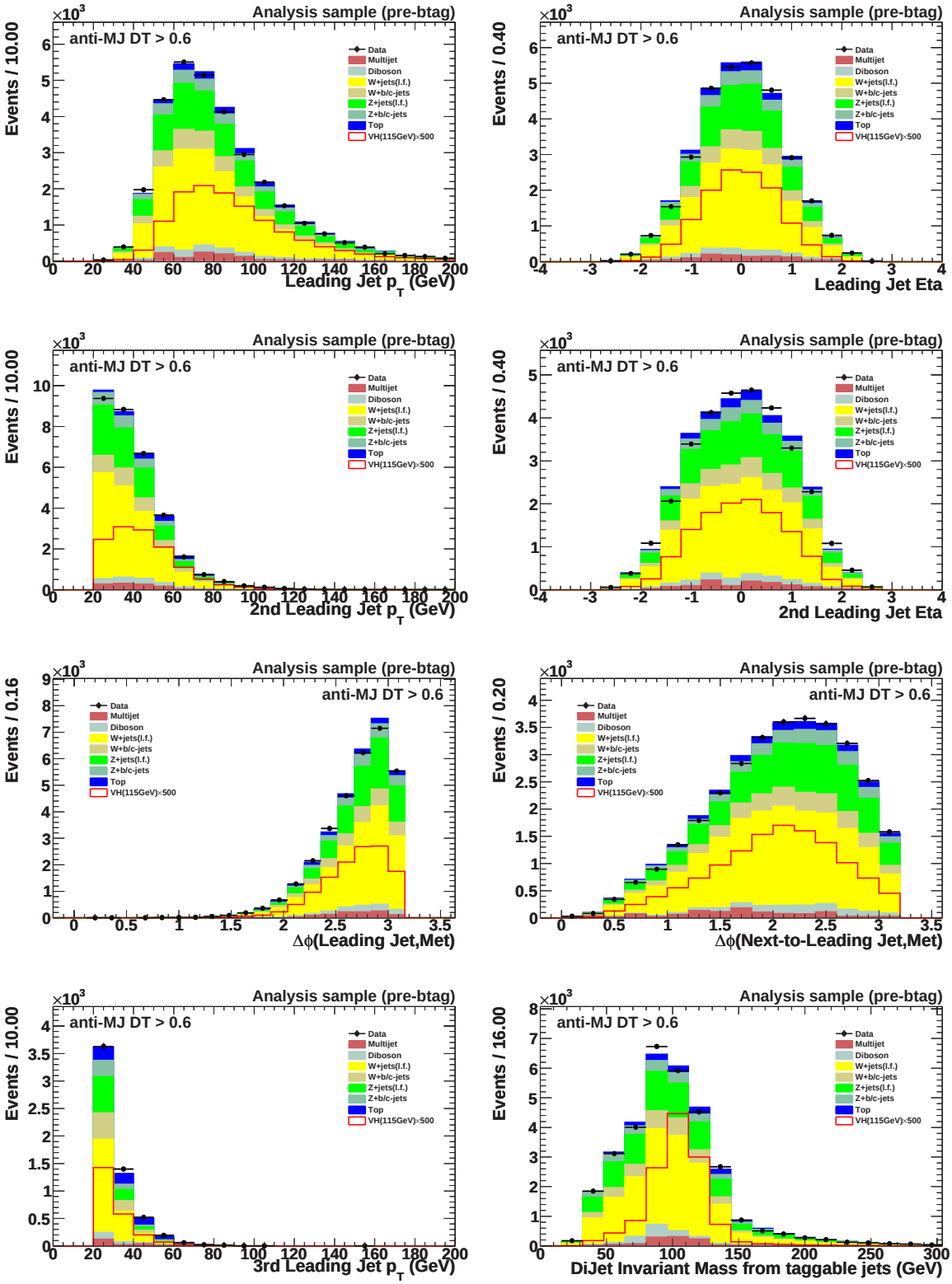

Figure 5.44: Pre b-tag signal sample after requiring multijet DT>0.6.

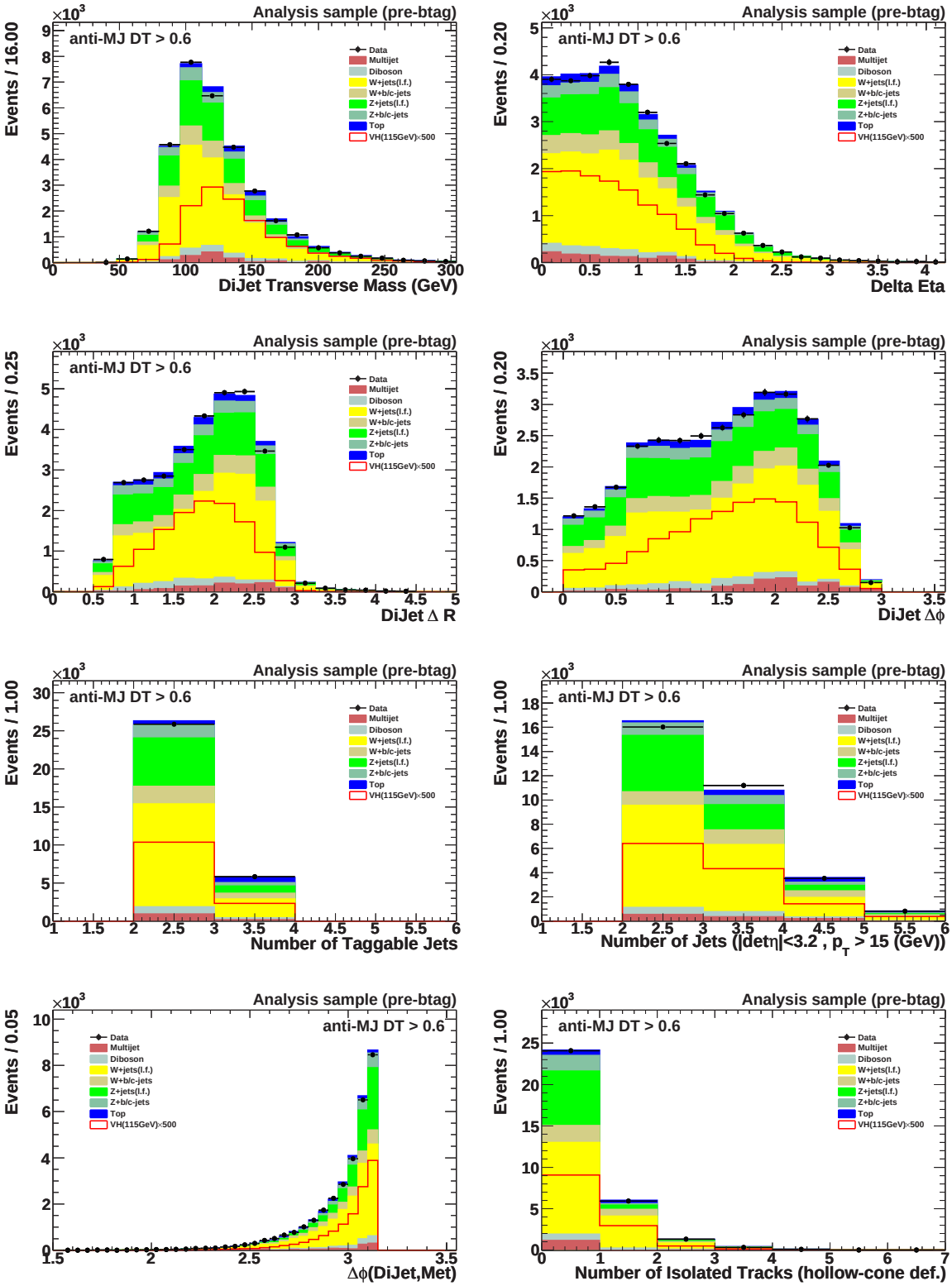

Figure 5.45: Pre b-tag signal sample after requiring multijet DT>0.6.

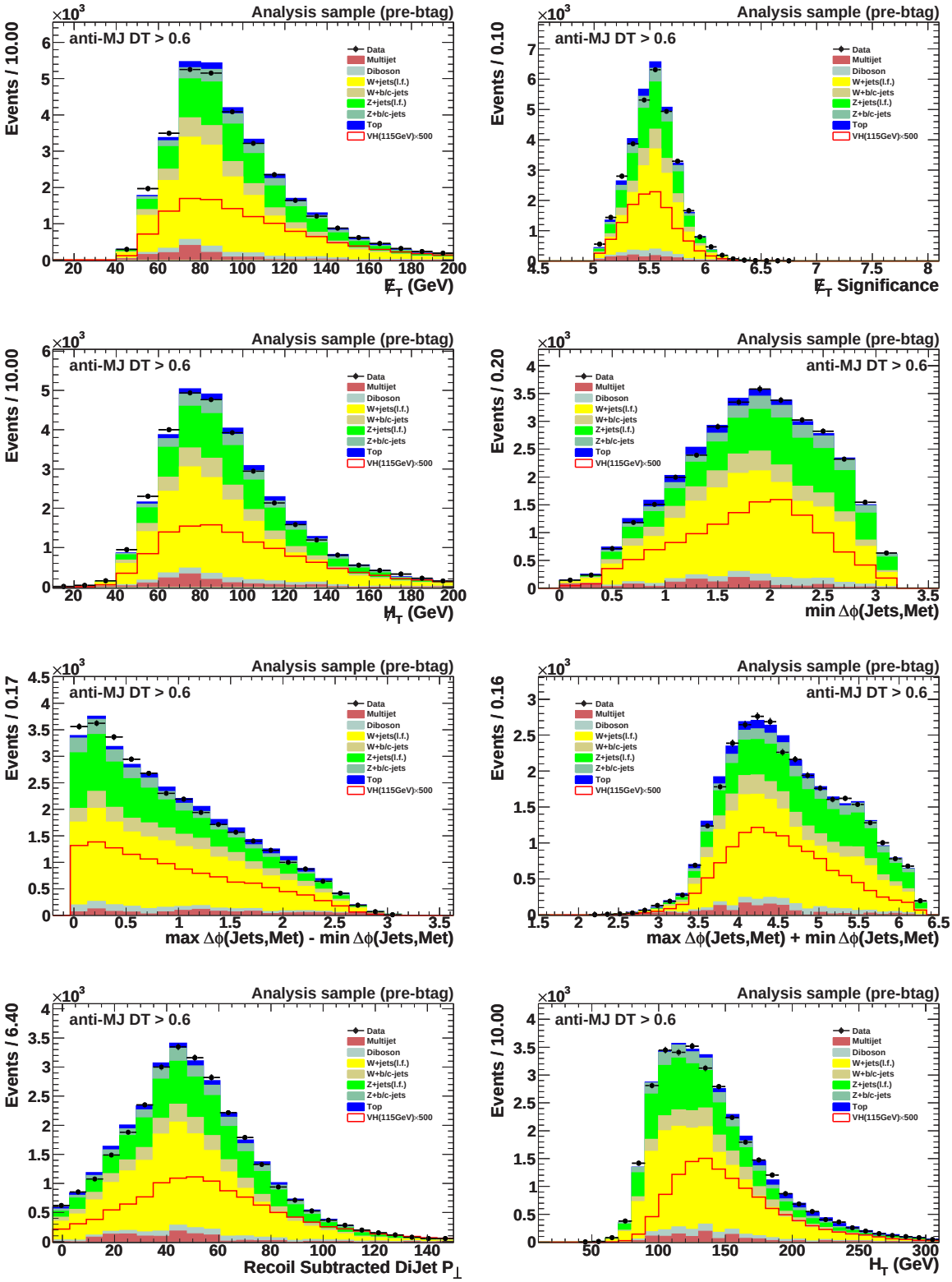

Figure 5.46: Pre b-tag signal sample after requiring multijet DT>0.6.

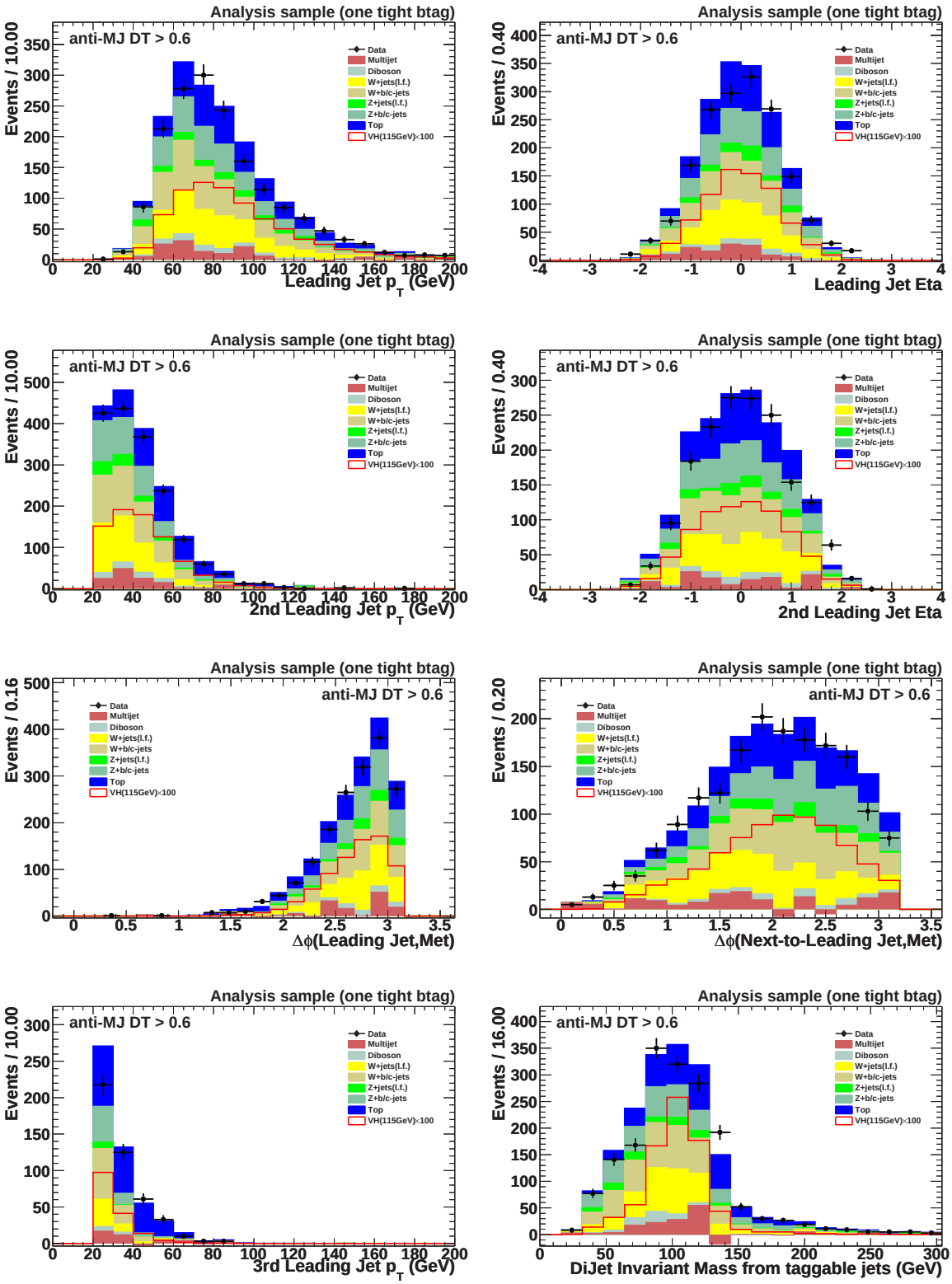

Figure 5.47: Signal sample with one tight b-tag after requiring multijet DT>0.6.

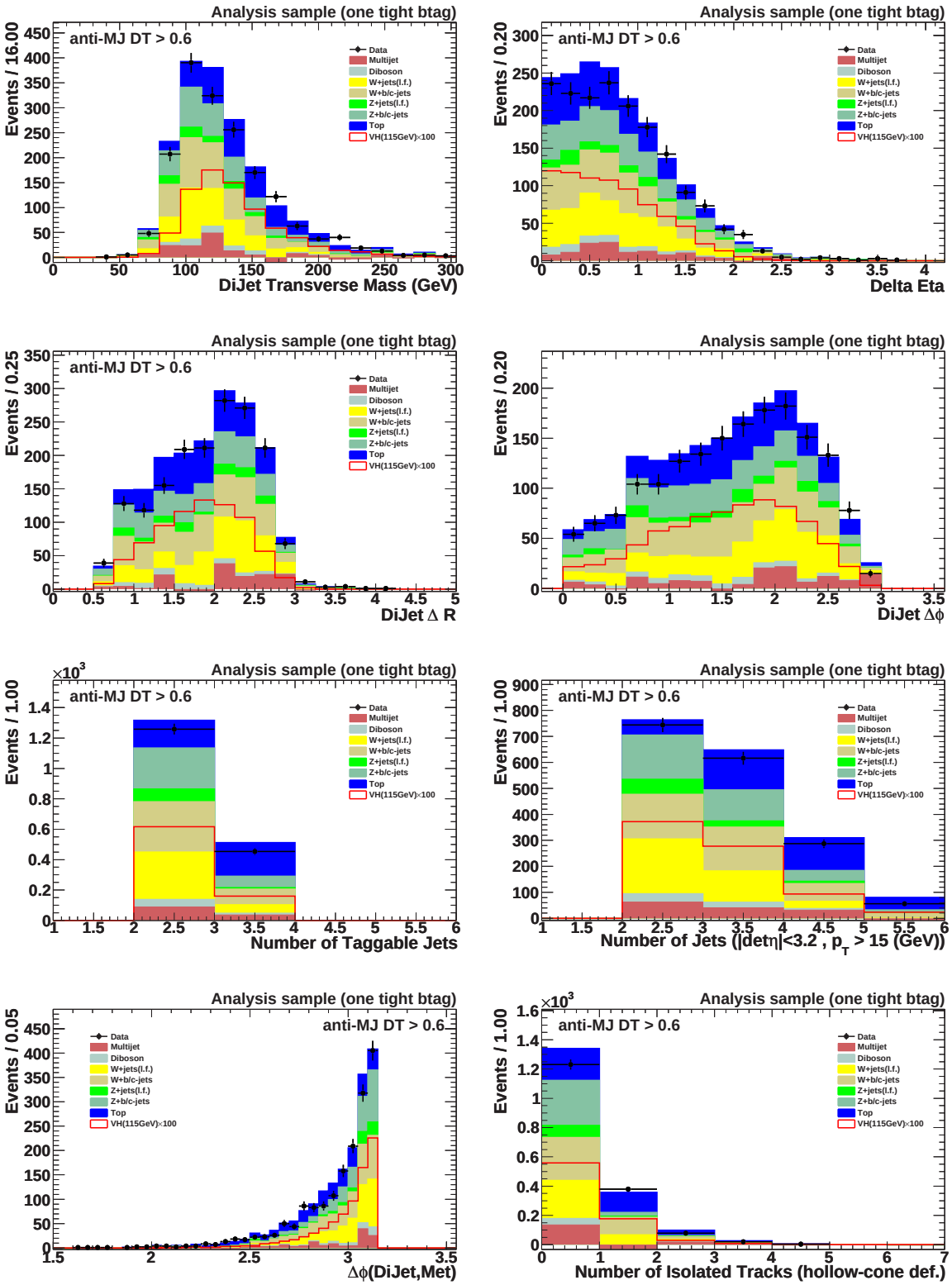

Figure 5.48: Signal sample with one tight b-tag after requiring multijet DT>0.6.

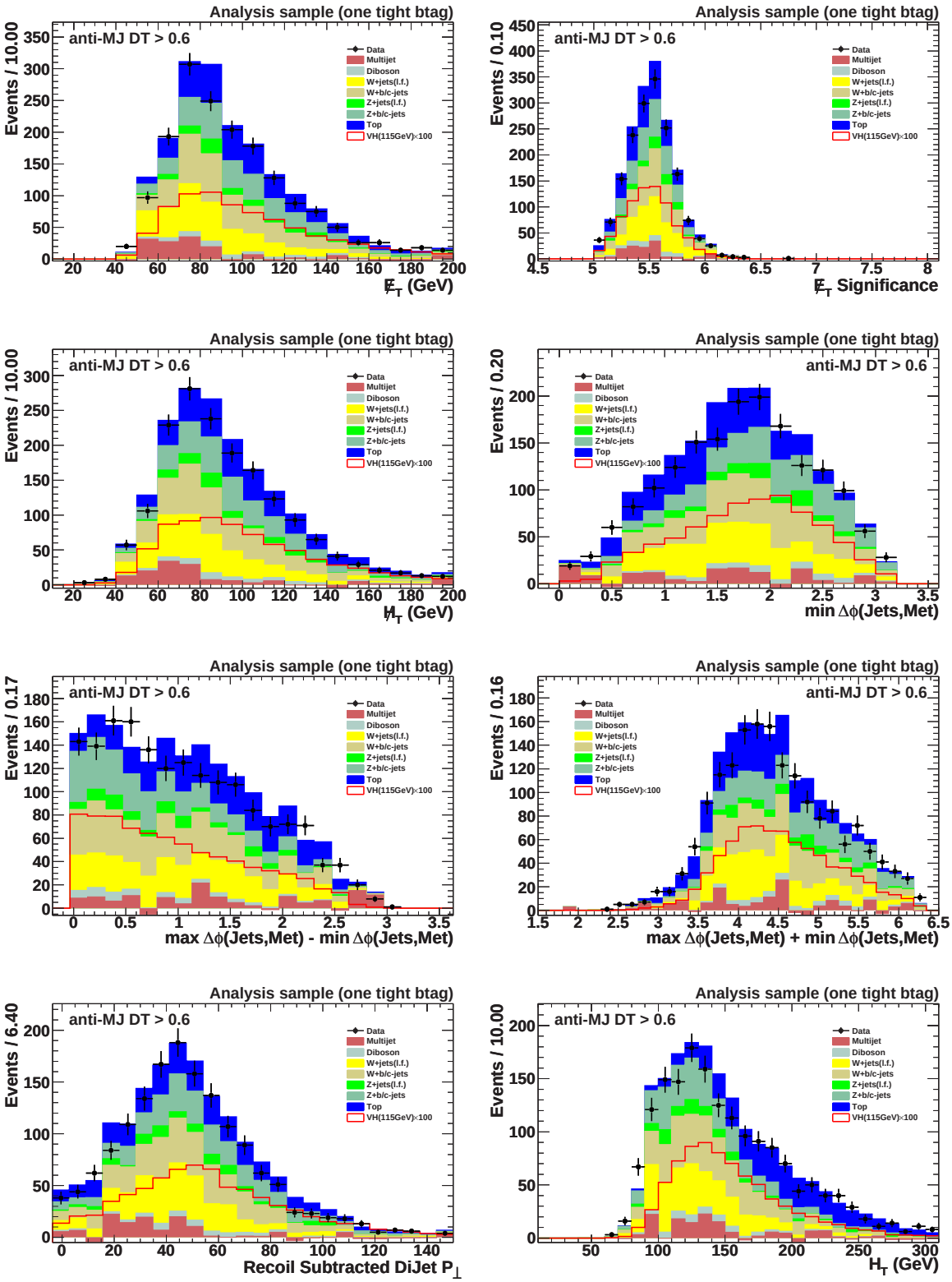

Figure 5.49: Signal sample with one tight b-tag after requiring multijet DT>0.6.

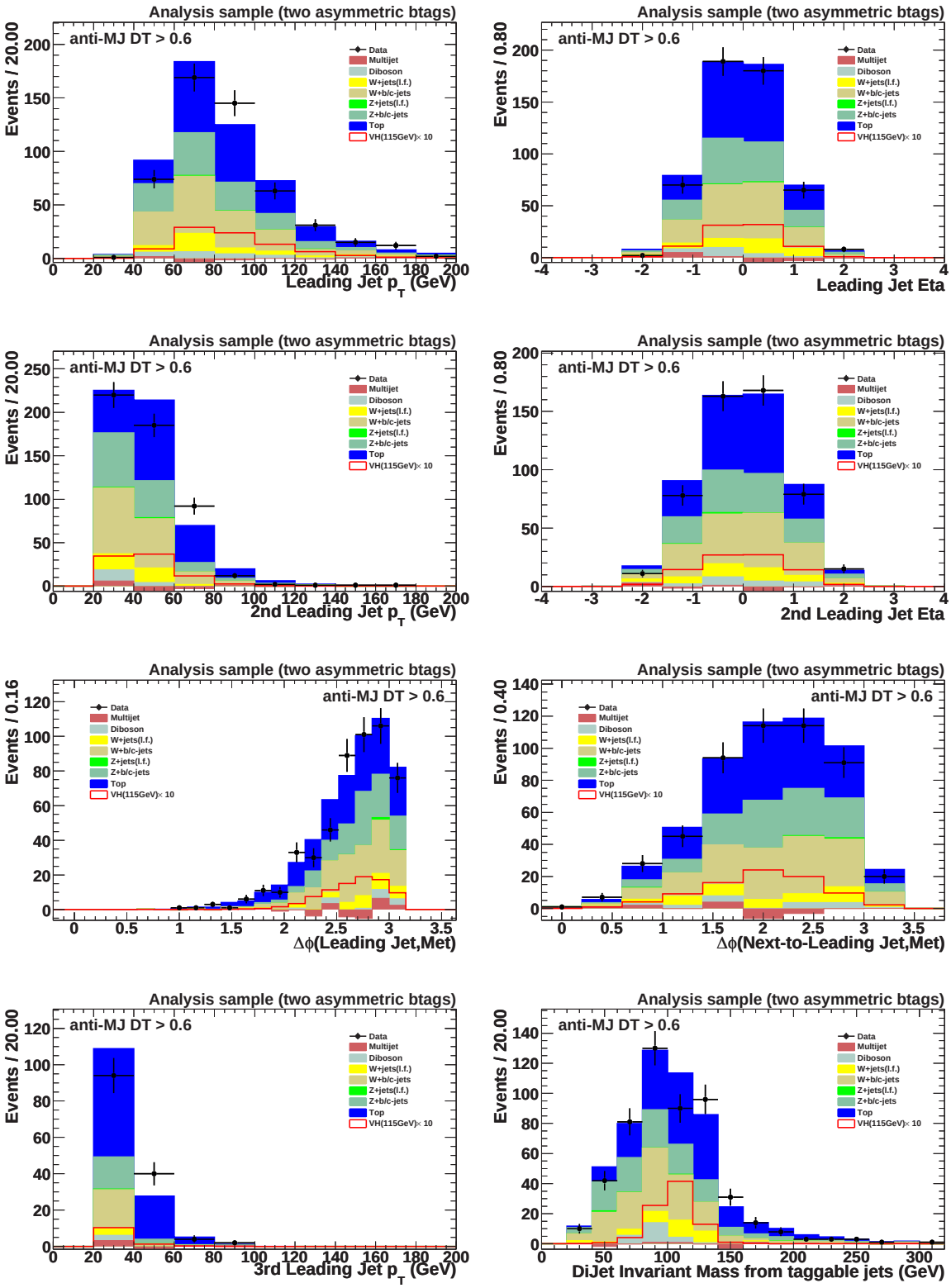

Figure 5.50: Signal sample with one tight and one loose b-tag after requiring multijet DT>0.6.

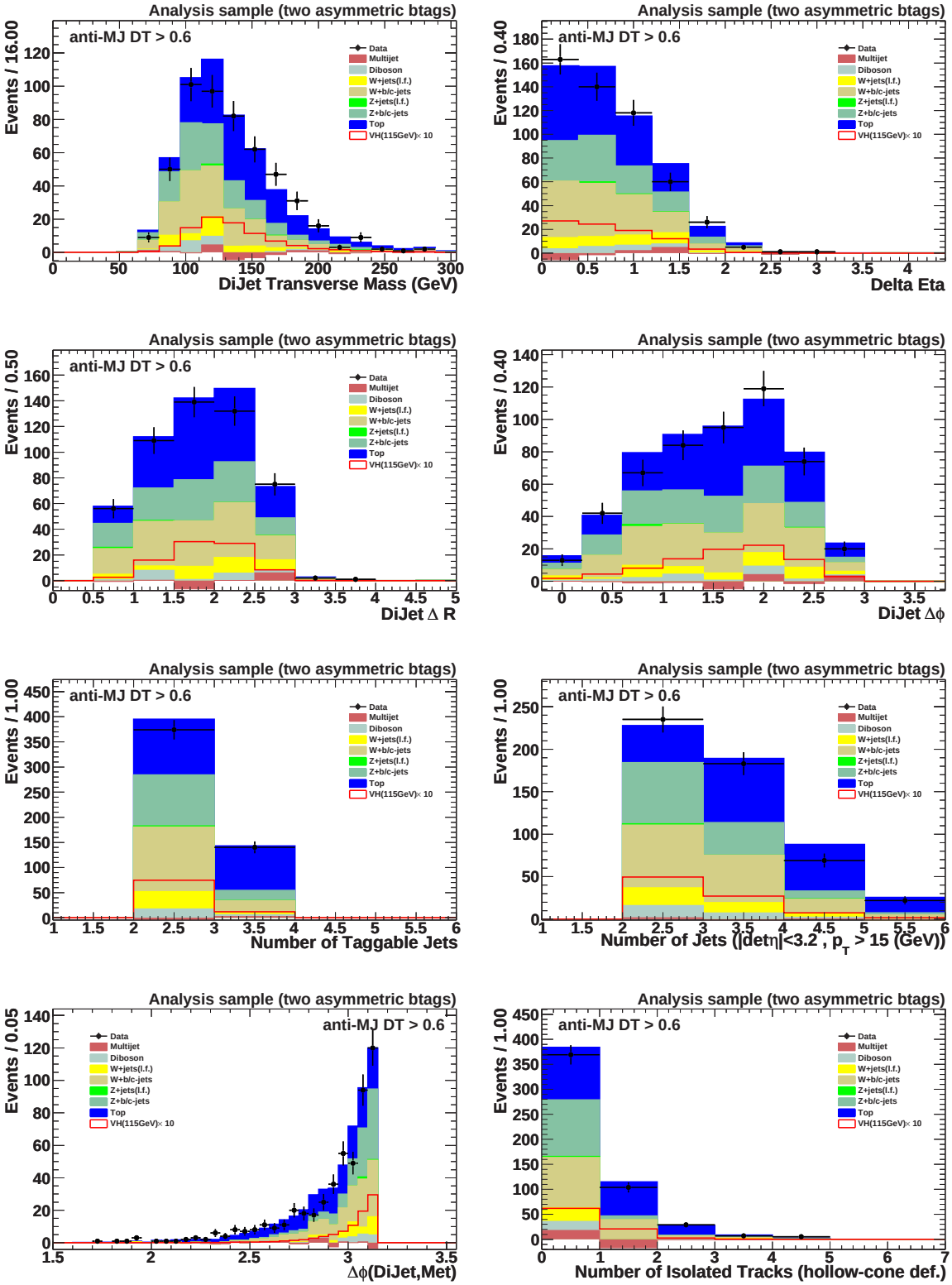

Figure 5.51: Signal sample with one tight and one loose b-tag after requiring multijet DT>0.6.

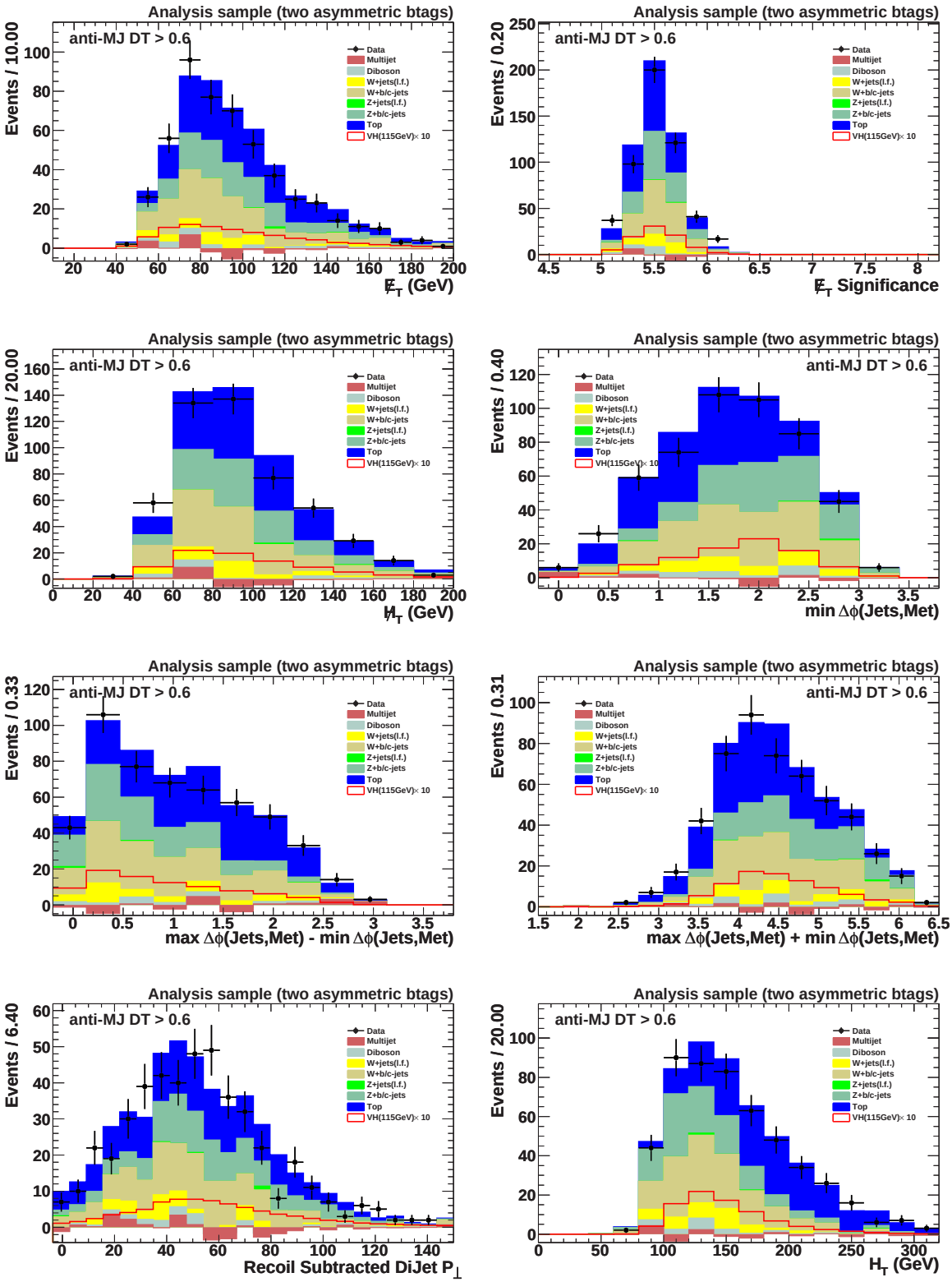

Figure 5.52: Signal sample with one tight and one loose b-tag after requiring multijet DT>0.6.

Sample	Before b-tagging	1 VT and 1 !L3 tag	1 VT and 1 L3 tag
ZH (115GeV)	13.73 ± 0.08	4.16 ± 0.05	4.66 ± 0.04
WH (115GeV)	11.64 ± 0.12	3.60 ± 0.07	3.99 ± 0.06
W+jets	15997.26 ± 65.18	366.54 ± 11.78	38.25 ± 5.56
W+b/c jets	3072.22 ± 25.53	434.98 ± 8.13	152.99 ± 4.66
Z+jets	7303.66 ± 79.50	94.06 ± 11.71	2.08 ± 0.99
Z+b/c jets	2128.67 ± 23.73	344.47 ± 8.01	122.09 ± 4.28
top	1215.56 ± 4.41	404.38 ± 2.42	199.07 ± 1.50
di-boson	1111.78 ± 10.13	60.03 ± 2.27	24.24 ± 1.19
Total Physics	30829.15 ± 109.11	1704.47 ± 20.42	538.72 ± 8.70
Instr. Bgrd	1195.55 ± 120.31	125.41 ± 31.91	-0.80 ± 7.55
Total Bgrd	32024.70 ± 162.42	1829.89 ± 37.89	537.91 ± 11.52
Observed	31718.00	1712.00	514.00

Table 5.11: Number of events after applying all selection cuts and after cutting on the multijet-DT output, before b-tagging and with single and asymmetric-double tags. Errors are statistical errors only.

dijet mass
H_T
$\Delta\phi(\not\!\!E_T, \text{dijet system})$
$\Delta R(\text{jet}_1, \text{jet}_2)$
$\not\!\!H_T$/ H_T
recoil subtracted dijet $P_\perp$
Transverse mass
Number of isolated tracks
leading jet p_T
$\Delta\eta(\text{jet}_1, \text{jet}_2)$
$\Delta\phi(\not\!\!E_T, \text{jet}_1)$
$\not\!\!E_T$ significance
third jet p_T
second jet p_T
$\not\!\!E_T$
$\max \Delta\phi(\not\!\!E_T, \text{jet}_\text{i}) - \min \Delta\phi(\not\!\!E_T, \text{jet}_\text{i})$
$\Delta\phi(\text{jet}_1, \text{jet}_2)$
$\min \Delta\phi(\not\!\!E_T, \text{jet}_\text{i})$
$\not\!\!H_T$
$\max \Delta\phi(\not\!\!E_T, \text{jet}_\text{i}) + \min \Delta\phi(\not\!\!E_T, \text{jet}_\text{i})$
$\Delta\phi(\not\!\!E_T, \text{jet}_2)$
Number of good jets
Number of taggable jets

Table 5.12: Ranking of variables in terms of discriminating power in the physics DT in Run IIa with one tight b-tag.

dijet mass
$\Delta\phi(\not\!\!E_T, \text{dijet system})$
Number of isolated tracks
$\Delta R(\text{jet}_1, \text{jet}_2)$
recoil subtracted dijet $P_\perp$
H_T
$\not\!\!E_T$
leading jet p_T
$\Delta\eta(\text{jet}_1, \text{jet}_2)$
third jet p_T
$\not\!\!E_T$ significance
$\not\!\!H_T$/ H_T
Transverse mass
second jet p_T
$\Delta\phi(\text{jet}_1, \text{jet}_2)$
$\max \Delta\phi(\not\!\!E_T, \text{jet}_\text{i}) + \min \Delta\phi(\not\!\!E_T, \text{jet}_\text{i})$
$\not\!\!H_T$
$\min \Delta\phi(\not\!\!E_T, \text{jet}_\text{i})$
$\max \Delta\phi(\not\!\!E_T, \text{jet}_\text{i}) - \min \Delta\phi(\not\!\!E_T, \text{jet}_\text{i})$
$\Delta\phi(\not\!\!E_T, \text{jet}_1)$
$\Delta\phi(\not\!\!E_T, \text{jet}_2)$
Number of good jets
Number of taggable jets

Table 5.13: Ranking of variables in terms of discriminating power in the physics DT in Run IIa with one tight and one loose b-tag.

dijet mass
H_T
Transverse mass
$\Delta R(\text{jet}_1, \text{jet}_2)$
third jet p_T
$\Delta\phi(\not\!\!E_T, \text{dijet system})$
recoil subtracted dijet $P_\perp$
$\Delta\eta(\text{jet}_1, \text{jet}_2)$
$\not\!\!H_T$/ H_T
$\not\!\!E_T$
$\not\!\!E_T$ significance
Number of isolated tracks
leading jet p_T
$\not\!\!H_T$
$\Delta\phi(\not\!\!E_T, \text{jet}_1)$
$\min \Delta\phi(\not\!\!E_T, \text{jet}_\text{i})$
second jet p_T
$\max \Delta\phi(\not\!\!E_T, \text{jet}_\text{i}) + \min \Delta\phi(\not\!\!E_T, \text{jet}_\text{i})$
$\Delta\phi(\text{jet}_1, \text{jet}_2)$
$\max \Delta\phi(\not\!\!E_T, \text{jet}_\text{i}) - \min \Delta\phi(\not\!\!E_T, \text{jet}_\text{i})$
$\Delta\phi(\not\!\!E_T, \text{jet}_2)$
Number of good jets
Number of taggable jets

Table 5.14: Ranking of variables in terms of discriminating power in the physics DT in Run IIb with one tight b-tag.

dijet mass
recoil subtracted dijet $P_\perp$
$\Delta\phi(\not\!\!E_T, \text{dijet system})$
Number of isolated tracks
H_T
$\Delta\eta(\text{jet}_1, \text{jet}_2)$
$\not\!\!H_T$/ H_T
third jet p_T
$\not\!\!E_T$
$\Delta R(\text{jet}_1, \text{jet}_2)$
$\not\!\!H_T$
$\not\!\!E_T$ significance
$\Delta\phi(\not\!\!E_T, \text{jet}_1)$
second jet p_T
$\Delta\phi(\text{jet}_1, \text{jet}_2)$
Transverse mass
leading jet p_T
$\Delta\phi(\not\!\!E_T, \text{jet}_2)$
$\min \Delta\phi(\not\!\!E_T, \text{jet}_\text{i})$
$\max \Delta\phi(\not\!\!E_T, \text{jet}_\text{i}) - \min \Delta\phi(\not\!\!E_T, \text{jet}_\text{i})$
$\max \Delta\phi(\not\!\!E_T, \text{jet}_\text{i}) + \min \Delta\phi(\not\!\!E_T, \text{jet}_\text{i})$
Number of good jets
Number of taggable jets

Table 5.15: Ranking of variables in terms of discriminating power in the physics DT in Run IIb with one tight and one loose b-tag.

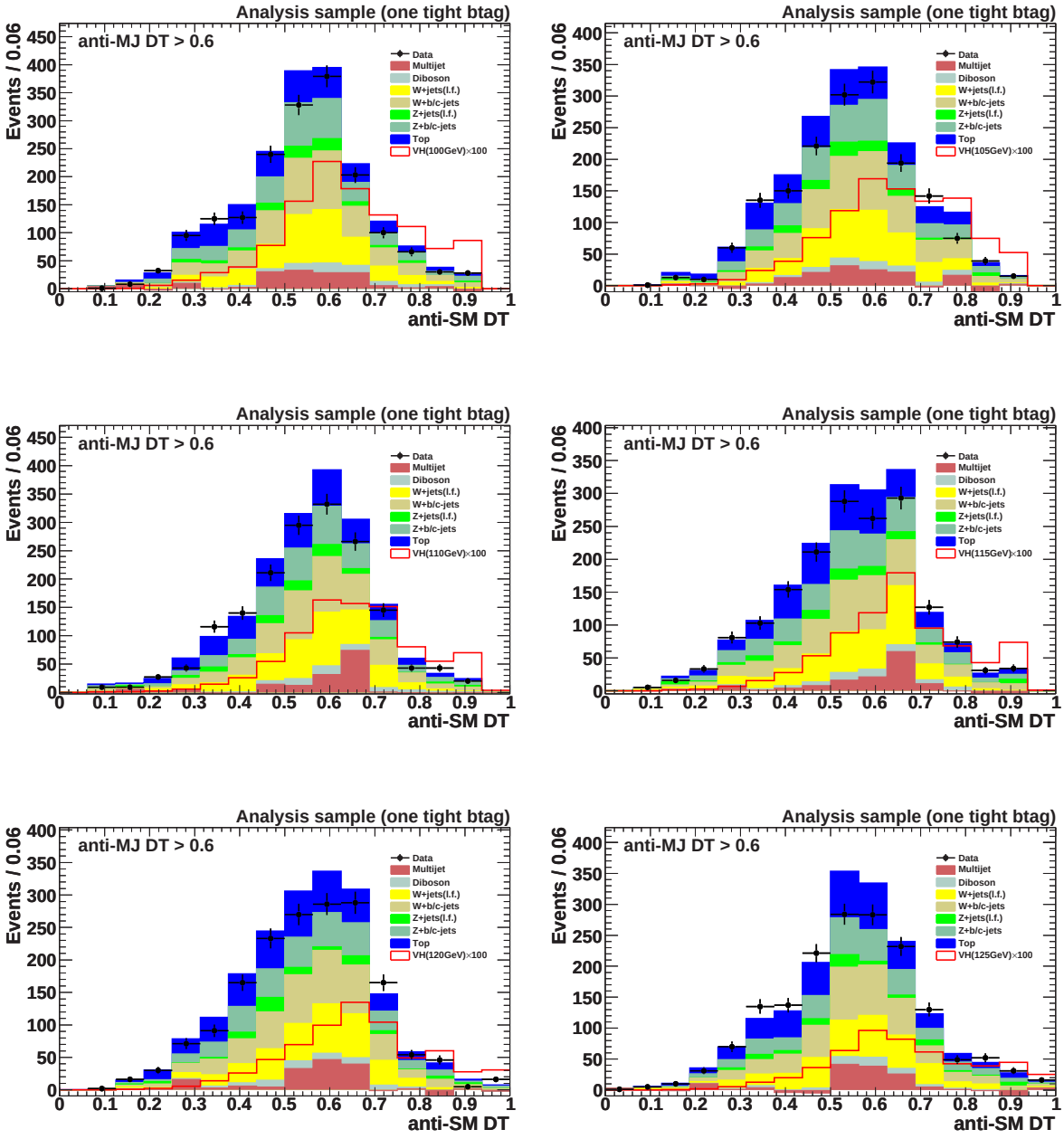

Figure 5.53: Physics DT distribution for different Higgs masses (100-125 GeV) in the single tag sample. The multijet DT output is required to be greater than 0.6.

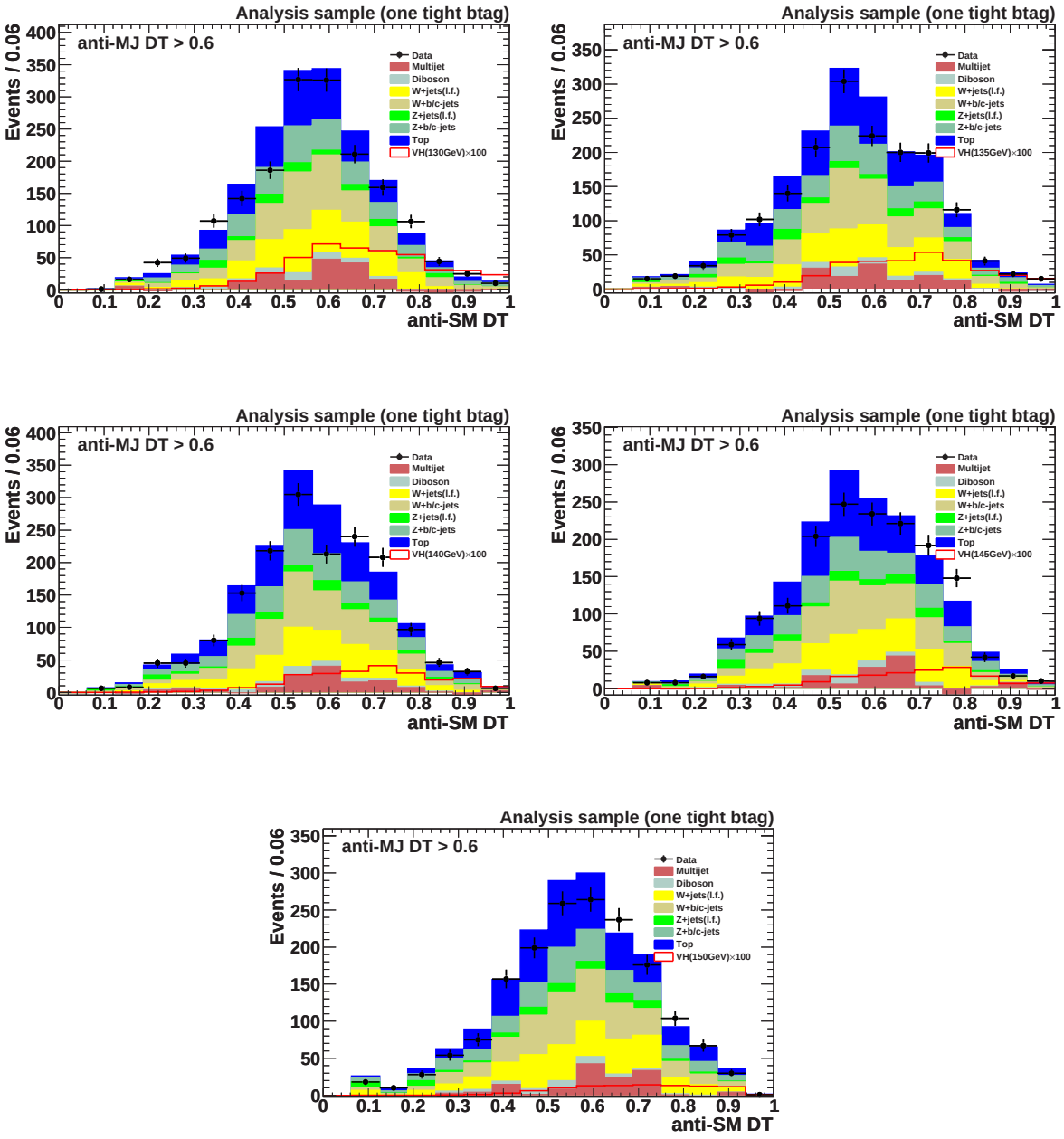

Figure 5.54: Physics DT distribution for different Higgs masses (130-150 GeV) in the single tag sample. The multijet DT output is required to be greater than 0.6.

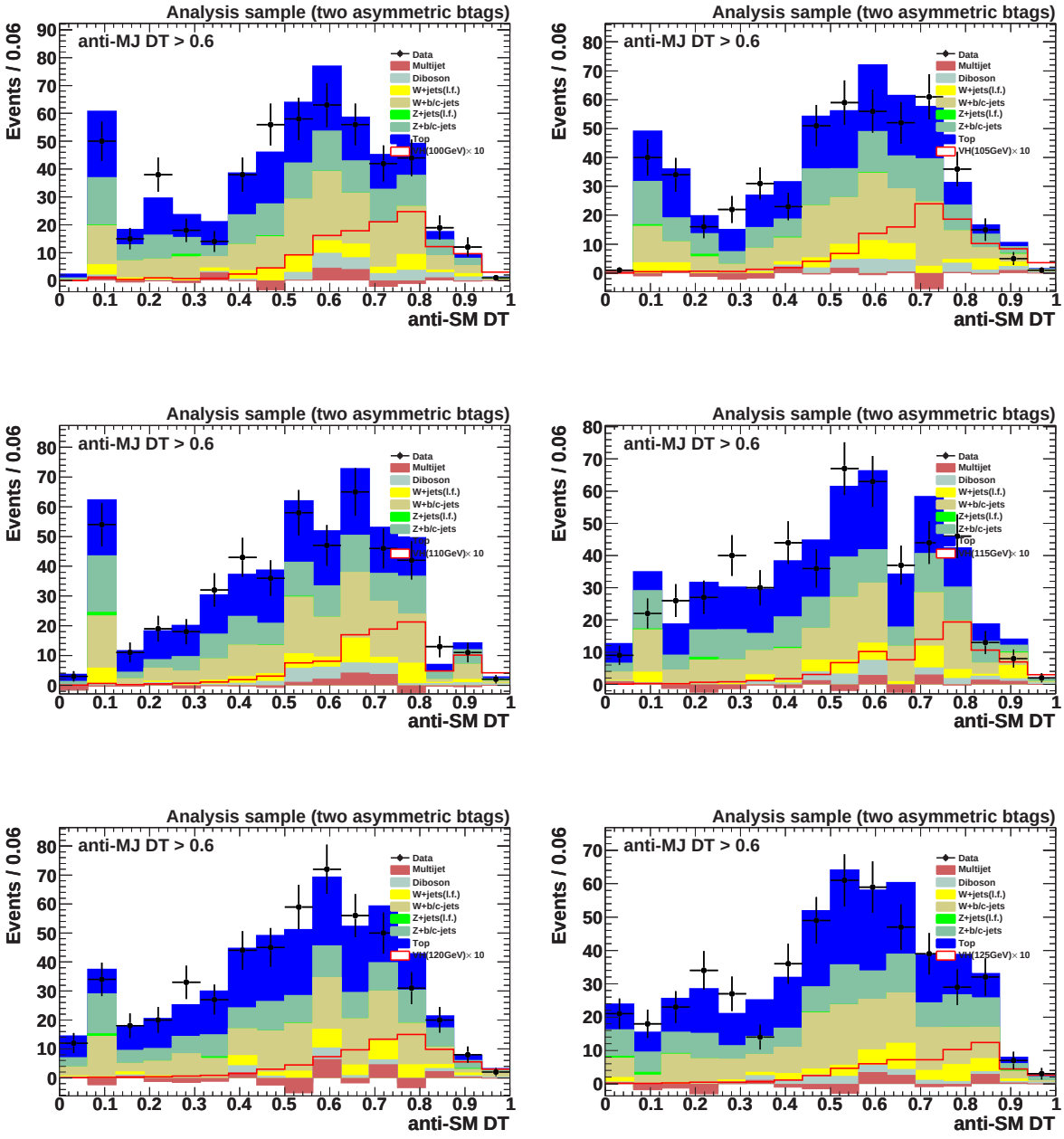

Figure 5.55: Physics DT distribution for different Higgs Masses (100-125 GeV)in the double tag sample. The multijet DT output is required to be greater than 0.6.

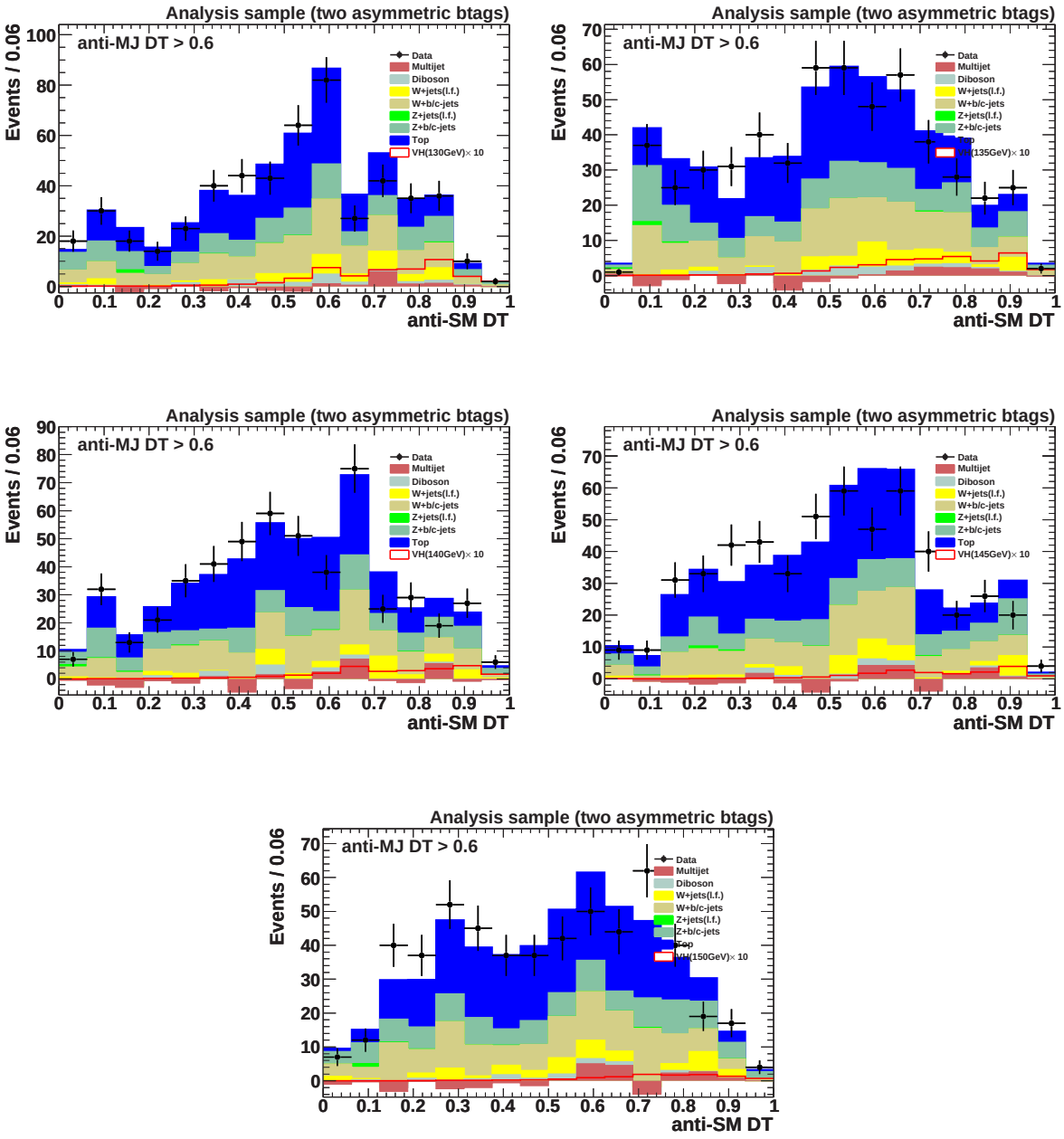

Figure 5.56: Physics DT distribution for different Higgs Masses (130-150 GeV)in the double tag sample. The multijet DT output is required to be greater than 0.6.

Chapter 6

Limit Calculation

6.1 Upper Limits on ZH Production

In the absence of excess of data over the expected background, as seen in previous chapter, we set an upper limit on the cross section for associated production of SM Higgs. A modified semi-frequentist confidence level (CL_s) approach, also known as LEP method is used for the limit setting procedure. The final discriminants which describes very well the data, expected background and signal are used as input for the limit calculation. In DØ, we have roughly 3 million collisions per second out of which only 100 - 120 events are recorded, therefore the data collected by the DØ can be fully described by the poison distribution.

We exclude the Higgs signal at 95% confidence level (CL) in case no event is obeserved and the likelihood of seeing no signal events (which means the observed events are compatiable with background), assuming a signal should be present, is less than 5%. The test statistic is a Poisson joint log-likelihood ratio (LLR) of the background only and of signal+background hypothesis, obtained by summing LLR values over the bins of final discriminant. Many simulated "pseudo experiments" are used to translate this test statistic in to confidence level. The impact of systematic uncertainities on the sensitivity of analysis is reduced by maximizing a profile likelihood function in which these uncertainities are given Gaussian constraints associated with their priors.

6.2 Limit Calculation

The likelihood ratio used as test statistic is defined for a single bin i as ratio of Poisson likelihoods

$$Q = \frac{P(data|s+b)}{P(data|b)} \tag{6.1}$$

where $P(data|s+b)$ is likelihood that data is consistent with signal + background hypothesis (also known as the test hypothesis) and $P(data|b)$ is likelihood that data is consistent with background only hypothesis (the null hypothesis). For a given bin this liklihood depends on number of predicted events, observed events and systematic uncertainities. This likelihood depends on terms which are of direct interest to the test and also on nuisance parameters which are not of immediate interest to the test but needed in order to estimate the parameters of interest. For each experiment, best fit model relative to nuisance parameter values are determined.

For a given bin i, if d_i is obeserved data events and s_i and b_i are predicted signal and background events then the combined likelihhod ratio Q can be written as

$$Q_i = \prod_i Q_i = \prod_i (\frac{e^{-s_i+b_i}(s_i+b_i)^{d_i}}{d_i!})/(\frac{e^{-b_i}(b_i)^{d_i}}{d_i!}) \tag{6.2}$$

The negative log-likelihood ratio for bin i with events d_i can be expressed as

$$\chi_{d_i} = -2\ ln\ Q_i = 2(s_i - d_i\ ln\ (1 + \frac{s_i}{b_i})) \tag{6.3}$$

The confidence level for signal+background hypothesis is defined as

$$CL_{s+b} = P_{s+b}(\chi \leq \chi_d) = \int_{-\infty}^{\chi_n} \frac{dP_{s+b}}{d\chi} d\chi \tag{6.4}$$

where $\chi_d = \sum_i \chi_d$. The probability distribution function P_{s+b} is defined by distribution of χ_d which is found by running a large number of pseudo-experiments. Outcome of these repeated experiments is simulated using the value of d and for all these experiments χ_d is calculated to get the distribution.

The CL_{s+b} estimator can lead to exclusion of signals even in the cases when there is no experimental sensitivity, a modified semi-frequentist confidence level CL_{s+b} is used.

$$CL_s = CL_{s+b}/CL_b \tag{6.5}$$

where CL_b is confidence level of background only hypothesis. The signal hypothesis is excluded at 95% confidence level if $CL_s < 5\%$.

For each pseudo-experiment, value of s_i and b_i is also simulated and systematic uncertainities are included in P_{s+b} and P_b as Gaussian smearing. To maintain correlation between bins and between signal and background, in each bin the signal and background prediction p_i is changed for each pseudo-experiment.

$$p'_i = p_i \prod_{j=1}^{N} (1 + \sigma_j^i L_j) \tag{6.6}$$

where p'_i are the systematically varied predictions for bin i and σ_j^i is contributed size of each of N source of uncertainity. L_j is a stochastic variable which is distributed as a Gaussian distribution. By cutting off p'_i at zero we ensure only positive value of signal and backgrounds.

The smearing procedure broadens the distribution thus making separation between two smaller. To reduce the degree of smearing of these two Probability Distribution Functions (PDFs), profile likelihood technique is used. For a given set of predictions, observations and systematic uncertainities, a model that best fit to the data obeservation is found by maximizing the likelihood over the space of all possible values of systematic uncertainities within the Gaussian constraints of predicted signal and background values. This fit is performed by minimizing

$$\chi^2 = 2 \sum_i (p'_i - d_i) - d_i \; ln \; (\frac{p'_i}{d_i}) + \sum_j L_j^2 \tag{6.7}$$

The L_j are fit to minimise the equation. For best fit, only bins with $s_i/b_i < 10^{-3}$ is used.

Sensitivity of experiment is also expressed as median expectation of limit which is the limit for which number of experiments having result above as well as below it will be same, in absence of the signal. This limit is calculated in a pseudo experiment in which background prediction is substituted for observed data events in Equation 6.2. The resulting CL_s is referred as CL_s^{exp} whereas CL_s for the observed data in the experiment is referred as CL_s^{obs}.

6.3 Systematic Uncertainties

In addition of statistical uncertainities we also assigned systematic uncertainities which arises due to experimental limitations or the theory on which experiment is based. Systematic uncertainities are determined by varying the source of uncertanities and looking at the resulting BDT output distributions. Uncertanities can arise from variety of sources like trigger simulation, jet energy calibration and resolution, jet reconstruction efficiency, lepton identification, b-tagging, theoretical cross sections used, including an uncertainity on luminosity measurement to estimate data.

We have broadly two type of systematic uncertainities:

- Scale systematics (also called flat systematics) that only affect the signal and/or background yields of final discriminants.
- Shape systematics that affect the shape of the final discriminants.

6.3.1 Scale Uncertainity

All the uncertainities arising from the normalization procedure are listed here. By varying the source of uncertainity, we assess its impact on overall normalization. These uncertainities are given as percentange (%) change from the nominal value.

- **Luminosity:** A 6.1% uncertainty comes from the error on the integrated luminosity on data. This is a normalization-only systematic uncertainty.
- **Trigger:** We apply a flat 2% uncertainty because of trigger parametrization.
- **Cross section:** The input cross sections for the SM processes suffer from theoretical uncertainities. The systematic uncertainties on the cross sections of the various SM processes involved varies from 6% for signal and for the production of (W/Z)+jets, to 10% for single and double top production.
- **Vector Boson $Z/Wp_T(Vp_T)$ reweighting:** The impact of Vp_T reweighting in the two-jet sample is estimated as a flat 2% normalization uncertainty and is combined with the existing 6% assigned to the cross section.
- **Heavy flavor ratio:** The uncertainty on the heavy flavor ratio in $(W/Z)b\bar{b}$ and $(W/Z)c\bar{c}$ cross sections is calculated within MCFM to be +19/-18% . We assign a 20% uncertainty on the ratio of heavy to light flavor production.
- **Multijet modelling:** After selection cuts, we compute all-flavor multijet event yields in the signal sample after the selection cuts. The heavy-to-all flavor multijet ratio is computed at all tag levels in the multijet control sample which has a very large statistics. The corresponding uncertainty is therefore negligible. A further uncertainty is due to the fact that we propagate this ratio to the signal sample. Finally we estimate the double-tagged multijet background from an inclusive single-tag sample. The shape is modelled very well in the high statistics multijet control sample, and the normalization uncertainty is again negligible. Furthermore, the same normalization is obtained in the sideband of the signal sample, although with a larger uncertainty.

  In our final selection after cutting on the multijet-DT output, the multijet contribution is reduced to a small (negligible) amount in the 1-tag (2-tag) samples. In

view of all the above effects, we assign a conservative 25% flat uncertainty. This is treated as a normalization-only systematic uncertainty.

- **Lepton identification:** Lepton identification efficiencies affect the lepton veto used in the selection of the signal sample. Muon identification efficiencies also affect the selection of the EW control sample. These uncertainities are within 1-2%.

6.3.2 Shape Sytematics

All the shape systematics are described below. Shape of the individual systematics were fluctuated by 1σ and there effect on the shape of final discriminant is used as uncertainity on that systematic.

- **Jet reconstruction and identification:** Jet-identification is more efficient in MC therefore scale factors provided by the Jet-ID group are used to remove MC jets to account for data/MC differences in jet reconstruction. Identification efficiencies are varied by -1σ of their uncertainties, and the result is symmetrized.

- **Jet energy scale:** Initial MC jet energies are shifted after modifying the JSSR shifting correction factors by $\pm 1\sigma$ of their uncertainties. The same approach is used for other jet systematics: energy resolution, reconstruction and identification, vertex confirmation, and taggability.

- **Jet energy resolution:** Initial MC jet energies are smeared, to match the energy resolution as measured in data, after modifying the JSSR smearing correction factors by $\pm 1\sigma$ of their uncertainties.

- **Vertex confirmation:** For Run IIb an additional requirement of vertex confirmation is applied on jets and therefore uncertainity in corresponding vertex confirmation scale factors, used to remove MC jets to account for data/MC differences in vertex confirmation, were varied by -1σ, and the result was symmetrized.

- **Taggability:** The taggability scale factors are used to remove MC jets to account for data/MC differences in taggability. They were varied by -1σ of their uncertainties, and the result was symmetrized.

- **b tagging:** Flavor-dependent scale-factors are used to weight MC events according to the flavor of the jets in the event to account for data/MC differences in efficiencies for direct tagging. These weights were varied by $\pm 1\sigma$ of their uncertainties.

- **ALPGEN parameters uncertainties:** Uncertainties arise in ALPGEN from the choice of MLM matching p_T threshold, the choice of MLM clustering radius, and

from two scaling parameters, the $k_\perp$- and Q-factor [93]. These are combined into two independent shape-only uncertainties: related to the MLM algorithm and related to the light and heavy flavor scaling parameters. The MLM algorithm uncertainty is only applied to V+jets samples with light flavor jets.

- **Underlying event and fragmentation modeling:** The dijet mass was found to be not consistent with respect to various PYTHIA tunes and also it does not agree on comparison of ALPGEN interfaced with PYTHIA to more precise HERWIG, therefore a shape-only systematic uncertainty is applied to all V+jets samples.

- **Parton Distribution Function (pdf) Uncertainty:** The signal acceptance and modeling is sensitive to the pdfs used in generation. To assess the impact of the uncertainties on these pdfs, a re-weighting is used. The signal has been generated using CTEQ6L1 pdf, but to assess the pdf uncertainty we perform a per-event re-weighting (based on the properties of the incoming partons) to CTEQ6.1M and the 20 pairs of associated error sets.

Impact of various uncertainities on the simulated samples can be seen in Table 6.1-6.4.

6.4 Results

The BDT outputs are used for calculating confidance level for data signal and background. If the CL_s is greater than the 5%, the signal is multiplied by a factor until $CL_s < 5\%$ within precision of 0.1%. This factor is the ratio of upper limit of the Higgs production cross section to the predicted cross section $\sigma^{limit}/\sigma^{predicted}$ where $\sigma^{predicted}$ is the cross section used to generate the signal distribution. 10^5 pseudo experiments simulated outcome are used for calculating upper limit within an accuracy of better than 0.1% in the CL, $4.9\% < CL_s < 5.1\%$. Upper limits are extracted as function of Higgs mass for $100\ GeV < m_H < 150\ GeV$ in the bins if 5 GeV.

Final discriminants for combined Run IIa and Run IIb samples is shown in Fig. 6.1.

We use standard DØ limit calculator package [94, 95] for getting limits. Fig. 6.2 shows the log-likelihood ratio χ_d (LLR) for combined single and double tag for each Higgs mass point considered. The log-likelihood ratio (LLR) plot consist of following values - the LLR values for the signal+background hypothesis ($\mathrm{LLR_{s+b}}$), background-only hypothesis ($\mathrm{LLR_b}$), and the observed data ($\mathrm{LLR_{obs}}$). The shaded bands represent the 1 and 2 standard deviation (σ) departures for $\mathrm{LLR_b}$. These distributions can be interpreted as follows:

	$\sum$ Bkgd	signal	Top	Diboson
Jet energy scale	3.7	3.0	0.4	5.8
Jet resolution	1.5	0.3	0.3	2.2
*Jet reco*ID*	0.3	0.6	4.1	1.1
Direct taggability	2.8	4.2	0.3	4.3
MC b-tag Heavy Flavor	3.3	0.7	3.6	3.6
MC b-tag Light Flavor	0.9	0.1	0.2	0.6
Trigger	1.7	0.8	1.2	2.5
Electron identification	0.3	0.4	0.6	0.3
Muon identification	1.0	0.9	1.8	0.9
Heavy-flavor fractions	8.9	–	–	–
Cross section	7.3	6.0	10.0	7.0
Luminosity	6.1	6.1	6.1	6.1
	Z+lf	Z+hf	W+lf	W+hf
Jet energy scale	5.9	5.3	6.6	5.2
Jet resolution	2.8	1.5	3.2	2.4
*Jet reco*ID*	1.1	1.0	1.3	1.1
Direct taggability	4.5	4.2	4.4	3.7
Vertex confirmation	–	–	–	–
MC b-tag Heavy Flavor	0.3	4.0	2.7	4.0
MC b-tag Light Flavor	8.3	0.1	3.6	–
Trigger	2.0	2.2	1.6	2.1
Electron identification	–	–	0.1	0.6
Muon identification	0.1	0.1	0.6	1.6
Heavy-flavor fractions	–	20.0	–	20.0
Cross section	6.3	6.3	6.3	6.3
Luminosity	6.1	6.1	6.1	6.1

Table 6.1: Relative systematic uncertainties (in %) on SM background expectations and on the ZH/WH signal ($m_H = 115GeV$) for the p17 single tag analysis. Top includes $t\bar{t}$ and single top. Shape dependent errors are in *italic* and the quoted numbers are just the integral values to give an order estimate. Uncertainties less than absolute value of 0.1 are displayed as 0. The normalization uncertainity on the multijet background is included in the cross section catagory for the total background.

	$\sum$ Bkgd	signal	Top	Diboson
Jet energy scale	3.2	3.4	0.5	6.7
Jet resolution	1.2	1.0	-0.2	1.5
*Jet reco*ID*	1.0	0.6	4.5	1.2
Direct taggability	2.7	4.1	0.4	4.5
MC b-tag Heavy Flavor	7.4	7.6	8.2	7.1
MC b-tag Light Flavor	1.2	0.1	0.5	1.1
Trigger	1.9	0.2	1.4	2.3
Electron identification	0.4	0.3	0.8	0.1
Muon identification	1.5	0.8	1.8	0.7
Heavy-flavor fractions	10.2	–	–	–
Cross section	8.6	6.0	10.0	7.0
Luminosity	6.1	6.1	6.1	6.1
	Z+lf	Z+hf	W+lf	W+hf
Jet energy scale	7.1	5.3	7.5	5.1
Jet resolution	3.7	1.3	2.9	2.4
*Jet reco*ID*	0.6	1.2	1.3	1.1
Direct taggability	3.7	4.2	4.6	3.8
MC b-tag Heavy Flavor	0.7	7.6	2.0	7.2
MC b-tag Light Flavor	13.8	0.5	10.1	0.8
Trigger	3.1	2.2	2.3	2.2
Electron identification	–	–	0.2	0.3
Muon identification	7.8	1.1	–	1.7
Heavy-flavor fractions	–	20.0	–	20.0
Cross section	6.3	6.3	6.3	6.3
Luminosity	6.1	6.1	6.1	6.1

Table 6.2: Relative systematic uncertainties (in %) on SM background expectations and on the ZH/WH signal ($m_H = 115GeV$) for the p17 two asymmetric tags analysis. Top includes $t\bar{t}$ and single top. Shape dependent errors are in *italic* and the quoted numbers are just the integral values to give an order estimate. Uncertainties less than absolute value of 0.1 are displayed as 0. The normalization uncertainity on the multijet background is included in the cross section catagory for the total background.

	$\sum$ Bkgd	signal	Top	Diboson
Jet energy scale	4.2	2.5	1.5	5.5
Jet resolution	1.8	0.5	0.9	0.7
*Jet reco*ID*	0.5	0.7	0.8	1.1
Direct taggability	1.3	1.9	0.5	1.6
Vertex confirmation	2.0	2.9	0.1	3.1
MC b-tag Heavy Flavor	3.2	1.8	4.2	4.4
MC b-tag Light Flavor	4.3	–	0.1	3.7
Trigger	3.1	3.6	3.6	3.6
Electron identification	0.2	0.2	0.5	0.3
Muon identification	1.3	1.0	1.9	1.1
Heavy-flavor fractions	8.0	–	–	–
Cross section	9.7	6.0	10.0	7.0
Luminosity	6.1	6.1	6.1	6.1
	Z+lf	Z+hf	W+lf	W+hf
Jet energy scale	6.5	5.1	7.7	6.2
Jet resolution	3.3	2.0	3.8	2.6
*Jet reco*ID*	1.1	0.6	1.1	1.0
Direct taggability	2.6	1.4	1.8	1.7
Vertex confirmation	2.9	2.3	3.2	2.8
MC b-tag Heavy Flavor	0.2	4.3	2.2	4.0
MC b-tag Light Flavor	24.9	0.5	11.8	0.6
Trigger	3.3	3.3	3.3	3.4
Electron identification	–	–	0.1	0.3
Muon identification	1.1	0.4	1.1	1.9
Heavy-flavor fractions	–	20.0	–	20.0
Cross section	6.3	6.3	6.3	6.3
Luminosity	6.1	6.1	6.1	6.1

Table 6.3: Relative systematic uncertainties (in %) on SM background expectations and on the ZH/WH signal ($m_H = 115GeV$) for the p20 single tag analysis. Top includes $t\bar{t}$ and single top. Shape dependent errors are in *italic* and the quoted numbers are just the integral values to give an order estimate. Uncertainties less than absolute value of 0.1 are displayed as 0. The normalization uncertainity on the multijet background is included in the cross section catagory for the total background.

	$\sum$ Bkgd	signal	Top	Diboson
Jet energy scale	3.2	2.6	1.5	6.3
Jet resolution	1.2	1.2	0.8	0.9
*Jet reco*ID*	0.2	0.7	0.8	1.0
Direct taggability	1.1	2.1	0.5	1.6
Vertex confirmation	1.7	3.1	0.2	3.1
MC b-tag Heavy Flavor	7.6	8.8	8.5	7.7
MC b-tag Light Flavor	2.6	0.1	0.6	2.3
Trigger	3.4	3.6	3.6	3.6
Electron identification	0.5	0.2	0.7	0.2
Muon identification	1.5	1.2	2.2	0.9
Heavy-flavor fractions	9.8	–	–	–
Cross section	7.9	6.0	10.0	7.0
Luminosity	6.1	6.1	6.1	6.1
	Z+lf	Z+hf	W+lf	W+hf
Jet energy scale	11.5	5.0	7.8	6.1
Jet resolution	4.8	2.1	3.9	2.8
*Jet reco*ID*	1.1	0.5	1.1	1.0
Direct taggability	0.8	1.3	1.8	1.6
Vertex confirmation	5.1	2.3	3.1	2.8
MC b-tag Heavy Flavor	1.1	8.0	2.0	7.9
MC b-tag Light Flavor	32.9	0.7	22.1	0.9
Trigger	3.6	3.4	3.5	3.4
Electron identification	–	–	0.6	0.5
Muon identification	–	0.5	0.9	1.8
Heavy-flavor fractions	–	20.0	–	20.0
Cross section	6.3	6.3	6.3	6.3
Luminosity	6.1	6.1	6.1	6.1

Table 6.4: Relative systematic uncertainties (in %) on SM background expectations and on the ZH/WH signal ($m_H = 115GeV$) for the p20 two asymmetric tags analysis. Top includes $t\bar{t}$ and single top. Shape dependent errors are in *italic* and the quoted numbers are just the integral values to give an order estimate. Uncertainties less than absolute value of 0.1 are displayed as 0. The normalization uncertainity on the multijet background is included in the cross section catagory for the total background.

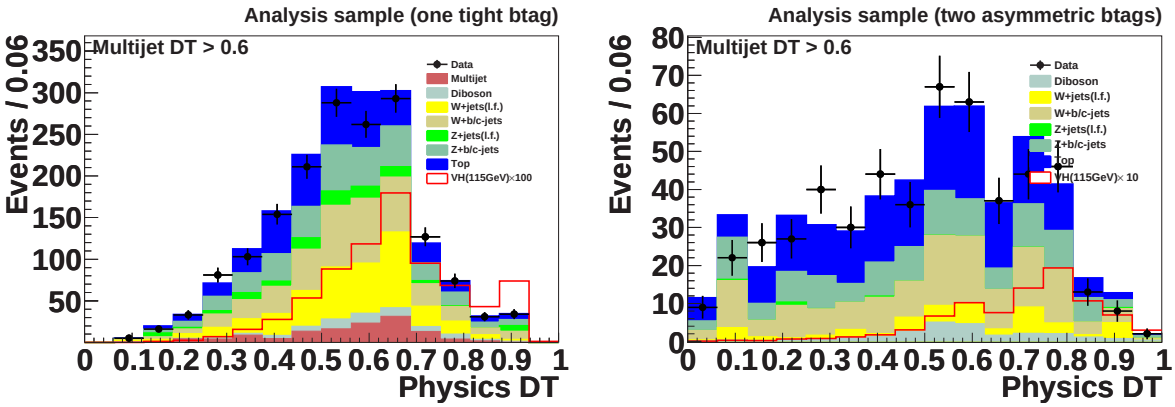

Figure 6.1: Inputs for limit calculation after a multi-jet decision tree cut of 0.6, and after data preparation, Run IIa and Run IIb combined. Left: 1-tag physics decision tree output in the 1-tag sample. Right: 2-tag physics decision tree output in the 2-tag sample. All inputs are for a Higgs mass of 115 GeV.

- The separation between $\mathrm{LLR_b}$ and $\mathrm{LLR_{s+b}}$ provides a measure of the overall power of the search. This is the ability of the analysis to discriminate between the s+b and b-only hypotheses.

- The width of the $\mathrm{LLR_b}$ distribution (shown here as 1 and 2 standard deviation (σ) bands) provides an estimate of how sensitive the analysis is to a signal-like fluctuation in data, taking account of the presence of systematic uncertainties. For example, when a 1-σ background fluctuation is large compared to the signal expectation, the analysis sensitivity is thereby limited.

- The value of $\mathrm{LLR_{obs}}$ relative to $\mathrm{LLR_{s+b}}$ and $\mathrm{LLR_b}$ indicates whether the data distribution appears to be more signal-like or background-like. As noted above, the significance of any departures of $\mathrm{LLR_{obs}}$ from $\mathrm{LLR_b}$ can be evaluated by the width of the $\mathrm{LLR_b}$ distribution.

Fig. 6.3 shows the cross section limit times branching ratio for the SM Higgs boson production, $\sigma(ZH)$ x $B.R(H \to b\bar{b})$, relative to the standard model production for each Higgs mass point considered. For a Higgs boson of mass 115 GeV, the observed and expected limits on the combined cross section of ZH and WH production multiplied by the branching fraction of $H \to b\bar{b}$ are factors of 3.7 and 4.6 times the SM value, respectively. The observed and expected limits for all 11 Higgs mass points are shown in Table 6.1.

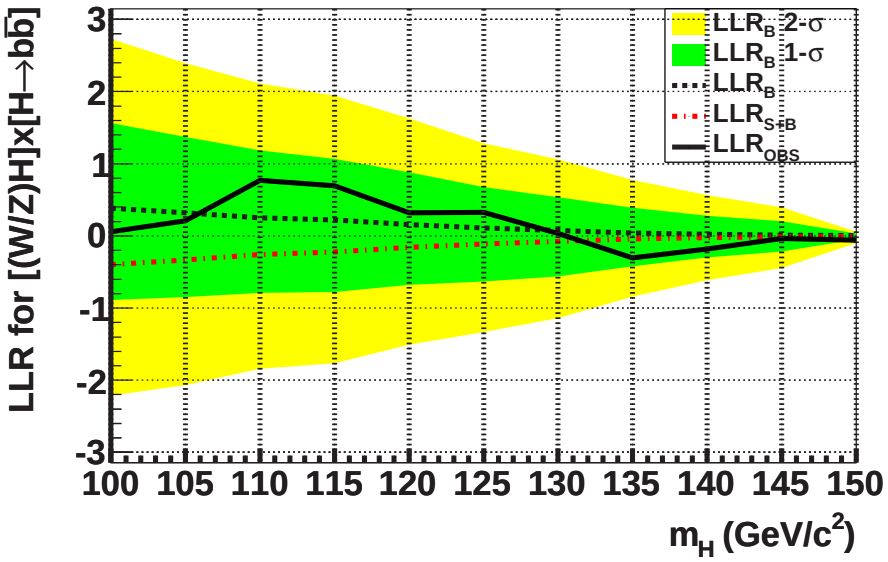

Figure 6.2: The log-likelihood ratios distribution for the combined result using boosted decision trees.

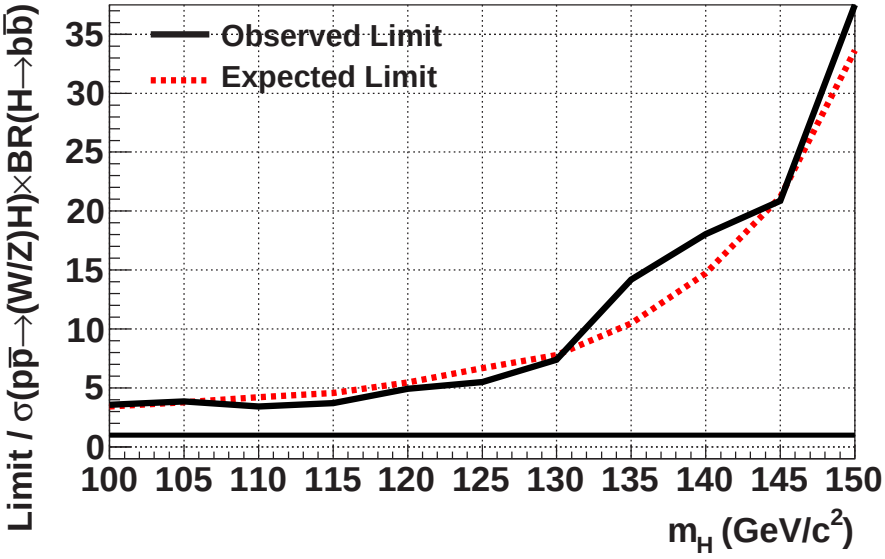

Figure 6.3: Expected and observed 95% CL upper limits on the cross section ratios for the combined result using the boosted decision trees.

m_H (GeV)	Observed	Expected
100	3.7	3.5
105	4.0	3.7
110	3.2	4.2
115	3.7	4.6
120	4.6	5.4
125	5.6	6.3
130	8.2	7.6
135	14.5	10.5
140	15.3	14.0
145	24.4	20.5
150	43.6	32.3

Table 6.5: Observed and expected ratios of excluded to SM production cross section multiplied by the branching fraction for $H \to b\bar{b}$, as a function of m_H.

Chapter 7

Conclusion

In this thesis we have presented a search for the associated production of Z and Higgs boson in the $\nu\bar{\nu}b\bar{b}$ final states, using 5.2 fb^{-1} of $p\bar{p}$ collisions data collected between 2002 to 2009, with the DØ detector at the Fermilab Tevatron collider. In addition of the cut based analysis various sophisticated techniques, like boosted decision tree, was used to reduce the potential backgrounds while retaining high signal efficiency. Data events were used to derive multijet background. A separate BDT was trained to get rid of most of the multijet background. Further application of b-tagging reduced most of the light flavour jets. Validity of background modeling was tested in separate control samples. Final separation between signal and remaining SM backgrounds was achieved by training a BDT. Systematic uncertainties were also incorporated into the output of training, the final discriminants. At every stage of the analysis good agreement between data and SM background predictions was achieved. In absence of any excess of data over background predictions, an upper limit was evaluated at 95% CL by comparing data with large number of pseudo experiments having background only and signal+background hypothesis.

Assuming a Higgs boson is present, we exclude combined ZH and WH production above 3.7 times the SM expectation for Higgs mass of 115 GeV. The result has been published in Physical Review Letters [96] and it was the best limit for any single low mass Higgs search channel in Tevatron at the time of its publication.

As we observe we have not found any hint of existence or non-existence of Higgs boson in this analysis but since the production cross-section at Tevatron is very low, it is extremely difficult to observe the Higgs even if it exists in any single search channel. Therefore sensitivity is increased by combining results from various Higgs channels and results from both the experiments, the CDF and DØ. The latest Tevatron combination of Higgs search using 8.6 fb^{-1} from both the experiments has excluded Higgs boson in the mass range 156 GeV to 177 GeV. For Higgs boson of mass 115 GeV the sensitivity has already reached 1.17 times the SM value. Tevatron will operate till September 2011 and

both the experiments are expected to record more than 10 fb^{-1} of data for the analysis. In addition, both the experiments, CDF and DØ, are working very hard to improve the analysis techniques so that better sensitivity can be achieved which is essential for possible observation of Higgs or exclusion of it for all allowed masses. At DØ our understanding of this channel is increasing day by day and we are expected to achieve SM sensitivity with the full data set in coming years.

Bibliography

[1] J. J. Thomson, Philosophical Magazine, 44, 5, 293 (1897).

[2] N. Bohr, Philosophical Magazine, 26, 1 (1913); M. Planck, *The Theory of Heat Radiation*, P. Blakiston's Son and Company, Philadelphia, Pennsylvania, (1914); W. Heisenberg, Journal for Physics, 33 (1925); E. Schrodinger, Phys. Rev. 28, 6 (1926).

[3] A. Einstein, "On the Electrodynamics of Moving Bodies", Annalen der Physik 17, 891 (1905); "On the General Theory of Relativity", Annalen der Physik 49, 769 (1916).

[4] E. Rutherford, Philosophical Magazine, 21, 669 (1911); Philosophical Magazine, 27, 488 (1913); Nature 92, 423 (1913).

[5] E. Rutherford, Philosophical Magazine and Journal of Science, 6th series, 37, 581 (1919).

[6] E. Goldstein, "Uber eine noch nicht untersuchte Strahlungsform an der Kathodeinducirter Entladungen," Berlin Akd. Monatsber., II, 691 (1886).

[7] J. Chadwick, Nature, 129, 312 (1932).

[8] P. A. M. Dirac, Proc. R. Soc., London A114, 243, 710 (1927).

[9] P. A. M. Dirac, Proc. R. Soc., London A117, 778, 610 (1928).

[10] P. A. M. Dirac, Proc. R. Soc., London A118, 779, 351 (1928).

[11] C. D. Anderson, Phys. Rev. 43, 491 (1932).

[12] W. Pauli letter of the 4th December 1930, Pauli Archive at CERN.

[13] E. Fermi, Z. Phys. 88, 161 (1934).

[14] R. P. Feynman, Phys. Rev. 76, 749 (1949); *QED : The Strange Theory of Light and Matter*, Princeton University Press, Princeton, New Jersey, (1985).

[15] J. Schwinger, *Quantum Electrodynamics I. A Covariant Formulation*, Phys. Rev. 74, 1439 (1948); *Quantum Electrodynamics II. Vacuum Polarization and Self Energy*, Phys. Rev. 75, 651 (1949); *Quantum Electrodynamics III. The Electromagnetic Properties of the ElectronRadiative Corrections to Scattering*, Phys. Rev. 76, 790 (1949).

[16] S. Tomonaga, Progr. Theoret. Phys. (Kyoto), 1, 27 (1946).

[17] S. Glashow, Nucl. Phys. 22, 579 (1961); S. Weinberg, Phys. Rev. Lett. 19, 1264 (1967); A. Salam, in *Elementary Particle Theory*, ed. N. Svartholm, Almqvist and Wiksells, Stockholm, 367 (1969).

[18] M. Gell-Mann, Phys. Lett. 8, 214 (1964); G. Zweig, CERN-Report 8182/TH401 (1964); H. Fritzsch, M. Gell-Mann and H. Leutwyler, Phys. Lett. B47, 365 (1973); D. Gross and F. Wilczek, Phys. Rev. Lett. 30, 1343 (1973); H.D. Politzer, Phys. Rev. Lett. 30, 1346 (1973); G. 't Hooft, Marseille Conference on Yang.Mills fields (1972).

[19] G. 't Hooft, Nucl. Phys. B35, 167 (1971); G. 't Hooft and M. Veltman, Nucl. Phys. B44, 189 (1972); G. 't Hooft, Nucl. Phys. B33, 173 (1971).

[20] P.W. Higgs, Phys. Lett. 12, 132 (1964);
F. Englert and R. Brout, Phys. Rev. Lett. 13, 321 (1964);
P.W. Higgs, Phys. Rev. Lett. 13, 508 (1964);
G.S. Guralnik, C.R. Hagen and T. Kibble, Phys. Rev. Lett. 13, 585 (1964);
P.W. Higgs, Phys. Rev. 145, 1156 (1966);
T. Kibble, Phys. Rev. 155, 1554 (1967).

[21] F.J. Hasert et al. (Gargamelle Collaboration), Phys. Lett. B46, 121 (1973); Phys. Lett. B46, 138 (1973); T. Eichten et al. (Gargamelle Collaboration), Phys. Lett. B46, 274 (1973).

[22] G. Arnison et al. (UA1 Collaboration), Phys. Lett. B122, 103 (1983); M. Banner et al. (UA2 Collaboration), Phys. Lett. B122, 476 (1983); G. Arnison et al. (UA1 Collaboration), Phys. Lett. B126, 398 (1983); P. Bagnaia et al. (UA2 Collaboration), Phys. Lett. B129, 130 (1983).

[23] G. Abbiendi. et al. (The ALEPH Collaboration, The DELPHI Collaboration, The L3 Collaboration and The OPAL Collaboration, The LEP Working Group for Higgs Boson Searches), Phys. Lett. B565, 61 (2003).

[24] *A Combination of Preliminary Electroweak Measurements and Constraints on the Standard Model*, [LEP Electroweak Working Group], arXiv:hep-ex/0612034 http://lepewwg.web.cern.ch/LEPEWWG/

[25] F. Abe et al. (CDF Collaboration), Phys. Rev. Lett. 74, 2626 (1995).

[26] S. Abachi et al. (DØ Collaboration), Phys. Rev. Lett. 74, 2632 (1995).

[27] *Combination of CDF and DØ Results on the Mass of the Top Quark*, (Tevatron Electroweak Working Group, CDF, DØ Collaborations), arXiv:1007.3178v1 [hep-ex].

[28] Stefano Catani, Nucl. Phys. B. 157, 1, 202 (2006).

[29] K. Nakamura et al., [Particle Data Group Collaboration], J. Phys. G37 (2010).

[30] T. Nakano and K. Nishijima, "Charge Independence for V-particles". Progress of Theoretical Physics 10, 581 (1955); K. Nishijima, "Charge Independence Theory of V Particles". Progress of Theoretical Physics 13, 285 (1955); M. Gell-Mann, "The Interpretation of the New Particles as Displaced Charged Multiplets". Il Nuovo Cimento 4, 848 (1956)

[31] [LEP/TEV EW WG Plots for Summer 2011] http://lepewwg.web.cern.ch/LEPEWWG/plots/summer2011

[32] *Combined CDF and DØ Upper Limits on Standard Model Higgs-Boson Production with up to 8.6 fb^{-1} of Data*, [The TEVNPH Working Group of the CDF and DØ Collaborations], arXiv:1107.5518 [hep-ex]; July 2011.

[33] *Precision Electroweak Measurements and Constraints on the Standard Model*, [ALEPH, CDF, DØ , DELPHI, L3, OPAL and SLD Collaborations, LEP Electroweak Working Group, Tevatron Electroweak Working Group and LD Electroweak and Heavy Flavour Groups], arXiv:0911.2604[hep-ex].

[34] http://www-cdf.fnal.gov/physics/exotic/r2a/20040722.lmetbj_wh_tc

[35] M. Carena *et al.*, *Report of the Tevatron Higgs Working Group*, arXiv:hep-ph/0010338; CDF and DØ Collaborations, *Results of the Tevatron Higgs Sensitivity Study*, FERMILAB-PUB-03/320-E (2003).

[36] [ATLAS Collaboration], *"Limits on production of the Standard Model Higgs boson in pp collisons at $\sqrt{s}$=7 TeV with the ATLAS detector"* [arXiv:hep-ex/1106.2748].

[37] S. Abachi et al., *The DØ Collaboration :The DØ detector* , Nucl. Instr. And Methods in Phys. Res. A **338**, 185 (1994).

[38] DØ Collaboration, *The Upgraded DØ Detector*, Nucl. Instrum. Methods in Phys. Res. A **565**, 463 (2006).

[39] *The DØ Upgrade Silicon Tracker Technical Design Report*, DØ Note 2169.

[40] *The DØ Upgrade Central Fiber Tracker Technical Design Report*, DØ Note 4164.

[41] M.Adams et al.,*Design Report of the Central Preshower Detector for the DØ Upgrade*, DØ Note 3014.

[42] J. Brzezniak, et al., *Conceptual Design of a 2 Tesla Superconducting Solenoid for the Fermilab DO Detector Upgrade*, DØ Note 2167.

[43] *The DØ Upgrade : Forward Preshower, Muon System and Level2 Trigger*, DØ Note 2894.

[44] *Design Report: The DØ Experiment at the Fermilab Proton-Antiproton Collider*, DØ Note 137 (1984).

[45] L. Groer, *DØ Calorimeter Upgrades for Tevatron Run II*, DØ Note 4240.

[46] R. Zitoun, *Study of the Non Linearity of the DØ Calorimeter Readout Chain*, DØ Note 3997.

[47] Junjie Zhu, Ph.D. Thesis, University of Maryland (2004).

[48] B. Abbott et al. (DØ Collaboration), Phys. Rev. Lett. **80** (1998); Phys. Rev. **D58** (1998).

[49] *DØ Run II Level 1 Trigger Framework Technical Design Report*, http://www.pa.msu.edu/hep/d0/ftp/l1/framework/l1fw_tdr_05june98.txt.

[50] D. Edmunds et al., DØ Note **3402** (1998).

[51] A. Boehnlein et. al., DØ Note **3630** (1999).

[52] Common Sample Group Skim Definitions, `http://www-d0.fnal.gov/Run2Physics/cs/skimming/p20_pass2_skims.html`

[53] M.L. Mangano *et al.*, JHEP **0307**, 001 (2003); version 2.11 was used.

[54] T. Sjöstrand, S. Mrenna and P. Skands, JHEP **0605**, 026 (2006); version 6.413 was used.

[55] E. Boos *et al.* (CompHEP Collaboration), Nucl. Instrum. Methods in Phys. Res. A **534**, 250 (2004).

[56] J. Campbell and K. Ellis, *MCFM - Monte Carlo for Femtobarn processes*, `http://mcfm.fnal.gov/`

[57] J. Pumplin *et al.*, JHEP **0207**, 012 (2002); D. Stump *et al.*, JHEP **0310**, 046 (2003).

[58] `http://www-d0.fnal.gov/computing/MonteCarlo/simulation/d0gstar.html`

[59] `http://wwwasd.web.cern.ch/wwwasd/geant/index.html`

[60] `http://www-d0.fnal.gov/computing/MonteCarlo/simulation/d0sim.html`

[61] `http://www-d0.fnal.gov/computing/algorithms/intro`

[62] W. Fisher, J. Haley, D. Price, *"Studies of Alpgen parameters, corrections and associated uncertainties"*, DØ Note 5966.

[63] R. Hamberg, W,L. van Neerven, and W.B. Kilgore, Nucl. Phys. **B359**, 343 (1991), and erratum in **B644**, 403.

[64] M. Cacciari *et al.*, JHEP **404**, 068 (2004); N. Kidonakis and R. Vogt, Phys. Rev. D **68**, 114014 (2003); N. Kidonakis, Phys. Rev. D **74**, 114012 (2006).

[65] T. Hahn *et al.*, *"SM and MSSM Higgs Boson Production Cross Sections at the Tevatron and the LHC"*, `arXiv:hep/ph:0607308v2`.

[66] The method is described for p14 in:
N. Makovec and J.-F. Grivaz, "Shifting, Smearing and Removing Simulated Jets", DØNote 4914 (2005)

[67] T. Bolton M. Shamim, *"Generator Level Reweighting of Z boson P_T"*, DØ Note 5565.

[68] G. Hesketh, *"Generator Level Re-weighting of the Inclusive W P_T Distribution"*, DØ Note 5786.

[69] U. Baur, R. K. Ellis and D. Zeppenfeld, *"QCD and weak boson physics in RunII. Proceedings, Batavia, USA, March 4-6, June 3-4, November 4-6, 1999"*.

[70] M. Voutilainen and C. Royon, *Jet p_T resolution using v7.1 JES for p17 data*, DØ Note 5381.

[71] S. Trincaz-Duvoid and P. Verdier, *Missing E_T Reconstruction in p17*, DØ Note 4474 (2004).

[72] S. Calvet, P. Verdier and E. Kajfasz, *Towards Missing E_T Certification and Unclustered Energies Studies*, DØ Note 4927 (2005).

[73] G. Borissov, *Status of DØ track reconstruction. Talk at All DØ Meeting, Feb 14, 2003.*

[74] G. Borissov, *Ordering a chaos or ... technical detail of AA tracking. Talk at All DØ Meeting, Feb 23, 2003.*

[75] A. Khanov, *HTF: histogramming method for finding tracks. The algorithm description*, DØ Note 3778 (2000).

[76] H. Greenlee, *The DØ Kalman track fit*, DØ Note 4303 (2003).

[77] H. Greenlee, *The DØ interacting propagator*, DØ Note 4293 (2003).

[78] A. Schawartzman and C. Tully, *Priamry Vertex Reconstruction by Means of Adaptive Vertex Fitting*, DØ Note 4918 (2005).

[79] A. Schawartzman and M. Narain, *Probabilistic Primary Vertex Selection*, DØ Note 4042 (2002).

[80] A. Schawartzman and M. Narain, *Secondary Vertex Reconstruction using the Kalman Fitter*, DØ Note 3908 (2001).

[81] V. M. Abazov *et al.*, Phys. Rev. D 76, 092007 (2007).

[82] A. Schwartzman, "Missing Et Significance Algorithm in RunII data", DØ Note 4254 (2003)

[83] V.M. Abazov *et al*, *"b-Jet identification in the D0 experiment"*, Nucl. Instrum. Methods in Phys. Res. A 620, 490 (2010).

[84] V. M. Abazov *et al.*, *"Observation of ZZ production in $p\bar{p}$ collisions at $\sqrt{s}$ = 1.96 TeV"*, Phys. Rev. Lett. **101**, 171803 (2008)

[85] P. Verdier, Y. Tschudi, *"Search for T-odd quarks in Little Higgs models with T-parity and first generation scalar leptoquarks in events with two acoplanar jets and missing transverse energy"*, DØ Note 5780 (2008)

[86] Y. Peters, *et al. "Study of the W+jets heavy flavor scale factor in p17"*, DØ Note 5406 (2007)

[87] L. Breiman *et al.*, *"Classification and Regression Trees,"* Wadsworth (1984).

[88] V. M. Abazov *et al.* [DØCollaboration], *"Evidence for production of single top quarks and first direct measurement of $|V(tb)|$,"* Phys. Rev. Lett. **98**, 181802 (2007) [arXiv:hep-ex/0612052].

[89] V. M. Abazov *et al.* [DØCollaboration], *"Evidence for production of single top quarks at DØ."* to be submitted to PRD, `http://www-d0.fnal.gov/Run2Physics/d0_private/eb/Run2EB_024/an_07/singletop_evidence_prd_v2.0_121307.pdf`

[90] `http://www-d0.fnal.gov/Run2Physics/top/public/fall06/singletop/DT_public_webpage/DecisionTrees.html#dt`

[91] Y. Coadou [CDF and DØCollaborations], *"Uses of multivariate analysis methods,"* PoS **TOP2006**, 016 (2006).

[92] Y. Freund and R.E. Schapire, *"Experiments with a New Boosting Algorithm,"* in Machine Learning: Proceedings of the Thirteenth International Conference, pp. 148-156 (1996).

[93] W. Fisher, J. Haley, D. Price *"Studies of Alpgen parameters, corrections, and associated uncertainties"*, DØ Note 5966.

[94] W. Fisher, *"Collie: A Confidence Level Limit Evaluator"*, DØ Note 5595.

[95] W. Fisher, *"Systematics and limit calculations"*, FERMILAB-TM-2386-E (2006).

[96] V. M. Abazov *et al,*, Phys. Rev. Lett. 104, 071801 (2010)